2009

High-Precision ID-TIMS U-Pb Zircon Geochronology of Three Cenomanian Bentonites from the Western Canada Foreland Basin

Ivan R. Barker

Recommended Citation

Barker, Ivan R., "High-Precision ID-TIMS U-Pb Zircon Geochronology of Three Cenomanian Bentonites from the Western Canada Foreland Basin" (2009). *Digitized Theses*. 4171.
https://ir.lib.uwo.ca/digitizedtheses/4171

High-Precision ID-TIMS U-Pb Zircon Geochronology of Three Cenomanian Bentonites from the Western Canada Foreland Basin

(Spine title: Zircon U-Pb Geochronology of Three Cretaceous Bentonites – Alberta)

(Thesis format: Monograph)

by

Ivan R. Barker

Graduate Program in Geology

Thesis submitted in partial
fulfillment of the requirements for the
degree of Master of Science

The School of Graduate and Postdoctoral Studies
The University of Western Ontario
London, Ontario, Canada

THE UNIVERSITY OF WESTERN ONTARIO
SCHOOL OF GRADUATE AND POSTDOCTORAL STUDIES

CERTIFICATE OF EXAMINATION

Supervisor	Examiners
____________________	____________________
Dr. Desmond Moser	Dr. Neil Banerjee
Co-Supervisor	____________________
	Dr. Sean Shieh
____________________	
Dr. Guy Plint	____________________
	Dr. Peter Ashmore

The thesis by

Ivan Richard Barker

entitled:

High-Precision ID-TIMS U-Pb Zircon Geochronology of Three Cenomanian Bentonites from the Western Canada Foreland Basin

is accepted in partial fulfillment of the
requirements for the degree of
Master of Science

Date____________________

____
Chair of the Thesis Examination Board

Abstract

The Western Canada foreland basin contains a rich record of Upper Cretaceous marine and tectonic change, yet is sparse in biostratigraphically useful fauna that permit continental and global correlation. However, numerous extensive bentonites have been mapped in Cenomanian strata and traced into the U.S. portion of the basin where relationships to globally correlated ammonite zones can be determined. The X, A-X and Bighorn River bentonites provide important calibration points for the Cenomanian Stage. Single zircon crystals from these bentonites were chemically-abraded and dated using high-precision U-Pb ID-TIMS geochronology techniques. The $^{206}Pb/^{238}U$ weighted-mean ages are: 95.87±0.10 Ma for the X-bentonite, 95.67±0.15 Ma for the A-X bentonite, and 94.29±0.13 Ma for the Bighorn River Bentonite (2σ confidence level). These new ages establish a more precise maximum age for the Cenomanian/Turonian boundary and allow for more accurate measurements of the timing and rates of Cenomanian tectonic and eustatic activity in western North America.

Keywords: U-Pb Isotope Geochronology, Tephrochronology, Upper-Cretaceous, Cenomanian, ID-TIMS, Zircon, Bentonite, Western Canada Foreland Basin, Stratigraphy, Blackstone Formation, Dunvegan Formation, Eustasy, Tectonics.

TABLE OF CONTENTS

LIST OF TABLES

LIST OF FIGURES

LIST OF APPENDICES

1. INTRODUCTION

1.1 Nature of the Investigation

The marine stratigraphic record preserves evidence of global processes such as marine circulatory, eustatic and climatic change (e.g. carbon isotope excursions), and regional processes such as basin subsidence due to tectonics, mountain building and erosion. Our understanding of the causes and rates of these processes that created the records is greatly enhanced if an absolute geochronologic framework can be established. This becomes possible if high-precision geochronology is integrated with lithostratigraphic analyses, as has been done in this study. A detailed lithostratigraphy for middle Cretaceous rocks over a large portion of the foreland basin in Alberta and British Columbia has been developed in recent years (e.g., Plint 2000; Varban and Plint 2005; Tyagi et al. 2007) and a generalized biostratigraphy exists that allows a broad differentiation of the geological Stages into 'lower' and 'upper' portions. However, reliable radiometric dates are lacking within these 'lower' and 'upper' portions. Previous workers such as Obradovich (1993) and Kowallis et. al. (1995), have measured bentonite ages from the middle Cretaceous time scale using ^{40}Ar/^{39}Ar radiometric methods in the Western Interior of the United States. Comparative studies between ^{40}Ar/^{39}Ar methods with U-Pb zircon methods, suggest that the U-Pb geochonometer can be more accurate and precise than the ^{40}Ar/^{39}Ar geochronometer (Schmitz and Bowring 2001a). No high-precision U-Pb zircon analyses, employing chemical abrasion, have been previously reported from the Western Canada Foreland Basin for the Upper Cretaceous Cenomanian Stage.

Three Cenomanian bentonites were sampled from outcrops of varying stratigraphic levels of the Western Canada Foreland Basin, and zircons were separated under ultra low-contamination conditions. The single zircon crystals were subjected to high-precision Isotope Dilution-Thermal Ionization Mass Spectrometry (ID-TIMS) employing chemical abrasion and an interlaboratory-calibrated EARTHTIME spike solution containing ^{202}Pb and ^{205}Pb (two isotopes of Pb that do not occur in nature). The new high-precision dates obtained through this study have the potential to deliver new insights into the correlation of strata across western North America and the evolution of the Western Canada Foreland Basin.

1.2 Geological Setting

1.2.1 The Western Interior Basin

1.2.1.1 Formation of the Western Interior Basin

The Western Interior Basin is one of the world's best known foreland basins, extending east-west for over 1000 km and north-south for over 5000 km, from the Canadian Arctic to the Gulf of Mexico, see Fig. 1.1 (DeCelles 2004). The Western Canada Foreland Basin is the portion of the Western Interior Basin that is located within

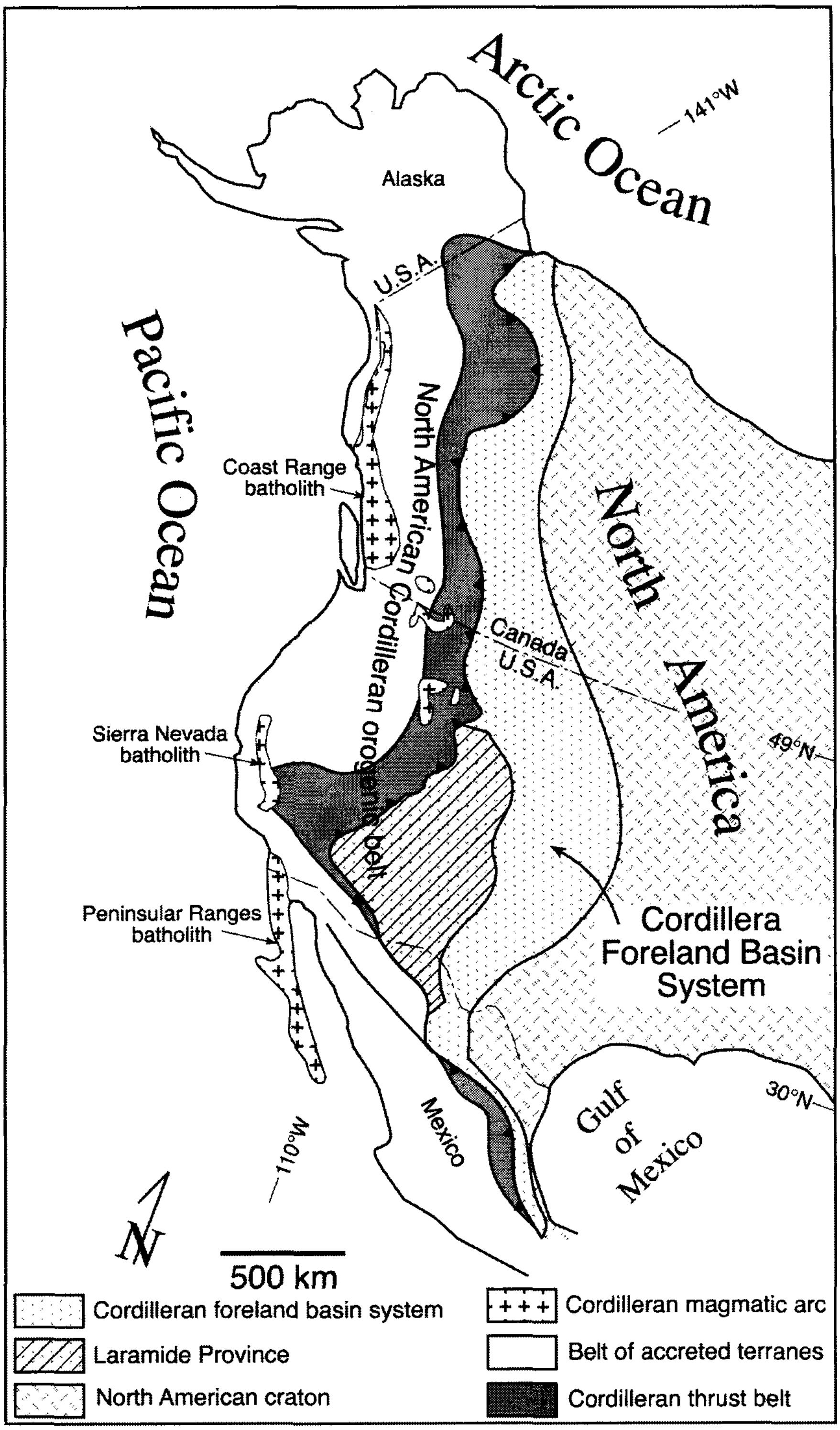

Figure 1.1. Regional map of the Western Interior Basin (termed Cordillera Foreland Basin System here) and the adjacent Cordilleran orogenic belt of North America. DeCelles (2004).

Canada and was the site of major flexural subsidence that led to multiple marine transgressions throughout the Late Jurassic and Cretaceous.

During the Late Jurassic, plate convergence and subduction occurred as the North American plate moved over the eastward subducting Kula-Farallon plate (Monger and Price 1979; Monger 1989); the North American and Kula-Farallon plates were converging at a rate of ~80 mm/yr, increasing to ~150 mm/yr by the Paleocene (Engebretson et al. 1984, 1985). As a result of the subduction-related events on the western edge of Canada, imbrication, shortening and thrusting of the pre-accretionary passive margin wedge occurred and the Rocky Mountain Cordillera began to form (Monger et al. 1982).

Orogenic thrust loading by the Cordilleran supracrustal thrust sheets added extra mass to the North American plate causing isostatic flexure and subsidence of the plate. The lithospheric flexure and regional subsidence caused the formation of a retro-arc foreland basin adjacent to the orogenic belt (Price 1973; Beaumont 1981; Jordan 1981; Fig. 1.2). The subsidence may have resulted from a combination of both the static load of the thrust sheets and dynamic forces (Fig. 1.3). Dynamic loading was caused by a drag force that was exerted by the asthenosphere on the underside of the continental lithosphere, which effectively broadened the wavelength of the regional subsidence (Mitrovica et al. 1989; Gurnis 1992). The static load of the thrust sheets generated a relatively narrow (<300 km), rapidly subsiding flexural foredeep and by Early Cretaceous to Turonian time a classical flexural foreland basin system, with a well developed

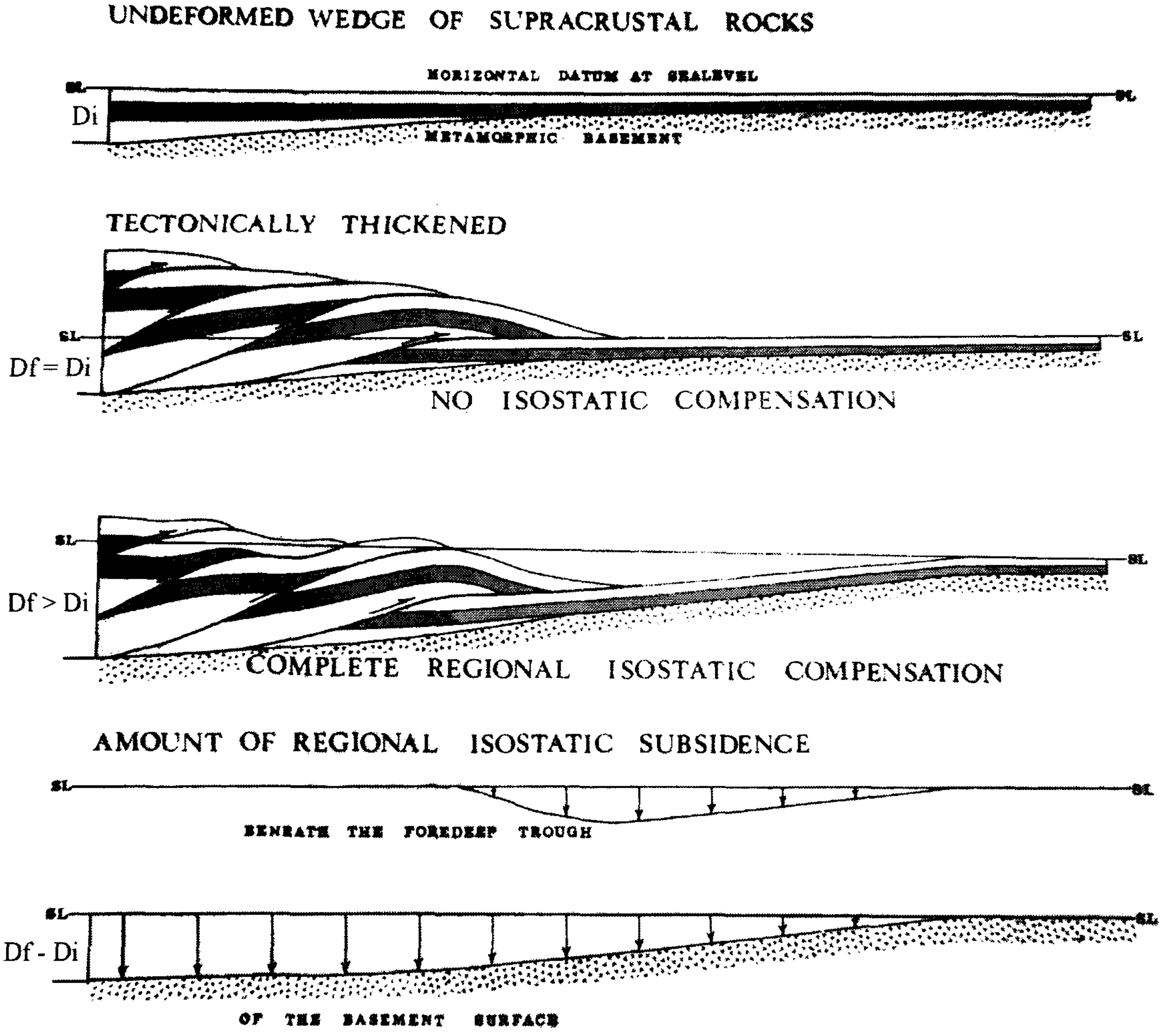

Figure 1.2. Conceptual model for the formation of the Western Interior Basin by regional isostatic flexure in response to orogenic loading of the Cordilleran thrust sheets. Where SL is sea-level; Di, is the initial depth to basement; Df, final depth to basement; Df - Di, amount of subsidence. When Df > Di, the basement isostatically compensates for the load. Modified from Price (1973).

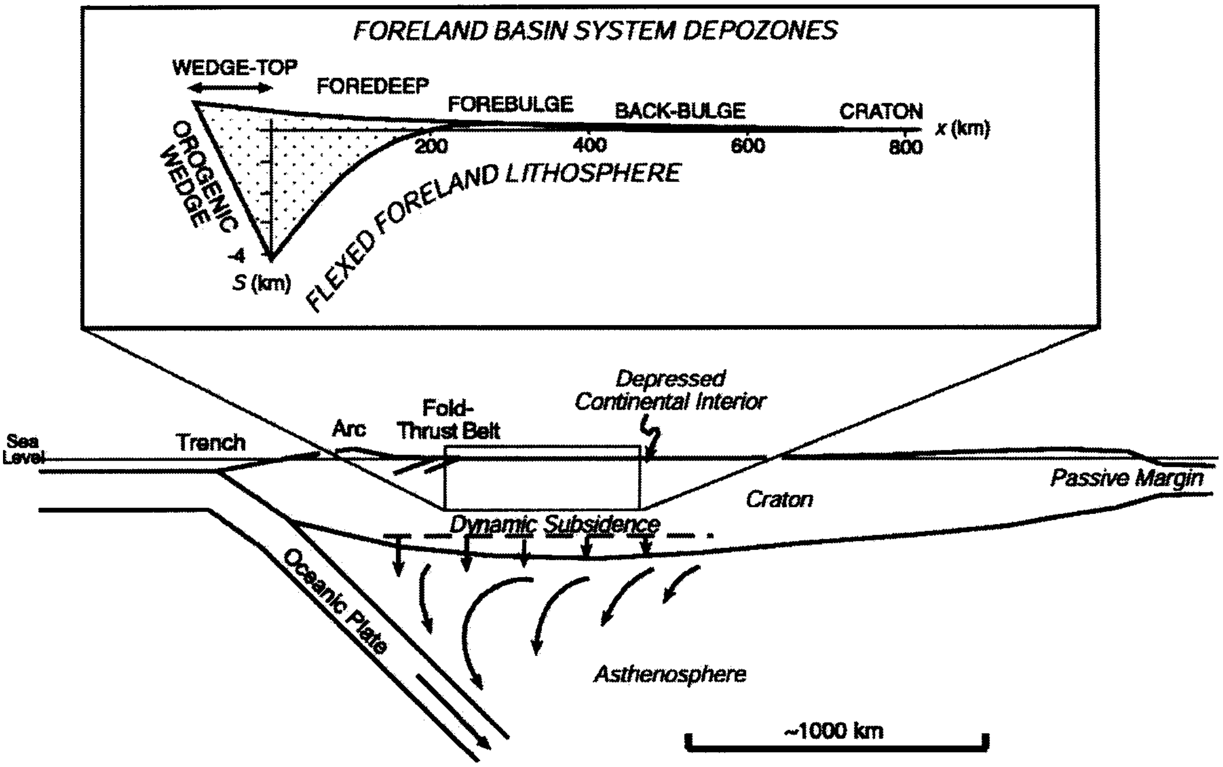

Figure 1.3. Conceptual model of a generalized retroarc system illustrating principal subsidence mechanisms. Upper panel shows the shorter wavelength subsidence. Lower panel depicts the longer wavelength, regional subsidence and the tilting of the craton down towards the trench. DeCelles (2004)

wedgetop, foredeep, forebulge and backbulge had developed (Jordan 1981; DeCelles and Currie 1996).

The basin underwent subsidence-driven widening due to the lateral propagation of the Cordilleran thrust sheets throughout Cretaceous time. The continental plate compensated for the laterally propagating thrust sheets through additional subsidence, which effectively increased the depth of the foreland basin (DeCelles 2004). A two dimensional kinematic-mechanical model proposed by Hardy et al. (1998) summarizes the development of a thrust wedge in the fold and thrust belt as having both gravitational and frictional work components. At any given time, the active thrust fault is one that has the minimal amount of gravitational and frictional work, but as dewatering and sedimentation of the thrust sheets occurs, frictional and increasing gravitational forces cause the thrust fault to become locked. Furthermore, displacement of the active fault may cause slight uplift, which imparts an additional amount of gravitational and frictional work, and it becomes energetically more efficient to activate another fault. Thrust faults propagate towards the foreland through time due to the combined result of the steepening of thrust faults, and increasing topographic (gravitational) load and frictional work on the hinterland faults. Reactivation of dormant faults could occur as the local topography above a fault is eroded, reducing the gravitational and frictional work components.

1.2.1.2 Western Interior Seaway

The Western Interior Basin underwent five major transgressive-regressive marine cycles between late Albian and early Maastrichtian time (~100 Megaanum [Ma] to ~71 Ma), the cycles were labeled T5-R5 to T9-R9 by Kauffman (1977). These cycles were the result of tectonic subsidence and eustatic sea level changes that were related to the joining and subsequent separation of the Boreal and Tethyan water masses; see Fig. 1.4 for a continental North America map showing the water masses. Beginning in middle Albian time, marine transgression (Cobban et al. 1994; DeCelles 2004) lead to the joining of the northern Boreal and southern Tethyan Seas, creating the Skull Creek-Joli Fou Sea by late Albian time (Tyagi et al. 2007). A major regression then occurred and the Skull Creek-Joli Fou Sea separated, causing the Tethyan Sea to have no connection with the Boreal Sea.

The Greenhorn cycle (T6-R6) began during the late Albian, peaked during the early Turonian and ended by the middle Turonian (Kauffman 1977). This cycle marked the most extensive flooding during the Cretaceous, leading to the eventual inundation of North America (Cadrin et al. 1995). The onset of the Greenhorn cycle initially resulted in the southward migration of northern Boreal waters forming the landlocked Mowry Sea during the latest Albian, which extended from the Arctic Ocean to Wyoming in the south (Fig. 1.4; Williams and Stelck 1975; Kauffman 1984; Schröder-Adams et al. 1996).

At the Albian/Cenomanian boundary (99.6 ±0.9; Ogg et al. 2005), continued transgression during the earliest Cenomanian caused the initial mixing of cool, brackish

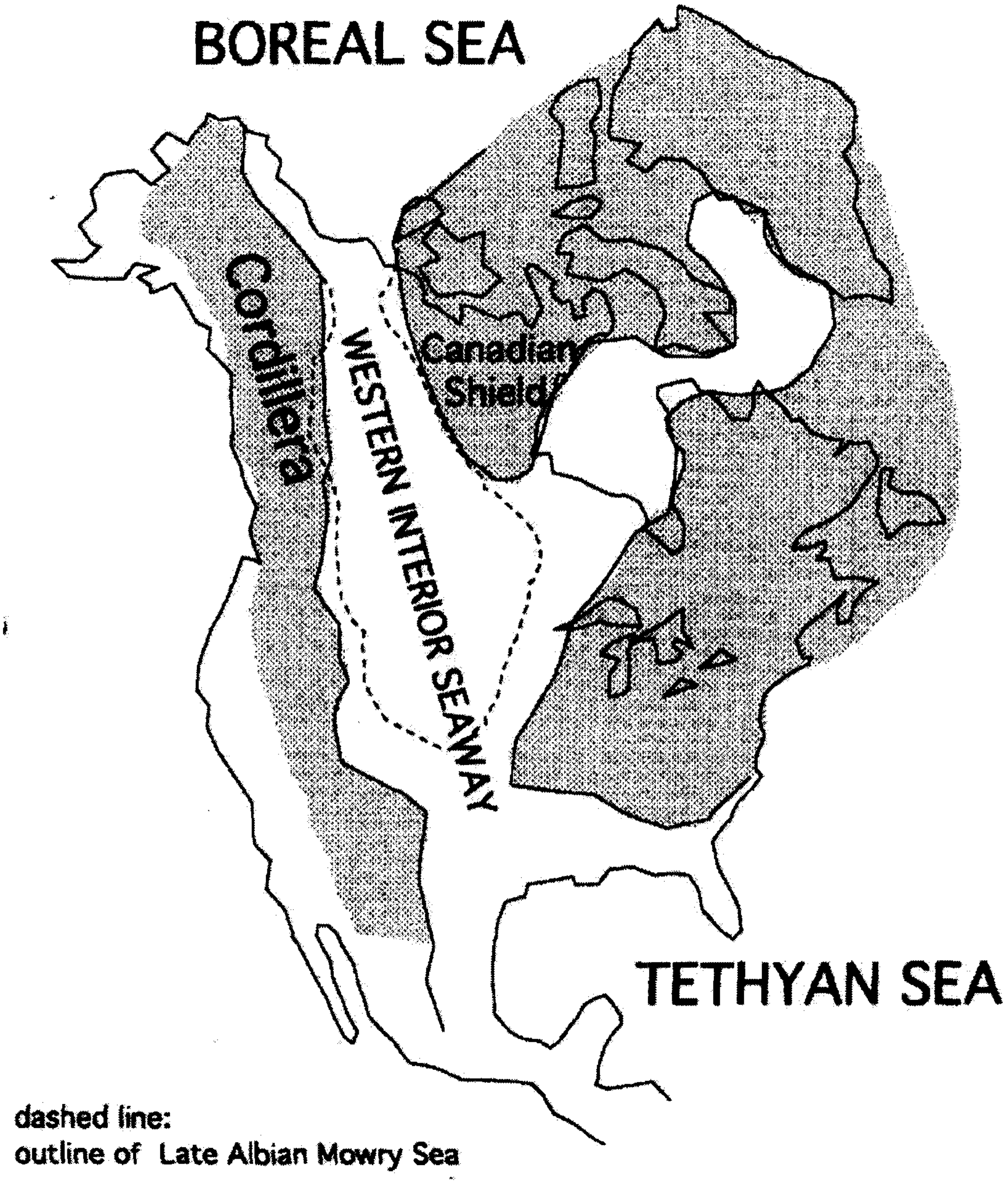

Figure 1.4. Regional map of the Western Interior Seaway, showing the location of the cool Boreal Sea, warm Tethyan Sea and intermediate late Albian Mowry Sea. Schröder-Adams et al. (1996).

Boreal waters with warm, normal salinity Tethyan waters, and the Western Interior Seaway began to form (Fig. 1.4; McNeil and Caldwell 1981; Bloch et al. 1993; Schröder-Adams et al. 1996). Due to the incomplete mixing of the water masses, the water column is interpreted to have become stratified (Schröder-Adams et al. 1996; Tyagi et al. 2007) and the bottom of the water column became anoxic, causing the loss of fauna.

In the latest Cenomanian and early Turonian a major sea-level rise allowed warm Tethyan waters to penetrate fully into the Western Interior Seaway. As a result, there was a northward migration of warm-water pelagic fauna at the Cenomanian/Turonian boundary (93.6 ±0.8 Ma; Ogg et al. 2005). At its greatest extent, the Seaway extended ~5000 km from the Beaufort Sea to the Gulf of Mexico and was ~1600 km wide, extending from western Ontario to the Rocky Mountain Trench, British Columbia (McGookey 1972; Kauffman and Caldwell 1993; Cadrin et al. 1995; Fig. 1.4).

1.2.1.3 Lithostratigraphy of the Western Canada Foreland Basin

The Colorado Group is the thickest and most regionally extensive succession of rocks in the Western Canada Foreland Basin. The Colorado Group extends in the subsurface east-west for 1300 km, from the foredeep adjacent to the Rocky Mountains to the forebulge in the Manitoba Escarpment (Bloch et al. 1993). The Colorado Group is an east-tapering wedge of marine shales that in northwestern Alberta is over 1500 m in thickness, thinning eastward to ~200 m in the Manitoba Escarpment (O'Connell et al. 1990; Schröder-Adams et al. 1996). The Colorado Group ranges from Albian to

Santonian in age and was deposited during the highest sea-level of the Mesozoic (Schröder-Adams et al. 1996).

The portion of the Colorado Group examined in this study is late Albian to Turonian in age and records the interaction between the Boreal and Tethyan water masses. This portion of the Colorado Group contains six regionally mappable lithostratigraphic units in the subsurface, beginning with the Joli Fou shale unconformably overlying the Mannville Group, and extending to the top of the Second White Specks Formation (Bloch et al. 1993). In ascending order this portion of the Colorado Group of Western Canada contains the Joli Fou, Viking, Westgate, Fish Scales, Belle Fourche and Second White Specks Formations; though the Joli Fou and Viking Formations are only included for comparison (Bloch et al. 1993); see Fig. 1.5 for the lateral stratigraphic relationships of the Colorado Group. The late Albian Westgate Formation was deposited in a low-salinity, cool, Boreal watermass, as the Boreal waters expanded southward during the initial stages of the Mowry Sea transgression (Schröder-Adams et al. 1996). The earliest Cenomanian Fish Scales Formation was deposited as the northern Boreal waters began to connect with the Tethyan waters. The water column was intensely stratified during deposition of the Fish Scales Formation, and bottom water anoxia resulted in the preservation of abundant fish debris. The middle to late Cenomanian Belle Fourche Formation conformably overlies the Fish Scale Formation. The early Turonian Second White Specks Formation was marked by maximum transgression of the Western Interior Seaway and prevailing anoxic bottom waters (Schröder-Adams et al. 1996).

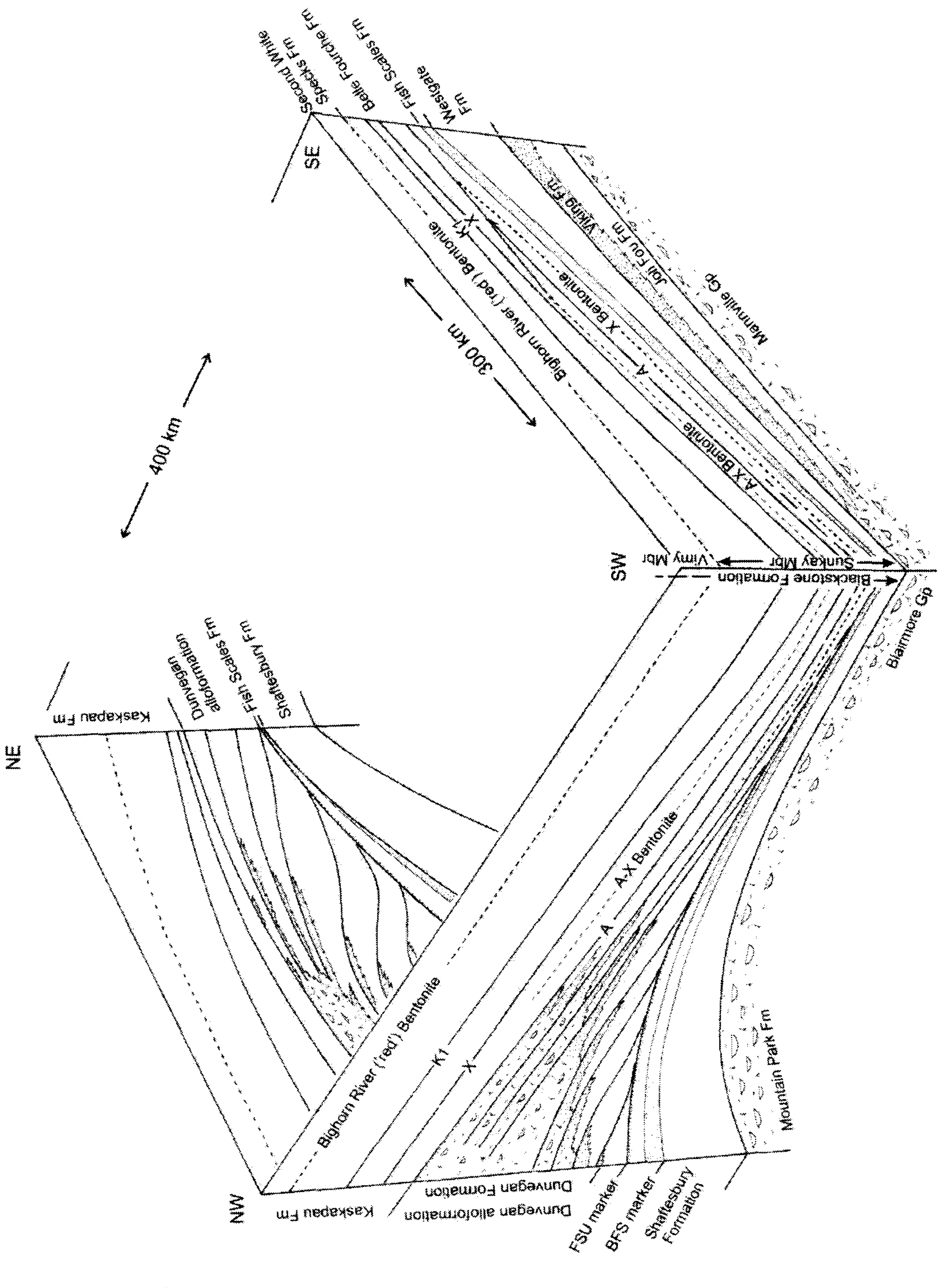

Figure 1.5. Diagram summarizing the lateral stratigraphic relationships of the Colorado Group, in relation to the Blackstone and Dunvegan formations. BFS = Base of the Fish Scales surface. FSU = Fish Scales Upper. Dashed lines indicate bentonites used in this study. Modified from Tyagi et al (2007).

During Cenomanian and Turonian time the mudstone dominated Blackstone Formation was deposited in the southern Alberta foredeep of the Western Canada Foreland Basin. The Greenhorn cycle (T6-R6) is expressed in outcrop as the Blackstone Formation, ending with the overlying Cardium Formation (Cadrin et al. 1995). The Blackstone Formation is also the outcrop expression of a large portion of the Colorado Group, which is the subsurface term (see Fig. 1.5 for the lateral relationships between the two). The Blackstone Formation thins rapidly eastward, from 950 m thick in northeastern British Columbia to 50 m thick east of the Foothills (Kreitner and Plint 2006). In ascending order the members of the Blackstone Formation are Sunkay, Vimy, Haven and Opabin (Stott 1963; Tyagi et al. 2007); the Haven and Opabin Members are outside the study interval. The Sunkay Member has equivalence to the Westgate, Fish Scales, Belle Fourche, and the lower portion of the Second White Specks Formation of the subsurface lower Colorado Group (Tyagi et al. 2007; Fig. 1.6). Tyagi et al. (2007) have shown that the lower portion of the Second White Specks Formation (as defined in the subsurface by Bloch et al. 1993) correlates to a higher part of the Blackstone Formation than previously believed, being correlative with the upper portion of the Sunkay Member in outcrop. Marine shales of the lowest one meter of the Sunkay Member at Burnt Timber Creek, Alberta, are equivalent to the Westgate Formation, as shown by the presence of *Miliammina manitobensis* microfauna (Tyagi et al. 2007). An overlying conglomerate at Burnt Timber Creek has equivalence to the Fish Scales Formation (Tyagi et al. 2007). Above the conglomerate, overlying mudstones at Burnt

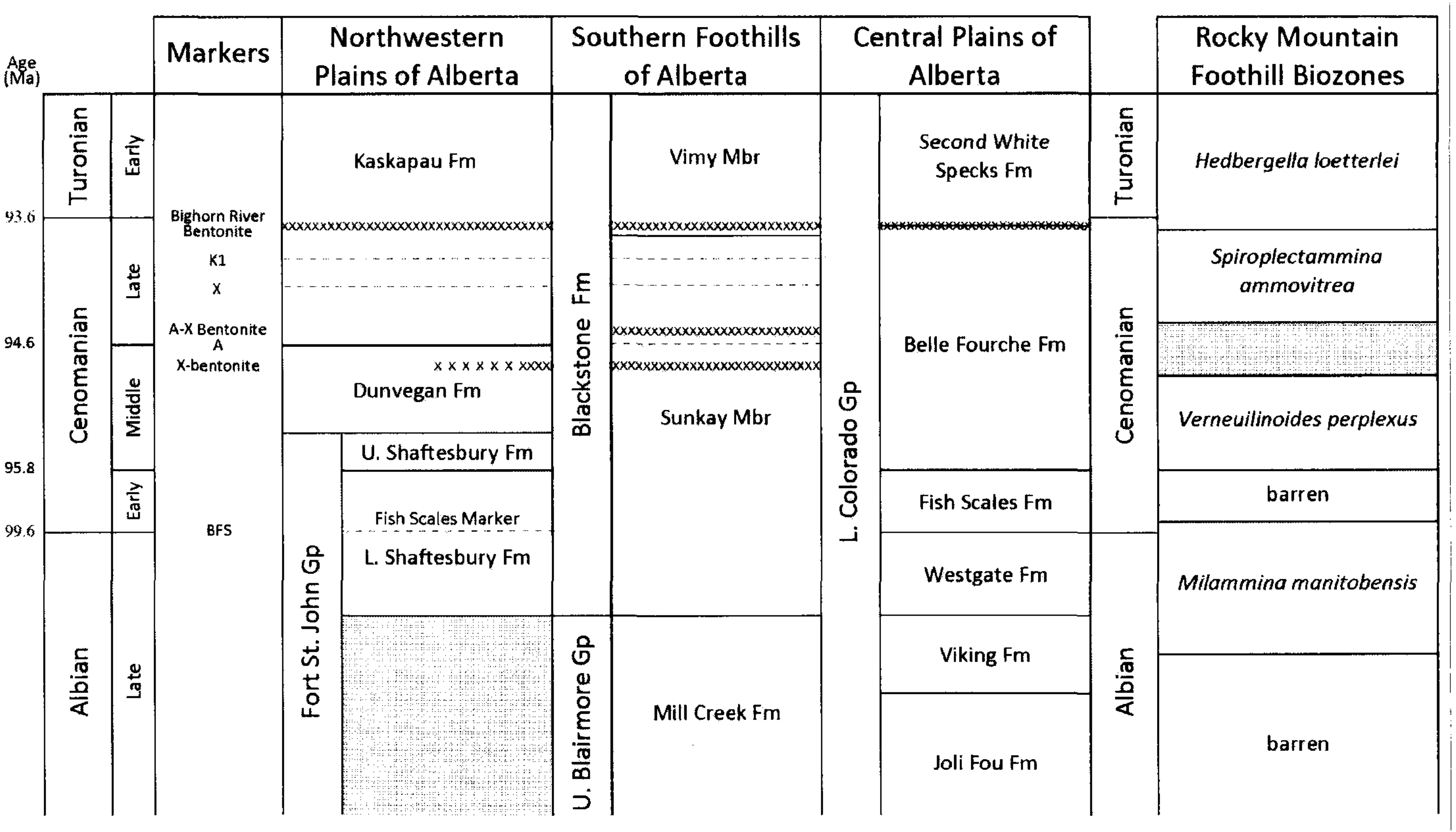

Figure 1.6. Chart summarizing the correlations between the Blackstone Formation in outcrop and the Colorado Group in the subsurface. Also indicates the correlation with biostratigraphic units. Note: The bentonites listed in this chart are the ones analyzed in this study. XXX, indicates bentonite layer. ---, indicates a bounding surface. K1 and X are bounding surfaces. BFS, Base Fish Scales; Fm, Formation; Mbr, Member; Gp, Group; U, Upper; L, Lower. After Tyagi et al. (2007) and Roca et al. (2008). This chart is not scaled. Dates are approximate and are from Gradstein et al. (1999) and Ogg et al. (2005).

Timber Creek contain foraminifera of the *Verneuilinoides perplexus* Zone, showing equivalence to the Belle Fourche Formation of the lower Colorado Group, and indicating that the member is of middle to late Cenomanian age (Tyagi et al. 2007). In the south and central Alberta Foothills, the Sunkay Member lies within the late Cenomanian *Dunveganoceras albertense* foraminiferal zone (Stott 1963; Tyagi et al. 2007), confirming that this member cannot be much younger than late Cenomanian in age.

The contact between the Sunkay and Vimy Members is interpreted to nearly approximate the Cenomanian/Turonian boundary (Stott 1991; Tyagi et al. 2007). At Burnt Timber Creek the Cenomanian/Turonian boundary was placed, based on biostratigraphic grounds, ~7 m above the base of the Vimy and ~3 m above a regional bentonite, named the Bighorn River Bentonite, by Tyagi et al. (2007); Fig. 1.6 shows the location of the Cenomanian/Turonian boundary in relation to the bentonite. The transgressive maximum of the Greenhorn Cycle is contained within the Vimy Member and the maximum high-stand conditions during the early Turonian caused the Vimy member to be deposited as a condensed section in the east portion of the basin (Leckie et al. 2000). The base of the Vimy Member at the west side of the basin closely approximates the first appearance of the *Mytiloides* [*Inoceramus*] *labiatus* foraminifera, which indicates an early Turonian age (Kauffman et al. 1993; Tyagi et al. 2007), and that this member has an equivalence to the Second White Specks Formation of the Colorado Group (Bloch et al. 1993; Leckie et al. 2000; Tyagi et al. 2007; Fig. 1.6).

In the northwest portion of the Western Canada Foreland Basin, the Blackstone Formation becomes divided into lower and upper shaley packages that are split by the sandstones of the deltaic Dunvegan Formation (Fig. 1.5). The lower shaley package is termed the Shaftesbury Formation and is equivalent to the lower portion of the Sunkay Member (Tyagi et al. 2007). The marine shales above the Dunvegan Formation were given the name Kaskapau Formation and are equivalent to the upper portion of the Sunkay and lower portion of the Vimy Member (Fig. 1.5; Tyagi et al. 2007; Roca et al. 2008).

The sandstone dominated Dunvegan Formation downlaps onto the radioactive "Fish Scales Upper" marker and is bounded by a prominent flooding surface on the top of allomember A (Plint 2000; Fig. 1.5). In the Foothills, the Dunvegan Formation grades laterally southward into the Sunkay Member of the Blackstone Formation (Stott 1963; Plint 2000). The Dunvegan Formation is of early to middle Cenomanian in age and represents a large delta complex that was deposited over ~2 m.y. on the western margin of the Western Interior Seaway (Plint 2000, 2002). The deltaic strata of this unit are believed to represent a major southeast-directed progradation of the shoreline, parallel to the Cordillera orogen (Plint 2003). This formation ranges in thickness from ~90 m in the southeast to ~270 m in the northwest and is divided into ten transgressive-regressive allomembers termed J to A in ascending order; each allomember is inferred to represent no more than 200 thousand years (k.y.; Plint 1996, 2000). Isopach maps have been constructed by Plint (2003) for each allomember, graphically showing the geometry of accommodation that is available for each allomember and can be interpreted in terms of subsidence patterns. Allomembers J to F show no thickening towards the Cordilleran orogen and were deposited at a time when subsidence was unimportant and there was little tilting of the basin floor (Plint 2003). The younger allomembers E to A show the progressive development of a depocenter along the western margin of the basin, and it is inferred that these allomembers were deposited during a time of pronounced southwestwardly subsidence. This renewed subsidence led to a major backstep of the Dunvegan delta complex in allomember A time, causing widespread marine transgression at the base of the overlying Kaskapau Formation (Plint 2003; Plint et al. 2009).

The Kaskapau Formation lies above the Dunvegan Formation and has equivalence to the upper portion of the Blackstone Formation in the northwestern Western Canada Foreland Basin, being a westward thickening, mudstone dominated wedge that is 950 m thick at its thickest point (Fig. 1.5). The Kaskapau Formation is a marine mudstone wedge that was deposited during the late Cenomanian to early Turonian Greenhorn transgression (Varban and Plint 2005), recording a phase of rapid flexural subsidence of the basin (Kreitner and Plint 2006). The lower Kaskapau Formation is divided into the A-X, Doe Creek and Pouce Coupe allostratigraphic units, in ascending order (Plint 2000; Kreitner and Plint 2006). Between the top of the Dunvegan Formation (top of allomember A) and the X marker is the A-X unit (Kreitner and Plint 2006). The X marker surface is a major flooding surface near the base of the Kaskapau Formation and defines the base of the Doe Creek unit. A second surface higher up truncates the Pouce Coupe and Doe Creek sandstones is called the K1 surface (Plint 2000; Kreitner and Plint 2006).

1.2.2 Cordilleran Magmatism and Volcanism

1.2.2.1 Cordilleran Magmatic Arc

The bentonite ash layers in the Western Interior Basin are inferred to be the result of magmatism and volcanic activity originating within the Corillera orogeny. The initiation of western North American magmatism during the Late Triassic was coeval with the rifting and separation of the North American plate from Pangea (Armstrong and Suppe 1973; Armstrong and Ward 1993). Beginning in the Early Cretaceous, eastward subduction of the Farallon plate beneath the North American plate initiated the development of the Cordilleran Magmatic Arc (Hyndman 1983; DeCelles 2004). Continental Andean-type magmatism began as a narrow belt, close to the magmatic front, and then spread craton-wards, with successive arc-building episodes stepping inland parallel to the continental margin, having a sharp seaward front and diffuse inland edge (Armstrong and Ward 1993). The magmatic belt was greater than 4000 km long, from Mexico to Alaska, and includes a high temperature batholith belt in the accreted terranes. Fig. 1.1 shows the magmatic arc in relation to the Cordilleran orogeny. The Cordilleran Magmatic Arc includes numerous calcalkaline granitoid intrusions (Hamilton and Myers 1967; DeCelles 2004) that are chemically and spatially variable over time. Spatially, sodic magmas occur near the magmatic front, calc-alkaline magmas occur over much of the width of the magmatic belt and alkaline or shoshonitic magmas may occur at distal inland areas (Miyashiro 1974; Armstrong and Ward 1993). Temporally, early magmatism may be more alkaline than later stages of the same episode or later parts of long multi-episodic histories in the same area (Armstrong and Ward 1993).

It is possible that additional factors other than subduction caused the Cordilleran Magmatic Arc, since magmatism is out of sequence with periods of crustal shortening. Periods of rapid upper crustal shortening are inferred to correlate with periods of magmatism. The major periods of shortening of the Cordilleran orogeny occurred during the Early Cretaceous (~140 Ma to 110 Ma) and Late Cretaceous to Eocene (~85 Ma to 55 Ma), but the Cordilleran Andean-type arc magmatism reached its peak between 100 Ma to 90 Ma (Coney and Reynolds 1977; DeCelles 2004). The Late Cretaceous magmatic episode occurred out of sequence in reference to Cordilleran shortening, indicating that there may be a slight amount of volcanic lag-time in between subduction-related events and volcanism (DeCelles 2004).

1.2.2.2 Local Source Batholiths

The transition between Cenomanian to Turonian time is marked by intense igneous intrusions as the magmatic arc migrated into western Montana and north-central Idaho (DeCelles 2004). Major composite batholiths formed on the edge of North America during Late Cretaceous time, and include the Idaho Batholith and the Sierra Nevada Batholith. These batholiths intruded into the Precambrian continental crust of North America, and generated a voluminous amount of peraluminous granitic rock (Foster and Fanning 1997).

The Idaho Batholith exists in north-central Idaho and western Montana. The main phase of the Idaho Batholith activity was during Upper Cretaceous to Eocene time and its plutonism spanned more than 30 million years (m.y.), being both episodic in space and time (Foster and Fanning 1997). U-Pb zircon data of the main phase granitoids are highly discordant, with lower intercept ages being biased, indicating mixed populations of inherited zircon. Inherited zircons sampled directly from the Idaho Batholith have ages between 800 Ma and 1820 Ma, with the majority centered around 1750 Ma to 1800 Ma, indicating that Paleoproterozoic crust dominates the source of the batholiths (Foster and Fanning 1997). U-Pb zircon and monazite data from a plutonic quartz diorite along the western border of the Idaho Batholith, indicate that the diorite was emplaced at 94 ± 1.4 Ma (Shuster and Bickford 1985; Toth and Stacey 1992). This indicates that the Idaho Batholith was emplaced at ~94 Ma, during the middle Cenomanian and could be a possible source for the bentonites dated in this study.

The Sierra Nevada batholith is located within the Cordilleran magmatic arc, and is believed to have been active between 220 Ma to 80 Ma, with very active periods between 160 Ma to 150 Ma and between 100 Ma to 85 Ma (Bateman 1992; Armstrong and Ward 1993; DeCelles 2004). The pulse of activity from 100 Ma to 85 Ma accounted for ~78% of exposed area of the batholiths (DeCelles 2004), and encompasses the study interval that is used here, therefore this batholith could be another source region for the bentonites dated in this study.

1.2.2.3 Ejecta Plume Information

Bentonite deposits (to be defined in 1.2.2.4 *Bentonites*) that are most useful for geochronology originate from a violent volcanic eruption making them widespread and isochronous. These ash deposits are typically the products of plinian (periodic explosive) events of dacitic to rhyolitic composition, and often include lithic fragments from previous eruptions (Pearce et al. 2004). Flank eruptions were generally divided into two classes by Branca and Del Carlo (2005). Class A eruptions are more frequent and include weak strombolian (fire fountains of lava from central crater) activity and weak eruption plumes. Magmatic events can last weeks to years and the eruptions are characterized by hornitos or small scoria cones. Class B eruptions include violent strombolian explosive activity that have long lasting, strong eruption plumes. The volcanoes from class B eruptions are characterized by large scoria cones having ash fallout that extend tens to hundreds of kilometers away from the source.

Pulsing volcanic jets can feed a fairly stable vertical ash column, having a column height that is a function of the particle mass and the prevailing atmospheric stratification; the column will stop rising once it reaches an altitude where it is no longer denser than the surrounding air. Advection-diffusion models dictate that the horizontal motion of ash particles and the expansion of an ash mass depends on the velocity and direction of prevailing winds, atmospheric turbulence and vertical motion due to ash particle terminal settling velocity; where the terminal settling velocity is generally controlled by particle size and density (Walker 1971; Scollo et al. 2007). If one simplifies the eruption column to a linear source, then it limits the validity of advection-diffusion models to regions that are located at horizontal distances greater than the height of the eruption column itself (Scollo et al. 2007).

Most ash sedimentation from strong volcanic plumes (Class B) occurs around the umbrella region, which is a term that is given to the atmospheric buoyancy height where the subvertical ash column may expand horizontally. The umbrella region is where the total ash particle mass is most highly concentrated, with the maximum being at the middle of the eruption column (Scollo et al. 2007). The ash column expands horizontally due to the ash particles and the surrounding air having the same density at this height (Sparks et al. 1997). Fig. 1.7 shows a diagram of the umbrella region as well as the corresponding graphs of the accumulation of ash per unit area and distance from the eruption column. The eruption plume may be directed downwind by the prevailing atmospheric winds, reflecting the effects of high-altitude wind patterns occurring tens of kilometers or more above the Earth's surface. The atmospheric winds disperse the ash plume linearly for kilometers away from the eruption column; this is seen for example by the east-west trending sedimentation of the 1980 eruption of Mount St. Helens (Carey and Sigurdsson 1982; Elder 1988).

Weak volcanic plumes (Class A) are most easily distorted by the wind, developing bent-over trajectories in the downwind direction (Slaughter and Earley 1965). Sedimentation from weak plumes (class A) occurs over all parts of the eruption column and in contrast to strong plumes (class B), the volcanic particles are not concentrated in any particular part of the column (Scollo et al. 2007). Distal deposits of both strong and

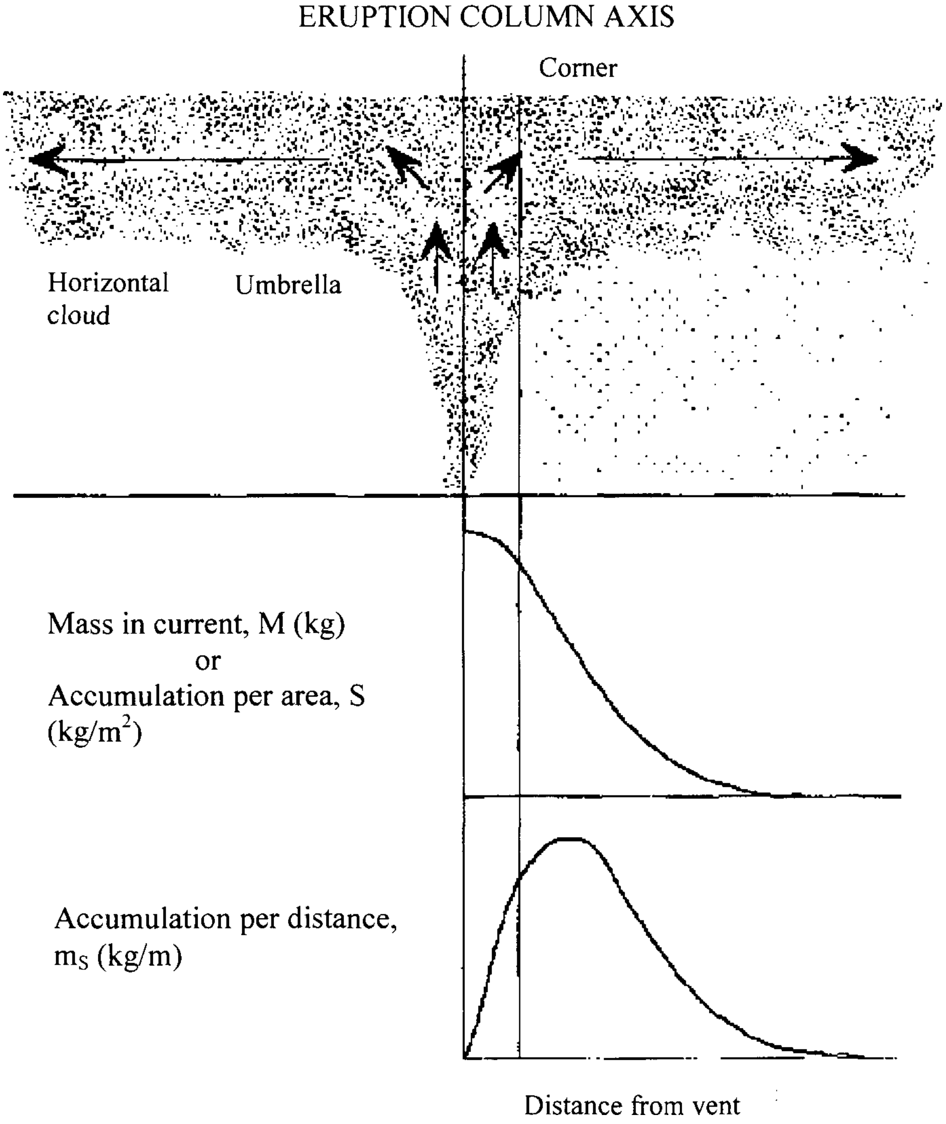

Figure 1.7. Schematic illustration of the relationship between an eruption column and the accumulation of tephra with distance from the vent. The tephra accumulation is shown as total mass accumulation beyond each distance or as mass per unit area (kg/m^2), and as mass per unit distance (kg/m) in an elliptical ring around the column. Bursuik et al. (1992).

weak plumes are usually thin, prone to contamination and easily removed from the ground by winds and water currents (Pearce et al. 2004).

Both weak and strong ash plumes are occasionally deposited in a bilobate pattern due to variable wind directions and velocities. Furthermore, fluctuations of eruptive intensity with time can increase the chances for a bilobate deposition pattern (Scollo et al. 2007). For example, during the 1968 and 1995 eruptions of the Cerro Negro Volcano in Nicaragua, the wind velocity and direction changed, causing two ash lobes to be deposited (Ernst et al. 1994; Hill et al. 1998).

1.2.2.4 Bentonites

Bentonites, first defined by Knight 1898, which consist mainly of clay minerals, originate as volcanic ashes that are typically generated during violent felsic eruptions. The ash layers may be deposited and preserved in low energy lakes and marine basins that allow for alteration to occur through submarine weathering. The alteration of the glassy pyroclastic material begins when the ash comes in contact with water. *In situ* subaqueous devitrification of the volcanic glass and the alteration of cristobalite, zeolite, feldspar and biotite leads to the formation of clays of the smectite group (Cadrin et al. 1995). Bentonites generally consist of these smectite clays with varying amounts of cristobalite, zeolite, biotite, quartz, feldspar and zircon, depending on the degree of diagenesis.

Bentonites are typically deposited over days to weeks as thin continuous beds, being both synchronous (occurring at the same time) and isochronous (equal in duration) with the eruptions that produced them (Obradovich and Cobban 1975; Cadrin et al. 1995). Biostratigraphy can produce only a relative time-scale and it is necessary to combine this data with radiometric ages of these thin, continuous and intercalated bentonite beds in order to produce an accurate and absolute time-scale that has a precision approaching 0.1% or better (Bowring and Schmitz 2003). Bentonites are excellent geochronological markers because they commonly yield minerals (e.g. biotite, sanidine, zircon) suitable for $^{40}K/^{39}Ar$, $^{40}Ar/^{39}Ar$ and U/Pb isotopic dating methods (Obradovich and Cobban 1975; Obradovich 1993; Cadrin et al. 1995).

1.2.3 Bentonite Sampling Localities

Geochronologic efforts were focused on three bentonites that were derived from magmatic activity in the Cordilleran Magmatic Arc. The X, A-X and the Bighorn River bentonites were selected since they are regionally well correlated in the subsurface (Fig. 1.8; Tyagi et al. 2007), and known to be deposited in succession during a period of distinct change in sedimentary basin and global marine chemobiological change. Fig. 1.9 shows the vertical stratigraphic column at Burnt Timber Creek, Alberta, and the relative stratigraphic spacing of the bentonites.

1.2.3.1 X-Bentonite

Tyagi et al. (2007) established that the X-bentonite is equivalent to the "A" bentonite of Gilboy (1988), however the X-bentonite has also been named the Grey-Red

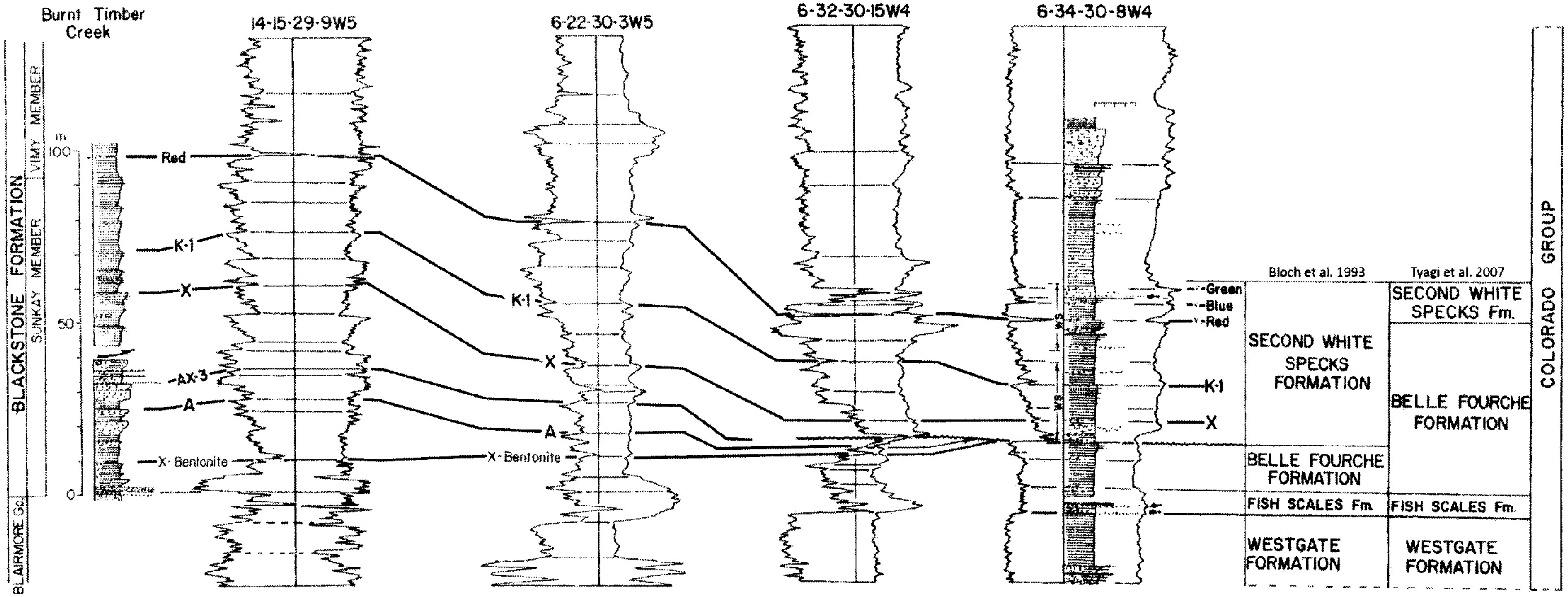

Figure 1.8. The regional well log correlations showing the stratigraphic equivalence of the west and east lithostratigraphic units of the Western Canada Foreland Basin. Only the major stratigraphic markers are shown for simplicity; this includes the K-1, X, AX-3 and A surfaces. The Red and X bentonites are shown on this diagram. The "Red" bentonite is the informal term for the Bighorn River Bentonite. The A-X bentonite was not regionally correlated by Tyagi et al. (2007) and is therefore not shown. Modified from Tyagi et al. (2007)

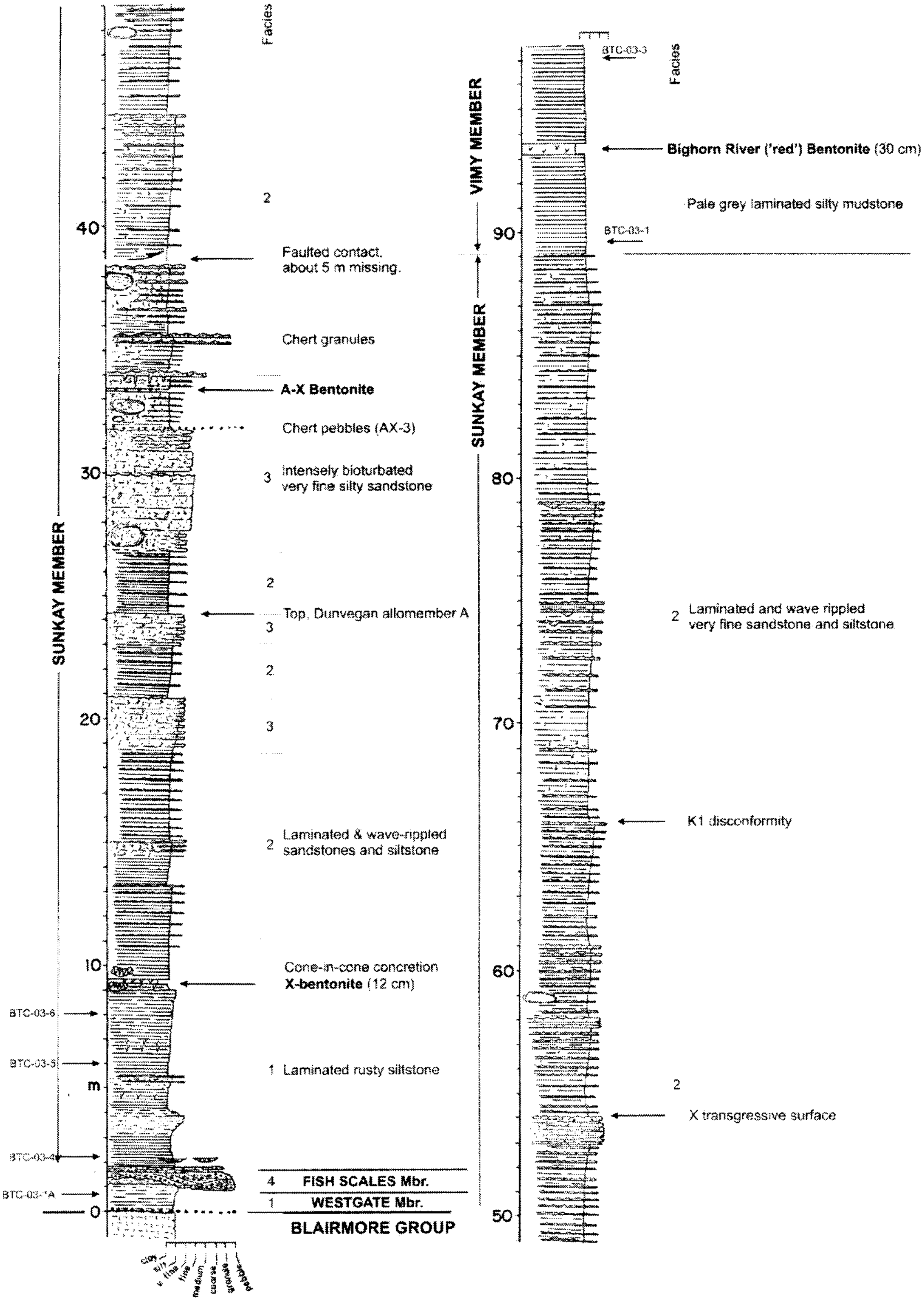

Figure 1.9. Stratgraphic column of Burnt Timber Creek, Alberta. Straitgraphic locations of the three bentonites used in this study are indicated. Mbr = Member. Modified from Tyagi et al. (2007)

bentonite, Soap Creek bentonite, F bed and Marker bentonite by various authors (Hattin 1965; McGookey et al. 1972; Cobban and Scott 1972). The X-bentonite is a key marker in Upper Cretaceous rocks, and is very widespread across the Western Interior Basin (Tyagi et al. 2007). Tyagi et al. (2007) placed the X-bentonite at Burnt Timber Creek, Alberta, site 1 (Fig. 1.10), 9.3 m above the base of the Sunkay Member of the Blackstone Formation (Fig. 1.9) and traced the bentonite northward, into allomember C of the Dunvegan Formation (Fig. 1.5 and 1.6). Allomember C of the Dunvegan Formation coarsens northward into a more nearshore facies, and as the formation coarsens the bentonite becomes no longer mappable presumably due to shallow water effects (Tyagi et al. 2007). X-Ray Diffraction analyses of the X-bentonite sampled from Manitoba and Colorado shows that it consists of pure montmorillonite clay, but there were differences of the mineralogy throughout the Western Interior Basin that have been ascribed to different post-depositional processes, including interaction with fluids (Cadrin et al. 1995).

In the United States, the X-bentonite lies within the middle Cenomanian *Acanthoceras amphibolum* ammonite zone (Tyagi et al. 2007) and is immediately overlain by the *Plesiacanthoceras wyomingense* Zone (Cadrin et al. 1995). In Canada no ammonite zones have been found, and therefore foraminiferal zones must be used in biostratigraphic correlations. The X-bentonite at Burnt Timber Creek lies near the top of the middle Cenomanian *Verneulinoides perplexes* Zone (Wall 1967). In the eastern part of the basin, in the Belle Fourche Member, the X-bentonite is found immediately above

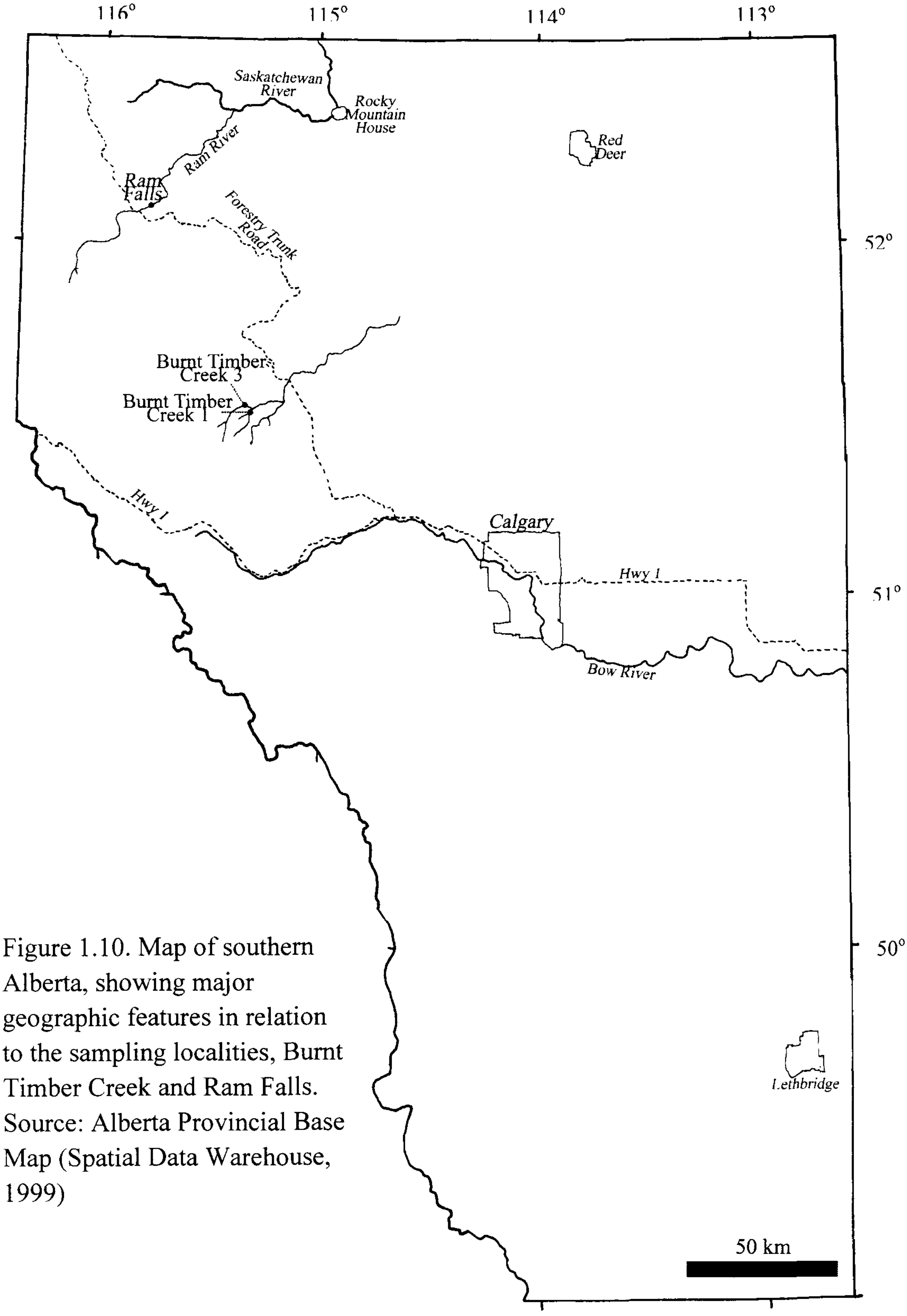

Figure 1.10. Map of southern Alberta, showing major geographic features in relation to the sampling localities, Burnt Timber Creek and Ram Falls. Source: Alberta Provincial Base Map (Spatial Data Warehouse, 1999)

distinctive small oyster *Ostrea beloiti* beds (McNeil and Caldwell 1974, 1981; Cobban and Hook 1980).

The X-bentonite is biostratigraphically constrained to have been deposited during middle Cenomanian time and has a generally accepted $^{40}Ar/^{39}Ar$ isotopic age of 94.96 ± 0.50 Ma (Cobban et al. 2006). Fig. 1.11 shows all of the localities where the previously-published correlative and dated bentonites were sampled. This bentonite was dated using $^{40}Ar/^{39}Ar$ radiometric methods at 94.93 ± 0.53 Ma by Obradovich (1993) (sample 24, collected at Natrona County, Wyoming), which was later recalculated using different standard calibrations, to 94.96 ± 0.50 Ma by Cobban et al. (2006). Fig. 1.12 shows how these dates compare, including their stated uncertainties.

1.2.3.2 A-X Bentonite

There have been no previously published findings on the A-X bentonite. As indicated by gamma ray well-logs, the A-X bentonite exists south of Calgary, Alberta, along the Rocky Mountain Foothills. It is believed that the A-X bentonite thickens southward and it has not been found north of Burnt Timber Creek (Plint 2008, pers. comm.). The A-X bentonite exists in the A-X Unit, which lies between the top of allomember A of the Dunvegan Formation and the X stratigraphic bounding surface, and extrapolates into the middle of the Sunkay Member of the Blackstone Formation (Fig. 1.5 and 1.6). The A-X bentonite lies immediately above the AX-3 erosional surface

Figure 1.11 Previous bentonite sampling localities across the United States western interior. This map also includes the location of the GSSP at Pueblo, Colorado. State capital cities are shown for geographic reference. Source: The United States (National Geographic Society, 1993)

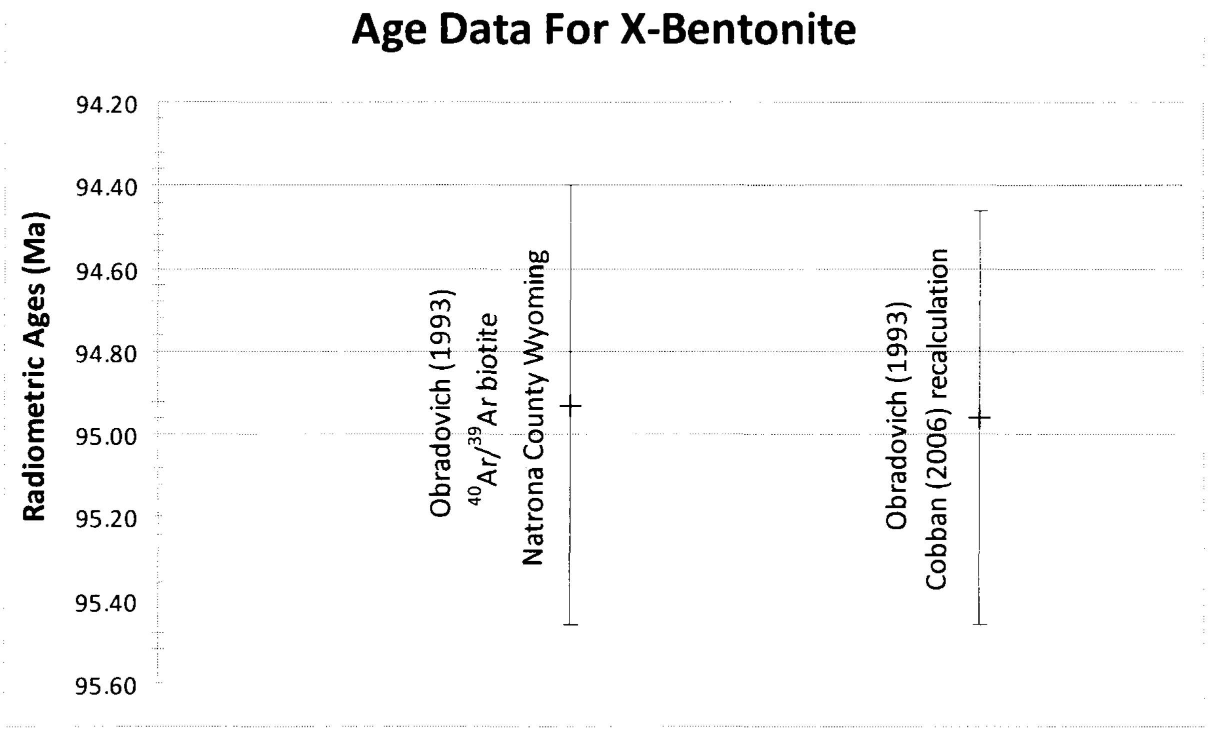

Figure 1.12. The previously published radiometric ages for the X-bentonite. Both are $^{40}Ar/^{39}Ar$ ages. Cobban (2006) recalculated the age obtained by Obradovich (1993) using updated $^{40}Ar/^{39}Ar$ standards.

(Plint 2008, pers. comm.; Fig. 1.9), which is in the *Ammobaculites gravenori* subzone of the *Verneuilinoides perplexus* foraminiferal zone.

1.2.3.3 Bighorn River Bentonite

The Bighorn River Bentonite was formally named by Tyagi et al (2007) who showed that it is equivalent to the "C" bentonite of Gilboy (1988). The Bighorn River Bentonite is also known as bed M (Knechtel and Patterson 1956), HL-3 marker bed (Hattin 1975), bed B (Elder 1988), PBC-11 (Kowallis et al. 1995), B-bentonite (Kowallis et al. 1995) and informally as the Red Bentonite (Tyagi et al. 2007). It is a widely mappable unit that is recognized across the Western Interior Basin (Kennedy 1984; Kowallis et al. 1995). In North America, the bentonite is traceable from British Columbia to New Mexico (Tyagi et al. 2007) and is a key marker in correlations of Upper Cretaceous stratigraphy and timescale calibrations.

In Utah, the Bighorn River Bentonite contains a magmatic mineral assemblage, including quartz, sanidine, plagioclase, biotite, zircon and apatite (Kowallis et al. 1995). It has been observed by Elder (1988), when the bentonite is greater than 10 cm thick it contains biotite, is yellowish-orange to greenish-grey in colour and is bioturbated near its upper contact. However, where it is thinner the bentonite becomes discoloured due to limonite alteration and may contain gypsum and biotite (Elder 1988). The Bighorn River Bentonite is generally consistent in thickness across large areas, indicating that post-depositional marine redistribution of the bentonite was minimal; local variations in thickness indicate minor areas of marine redistribution. Furthermore, Elder (1988) found that the zircons from the Bighorn River Bentonite doubled in size from southern Utah to central Colorado, and as indicated by the bentonite isopach patterns, inferred that there was a south-southeast drift of the volcanic plume. This suggests that the source area for the Bighorn River Bentonite was in the Cordilleran magmatic arc, close to the United States-Canada border.

Tyagi et al. (2007) documented the Bighorn River Bentonite at Burnt Timber Creek, site 1, where it is located 4 m above the base of the Vimy Member of the Blackstone Formation and 93.2 m above the base of the Sunkay Member (Fig. 1.9). Tyagi et al. (2007) has proposed that the bentonite defines the base of the Second White Specks Formation of the Colorado Group (Fig. 1.6; Tyagi et al. 2007).

In the entire United States portion of the Western Interior Basin, the Bighorn River Bentonite lies within the latest Cenomanian *Neocardioceras juddii* ammonite zone (Kowallis et al. 1995). However in Canada, *N. juddii* has not been found, but at Burnt Timber Creek the Bighorn River Bentonite lies a few meters below the first appearance of the bivalve *Mytiloides* [*Inoceramus*] *labiatus* and is within the *Hedbergella loetterlei* foraminiferal zone, which is of late Cenomanian to early Turonian age (Tyagi et al. 2007).

Using K-Ar isotopic methods on biotite grains that were extracted from the Bighorn River Bentonite, Obradovich and Cobban (1975) obtained an age (sample 14, collected in Cascade County, Montana) of 88.9 ± 0.9 Ma (1σ; this was later recalculated, using the conversion factor of Dalrymple (1979), to 91.1 ± 0.9 Ma by Elder 1988). Elder (1988) also used K-Ar biotite methods (collected at Pueblo, Colorado) and obtained an age of 88.3 ± 3.3 Ma (1σ). Obradovich (1993) used $^{40}Ar/^{39}Ar$ isotope methods on three biotite flakes extracted from the bentonite (sample batch 20), yielding ages of 93.30 ± 0.40 Ma (collected in Thayer Country, Nebraska), 93.78 ± 0.49 Ma (collected in San Juan County, New Mexico) and 93.59 ± 0.58 Ma (collected in San Juan County, New Mexico). Kowallis et al. (1995) used three multigrain zircon fractions (FC-PBC-11, collected at Four Corners, Colorado) to obtain an average U/Pb isotopic date of 93.50 ± 0.40 Ma. Fraction 1 (n = 300) had a $^{206}Pb/^{238}U$ age of 93.3 ± 0.2 Ma, Fraction 2 (n = 60) had a $^{206}Pb/^{238}U$ age of 93.60 ± 0.10 Ma and Fraction 3 (n = 152) had a $^{206}Pb/^{238}U$ age of 95.6 ± 0.1 Ma (these individual components are believed to be at the 2σ level). Furthermore, Kowallis et al. (1995) used $^{40}Ar/^{39}Ar$ single-grain dating on sanidine to obtain an age of 93.33 ± 0.50 Ma. The generally accepted date for this bentonite is 93.30 to 93.40 Ma (Obradovich 1993). Fig. 1.11 shows all of the previously-published sampling localities of the radiometrically dated equivalents to the Bighorn River Bentonite. Fig. 1.13 compares all of the previously published dates and shows their stated uncertainties.

1.2.3.4 Intercontinental Link to the GSSP at Pueblo, Colorado

A Global Stratotype Section and Point (GSSP) serves as a practical classificatory "golden spike" for a distinct subdivision of geologic time. A GSSP serves as the best

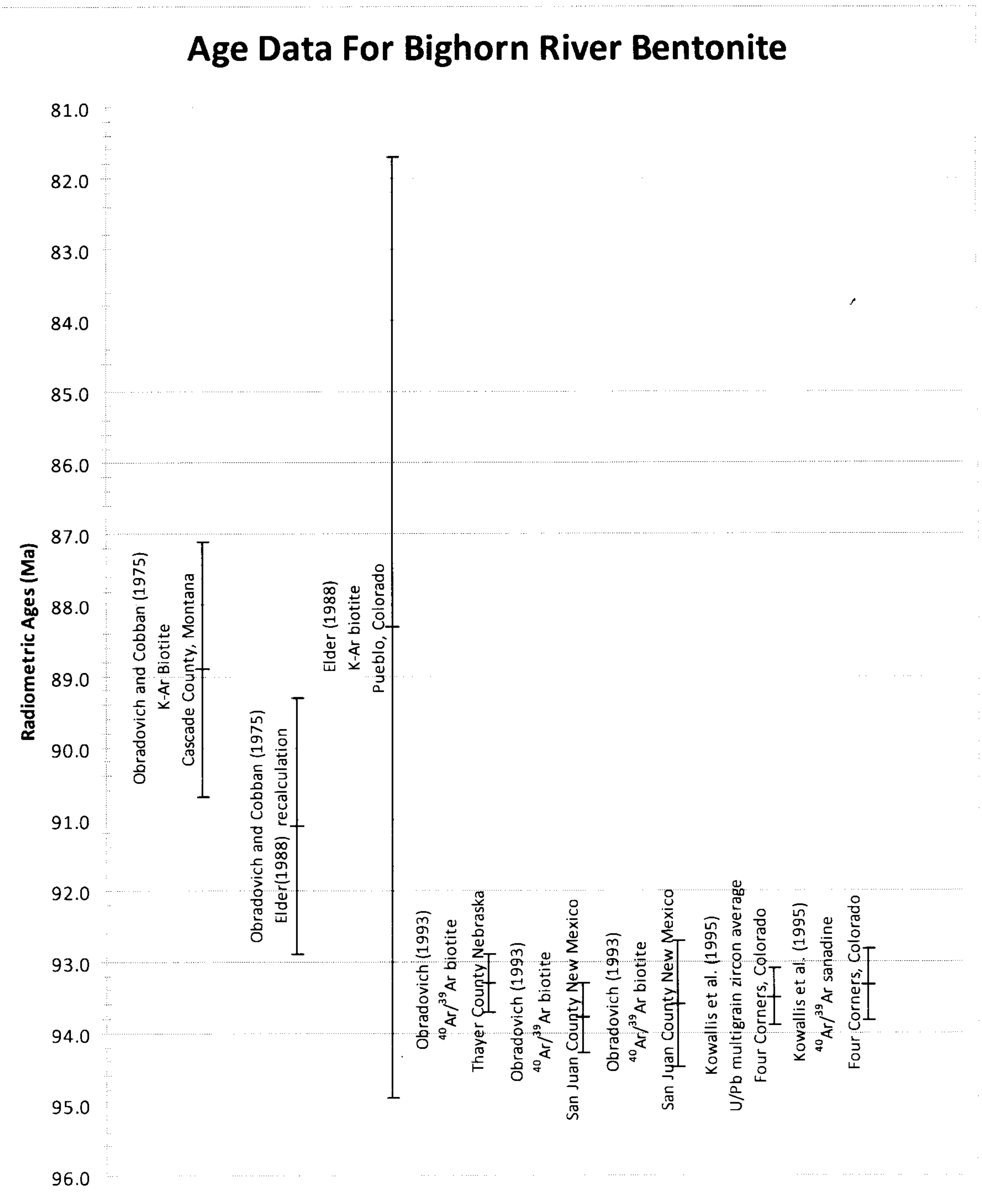

Figure 1.13. The previously published radiometric ages for the Bighorn River Bentonite. All of the ages are either ^{40}Ar/^{39}Ar or K-Ar except for the U/Pb multigrain zircon average age determined by Kowallis et al. (1995). Three individual analyses by Obradovich (1993) are shown as well.

standard of reference for a geochronologic boundary of a system, with an emphasis placed on global correlation. The guiding criterion for a GSSP is generally placed on biostratigraphic guidelines, however, a GSSP should also have other elements of correlation such as, radiometrically-datable horizons, chemostratigraphic horizons and magnetic polarity reversal horizons; GSSPs should be defined in such a way for them to be correlatable by as many different lines of age-significant information as possible (Walsh et al. 2004).

The Cenomanian/Turonian boundary is defined by the GSSP at Pueblo, Colorado (Kennedy et al. 2005). The base of the Turonian at Pueblo is at the base of bed 86 of the Bridge Creek Limestone Member of the Greenhorn Limestone Formation (Kennedy et al. 2005). The base of the Turonian corresponds to the first occurrence of the ammonite, *Watinoceras devonese*. The *Neocardioceras juddii* ammonite zone exists in the upper Cenomanian bed 84, which is just below bed 86. See Fig. 1.14 for the stratigraphic column of the Cenomanian/Turonian boundary at Pueblo.

A correlative equivalent to the Bighorn River Bentonite can be found in the GSSP section at Pueblo. Carbon isotope data obtained from Ram Falls, Alberta, strongly suggests that the Bighorn River Bentonite correlates with the "B" bentonite, of bed 80 (Plint 2009, pers. comm.; Fig. 1.14). Kennedy et al. (2005) tried to date the "B" bentonite at Pueblo, however failed to obtain any satisfactory dates since the bentonite is thin and weathered there (it is unclear whether Kennedy et al. 2005 tried to obtain $^{40}Ar/^{39}Ar$ or U-Pb age data). The base of the Turonian is defined by the ammonite *Watinoceras devonese*, which appears 1.3 m above the equivalent of the Bighorn River

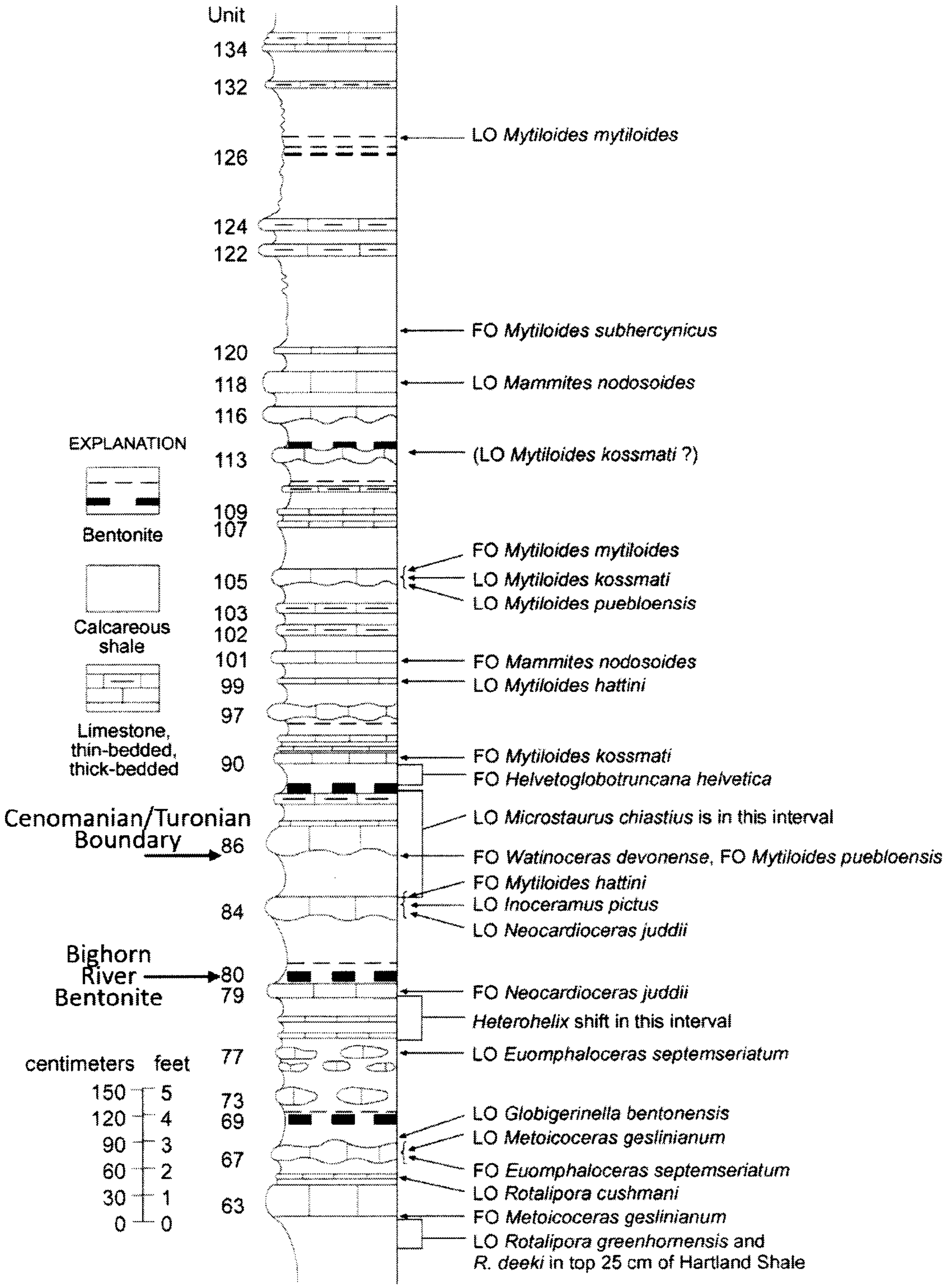

Figure 1.14. The stratigraphic column of the GSSP at Pueblo, Colorado. The locations of the bentonites are marked on the column, as well as bed numbers and ammonite zones. Note that the Bighorn River Bentonite is believed to correlate with bed 80. FO = First Occurrence, LO = Last Occurrence. Modified from Kennedy et al. (2005).

Bentonite at the GSSP (Kennedy et al. 2005), and this is correlated to Burnt Timber Creek where it is inferred that the Bighorn River Bentonite lies a few meters below the Cenomanian/Turonian and therefore this bentonite has been proposed to be a good approximation of the Cenomanian/Turonian boundary (Tyagi et al. 2007).

The Bighorn River Bentonite may presently provide the most accurate means of calibrating the age of the Cenomanian/Turonian boundary. The ammonite zones at the GSSP are correlative across the United States portion of the basin, and furthermore *N. juddii* has been found in southern England, France, Germany and Czech Republic, giving it strong global correlative power (Kennedy et al. 2005, and references therein). However, additional global correlative tools exist at the GSSP, which allow for the world-wide correlation of the Bighorn River Bentonite. Spanning this boundary, sediments worldwide become organic-rich, and characterized by a positive $\delta^{13}C$ anomaly, being deposited under anoxic conditions (Fig. 1.15 shows two detailed $\delta^{13}C$ curves at Pueblo, Colorado, in comparison the stratigraphic section and a curve from Eastborne, England). $\delta^{13}C$ is defined as:

$$\frac{R_{sample} - R_{standard}}{R_{standard}} \times 1000 \qquad \text{Eq. 1.1}$$

Where R is the ratio of the heavy element to the light element. This worldwide geochemical event, termed Oceanic Anoxic Event II (OAE II), is the most widespread and best defined OAE of the middle Cretaceous (Turgeon and Creaser 2008). During OAEs, wide-spread marine bottom water anoxia leads to the gradual extinction of deep water fauna and a large amount of carbon is buried on the ocean floor. OAE II sediments

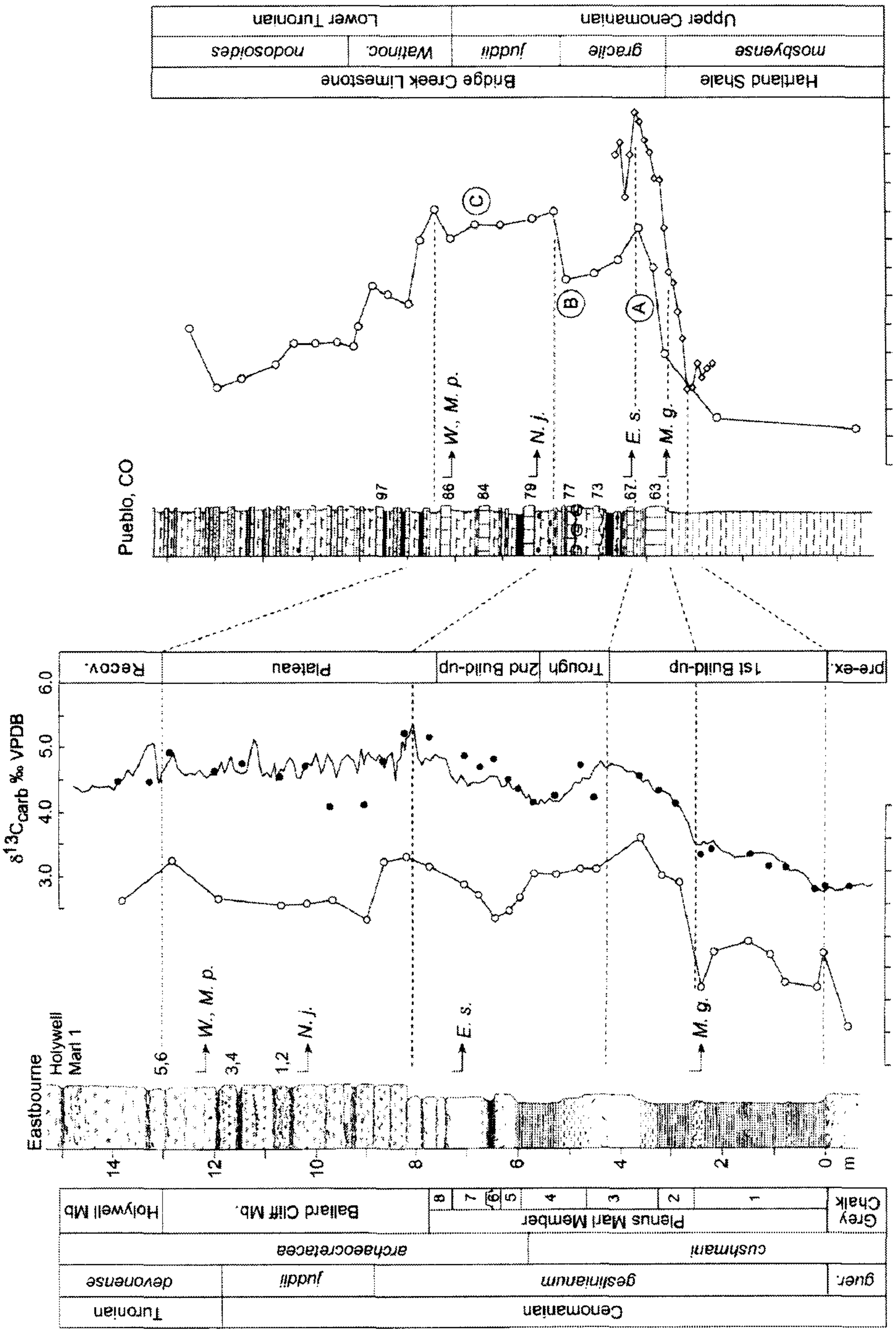

Figure 1.15. Stable isotope curves and correlation of the Cenomanian/Turonian boundary at Pueblo, Colorado and Eastbourne, Sussex, England. Macrofossil markers are: M.g. = first occurrence of the ammonite *Metoicoceras geslinianum*. E.s. = first occurrence of the ammonite *Euomphaloceras septemseriatum*. N.j. = first occurrence of the ammonite *Neocardioceras juddii*. W., M.p. = first occurrence of the ammonites *Watinoceras*, and the bivalve *Mytiloides puebloensis*. Kennedy et al. (2005).

are enriched in isotopically heavy organic carbon ($\delta^{13}C_{org}$ >- 26 ‰) (Arthur et al. 1988; Prokoph et al. 2001), but have a negative carbonate ($\delta^{13}C_{carb}$) excursion down to ~0 ‰. These shifts are believed to have resulted from an increased burial of ^{13}C-depleted organic carbon in response to the anoxic conditions (Arthur et al. 1988). The peaks and troughs in the $\delta^{13}C_{org}$ curve can be correlated to other sections in other parts of the basin, as seen in Fig. 1.16, and the $\delta^{13}C$ excursion has been recognized globally in both continental and oceanic contexts, in areas such as southern England, northern Spain, northern Tunisia and Japan (Kennedy et al. 2005, and references therein). Based on Milankovitch orbital cyclicity (Milankovitch 1941), the duration of the OAE II is estimated to range from ~240 k.y. in Morocco (Kuhnt et al. 1997) to ~720 k.y. in Colorado (Sageman et al. 1997).

1.3 Zircon and U-Pb Isotopic Dating Background

1.3.1 Zircon

1.3.1.1 Zircon Crystallization in Plutonic Settings

Zircon ($ZrSiO_4$) is a tetragonal orthosilicate that is considered to be a very robust geochronometer. It is able to survive intense conditions, retaining a high fidelity record of its crystallization history due to the slow volume diffusion rates of U, Th and Pb at crustal temperatures (Cherniak and Watson 2000; Schmitz and Bowring 2001b). The crystallization of zircon in an igneous system begins as the magma cools through the temperature of zirconium saturation, which is generally a function of magma composition

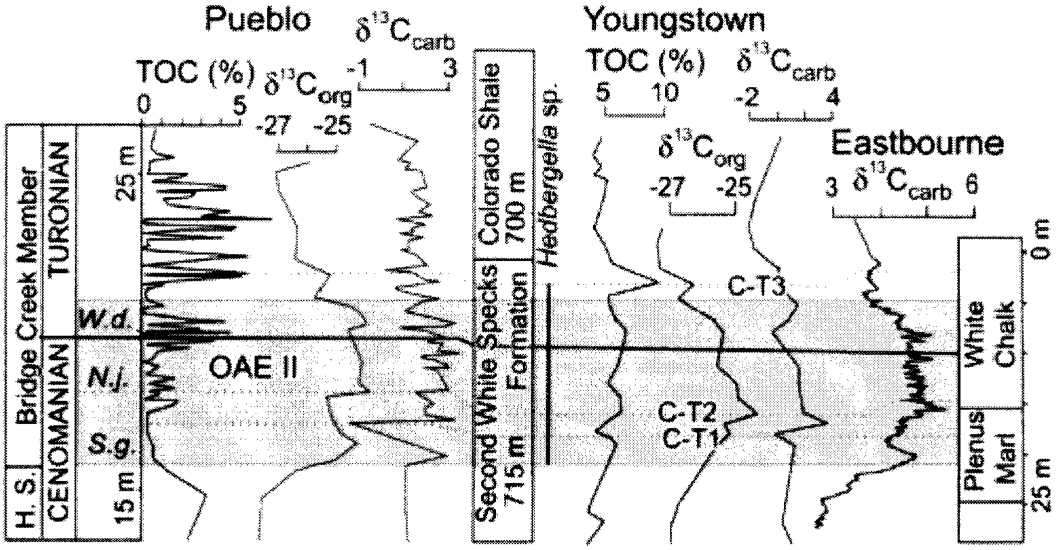

Figure 1.16. Biostratigraphic and lithostratigraphic correlations of high-resolution geochemistry at the Cenomanian/Turonian boundary from three localities, Pueblo, Colorado; Youngstown, Alberta; and Eastbourne, United Kingdom. The gray area denotes the OAE II. TOC = Total Organic Carbon. Prokoph et al. (2001).

(Watson and Harrison 1983). Volcanic zircons, such as those found in ash layers, are most commonly produced in magmatic bodies with compositions of intermediate to high silica saturation. Typical igneous zircons can range in size from 20 to 250 μm in the longest dimension, having euhedral to subhedral face development. Form and size depend upon when and where zircon forms in the crystallization history of a rock. Small, acicular crystals may form due to local saturation at the edge of an early crystallizing phase (Bacon 1989), whereas late-crystallizing crystals tend to be anhedral since they may have grown in the interstices between earlier-formed minerals (Scoates and Chamberlain 1995). Larger, euhedral crystals, with length-to-width ratios of 1:2 to 1:4 often form in zircon saturated melts. Zircons that crystallized very rapidly in volcanic rocks have very large length-to-width ratios (up to 1:12) producing prismatic to acicular morphologies (Hoskin and Schaltegger 2003).

Zircons have the unique property of possessing multiple isotopic "clocks" within their crystal structure that are set practically when the zircon crystal forms. The radioactive decay chains in zircon include: ^{238}U decaying to ^{206}Pb and ^{235}U decaying to ^{207}Pb, having 4468 million year and 704 million year halflives, respectively; these can be compared to test for agreement or "concordance" (see section 1.3.2.3 *U-Pb Concordia*; Wetherill 1956; Davis et al. 2003). Zircons usually contain concentrations of U that are greater than the surrounding magmatic average and the lattice configuration prevents all common Pb isotopes (including common ^{204}Pb) from entering during the crystallization process at levels higher than ppb (Watson et al. 1997), thereby minimizing accuracy-limiting corrections for common Pb. Due to the highly refractory nature and sluggish diffusional properties of non-metamict zircon crystals, it normally preserves the original U content and the accumulated radiogenic Pb concentrations, allowing a single zircon grain to retain a pristine radiometric record (Davis et al. 2003).

Zircon may survive melting events as xenocrysts that are incorporated into younger magma and nucleating new zircon growth. The older inherited domain is often a "core" that is isotopically older than the newly formed domains. Isotopic mixing between the older core and younger rims may occur when the crystal is dissolved during high-precision isotopic dilution analysis. In volcanic rocks of felsic composition, inheritance is moderately common, which may be problematic for dating eruptive events originating from silicic volcanoes, since inheritance may produce an older and inaccurate ash eruption date. Growth histories can be deduced on the basis of crystal petrography, cathodoluminescence (CL) zonation patterns, mineral inclusions, geochemistry and U-Th-Pb systematics (Schmitz and Bowring 2001b), allowing one to screen and/or test for age heterogeneities within single crystals.

1.3.1.2 Zircon Residence Time

Residence of a mineral within a magma chamber is defined as the ability of the mineral to retain radiogenic parent and daughter nuclides against diffusive loss at ambient magmatic temperatures, while the mineral resides within the magmatic chamber (Schmitz and Bowring 2001a). Due to their refractory nature, zircons found within some felsic magma chambers may begin crystallizing well before eruption, retaining U, Th and radiogenic Pb even at temperatures above the ambient magma chamber temperature (Schmitz and Bowring 2001a). This phenomenon is a result of the closure temperature for the diffusive loss of radiogenic Pb in zircon being at a higher degree than that of typical magmatic temperatures (closure temperature is greater than 900°C; Crowley at al. 2007). After zircon crystallizes within a magma chamber, the zircons may become suspended and reside within the convecting portion of the magma, until eruption when the zircons may be ejected with the magma (Reid et al. 1997). While the zircon crystal resides within the magma chamber, it retains the original radiogenic parent and daughter nuclides which can cause the isotopic date to be older than the eruption age by 1 to 200 k.y.; this time interval is termed the "residence time". Simon et al. (2008) has recommended that all U/Pb zircon age uncertainties be expanded by +0/-200 ka in order to compensate for possible undetectable residence time.

In a study of the Bishop Tuff which originated from the Long Valley caldera, Reid and Coath (2000) found very short zircon residence times. Relatively young eruptions are often used in residence time studies since the ability to resolve absolute age differences decreases with increasing age on a geological timescale. The zircons from the Bishop Tuff have cores dating to 823 ± 11 ka ($^{206}Pb/^{238}U$) and rim ages of 839 ± 36 ka and 845 ± 36 ka. Even though the rim ages differ within the population, the core-rim ages indicate that the zircons crystallized quite quickly, within a few tens of thousands of years, signifying that the zircons are devoid of xenocrystic inheritance. If the eruption age is the same as this crystallization age, then the zircons did not reside long within the magma chamber. It is believed that the eruption age of the Bishop Tuff is 760 ± 1 ka, as determined by sanidine $^{40}Ar/^{39}Ar$ dating methods (van der Bogaard and Schirnick 1995), but the zircon crystallization age ranges from approximately 823 to 845 ka, and upon first inspection, suggests slightly over 100 k.y. of zircon residence time.

These results are improved upon in a study by Crowley et al. (2007). In this study, 19 zircons were isotopically dated through ID-TIMS and 17 of the grains gave a weighted-mean age of 767.1 ± 0.9 ka, which overlap within error of the recalculated $^{40}Ar/^{39}Ar$ sanidine eruption age of 783 ka to 761 ka (Sarna-Wojcicki et al. 2000), indicating very little residence time. It is unlikely that the oldest part of any grain resided in the magma for more than a few tens of thousands of years. The studies by Reid and Coath (2000) and Crowley et al. (2007) illustrate the necessity of an accurate comparison between $^{40}Ar/^{39}Ar$ and U/Pb isotopic methods when high-precision is required, which will be explored more in 1.3.2.4 *Comparison of U-Pb and* $^{40}Ar/^{39}Ar$ *Dating.*

In contrast to the Bishop Tuff results, Reid et al. (1997) extracted zircons from two lava flows that were extruded from the Long Valley caldera in east-central California. The lavas, Deer Mountain and the Inyo Dome, are believed to have originated from the same magma reservoir and contain large zircons. The Deer Mountain eruption dates to 115 ka, whereas the Inyo Dome eruption dates to 0.6 ka. As determined by ^{238}U-^{230}Th ion microprobe methods, most zircon growth occurred more than 100 k.y. before the first (Deer Mountain) of the two eruptions. Furthermore, the Deer Mountain lava erupted more than 100 k.y. before the Inyo Dome tapped the same magma body, indicating that the magma chambers may be long lived and zircon residence times may be as great as 200 k.y.

Often in altered tephras such as bentonites, zircon is the sole surviving igneous phase, making it impossible to determine the age of an eruption through other, independent methods such as $^{40}Ar/^{39}Ar$ geochronology. Residence times may only be recognizable by isotopic evidence that is synthesized from independent methods and from precise individual U-Pb analyses that have a variable age distribution. However, in sufficiently old magma bodies (10 Ma to 100 Ma) analytical uncertainties for single zircon crystal analyses become sufficiently large enough to mask the age distributions that are imparted by variable magma residence times (Simon et al. 2008). Simon et al. (2008) suggests that the mean U-Pb zircon age calculated from a suite of analyses for a sufficiently old magma will be biased by 30 k.y. to 300 k.y. from the eruption age. Furthermore, Simon et al. (2008) suggests that large explosive eruptions, such as those that would produce trans-continental bentonite layers, result in a relatively narrow range of pre-eruption ages of approximately 50 k.y. to 135 k.y. and therefore zircon age uncertainties should be expanded by +0/-200 k.y. Zircon residence times are of great importance when trying to establish a high-resolution chronostratigraphy, such as that in the following study.

1.3.2 U-Pb Isotopic Dating Background

The following information is drawn from Faure and Teresa (2005) unless otherwise noted.

1.3.2.1 Isotopic Dating

The long-lived radioactive isotopes of certain elements decay over time, producing stable daughter end-products. Parent-daughter isotope relationships provide a useful method for dating the minerals in which these isotopes collect. There are four major assumptions for the isotopic dating of a mineral:

1. The mineral has not gained or lost isotopic parent or daughter atoms through the mineral's history and the number of atoms only changes through the process of radioactive decay.
2. The decay-constant of the parent nuclide is known accurately, is independent of time, and is not affected by any physical conditions.
3. The appropriate number of initial daughter atoms is used in calculations.
4. The measurement of the daughter and parent atoms is accurate and representative of the mineral that is being dated.

When a long-lived radionuclide (N) decays within a mineral to an amount of radiogenic daughter atoms (D*), the number of daughter atoms in the mineral may be calculated through the equation:

$$D^* = N_O - N \qquad \text{Eq. 1.2}$$

Where N_O is the initial number of parent atoms present in the mineral. The Law of Radioactivity is stated as:

$$D^* = N_O\left(1 - e^{-\lambda t}\right) \qquad \text{Eq. 1.3}$$

Where λ is the decay-constant of the parent isotope and t is time since radioactive decay started. This equation states that the number of radioactive parent atoms will decrease exponentially with time and the daughter atoms will increase. Calculating the isotopic date of when the daughter atoms started to collect is based on the equation:

$$t = \frac{1}{\lambda}\ln\left(\frac{D - D_O}{N} + 1\right) \qquad \text{Eq. 1.4}$$

Where D_O is the initial amount of daughter atoms and D is the number of radiogenic daughter atoms. This equation is only valid in a closed system setting.

The degree of an isotopically closed system, where no radiogenic daughter or parent is gained or lost, is dependent on the following factors:

1. How well the mineral can retain the parent and daughter elements from diffusive loss.
2. The physical and chemical properties of the parent and daughter elements themselves.
3. The metamorphic alteration history of the mineral in response to pressure and temperature changes.
4. The rate of cooling that follows the last thermal episode.
5. The amount of interaction of the mineral with aqueous solutions.

If the system is closed to the loss of radiogenic parent or daughter atoms, secular equilibrium may exist. Secular equilibrium indicates that with increasing time, the rate of decay of all unstable intermediate daughter products becomes equal to that of its long-lived parent isotope, in other words, the rate of decay of the long-lived radionuclide becomes equal to the rate of production of the stable end-member daughter product, and is represented by the equation:

$$N_1\lambda_1 = N_2\lambda_2 \qquad \text{Eq. 1.5}$$

Where $N_1\lambda_1$ is the daughter product and $N_2\lambda_2$ is the long-lived parent.

1.3.2.2 U-Th-Pb Isotopic Systematics

Uranium (U; Z=92) and Thorium (Th; Z=90) are members of the actinide series of elements that have 5*f* orbitals that are progressively filled with electrons. U and Th both occur in nature in the tetravalent oxidation state. U and Th have similar ionic radii (U^{4+} = 1.05 Å, Th^{4+} = 1.11 Å), the same charge, similar electron configurations, and therefore have very similar chemical properties and may easily substitute for each other in zircon. Although under oxidizing conditions, U forms the uranyl ion (UO_2^{2+}) which is soluble in water, making U a mobile element under oxidizing conditions, and Th is insoluble in water.

This study focuses primarily on U and Pb istopes that are isolated from single zircons, and therefore Th is largely disregarded in the following discussion. U has three isotopes: ^{238}U, ^{235}U and ^{234}U. The decay of ^{238}U to stable ^{206}Pb gives rise to the uranium series, in which ^{234}U is an unstable intermediate daughter product. This decay series may be summarized by the equation:

$$^{238}_{92}U \rightarrow\ ^{206}_{82}Pb + 8^4_2He + 6\beta^- + Q \qquad \text{Eq. 1.6}$$

Where Q is the sum of decay energies and is equal to 47.4 MeV/atom. In this decay series for each atom of ^{238}U that decays, eight α-particles and six β-particles are emitted.

The decay of ^{235}U to stable ^{207}Pb gives rise to the actinium series and may be summarized by the equation:

$$^{235}_{92}U \rightarrow\ ^{207}_{82}Pb + 7^{4}_{2}He + 4\beta^{-} + Q \qquad \text{Eq. 1.7}$$

Where Q is equal to 45.2 MeV/atom. In this decay series for each atom of ^{235}U that decays, seven α-particles and four β-particles are emitted.

Even though 43 isotopes of 12 elements are formed through these decay chains (including ^{232}Th), each decay system always leads to a specific stable isotope of Pb. The half-lives of ^{238}U, ^{235}U and ^{232}Th are much longer than their intermediate daughters and if it is a closed system, secular equilibrium may be established (1.3.2.1 *Isotopic Dating*), so that the radionuclides appear to have decayed directly to Pb:

$$^{238}\text{U} \rightarrow {}^{206}\text{Pb} \qquad {}^{235}\text{U} \rightarrow {}^{207}\text{Pb} \qquad {}^{232}\text{Th} \rightarrow {}^{208}\text{Pb}$$

The accumulation of the Pb daughter product may be best described by the Law of Radioactivity (Eq. 1.3) and the equations may be written in terms of atomic Pb. In the following equations the radiogenic Pb is normalized as a ratio over ^{204}Pb because it is the only nonradiogenic isotope of Pb:

$$\frac{^{206}Pb}{^{204}Pb} = \left(\frac{^{206}Pb}{^{204}Pb}\right)_i + \frac{^{238}U}{^{204}Pb}\left(e^{\lambda_1 t} - 1\right) \qquad \text{Eq. 1.8}$$

$$\frac{^{207}Pb}{^{204}Pb} = \left(\frac{^{207}Pb}{^{204}Pb}\right)_i + \frac{^{235}U}{^{204}Pb}\left(e^{\lambda_2 t} - 1\right) \qquad \text{Eq. 1.9}$$

Where *i* indicates the initial ratio in the mineral, and the U/^{204}Pb ratio is calculated from a measured concentration, determined by a solid source mass spectrometer.

1.3.2.3 U-Pb Concordia

The ejection of α-particles during the U decay process (1.3.2.2 *U-Th-Pb Isotopic Systematics*) may cause radiation damage to the zircon crystal lattice (metamictization), which will be prone to a high degree of Pb-loss through chemical leaching if the ambient temperature drops below ~150 °C (self-annealing temperature of zircon). This Pb-loss causes problems in radiogenic age calculations, but the effect on U-Pb systematics may be minimized by calculating an age based on the ^{207}Pb/^{206}Pb ratio, since this is insensitive to recent Pb-loss if no isotope fractionation is present. The above equations (eqns. 1.8 and 1.9) may be combined to form the following equation:

$$\frac{{}^{207}Pb/{}^{204}Pb - \left({}^{207}Pb/{}^{204}Pb\right)_i}{{}^{206}Pb/{}^{204}Pb - \left({}^{206}Pb/{}^{204}Pb\right)_i} = \frac{{}^{235}U}{{}^{238}U}\left(\frac{e^{\lambda_2 t}-1}{e^{\lambda_1 t}-1}\right) \qquad \text{Eq. 1.10}$$

Some observations about this equation (Eq. 1.10):

1. This equation involves the ^{235}U/^{238}U ratio, which is a constant; the atomic ^{238}U/^{235}U ratio is 137.88 (Steiger and Jäger 1977).
2. The equation only involves ratios of number of Pb atoms; no knowledge of U and Pb concentrations are needed.

3. The left side of the equation is the same as $\left(\frac{^{207}Pb}{^{206}Pb}\right)^*$ where the * indicates radiogenic isotopes.

4. Since this equation only uses Pb atoms, enough geological time has to have elapsed to allow a sufficient accumulation of radiogenic Pb.

The equation above may not be solved for t through algebraic methods and therefore t must be interpolated within a table; these dates are called Concordia dates (Wetherill 1956). When a curve is plotted with the axis:

$$\frac{^{206}Pb^*}{^{238}U} = e^{\lambda_1 t} - 1 \qquad \text{Eq. 1.11}$$

$$\frac{^{207}Pb^*}{^{235}U} = e^{\lambda_2 t} - 1 \qquad \text{Eq. 1.12}$$

A curve called a Concordia curve may be constructed (Fig. 1.17) which combines all of the dates based on the two U-Pb isotopic decay chains. The Concordia curve represents the locus of agreement of ages calculated with each of the two isotopic U-Pb ratios (concordance) and shows the effect of Pb-loss or inheritance (displacement beneath the Concordia curve). The two U-Pb dates will be concordant if the mineral:

1. Has remained closed to the addition of U, Pb and intermediate daughters through its history.
2. Is not a mixture of different age components.
3. Has remained closed to Pb-loss through its history.
4. Accurate decay-constants are used for ^{238}U and ^{235}U.

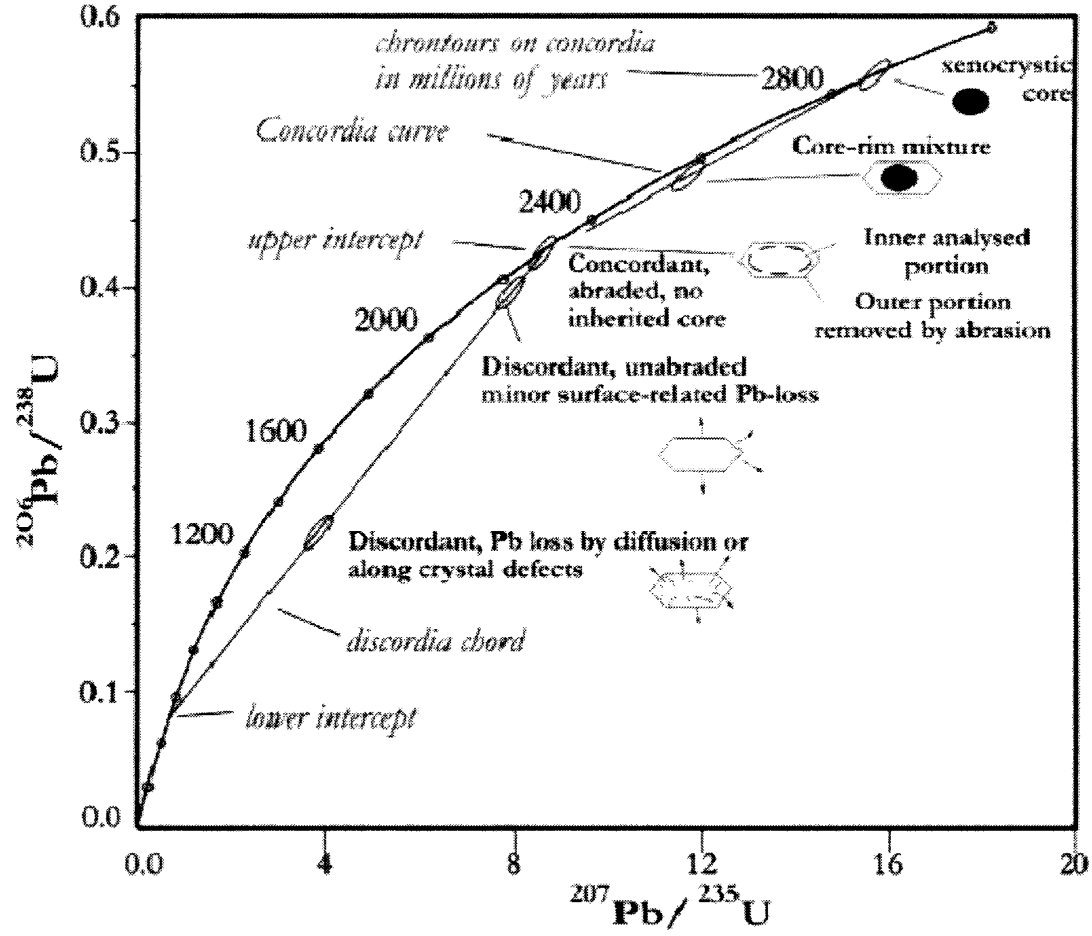

Figure 1.17. Wetherill Concordia diagram with annotations. The Concordia diagram illustrates situations commonly encountered including inherited grains, mixed-age crystals that may define a chord, concordant data on single-domain crystals and discordant analyses on crystals with surface-correlated Pb-loss due to radiation damage. Parrish and Noble (2003).

5. The isotopic composition of U is normal and has not been modified though fractionation.

6. All analytical results are accurate and free of systematic errors.

If the zircon has experienced alteration resulting in Pb-loss or a secondary mixed component, a linear array called a mixing line may result between two points along the Concordia curve (Parrish and Noble 2003). An upper intercept of the Concordia curve with a mixing line may result and indicate the presence of an inherited component, whereas the lower intercept may indicate the age of the younger overgrowths. The position along the mixing line that connects the points may be controlled by the proportion of cores to overgrowths in that sample. However it could also be interpreted that the upper intercept is the undisturbed radiometric age, and the lower intercepts represents the age of total Pb resetting, where the position along the Discordia line indicates various degrees of Pb-loss.

1.3.2.4 Comparison of U-Pb and $^{40}Ar/^{39}Ar$ Dating

It has recently been recognized that $^{40}Ar/^{39}Ar$ ages are systematically younger than U-Pb isotopic ages of minerals from rapidly cooled rocks, resulting in a ~ 1% bias when comparing $^{40}Ar/^{39}Ar$ and $^{206}Pb/^{238}U$ isotopic ages dates between the interval of 28 Ma and 4500 Ma (Renne et al. 1999), such that $^{40}Ar/^{39}Ar$ ages are underestimated. For example, geochronological analysis of $^{40}Ar/^{39}Ar$ analysis on sanidine and biotite from the Fish Canyon Tuff standard yield ages ranging between 27.5 Ma to 28.05 Ma (Renne et al.

1994; Lanphere and Baadsgaard 2001; Schmitz and Bowring 2001a), whereas a single-grain ^{206}Pb/^{238}U zircon analysis from the same tuff yields an age of 28.41 ± 0.1 Ma (Oberli et al. 1990); the ^{206}Pb/^{238}U ages are ~1 Ma older than the ^{40}Ar/^{39}Ar ages (Schmitz and Bowring 2001a). Renne et al. (1998) and Renne (2000) believe that this bias lies within uncertainties of the ^{40}K decay-constant, and from poor quality ^{40}Ar*/^{40}K and ^{40}Ar/^{39}Ar standards. Min et al. (2000) summarized various experimental data for the ^{40}K decay-constant and provided the first attempt at a systematic cross-calibration of the K-Ar system to the U-Pb system; their findings support the ^{40}K decay-constant-derived bias of ~1%.

^{238}U and ^{235}U have the most precisely known decay-constants, with 2σ statistical uncertainties on the order of 0.108% and 0.136% respectively (Jaffey et al. 1971; Villeneuve et al. 2000; Schmitz and Bowring 2001a). When systematic U decay-constant uncertainties are incorporated, the total uncertainties increase to 0.20% (^{235}U) and 0.16% (^{238}U) (Ludwig 1998, 2000; Schmitz and Bowring 2001a). The ^{40}K decay scheme has two decay-constants (^{40}Ca and ^{40}Ar) that have a combined uncertainty of 0.36% (Beckinsale and Gale 1969; Villeneuve et al. 2000). The ^{40}K decay-constant has approximately twice the uncertainty of the U decay-constants and the ^{40}K decay-constant uncertainty needs to be accounted for when comparing ages of different isotopic systems (Villeneuve et al. 2000).

In order to facilitate an accurate cross-calibration between decay schemes, the magnitude of the uncertainties that result from introducing a solution spike during U-Pb isotopic analyses must be well known and constrained (see section1.4.2 *Solution Spikes*

(Tracers)). The uncertainty in the Pb/U ratio of a tracer spike solution is in the range of 0.1% to 0.25% and as analytical uncertainties drop to less than 0.1%, tracer calibration becomes a large hindrance to the accurate cross comparison of data between different laboratories. The biases between laboratories were studied, and on average the uncertainties were as great as 0.5% (Parrish et al. 2006). In order to facilitate the inter-calibration of the U-Pb and ^{40}Ar/^{39}Ar chronometers, and the comparison of data between geochronology laboratories, a production of a mixed ^{202}Pb-^{205}Pb-^{235}U-^{238}U spike was undertaken by the EARTHTIME initiative (*www.earth-time.org*; Bowring et al. 2005). The U-Pb EARTHTIME spike was distributed to the international community to allow for the cross calibration between the decay schemes and then further calibrated using various standard materials. The EARTHTIME spike is used in the following study. The U-Pb isotopic system presently has the highest precision and accuracy of all the geochronological isotopic systems and other isotopic dating schemes should be compared with the U-Pb isotopic system, with use of the standardized U-Pb EARTHTIME spike, in order to reproduce coherent and accurate results.

1.4 Background to Isotope Dilution U-Pb Geochronology

1.4.1 Introduction to Isotope Dilution-Thermal Ionization Mass Spectrometry

The isotopic analytical methodology used here is the Isotope Dilution Thermal Ionization Mass Spectrometry (ID-TIMS) technique. Generally, ID-TIMS requires the addition of an isotopic tracer (spike, to be defined in 1.4.2 *Solution Spikes (Tracers)*) to a dissolved sample. This mixture is then transferred onto a filament, and the isotopic composition of the mixture is measured by separating the charged ions based on their masses in a magnetic field. ID-TIMS is advantageous to other isotopic dating methods because it is one of the most accurate and precise methods available due to an insensitivity to chemical yields or mass spectrometer sensitivity (Parrish and Noble 2003). Therefore, if background contamination and interference is minimized, only a small amount of sample is required and low concentrations of many elements can be measured with great accuracy (Faure and Teresa 2005). ID-TIMS has other beneficial aspects, such as a reasonable ionization efficiency, a simple mass spectrum, excellent signal-to-noise characteristics, small-order mass fractionation, negligible Pb and U contamination of samples by the instrument, and it lacks reliance on mineral standards in the calibration process (Parrish and Noble 2003).

1.4.2 Solution Spikes (Tracers)

In order to create a solution that is suitable for isotopic analysis by ID-TIMS, a spike (tracer) of known quantity must be mixed with an unknown quantity of the analyte that is isolated from a dissolved grain using an anion exchange chromatographic procedure. A spike is defined as a solution that contains a known concentration of a particular element whose isotopic composition has been changed through the enrichment of one of its isotopes; the concentration and isotopic composition of the spike is accurately known and verified separately (Faure and Teresa 2005). The sample being analyzed has a known weight and isotopic composition, but has an unknown concentration of the desired element (analyte). The analyte of the sample is mixed to isotopic homogenization with the known amount of the spike solution. The known isotopic composition and weight of the spike, along with the mass ratio of the isotopes, is used to calculate the amount of the analyte element that is in the dissolved sample (Faure and Teresa 2005). For example, if a ^{205}Pb tracer is added to a sample and analyzed via ID-TIMS, the mass spectrum of each Pb isotope is measured in proportion to the spike producing mass ratios, and by using the spike, the concentration of total Pb in the sample can be calculated.

In 1975 Krogh and Davis synthesized ^{205}Pb through a cyclotron-produced (p,2n) reaction on ^{206}Pb via the short-lived and intermediate ^{205}Bi. Before this instance, ^{205}Pb had been synthesized through neutron capture on ^{204}Pb, followed by calutron isotope separation, but the 1975 synthesis was the first to be widely applied in a tracer mixture with ^{235}U (Parrish and Noble 2003). In 1987 Parrish and Krogh synthesized ^{205}Pb on a large scale at the Canadian cyclotron facilities of the TRIUMF physics consortium. This synthesis occurred by plating a silver cyclotron target with ^{206}Pb and subsequently bombarding it with ~27 MeV protons to produce short-lived ^{205}Bi, which subsequently decayed to ^{205}Pb (Parrish and Noble 2003). This new synthesis of ^{205}Pb was made available to many laboratories, in the form of a concentrated ^{205}Pb spike, which was 95% ^{205}Pb and 5% ^{206}Pb, and allowed many laboratories to reach "state of the art" (Sandra Kamo, 2008, pers. comm.).

1.4.3 ID-TIMS Instrumental Configuration

The following information is drawn from Fisons PLC (1992), unless otherwise noted.

All modern-day mass spectrometers are based on the original design by Neir (1940). The Neir-type mass-spectrometer, which includes the Thermal Ionization Mass Spectrometer (TIMS), has three main components: a source of a mono-energetic beam of ions, a magnetic analyzer and an ion collector (Faure and Teresa 2005). In a TIMS system, the mono-energetic beam of ions is produced through thermal ionization of a filament, and the process may be best described by the formula:

$$\frac{n^+}{n_o} = exp - \frac{(I-O)}{kT} \qquad \text{Eq. 1.13}$$

Where n^+ is the concentration of positively charged ions above a surface of work with the function of O at a temperature of T, n_o is the neutral atom density, and I is the ionization potential of the element that is being analyzed. From this equation one may see that to get the highest degree of ionization of the filament, a high degree work function is required and the filament must be operated at the maximum temperature possible. Due to these two factors, the filament will usually be made of rhenium (Re), but it can also be made out of Ta or W (Faure and Teresa 2005). There are three types of filament configurations that may be used for ID-TIMS analyses and they are triple, double or single filaments; the mass spectrometer used in the following study is equipped with a single Re filament. A single filament is usually easier to prepare versus a double and triple filament where one must transfer the sample from a separate evaporation filament. When a solid sample is to be analyzed on a single filament, the solid undergoes a chromatographic dissolution process so that the salt of the analyte (element to be determined) can be deposited onto the filament (Faure and Teresa 2005). The temperature of operation of the single filament is lower than that of a double or triple filament to prevent rapid evaporation of the sample.

The internals of the mass spectrometer are under a high-vacuum in order to send ions down the flight tube, usually on the order of 10^{-6} to 10^{-9} Pa (Faure and Teresa 2005); there are three main reasons behind this. The first reason is to prevent ion scattering. Ions may collide with residual gas molecules, causing a modified ion trajectory, which would lead to a mass spectrum with broadened peaks and peak tailings that would affect adjacent peaks. The second reason is that the presence of active gases in the source region may affect the sample, such as metal oxide beams being generated. The third reason is that the high voltages used in the source require a high vacuum to prevent electrical breakdown, which is also known as flashover. The pressure (or lack of) per unit area within a mass spectrometer may be calculated by the equations:

$$P = {}^{1}/_{3}\, n\, m\, V_{rms}^{2} \qquad \text{Eq. 1.14}$$

$$V_{rms} = \left(\frac{3\,K\,T}{m}\right)^{-\frac{1}{2}} \qquad \text{Eq. 1.15}$$

Where m is the mass of the molecule, n is the number of molecules in a unit volume, K is the Boltzman's constant (1.38 x 10^{-23} PaM^{2}K^{-1}) and T is the temperature of the gas. The type of pump used to evacuate the mass spectrometer is dependent on the type of gas flow present and there are two types of gas flow that may occur within a mass spectrometer, viscous and molecular flow. Viscous flow occurs when the gaseous molecules occupy a space at pressures greater than 1 Pa. These molecules constantly collide, acting as a predictable fluid. Since the flow is predictable, a small hose may be used for rough pumping, but as molecules are removed from the chamber, others will immediately occupy the empty space. Molecular flow occurs when gaseous molecules are so far apart from each other that they no longer exert any influence on each other and their motion is random. The movement of the molecules cannot be relied upon to push or start a flow pattern, and therefore a vacuum pumping system must have a large diameter intake to increase the probability of a randomly moving molecule to enter into the pumping system. There are five types of pumps used to remove gaseous molecules from a TIMS system and they are: a rotary vane pump, a turbo molecular pump, an ion pump, a liquid nitrogen cold trap and a titanium sublimation pump. A rotary vane pump removes gases by compressing them through an offset rotor with spring loaded vanes to a point that is slightly above atmospheric pressure and then expelling the compressed gas to the atmosphere; this is enough to produce rough pressures of 1×10^5 Pa to 1 Pa. A turbo molecular pump (TMP) uses a high speed axial compressor to compress gases that are taken in from the low pressure side of the pump and then exhausts the gas to the vacuum foreline, to be pumped away by the rotary pump. An ion pump has two electrodes that are connected to a high voltage supply (5 kV). Electrons flow from the cathode to anode in a spiral motion due to the presence of an applied magnetic field, creating a potential that the electrons will collide with gaseous neutral atoms, ionizing them. The electron then travels to the anode and the positive ion to the cathode. The molecules on the cathode are released from the surface in a process called sputtering, after which they are then buried by pumped gas molecules. The liquid nitrogen cold trap has a high pumping speed for condensable gases. This type of pump is most useful in the source region of the mass spectrometer, because after a sample change and re-evacuation of the chamber, residual gases are present that consist mainly of water; the trap may help improve pressures by 5 to 10 fold. A titanium sublimation pump (TSP) utilizes an air cooled chamber that surrounds a titanium/molybdenum alloy filament to create a vacuum. When the filament is heated, a titanium vapour is produced that condenses on the surrounding surfaces, reacting with active gases to form a stable compound that may be removed at high speed.

After the mass spectrometer is pumped down an accelerating voltage is applied to the filament, the filament becomes heated to volatilize the deposited elements, ionizing them into the vacuum. A high voltage electric field is applied and the ions are accelerated down the flight tube, being collimated into a beam (Faure and Teresa 2005). The ions are focused through a series of five, in sequence, lens plates that are contained within the collimator. The lens plates, from closest to the filament to the farthest are, the extraction plate, the D-plates, the slit plate, the Z-plates and the defining aperture; see Fig. 1.18 for an arrangement of the magnetic lenses. The extraction plate is biased negatively with respect to the filament and source potentials. It provides a draw-out field for the positively charged ions that are ejected from the source. The first Y-focus lens (D-plate) has a potential on it that may be controlled and is used to focus the beam. Furthermore, the ion beam may be deflected in the Y-axis by changing the bias of the

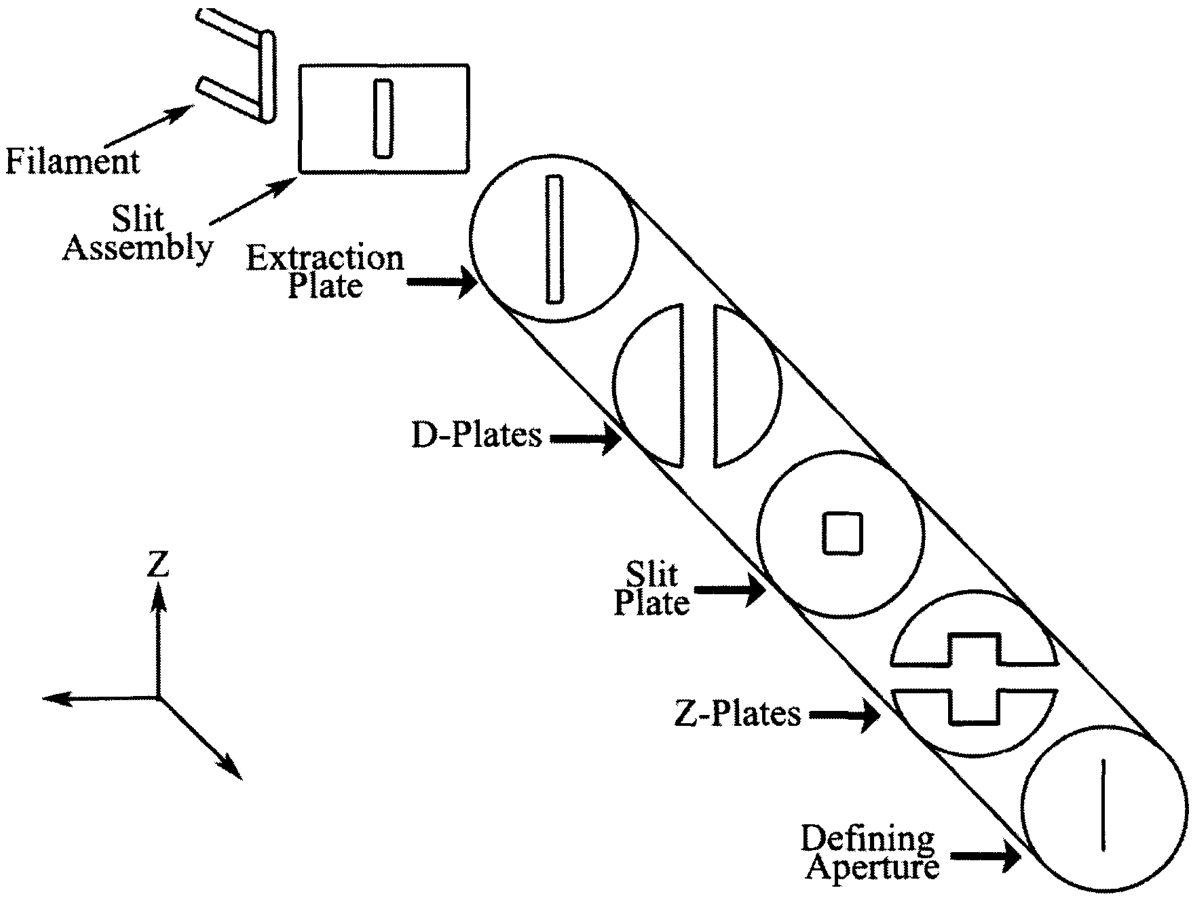

Figure 1.18. A schematic diagram of the lens plates (collimator), in which ions are produced from the hot sample filament and focused through the collimator. Varying biases are applied to the lenses to achieve focus. Modified from Fisons PLC (1992).

lens. The second Y-focus lens (slit plate) also operates in the Y-axis and its potential may also be controlled. The combined effect of the two Y-focus lenses is to provide a partial zoom feature, which may help to maximize the size of the beam that is transmitted into the electro-magnetic analyzer. The Z-focus lens works similarly to the D-plate, except it operates in the Z-axis, therefore the potential may be controlled and it will deflect the ion beam in the Z-axis. The final lens plate in the collimator is the source defining slit for the magnetic analyzer and it is located at the object point of the nominally stigmatic magnetic analyzer.

The ions exit the source chamber at ~8000 V and travel to the analyzing magnet, which has magnetic field lines perpendicular to the directional vector of the ions (Faure and Teresa 2005). The strength of the magnetic field that is required to turn the ion beam through a bend in the flight tube with a radius r in the flight tube is represented by the equation:

$$B = 143.95 \, \frac{(m\,V)}{r} \qquad \text{Eq. 1.16}$$

Where B is the strength of the magnetic field in gauss, m is atomic mass of the ions, V is the voltage (potential difference) applied to the electromagnet and r is the radius of the curve. When analyzing various ions, the path of the differently charged ions can be calculated by the equation:

$$r = \frac{143.95}{B} \left(\frac{m\,V}{e}\right)^{1/2} \qquad \text{Eq. 1.17}$$

Where r is now the radius that the path of the ion dictates and e is the charge of the ion (Faure and Teresa 2005). Combined with a curve in the flight tube, ions are deflected based on their atomic mass; heavier ions are deflected less than lighter ones. The ion beam is separated according to the mass-to-charge ratio of the ions, which can be seen in the preceding equations (eqns. 1.16 and 1.17) if the magnetic field strength and potential difference remains constant allowing $r \propto \sqrt[2]{m}$ (Faure and Teresa 2005).

The differentiated ion beams are sent to an ion collector, which resides behind a slit plate. In single collector machines, the intensities of each ion beam are measured by switching the magnetic field in a fixed cycle and each beam is in turn brought into focus at the collector. The width of the refocused ion beam, by the time it is received by the collector, can be described by the equation:

$$W_s \times m + aberrations \qquad \text{Eq. 1.18}$$

Where W_S is the width of the source slit and m is the magnification of the beam. Aberrations are the result of the imperfect refocusing of an ion beam, geometric coefficients that are a function of the source slit dimensions and angular spread of the ion beam as it exits the ion source. The ion beam being analyzed is focused through the slit plate, and all other beams hit the grounded slit plate and are neutralized (Faure and Teresa 2005). In the collector, the Faraday bucket detector is used for ion beams up to 10^{-10} A and when the ion beam is less than $5\text{x}10^{-13}$ A, a multiplier system such as an Axial Daly detector is used; the Daly multiplier system is used in the following study, since it is the most sensitive and is able to amplify small signals such as those from young zircons. When the focused ion beam enters the Daly detector, the ions are deflected to an electrode (Daly doorknob), which has a voltage applied to it and maintains a potential of ~(-)20 kV. When the ion beam strikes the doorknob, a release of secondary electrons occurs (~6 per inch) which are repelled towards the adjacent scintillator. The collision of the electrons with the scintillator causes a release of photons (scintillations; ~200 per electron). There are two types of Daly detectors, analog and pulse counting. Analog detectors have scintillators that are made of a material that exhibits a long lasting photon release and therefore is either on or off. Pulse counting detectors incorporate a quartz plate that is covered with a phosphor enriched organic plastic, which is much more sensitive to varying intensities of photon release. The scintillator face is coated with aluminum to prevent an electron charge build-up and reflect photons into a photomultiplier tube (Podstawskyj 2008, pers. comm.). In the photomultiplier tube, the ejected photons pass through a curved quartz plate that focuses the light onto a copper alloy cathode causing a cascade of electrons that can be detected as a signal upon further amplification. Fig. 1.19 is a schematic representation of the entire mass spectrometer unit.

The signals produced from a mass-spectrometer are a series of peaks and valleys, representing the mass spectrum of the element. An individual peak signifies a mass-to-charge ratio and identifies each isotope in the mass spectrum of the element being analyzed, while the height of the peak is proportional to the relative abundance of the isotope (Faure and Teresa 2005). Since the peak height is only an indication of the

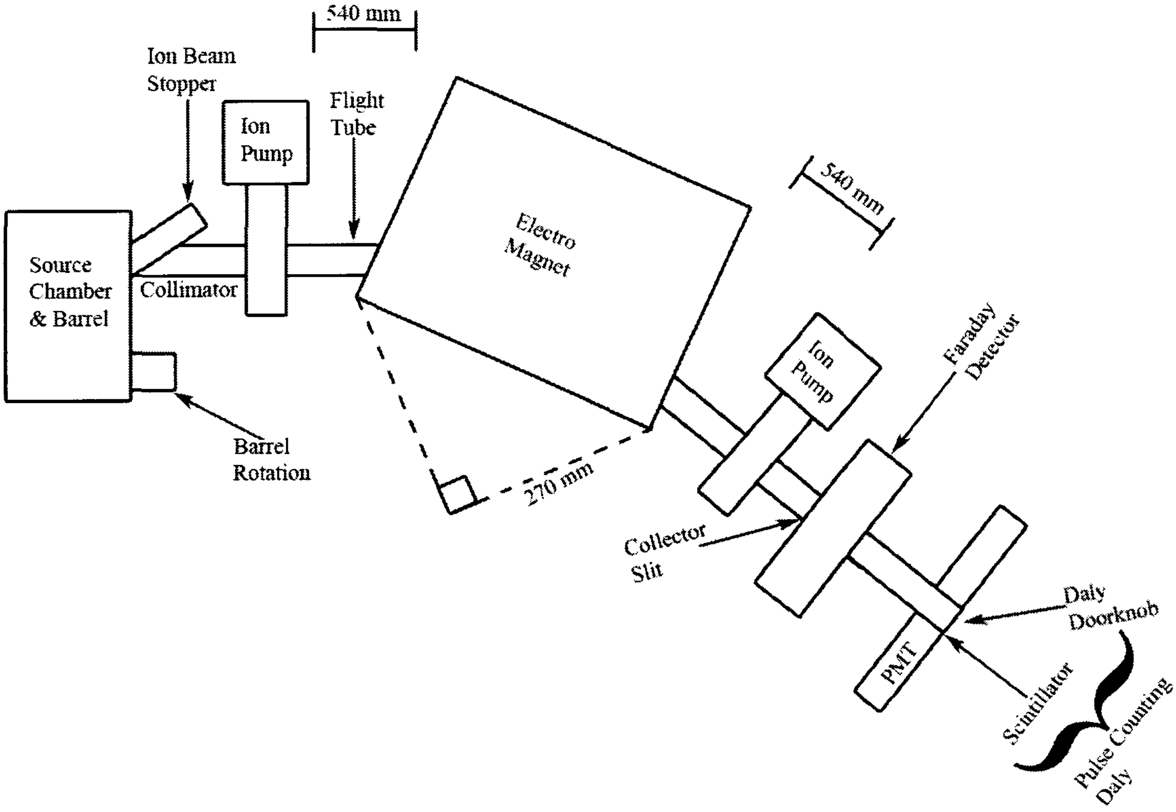

Figure 1.19. A schematic representation of the mass spectrometer system. The sample is loaded into the source chamber where the sample is ionized on the hot filament. The ion beam is sent down the flight tube and focused through the collimator. The magnetic analyzer separates the ions based on weight, and sends the beam to the collector slit, where the signals are detected by the Faraday or Daly detectors. PMT = Photomultiplier tube. Modified from Fisons PLC (1992).

relative abundance, the isotopic ratios are calculated from the intensities of the ion beams.

The ratio of the ion beam intensities often do not exactly correspond with the isotopic ratios, due to a phenomenon called thermal fractionation. The chromatography process used to prepare the sample preferentially favours isotopic species of lighter mass and therefore isotopic ratios are biased towards an increasing intensity of the light isotopes. As a measurement proceeds, ratios will fall continuously with time as light isotopes become depleted from the sample. The accuracy of a measurement is dependent upon achieving reproducible fractionation from the samples and an isotopic standard may be used to determine the magnitude of the biasing factor and then correcting for the effects.

1.4.4 ID-TIMS and Zircon U-Pb Geochronology

The first U-Th-Pb ID-TIMS analyses on zircon were during the 1950's and was performed by Tilton et al. (1955, 1957) and Wetherill (1956). These early analyses utilized a procedure involving the flux-assisted decomposition of zircon, which incorporated spikes enriched in ^{208}Pb, ^{230}Th and ^{235}U, and then analyzing the zircon solution on custom mass spectrometers that lacked computerized components (Parrish and Noble 2003). During the 1960's and 1970's progress was made to the zircon ID-TIMS methodology in order to decrease contamination levels and required sample size. These improvements came in the form of improved vacuum systems, computer automated data acquisition and the synthesis of a ^{205}Pb spike solution (Krogh and Davis 1975; Parrish and Noble 2003). Mattinson (1972) adapted FEP and TFE Teflon-ware for the distillation and production of ultra-pure acids, which effectively decreased Pb contamination. Sub-boiling Teflon stills that were contained in steel pressure vessels were used for the high temperature decomposition of zircon. The dissolution of zircon could be executed at 210 °C, with greatly decreased Pb contamination during laboratory procedures (Krogh 1973). During the 1980's great developments arose as mass spectrometers became commercially available, multiple ion collection became available using mixed detector arrays (Roddick et al. 1987) and air abrasion was developed to remove the outer radiation damaged areas that were susceptible to Pb-loss (Krogh 1982). The combined effect of all these developments was that the U-Pb isotopic composition of a single zircon containing sub-nanogram quantities of Pb could be analyzed precisely. However, in 1994, Mattinson subjected zircons to an aggressive HF-HNO_3 acid leaching procedure to induce partial dissolution of the internal and external soluble portions of zircon grains that experienced Pb-loss from radiation damage and fluids. The chemical abrasion method of Mattinson (1994) superseded air abrasion, and has become a new standard method for ID-TIMS geochronology.

One of the most crucial advances in ID-TIMS geochronology was the use of a silica gel and phosphoric acid as an efficient and stable Pb^+ (and UO_2^+) ion emitter (Cameron et al. 1969), and over the past 35 years the U and Pb contamination in the gel has decreased, increasing the ionization efficiency by an order of magnitude (Gerstenberger and Hasse 1997). This stable ion emission from the silica gel and phosphoric acid allowed for peak switching of the U and Pb isotopes on a single collector mass spectrometer (Parrish and Noble 2003). The most important result from these advancements is that from 1985 to present time Pb blank levels dropped from 5 to 20 pg down to <1 pg, allowing for much more precise experimental data (Parrish and Noble 2003).

2. SAMPLING, SAMPLE PREPARATION AND ID-TIMS ANALYTICAL METHODOLOGY

2.1 Collection

During the first week of June 2007, fieldwork was undertaken in the Alberta foothills and 15 bentonite samples were collected from nine localities (Appendix A). These bentonite layers were identified and correlated based on previous field work and notes by Guy Plint and his students (Tyagi et al. 2007; and Plint Unpublished Data), and were chosen due to their widespread occurrence and position relative to important marker boundaries. The amount of sample collected varied (Appendix A) and was based on the thickness of the bentonite layers. All layers were initially cleared of any surface contamination and four different methods were used to extract the bentonite samples; these methods were designed to minimize the amount of contamination from the surrounding sedimentary layers and from weathering. The first method utilized a 1" inner diameter galvanized steel pipe that had a sharpened edge on one end and a flattened surface on the other. The steel pipe was washed thoroughly before use with soap and a cotton barrel squeegee. The cleaned pipe was aligned with the bedding angle of the bentonite layer and was driven in with a rubber mallet. The core tube was pulled out from the layer and extruded into a sample bag using a 1" diameter piece of wooden doweling, capped with a metal stub; the last inch of the sample was discarded to avoid surface contamination from the stub. The next method was identical to the first method, only a smaller ¾" inner diameter steel pipe was used. The third method was only used when the bentonite was very thick and involved using a clean plastic trowel to remove the outer 5 cm of the bentonite and then digging out the sample and depositing it into a sealable plastic bag. The final method was used in order to preserve the bentonite's layered structure, if present. A trench was dug, leaving a raised section that was about the size of a plastic sealable container. The container was placed over the raised portion of the bentonite and the raised section was lifted into the container, so the structures were left undisturbed.

2.2 Low-Contamination Mineral Separation

All mineral separation occurred at the Jack Satterly Geochronology Laboratory, University of Toronto. Great care was taken to avoid contamination when isolating and analyzing the zircon grains. All equipment was kept in very clean condition to prevent sample cross contamination. During processing, samples and containers were placed on clean sheets of craft paper, on a pre-cleaned surface. All of the equipment used to extract the zircons from the host rock was first cleaned with ethyl alcohol and then air-dried with compressed air. When the disk mill was required, sterilized bags, made with 3 mm plastic sheets and a heat sealer, were inserted into the disk mill, to obstruct the intake of contaminants and dust exhaust. Large fans created suction, removing excess dust from the workspace that could contaminate future samples.

2.3 Mineral Separation

Samples were weighed before disaggregation and a maximum of ~250 g of a bentonite sample was placed into a clean Osterizer 14 speed blender cup. 1 cup of water was added, along with ~5 ml of Sunlight dish detergent. The sample was blended on both low and high speeds for 5 minutes, or until a complete water-based slurry, with no consolidated fraction, was created; this process was repeated until the entire sample was in a fully disaggregated form. If the bentonite sample was fully consolidated, a hammer was used to initially break down the sample and a disk mill was used to break the sample into a small ~150 μm particle fraction.

The slurry or dry pulverized sample was passed over a Wilfley table, resulting in a crude separation based on the mineral density. The two fractions, light and heavy minerals, were sorted into two separate containers. For drying, the light and heavy fractions were placed in a filter-paper lined funnel, which was then placed into a large Erlenmeyer flask. The sample was saturated in ethyl alcohol, drained under suction and placed on a hot plate, on low heat, under a heat lamp. The sample was heated until it was dry and was then put into a new, clean glass container.

The Wilfley heavy fraction was placed onto a size 70 (200 μm pores) mesh sieving cloth. The samples were separated into coarse and fine fractions. Zircons are generally less than 200 μm in size and any undesired large non-zircon grains that were included into the Wilfley heavy fraction were excluded.

The 70 mesh fine fraction was passed through a Frantz electro-magnetic separator. Metamict zircon grains are partially paramagnetic, and may be separated from non-magnetic grains by applying a magnetic field while passing them down a tilted track. Magnetic grains are drawn to one side of the track, while the non-magnetic, non-metamict grains remain on the other side of the track under the influence of gravity. The sieved heavy fraction was added to the Frantz hopper shaker, which continuously added the sample onto the track. The Frantz was set at a 10^{0} tilt and the magnetic field was incrementally set from 0.5, 1.0 and 1.7 A (max field). Both of the magnetic and non-magnetic fractions were isolated at the end of the Frantz track and collected.

Using methylene iodide (MI), zircon was isolated from less dense minerals such as apatite. The non-magnetic fraction was placed into the bottom of a centrifuge tube and MI was filtered into it; in this mixture, due to their specific gravity, zircons sunk to the bottom, while other grains floated to the top of the MI. The bottom end of the centrifuge tube was then frozen in chilled alcohol, locking in the zircons and allowing the light fraction to be removed. Alternatively, and the preferred heavy liquid method, involved using a separatory funnel to drain the heavy fraction first, leaving only the light fraction in the separatory funnel; this method was preferred due to a lower risk in losing the desired zircon grains. Both fractions were then washed in acetone before the sample was dried under a heat lamp.

2.4 Secondary Electron Microscopy and Multi-Spectral Cathodoluminescence (SEM-CL)

The secondary electron microscope (SEM) that was used in the following study was a Hitachi Secondary Electron Microscope Model S-2500C with a tungsten filament. Carbon coated sectioned zircons were mounted to an SEM stub with double-sided carbon tape. Electrodag 502 carbon paint was used to connect the SEM stub to the top of the slide, in order to allow surface electron discharge. The slide was put into the vacuum chamber and was pumped down a current of 5 μA to 10 μA was reached (atmospheric is 100 μA) before the accelerating voltage was turned on. The accelerating voltage was set to 10 kV and the aperture was set to the 3 opening. The electron beam was rastered across the sample, creating secondary electron (SE) topographic images, which were captured digitally using the Gatan Digital Micrograph software package.

The Gatan ChromaCL detector at the University of Western Ontario reveals submicron scale variations in the electron stimulated light that is emitted from crystal surfaces; these variations are a proxy for trace element and structural variations within a crystal. The zircon grain mount was inserted into the SEM by the same method discussed above. The SEM accelerating voltage was set to 25 kV, with a working distance of >13 mm and the aperture set to the 1 opening (this setting caused the epoxy to bubble, but created a large CL signal). The light guide for the Gatan ChromaCL detector system was inserted between the sample and pole piece, and the accelerating voltage of the SEM was turned on. Electron stimulated light was collected using a diamond turned parabolic mirror that is coupled with a diffraction grating. The grating dispersed the light and directed it into an array photomultiplier tube (PMT), which was then amplified and sensed by the Digiscan input electronics. The Gatan ChromaCL detector collects the light in four parallel channels using the Gatan *DigitalMicrograph* digital imaging software and the Digiscan beam controller. The spectral range of this detector is between 300 nm to 850 nm and the images consist of the red, green and blue visible spectra channels, plus ultraviolet, which is expressed as magenta in the visible spectra. The dwell time per pixel was set to 80 μs. The penetration and excitation depth of a crystal may vary on the accelerating voltage and the material being imaged, but are typically in the range of 2 μm to 8 μm.

2.5 ID-TIMS Chemistry

A total of four bentonites were used for analyses by ID-TIMS (Bighorn River, A-X, X and Green). These bentonites were chosen since they are widespread, have previously published results (e.g. Obradovich 1993, Kowallis et al. 1995, Cobban et al. 2006) and have great stratigraphic significance. However, only three of these benonites (Bighorn River, A-X and X) had statistically usable grain yields. The total zircon population per bentonite was initially analyzed with a stereo microscope and a batch of the larger, better quality grains were selected (~ 60 grains). These batches of grains were transferred to quartz crucibles (one crucible per grain batch), while a furnace was preheated to 450 °C. The crucibles were placed into a ceramic tray and the grains were annealed in the furnace at 1000 °C for 30 hours. The annealing process fixed any crystal lattice damage and effectively caused the lattice to increase the retentivity of Pb atoms during the proceeding HF chemical abrasion process. After the 30 hours, the furnace temperature was ramped down.

The batch of annealed zircons was processed by HF chemical abrasion following the procedure of Mattinson (1994). This procedure removed inclusions and sections of grains that may have been altered from metamictization. The chemical etching step used different Teflon bombs than the 4 cycle-cleaned bombs, which will be discussed later; the bombs used here were not as rigorously cleaned. The annealed zircons were placed into the bombs with HF and HNO_3 and were then placed into a Yamato DX400 Drying Oven at 195 °C for 17 hours. After etching, the zircons were transferred to a petrie dish and the HF solution was decanted with a pipette. The zircons were then washed with acetone and H_2O. The big, gem quality zircons that existed after the chemical etching process were selected from each sample (six zircons from the Bighorn River and X bentonites, and ten from the A-X bentonite) and imaged using the *CoolSNAP* software package. A scale bar was added to the images in Adobe *Photoshop* and the dimensions of each grain were measured. The weight of each grain was calculated using the formula: Length(μm) x Breadth(μm) x Height(μm) x ρ_{zirc}, where Height = Breadth x Flatness Factor and $\rho_{zirc} = 4.7 \times 10^{-6}\ \mu g/\mu m^3$.

Bombs made out of Teflon were used in the dissolution process, but in order to eliminate contamination, a rigorous 4-cycle cleaning method was employed. The bombs are made out of Teflon because Teflon is a very clean material in regards to contaminants, it is easy to clean and it is easy to work with. 6.2 N HCl was added to the

Teflon bombs during cycle one. The Teflon bombs may expand when heated and therefore Teflon jackets around the bombs were required to prevent evaporation. The bombs were also placed inside NiCu alloy cylinders which were compressed under a screw in a metallic carousel. The bombs were then placed into a drying oven and heated to 195 °C for 48 hours; the HCl was subsequently drained. Four drops of HF and four drops of HNO_3 were added to the bombs during cycle two, and the bombs were placed into the oven for the same temperature and lengths as cycle one; the solution was subsequently drained. Cycle three and four involved the addition of HF, and was run at the same temperatures and lengths as the previous cycles. After the cycles were completed, they were drained and rinsed with Milli-Q ultra-pure H_2O. A solution of ½ HF and ½ HNO_3 was put into the cleaned bombs and the bombs were reassembled and placed back into the oven.

The dissolution process followed here is adapted from the methods by Krogh (1973). The selected etched zircon grains were put into separate Savillex Teflon capsules. HF was added to the capsules and the capsules were put onto a hot plate. HNO_3 was added to the capsules along with the T535 ^{205}Pb-^{233}U-^{235}U EARTHTIME spike. The zircons and HF solution was pipetted into the 4 cycle-cleaned bombs and put into the oven at 195 °C for 120 hours causing the dissolution of the zircon grains. The solution was dried down on a hot plate to a precipitate after the dissolution process was complete. 10 drops of 3.1 N HCl was added to the precipitate in the bombs, converting the solution from a fluoride solution to a chloride solution. The bombs were put back into the oven at 195 °C for 12 hours.

Columns made out of Teflon shrink wrap were used in an anion chromatography exchange step, which is based on the procedure by Krogh (1973). The columns had a polyethylene frit at the bottom that acted as a sieve, holding resin. The columns were precleaned in HCl and the HCl was removed by rinsing the columns thoroughly with H_2O. The columns were placed onto a post and rinsed again with H_2O. When the H_2O was half-way drained through the column, 12 drops of Eichrom anion exchange resin was added. The resin is negatively charged and positive ions stuck to the resin until they were flushed through. A larger number of columns were injected with the Eichrom resin than were required, since some columns became unusable due to airlock in the neck of the columns. After the resin was injected into the columns, two rinses of H_2O were done, followed by two rinses of HCl. The procedure was completed with two rinses of H_2O, and then an extra H_2O and HCl rinse that flushed any extra ions through the resin.

3.1 N HCl was added to the columns to precondition them since the dissolved zircon mixture was converted to a chloride form. The dissolved zircon mixture was added to the columns and the used bombs were washed out with H_2O. 3.1 N HCl was added to the columns to drain through any undesirable ions, such as Zr^{4+}, in the sample. The HCl was added in the sequence of two drops, two drops and then five drops. The bombs were then placed under the columns to catch the Pb and U ions from the columns. A Pb elute step was executed where 25 drops of 6.2 N HCl was added to the columns to flush through Pb ions. A U elute step was executed where 10 drops of H_2O was added to the columns to flush through U ions. 10 extra drops of H_2O created a final flush through the columns.

The U-Pb solution in the bombs was mixed with two drops of 0.05 N H_3PO_4, which is hydroscopic, causing the solution to never fully evaporate. The bombs were put onto a hot plate for 30 minutes, enough time for HCl and H_2O to evaporate, but the phosphoric acid containing U and Pb remained. SK silica gel was sonicated and then 1.5 mL of the silica gel was added to the phosphoric acid mixture. The mixture was dropped onto a single Re filament and the filament assembly was assembled. A current of 1.5 A was applied to the filament to fuse the sample onto the filament. The filament assembly was attached to a mass spectrometer barrel, along with filaments that were loaded with standards. These standard solutions are used to confirm barrel load sequence, test whether the mass spectrometer is working properly and check fractionation levels. The standards are not needed to calibrate the mass spectrometer, unlike other isotopic dating methods.

Historically, 0.5 N phosphoric acid was used in the ID-TIMS process, and the 0.5 N phosphoric acid would produce a film of volatiles that coated the source chamber of the mass spectrometer and condense on the slit plates. To prevent this, filaments were put into a degasser and a current was run through the filaments under vacuum, to outgas the volatiles. However, 0.05 N phosphoric acid was used here, and therefore the degasser was not used.

2.6 Mass Spectrometer

The loaded mass spectrometer barrel was placed into a 1987 Micromass VG354 Solid Source mass spectrometer. Once the barrel was loaded into the source chamber and the mass spectrometer pumped down, the flight tube was opened to the source, allowing the ion beam to travel down the flight tube. A knob on the back of the source allowed manual rotation of the barrel and was used to center the filaments axially with the collimating slit plates. The initial accelerating voltage applied was 8 kV and once the mass spectrometer was turned on, the filament started to increase in temperature. Heating up the filament incrementally, by adjusting the current, created a greater ionization efficiency of the elements on the filament as the sample load melted and equilibrated; this also caused minor background noise. A discriminator knob was used to help eliminate background noise by varying the rejection limits on the background signal, but this partially eliminated low intensity signals and therefore less noise was fundamentally preferred. Each 0.1 A increase to the filament current increased the temperature by ~30 °C, but the temperature of the filament was still checked via a micro-optical pyrometer. The temperature was incrementally increased until signal peaks appeared. Analysis of the grains began when the filament was heated up to 1300 °C in the first analysis, but Pb was unstable at this temperature, and therefore later analyses had the temperature ramped up to 1380 °C before analyses began.

The Daly detector system was used in this study because the desired ion beams were very small due to the relatively young age of the samples, and the Daly detector amplifies small signals. The Daly detector system uses beam peak switching to analyze the different isotopic peaks, and there is some signal loss in between the peak jumps, termed "dead-time". Dead-time was measured in nanoseconds and was corrected through calibration of the software with the standards on the barrel. The most intense signal, the ^{206}Pb peak, was used to fine-tune the settings of the mass spectrometer. The beam and slit plate potentials were adjusted to focus the ion beam into the collector and maximize the signal. The magnetic analyzer was adjusted so that flat-topped signal peaks were aligned with the collector with the left and right sides of the peaks being half intensity.

The mass-spectra were displayed and recorded in the *Sector 54* software package. The software ran the analyses as "blocks", where each block consisted of ten cycles and each cycle was ten sequences, or scans across a mass spectrum. The benefit of this is that sudden signal spikes due to signal instability can be identified and if it is justified, entire blocks of data could be eliminated post-analysis. In cases of very low signal-to-noise conditions, the length of the cycles was increased to improve precision. The *Sector 54* software automatically corrects for thermal fractionation based on a value determined with the standard U and Pb isotopic solutions that are on the same barrel as the samples being analyzed. A dead-time correction of 22.5 ns was also applied within the *Sector 54* software, to correct for non-counts during electronic counting. The *Sector 54* software calculated an internal 1σ error that is based on the variability within the ratios in a given sequence.

The compiled data were initially reduced using the *Utildbu* (Utilage U-Pb Data Reduction with U Double Spike) software program. Within *Utildbu*, the block means could be analyzed, and various ratios could be rejected if seen as outliers, due to an instable beam or due to heterogeneities and sputtering effects of the silica gel ionization medium. In the *Utildbu* program various corrections were applied. A Daly detector fractionation correction of 0.05% per amu was applied, and additionally, a thermal fractionation correction of 0.1 ± 0.038% (1σ) was applied. No U fractionation correction was applied at this point, since the EARTHTIME spike was applied, which has precisely known concentrations. To correct for a ^{206}Pb deficiency, which occurs due to an exclusion of ^{230}Th in the magma chamber as zircon chemically fractionates Th and U relative to the magma (Schmitz and Bowring 2001a), a correction was applied to the ^{206}Pb ratios using the general Th/U ratio of magma equal to 4.2. Additionally, U has a lower dead-time than Pb, and when U ratios are desired, such as in this study, a different dead-time correction of 20.5 ns was applied. The 1σ uncertainty was calculated in *Utildbu* by taking the square root of the square of the 1σ internal error produced by the *Sector* 54 software package and summing it with the square of each individual correction made in *Utildbu* (Kamo 2009, pers. comm.).

2.7 *Isoplot* Data Reduction

The source of the following information on the Isoplot software package is from Ludwig (2003), unless otherwise noted.

Isoplot is a Microsoft *Excel* add-in program that is designed to aid in the interpretation of radiometric data. *Isoplot* facilitates the construction of U-Pb Concordia plots (Wetherill 1956) and the calculation of ages either using conventional Concordia intercepts or by using the "Concordia Age" algorithm (Ludwig 1998). It can also be used to calculate a weighted-mean of multiple U-Pb dates obtained from a sample.

The measured $^{206}Pb/^{238}U$-$^{207}Pb/^{235}U$ isotopic ratios, corrected for fractionation and isotopic spike, were used to plot data on a Concordia diagram and calculate a Concordia age based on concordant analyses (Ludwig 1998). This age is considered to be the most-probable age corresponding to a data-point (or weighted-mean data-point), assuming that the true location of the data point falls precisely on the Concordia curve (i.e. the analyzed zircons have remained in an isotopically closed-system). The Concordia age algorithm considers only the assigned data-point errors, without consideration of the actual scatter of the data points from one another or the Concordia curve. The mean square of weighted deviations (MSWD) is reported when obtaining a Concordia age, which indicates the "goodness-of-fit" (ratio of observed scatter to expected scatter), and if the MSWD is greater than unity then there is an under-estimation of analytical errors or the presence of non-analytical data scatter. However, if the MSWD is less than unity, then the analytical errors have been over-estimated. Since there is only a single degree of freedom involved, the MSWD can be as high as 3.6 before the probability-of-concordance drops below 5%.

Decay-constant errors may be considered in the Concordia isotopic age calculation. Ages calculated directly from the $^{206}Pb/^{238}U$, $^{207}Pb/^{235}U$ and $^{207}Pb/^{206}Pb$ ratios are independent of errors in the U decay-constants, and the effects of these errors on the age errors are often ignored. The position of the Concordia curve is easily affected by the decay-constant errors (and the location of the most-probable concordant age), and the age errors are exaggerated by the decay-constant errors. The evaluation of concordance (on which the validity of a Concordia age depends) should only be made when the decay-constant errors are taken into account, and furthermore, decay-constant errors are required when comparing various isotopic decay-schemes.

Isoplot used the following parameters in the calculation of the Concordia diagram:

^{238}U decay-constant: $1.55125\text{x}10^{-10}$
^{235}U decay-constant: $9.8485\text{x}10^{-10}$
^{238}U half-life: $4.46831\text{x}10^{9}$
^{235}U half-life: $7.0381\text{x}10^{8}$
^{238}U decay-constant uncertainty % 2σ: 0.107
^{235}U decay-constant uncertainty % 2σ: 0.136
^{234}U decay-constant uncertainty % 2σ: 0.2
^{230}Th decay-constant uncertainty % 2σ: 0.3
Natural (Present day) ^{238}U/^{235}U: 137.88

Isoplot can plot the data as a classical error-weighted average, which weights the data points by their assigned errors only, which in *Isoplot*, is the inverse-square of the inputted errors. If the probability-of-fit (the probability that the assigned errors will yield at least the amount of scatter actually observed) is more than 15%, then the 95% confidence level error is calculated by multiplying 1.96 times the 1σ assigned error. However, if the probability is less than 15%, then the 95% confidence level error is calculated by multiplying the Student's-t by the square root of the MSWD. Furthermore, if the probability-of-fit is low, *Isoplot* will calculate a somewhat more complicated error-weighted average using the assumption that data-point scatter arises from two sources, the assigned (presumably Gaussian) errors and a constant but unknown "external" (also Gaussian) error.

3. SAMPLE SITES AND ZIRCON DESCRIPTIONS

3.1 X-Bentonite

The X-bentonite analyzed in this study was sampled from Burnt Timber Creek, site 3 (NTS Grid Coordinates: E 257121 82-O/11, Fig. 3.1), which is ~2 km upstream of the X-bentonite sampled by Tyagi et al. (2007) (site 1; Fig. 1.10). The X-bentonite used here was ~30 cm thick, whereas the X-bentonite sampled by Tyagi et al. (2007) was only ~12 cm thick, although in the United States the X-bentonite can exceed 1 m in thickness (Tyagi et al. 2007). The X-bentonite at Burnt Timber Creek 3 was brownish-grey and in total, 1745 g of the X-bentonite was collected. See Fig. 3.2 for the X-bentonite at Burnt Timber Creek 3, and how it was collected.

The mineral separation process of the X-bentonite from Burnt Timber Creek 3 isolated a large number of zircon crystals (greater than 400 crystals). Fig. 3.3 shows a representative population of the zircon grains. As a whole, the population of zircon grains ranged in size from 80 μm to 400 μm in the longest dimension and seemed to be magmatic in origin. The magmatic origin of these grains is indicated by the euhedral to subhedral features, the presence of slender, elongated needle type zircons (rapidly crystallized) and the abundance of well defined crystal faces on the smaller, euhedral grains. However, it is evident that many of the grains with a large girth exhibit slight rounding of the crystal ends, indicating possible metamorphic influences. A large

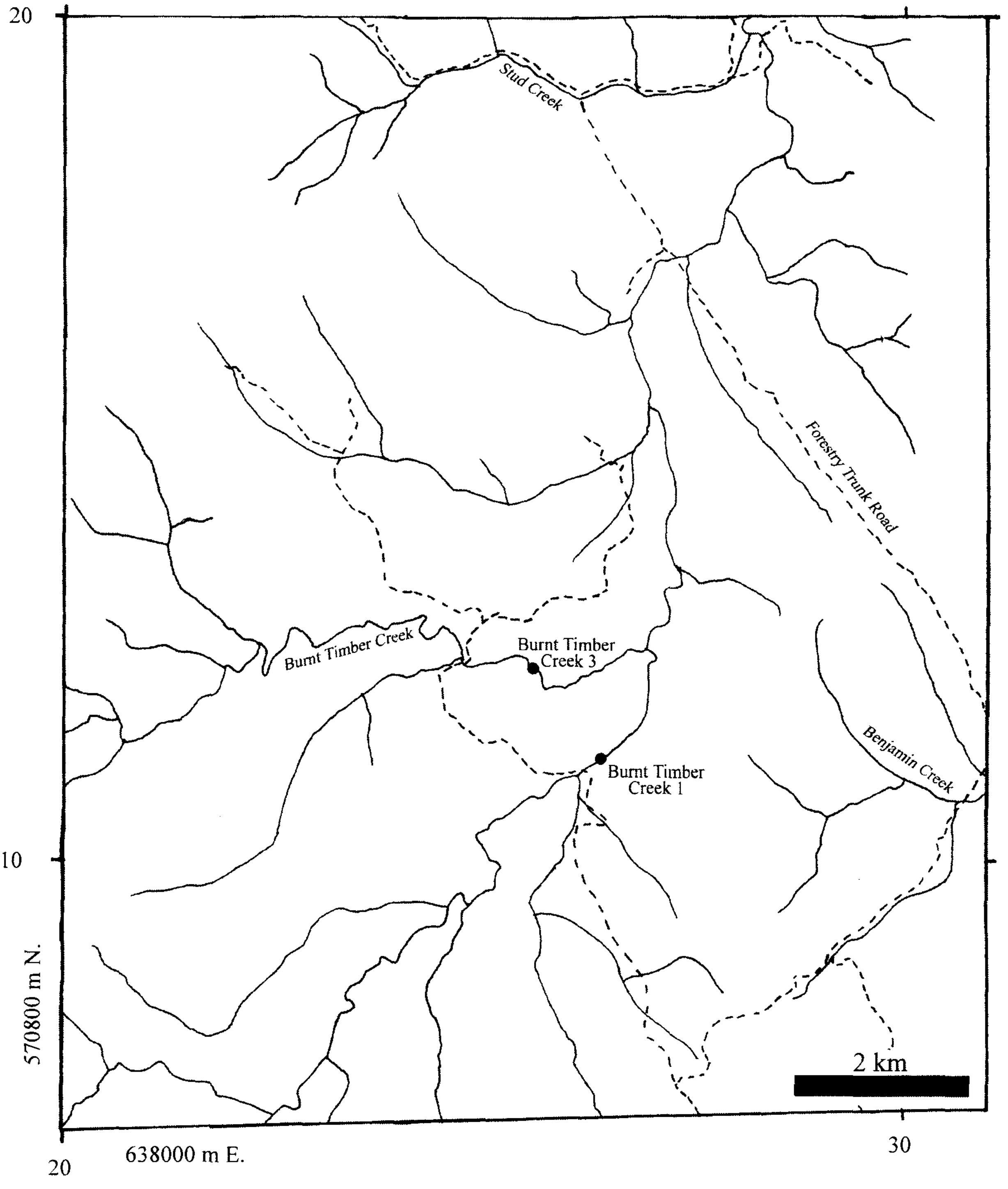

Figure 3.1. Location map of Burnt Timber Creek, Alberta. Map is annotated with the NTS (National Topographic Survey) grid. Burnt Timber Creek 1 and 3 are shown on this map. Burnt Timber Creek 1 is where the A-X bentonite was collected, and Burnt Timber Creek 3 is where the X-bentonite was collected. Source: Burnt Timber Creek 82-0/11 (NRCan 1996).

Figure 3.2. Field photograph of the X-bentonite at Burnt Timber Creek 3. The X-bentonite was thick enough here, that a trowel was used to collect the sample. Person's arms for scale.

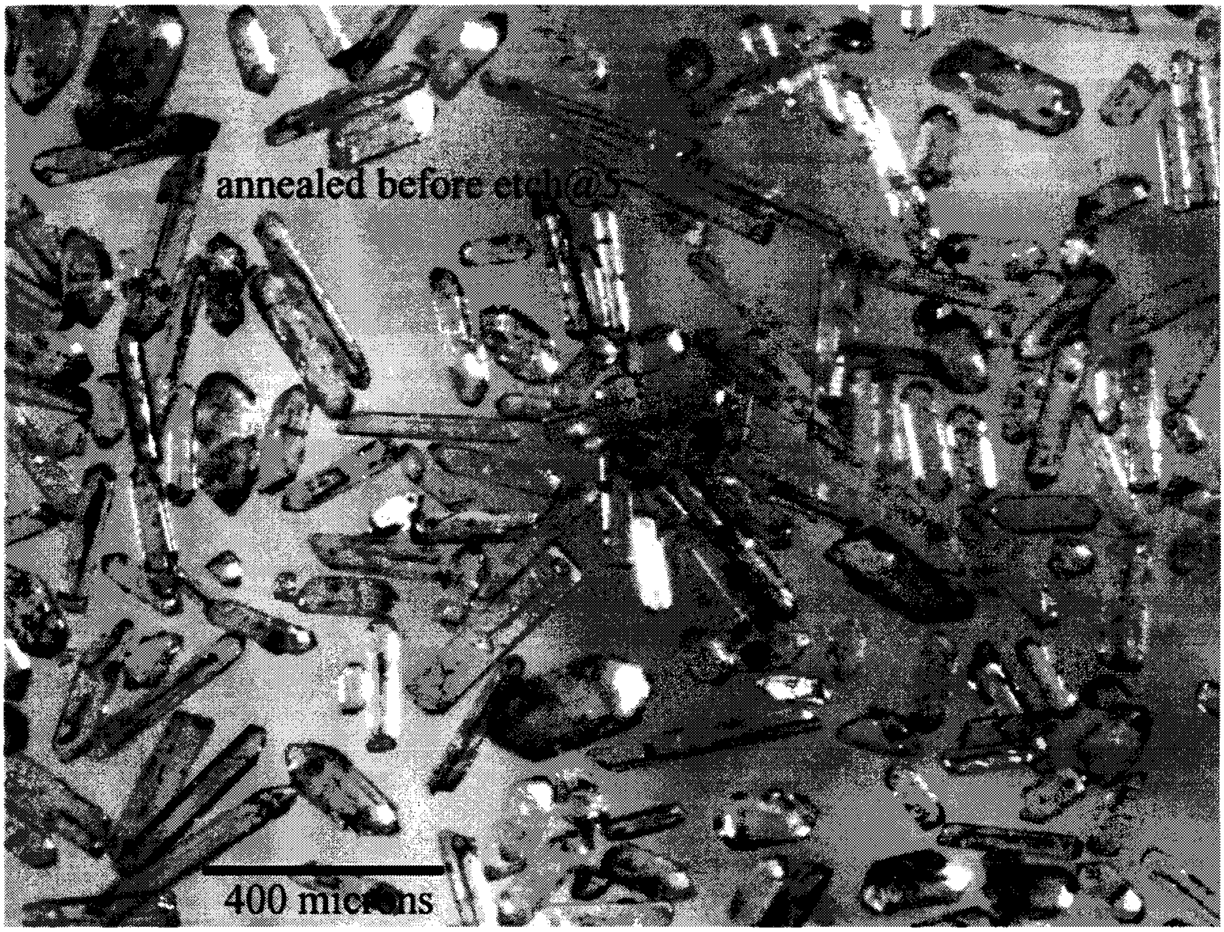

Figure 3.3. Representative zircon population of the X-bentonite. This image was taken after the grains were annealed for 30 hours. Note that a large portion of the grains were long needle type, many were shorter and fatter, and there is a large size variation. The brown staining on some of the grains is surficial, and it is seen that many grains contain fluid inclusions.

portion of the separated zircons were slightly brown-pink in colour indicating a possible slight degree of metamictization, or surficial staining.

32 zircon grains of the X-bentonite were analyzed via SEM-CL techniques to inspect internal growth zonation and heterogeneities (Appendix C). These grains were chosen at random and unfortunately, during the polishing process, many of the crystals became fractured and were abraded to the point where internal characterization became difficult through SEM-CL. Fig. 3.4 shows the degree of fracturing of the grains, and the corresponding CL signal; the CL signal is still present however, though slightly distorted. Many of the grains exhibited internal oscillatory zoning, being visible through the repetition between yellow and grey bands (the colours indicate various structural and chemical heterogeneities, possibly variations in U content). Sector zoning is visible in some of the zircons, where the light yellow and dark grey colours do not follow the oscillatory zoning, instead follow grain vertices. See Fig. 3.5 for a select representation of the oscillatory zoned grains. Only one of the zircon CL images presents an indication that there may be internal inheritance, and this can be seen in Fig. 3.6 through the interruption of the regular growth zoning by resorption discontinuities. A large proportion of the grains have dark gray centers under CL that are not typical of a core, but of a "nucleus". The nuclei are often at the center of sector zonation, and may provide a small amount of xenocrystic zircon. The nuclei can be seen in Fig. 3.7. Some of the zircons possess inclusions that gave a violet CL signal in the GATAN imaging interface, indicating activation of the ultraviolet (UV) channel. A representation of the UV CL stimulation can be seen in Fig. 3.8.

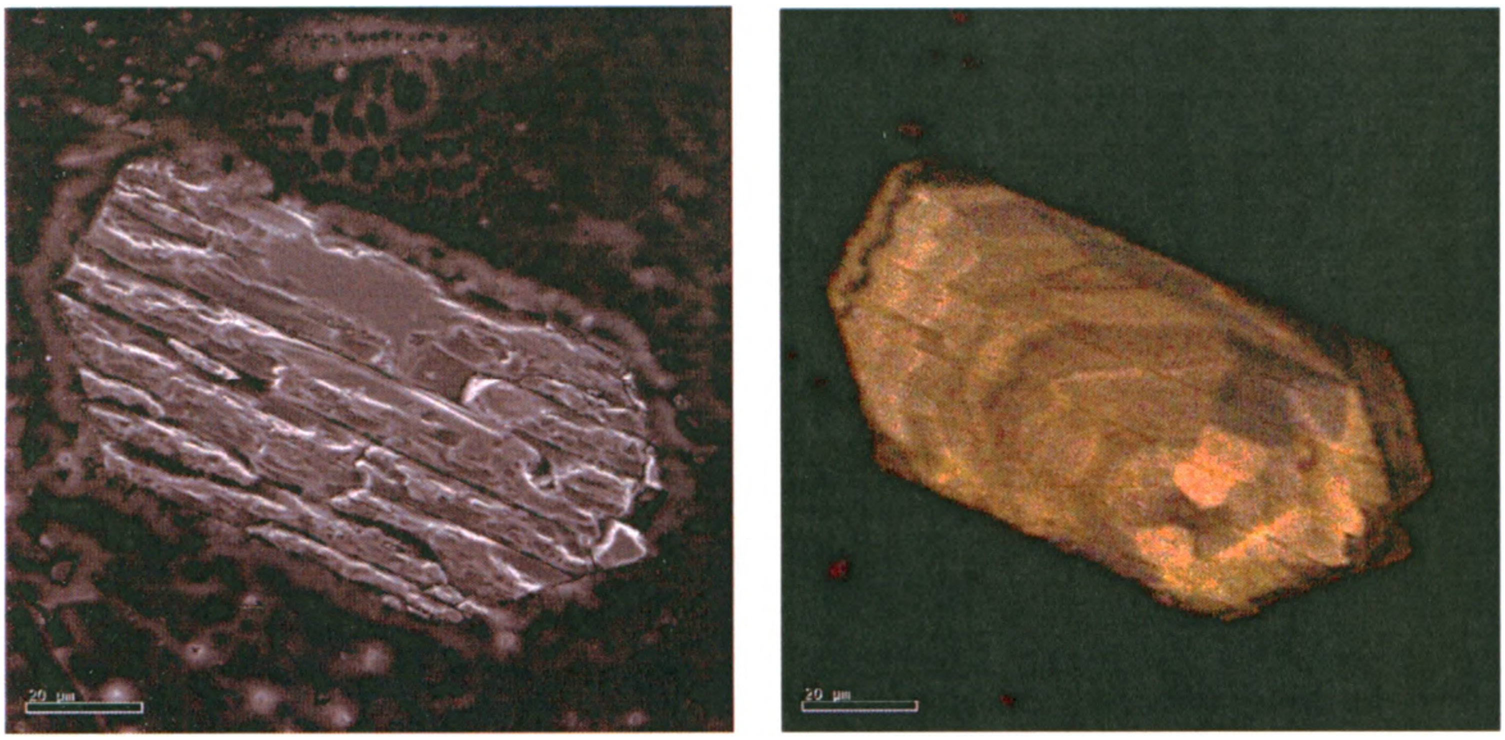

Figure 3.4. SE (Left) and CL (Right) images of the X-bentonite showing the fracturing of the grains during the polishing process and how it affects the CL response.

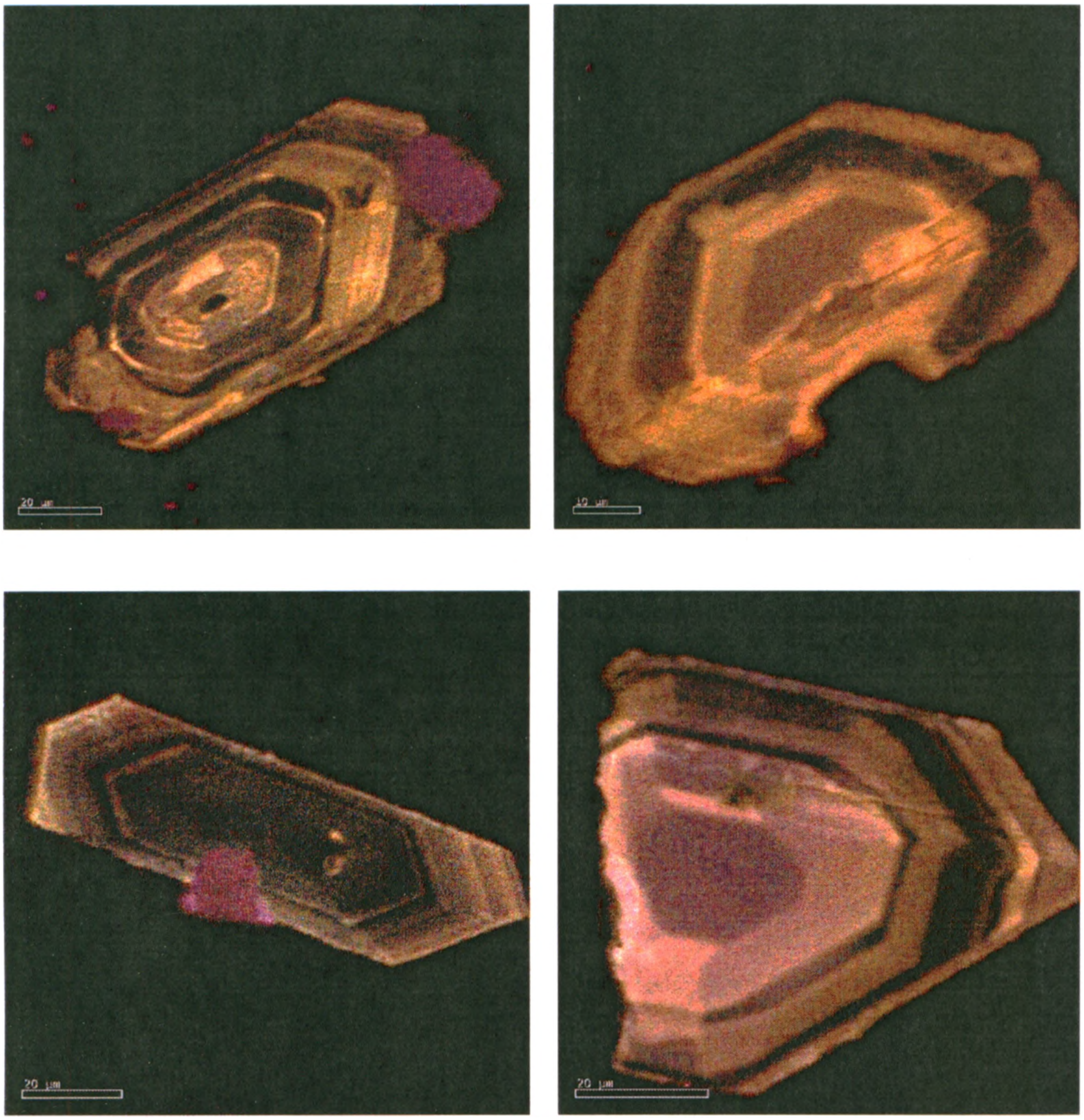

Figure 3.5. Representative CL patterns of zircons from the X-bentonite. All show oscillatory zoning, and some show sector zoning (Bottom right image).

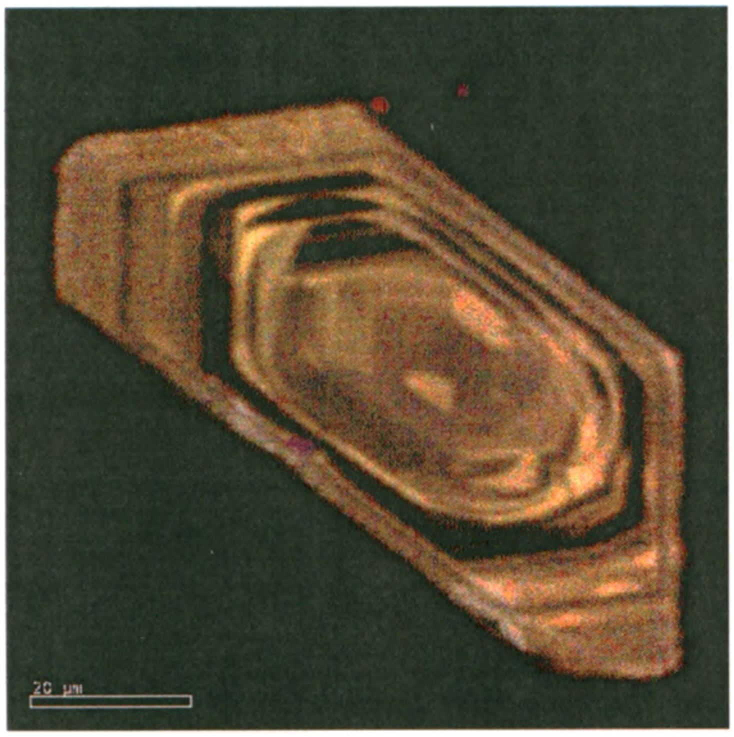

Figure 3.6. CL image of a possible xenocrystic core in a zircon from the X-bentonite. Note the truncation of the oscillatory zonation, which gives the outline of a core.

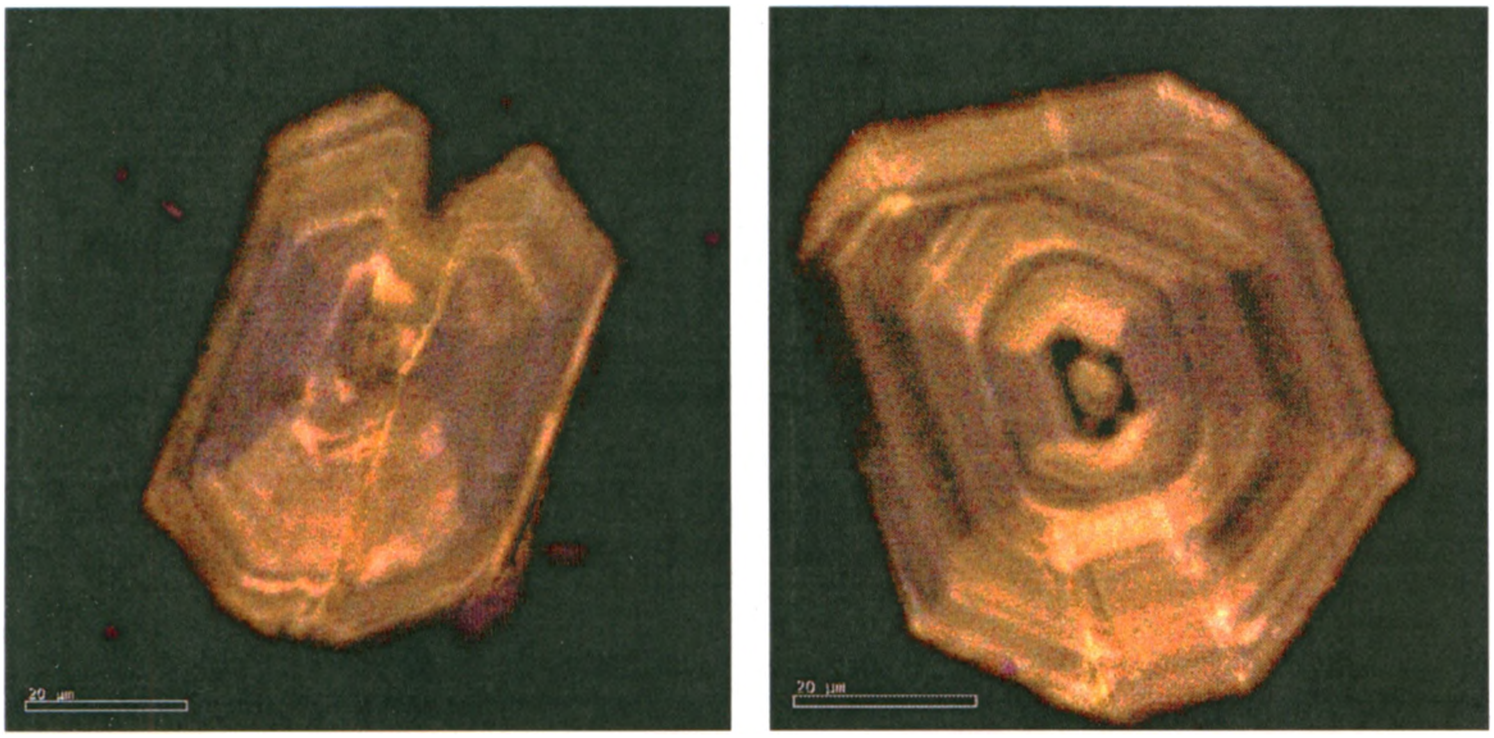

Figure 3.7. CL images of zircons from the X-bentonite and show the small nuclei in the center of the grains. These grains also show a high degree of sector zonation.

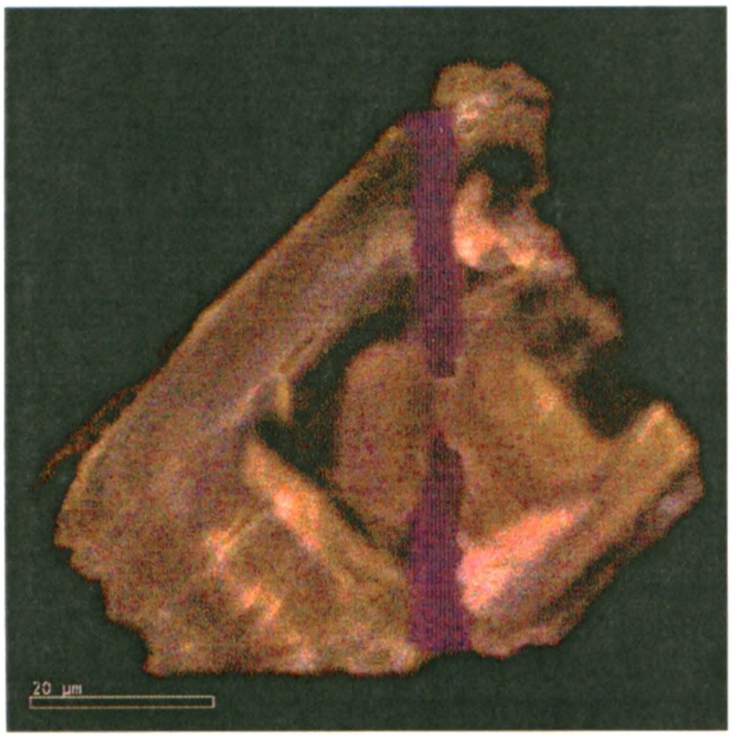

Figure 3.8. A CL image of a mineral inclusion in a zircon from the X-bentonite that activates the UV channel, shown as the violet colour.

In total, six zircon grains from the X-bentonite were used in the ID-TIMS analyses. Three grains were chosen and analyzed in May 2008 (Fig. 3.9), and three more were chosen and analyzed in September 2008 (Fig. 3.10). The three nearly gem quality grains (based on their pristine nature) chosen in May 2008 were small in size, but equant and multifaceted in morphology, free of any internal defects. Three larger grains were chosen in September 2008, and were approximately triple the size of the ones previously chosen. The three larger grains were chosen to provide more precise isotopic results since these grains are believed to contain more radiogenic U and Pb. The September 2008 grains had a more elongated and tabular morphology, though one grain showed slightly rounded features. All of the grains analyzed in September 2008, exhibited internal defects and cracking, but no visible xenocrystic inheritance was readily detectable.

3.2 A-X Bentonite

The A-X bentonite was sampled from Burnt Timber Creek, site 1 (NTS Grid Coordinates: E 263111 82-O/11, Fig. 3.1), which is the location that Tyagi et al. (2007) used in their study of the stratigraphy of the Colorado Group (Fig. 1.10). The A-X bentonite at Burnt Timber Creek 1 was ~3.5 cm thick and brownish, with various patches of darker orange-brown and grey. In total, 115 g of the A-X bentonite was collected. See Fig. 3.11 for the A-X bentonite at Burnt Timber Creek 1, and how it was collected.

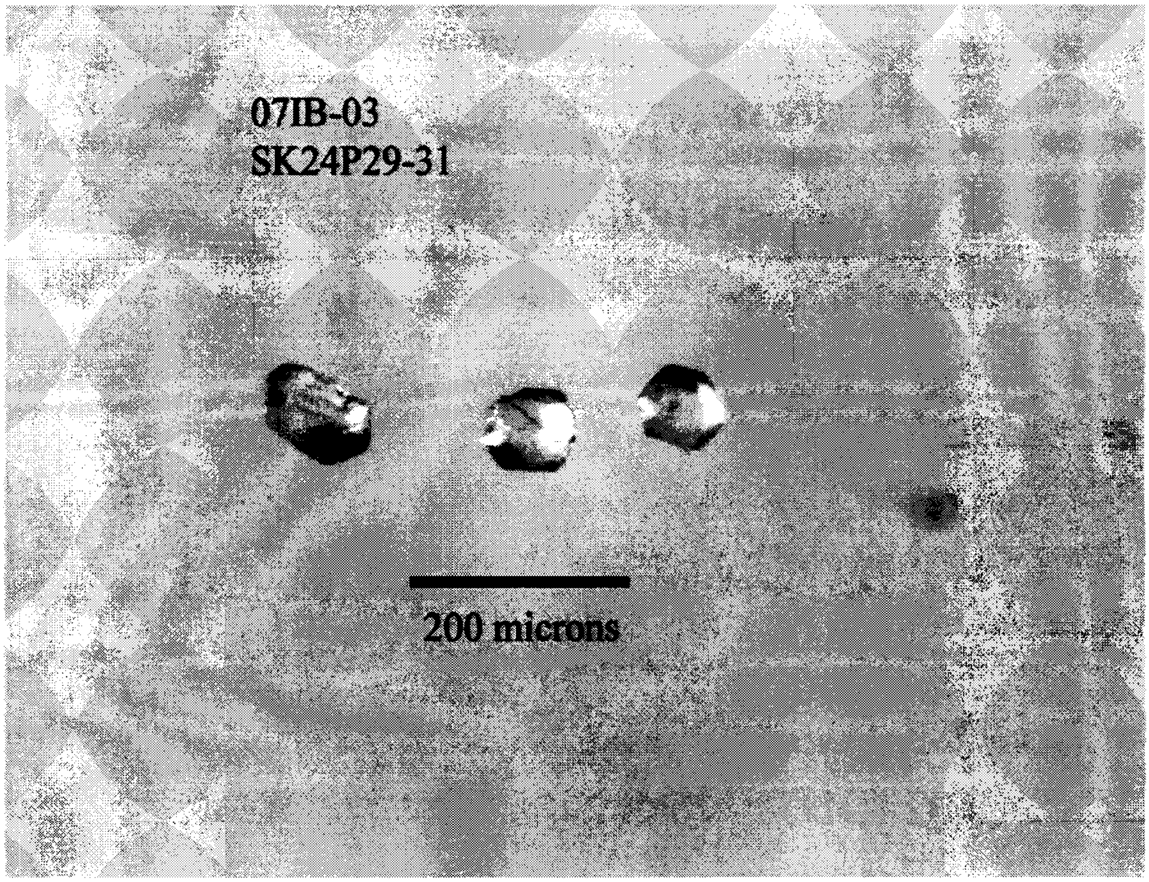

Figure 3.9. Three zircons from the X-bentonite that were dated with the ID-TIMS methodology in May 2008. These zircon grains are gem quality, though slightly small in size.

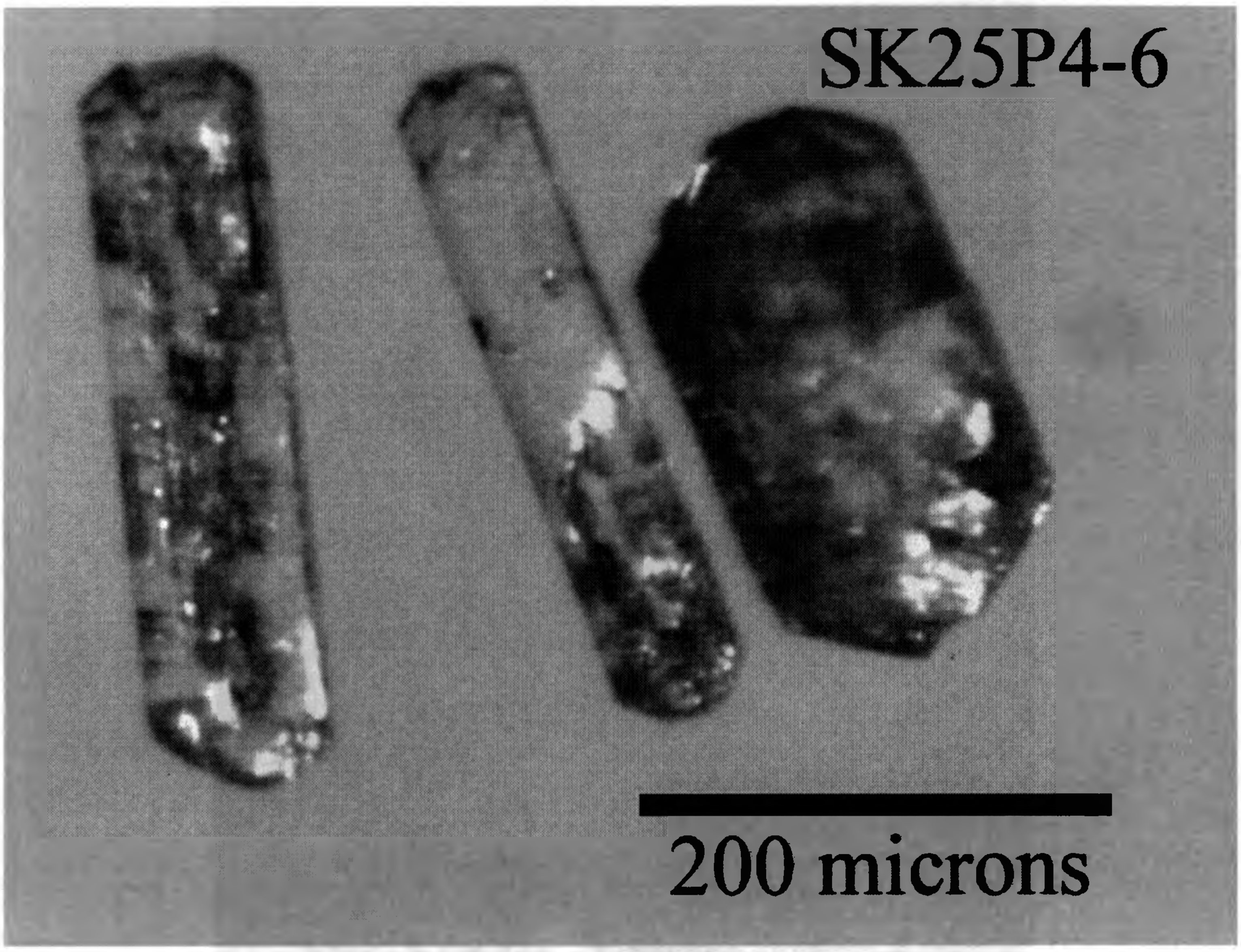

Figure 3.10. Three zircons from the X-bentonite that were dated with the ID-TIMS methodology in September 2008. These grains have internal fracturing, but are very large in size.

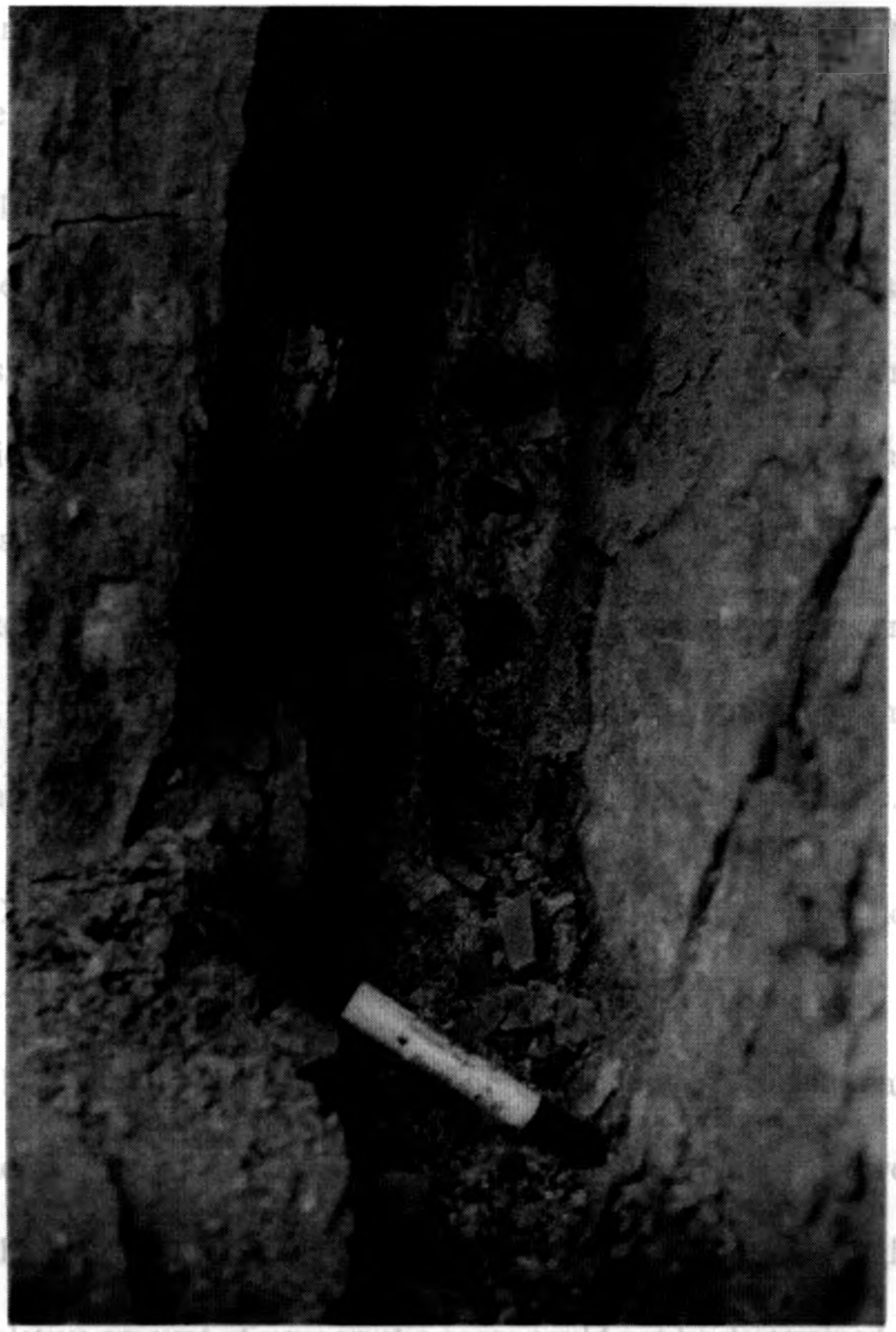

Figure 3.11. Field photograph of the A-X bentonite at Burnt Timber Creek 1. The A-X bentonite was collected using a thin metal pipe, which is what the four holes in the bentonite layer are caused from. Marker for scale.

The mineral separation process of the A-X bentonite from Burnt Timber Creek 1 isolated a large number of zircon crystals (greater than 400 crystals). Fig. 3.12 shows a representative population of the zircon grains. These grains ranged in size from 70 μm to 350 μm, but were mainly (80%) small in size (<125 μm), existing in both subhedral and euhedral forms. The long, needle-like habit was not as abundant as compared to the zircon population of the X-bentonite. Most crystals seemed to possess a stunted, subhedral characteristic, with low length to width ratios (slowly cooled). The larger grains were often prismatic and often possessed internal cracking defects and brown discolouration. In general, a large proportion of the total population had smoky exteriors and partially metamict interiors indicating possible xenocrystic inheritance.

The A-X Bentonite was not analyzed using the SEM-CL method, however the zircons were analyzed by UV light that was attached to a Nikon SMZ1500 stereo microscope. This method has the potential to highlight core and rim structures of zircons through the fluorescence of REE or U (Moser 2009, pers. comm.). However, it was observed that the A-X zircons failed to fluoresce when subjected to UV light, and therefore the relative amount of xenocrystic cores could not be determined.

In total, ten zircon grains from the A-X bentonite were used in ID-TIMS analyses. Six grains were chosen and analyzed in September 2008 (Fig. 3.13), and four more were chosen and analyzed in November 2008 (Fig. 3.14). The six grains chosen in September 2008 ranged in size and quality. These grains had many internal defects, but were chosen on the basis of their size. The grains that were chosen in November 2008 were not quite as large as the ones chosen earlier, but were seemingly much more

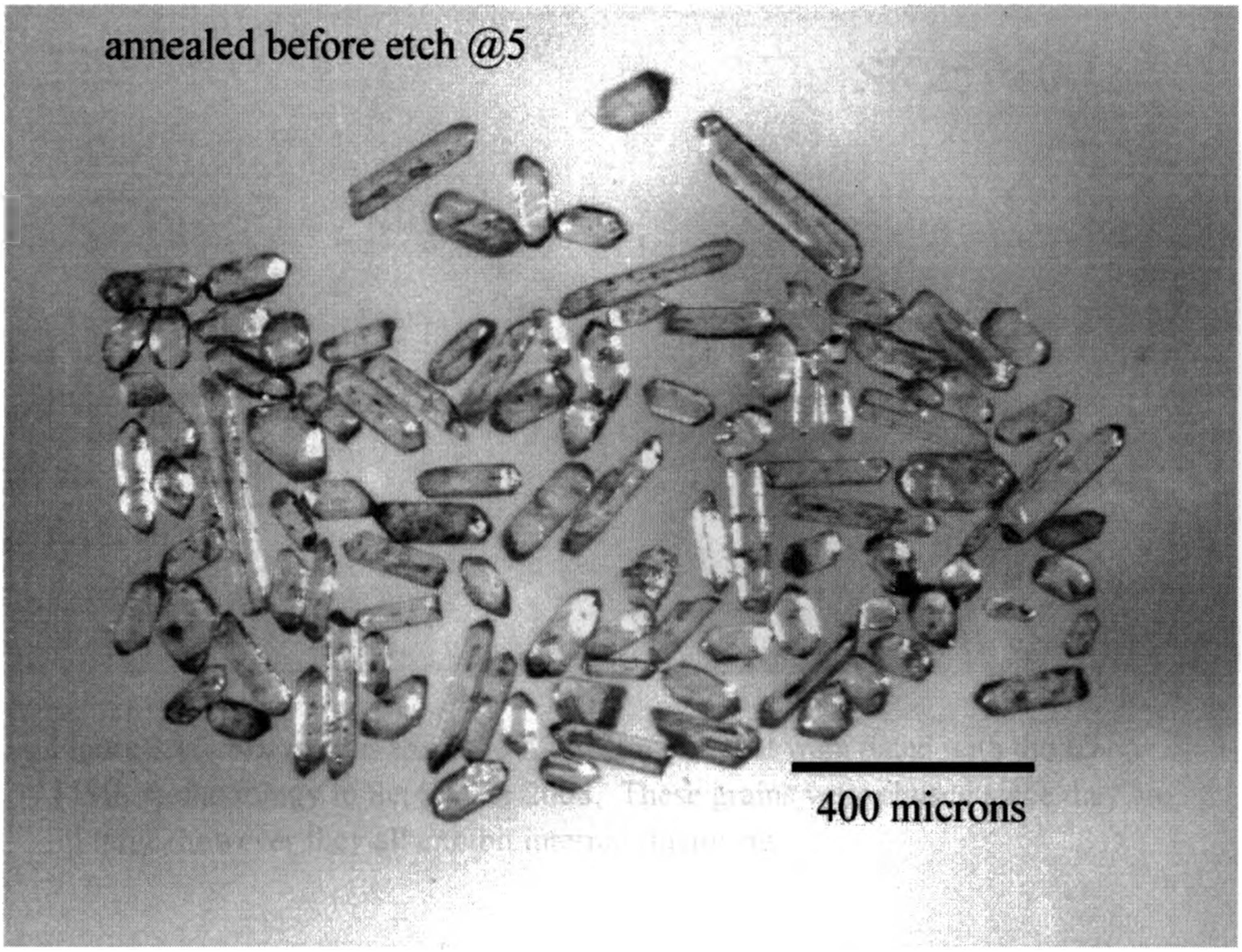

Figure 3.12. Representative zircon population of the A-X bentonite. This image was taken after the grains were annealed for 30 hours. Note that a large portion of the grains were euhedral, small and stubby. The elongated, needle-grains are not as abundant in this population as it was in the X-bentonite.

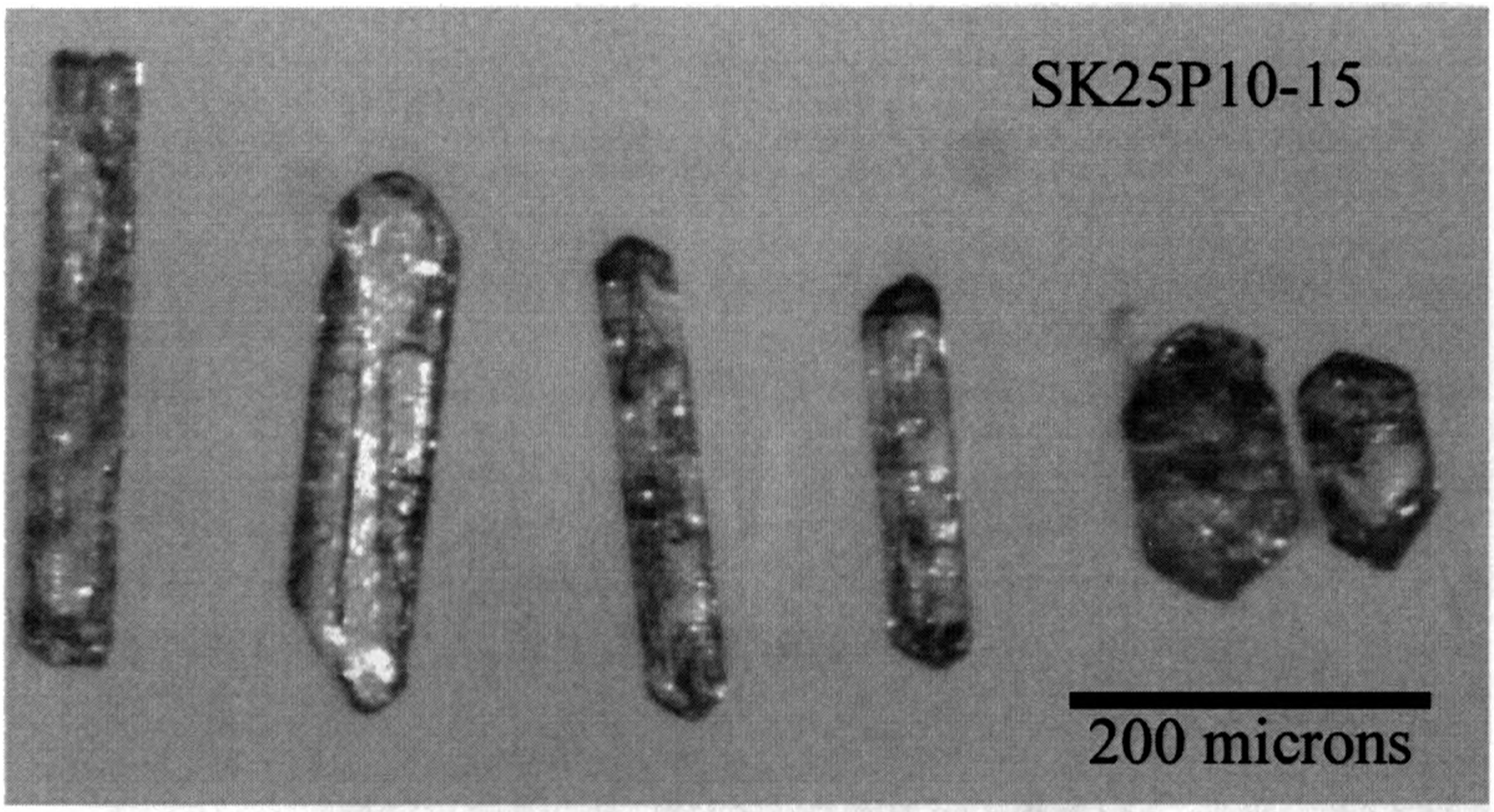

Figure 3.13. Six zircons from the A-X bentonite that were dated with the ID-TIMS methodology in September 2008. These grains were chosen since they are all large, however they all exhibit internal fracturing.

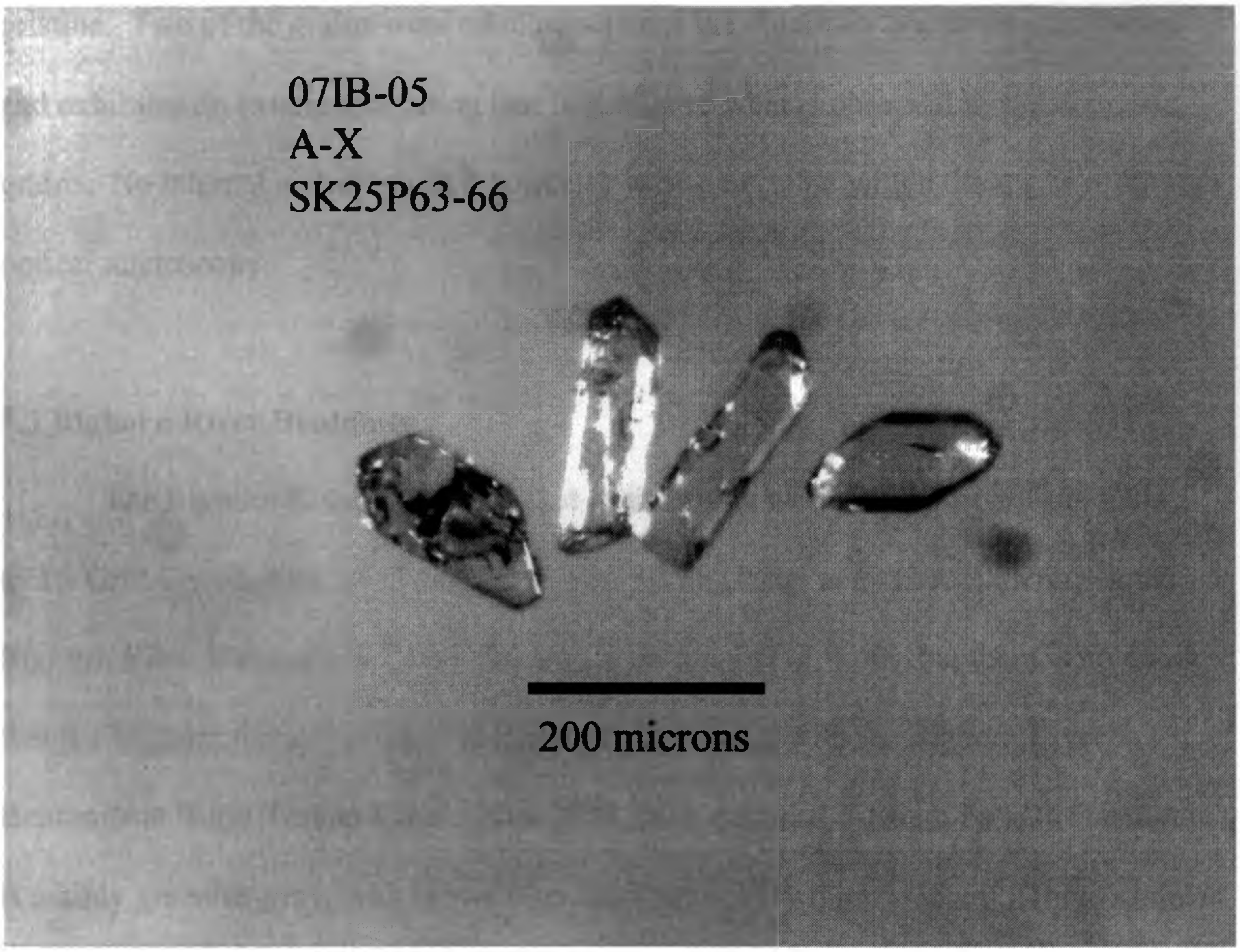

Figure 3.14. Four zircons from the A-X bentonite that were dated with the ID-TIMS methodology in November 2008. These grains were not as large, and as elongated as the grains chosen in September 2008, but are visibly more pristine. Note that the zircon on the left-most side contains an optical discontinuity, this is likely not an inclusion.

pristine. Two of the grains were tabular, whereas the other two grains were subhedral and exhibited an external rounding that is similar to what is observed in metamorphic grains. No internal inclusions or inheritance were detectable within these grains through optical microscopy.

3.3 Bighorn River Bentonite

The Bighorn River Bentonite used in this study was sampled from Ram Falls (NTS Grid Coordinates: 811721 83-B/4, Fig. 3.15). Tyagi et al. (2007) identified the Bighorn River Bentonite at Burnt Timber Creek site 1 (Fig. 1.10), but there is no doubt that the Bighorn River Bentonite at Ram Falls correlates with the Bighorn River Bentonite at Burnt Timber Creek (Plint 2008, pers. comm.). At Ram Falls the bentonite is mainly greenish-grey, with brown alteration and is very thick, ~35 cm. Three samples were collected, ~115 g was collected as a first sample, ~570 g was collected as a second sample and a plastic container of unknown weight was collected for the purpose of thin section creation. See Fig. 3.16 for the Bighorn River Bentonite at Ram Falls.

The Bighorn River Bentonite hand sample collected from Ram Falls was 11.5 by 11.5 by 8 cm in size and was generally a pale green to grey colour, as seen in Fig. 3.17. The hand sample seemingly consisted of two main phases, dark matrix and large white clay clasts. The hand sample showed multiple normally graded beds, which became visible when injected with epoxy, with the coarser grains being about 0.5 cm in diameter and the finer areas containing purely matrix material. Distributed in some of the coarser areas were bands of a dark mineral that were less than 0.5 mm wide.

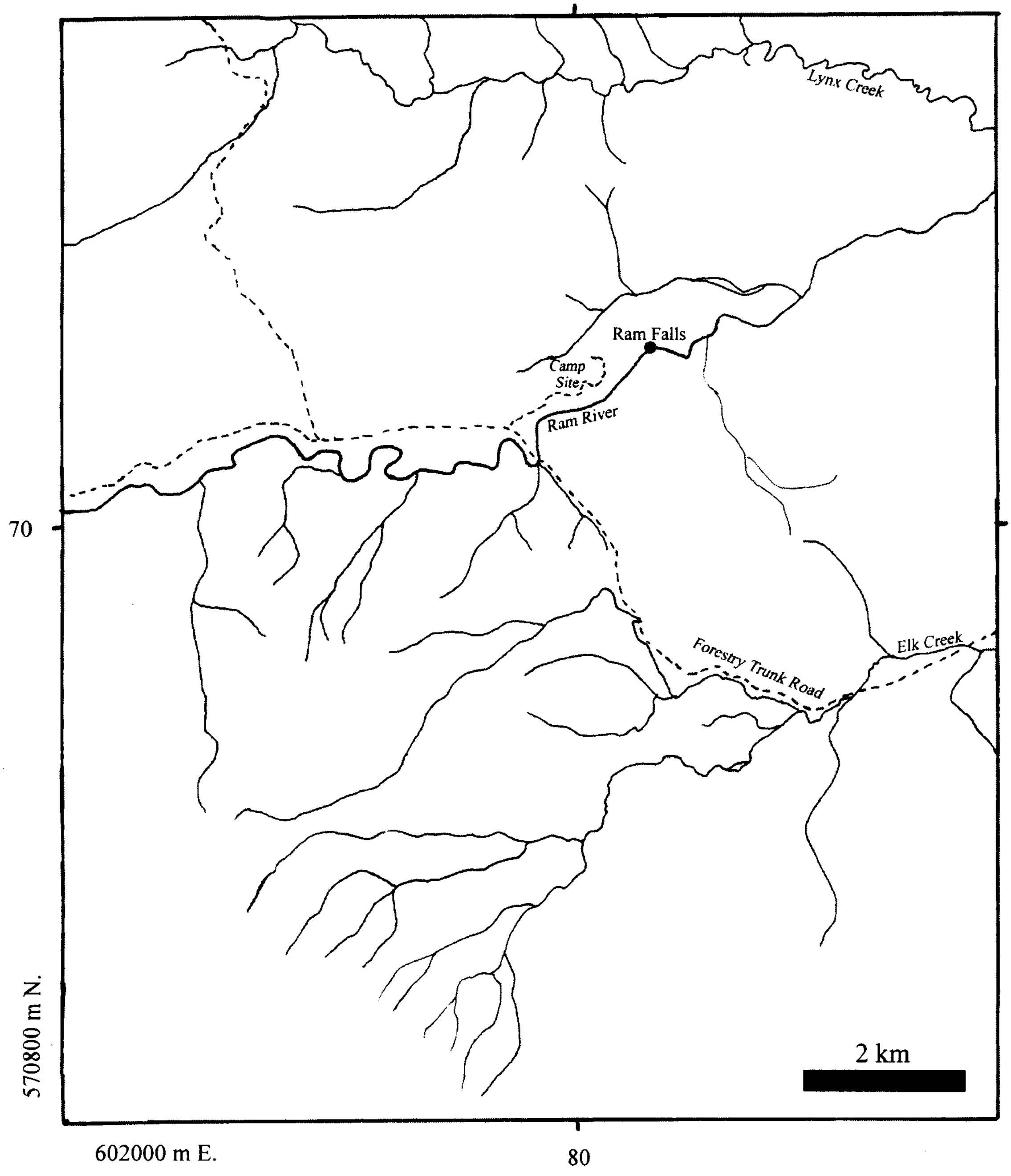

Figure 3.15. Location map of Ram River, Alberta. Map is annotated with the NTS (National Topographic Survey) grid. The location shown here that is labeled Ram Falls is the site that the Bighorn River Bentonite was collected from, and the location that is referred to in this study. However, the actual "Ram Falls" is about 1 km downstream. Source: Elk Creek 83-B/4 (NRCan 1977).

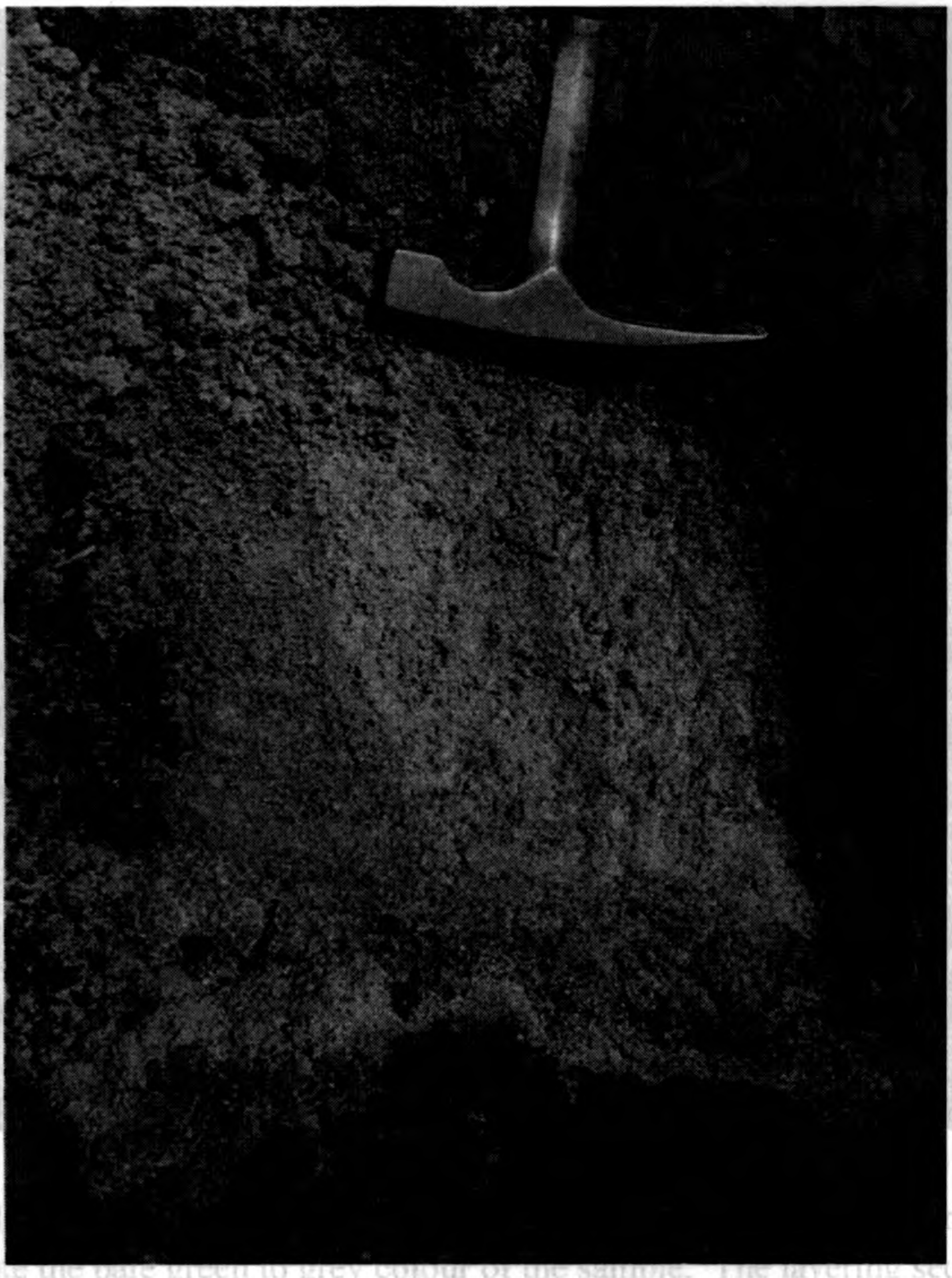

Figure 3.16. Field photograph of the Bighorn River Bentonite at Ram Falls. This bentonite was ~35 cm thick. Layering structures can be faintly seen, as evidenced by light and dark grey bands. Hammer for scale.

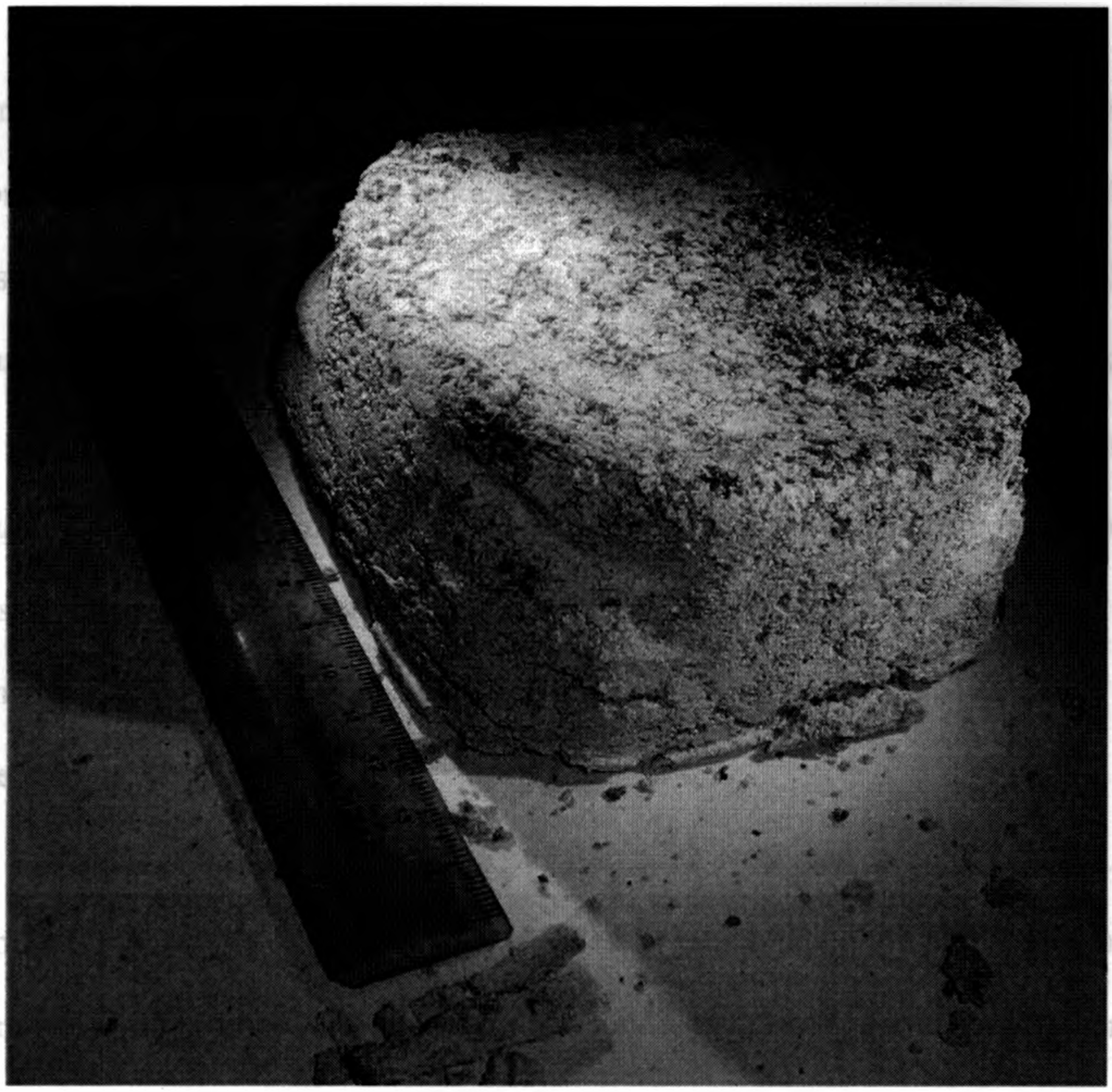

Figure 3.17. Hand sample of the Bighorn River Bentonite collected from Ram Falls. Note the pale green to grey colour of the sample. The layering sequences are not visible in the hand sample, but became visible when the sample was injected with epoxy to make thin sections.

There were a fair number of zircons present (~100 to 200 crystals) in the disaggregated Bighorn River Bentonite sample after the mineral separation procedure was completed. Fig. 3.18 shows a representative population of the zircon grains. These zircons ranged in size from 70 μm to 340 μm, though many (~50%) were around 125 μm. Various zircon morphologies were present in the disaggregated sample, including long needle grains, short subhedral grains, and multi-faceted grains. While a large proportion of the grains were crack-free and clear, 10 % to 20% contained brown discolouration and possessed cracks or slight surface frosting. A high proportion of the larger grains contained some type of inclusion and in general, the smaller grains were seemingly more pristine than the larger grains.

15 zircon grains of the Bighorn River Bentonite were analyzed via SEM-CL (Appendix C). Most grains were heavily abraded by polishing during preparation of the grain mount, similar to the X-bentonite grains (Fig. 3.4). The Bighorn River Bentonite grains were chosen at random and, of the 15 grains analyzed, 13 of them showed simple volcanic oscillatory zoning, which was visible through the repetition of yellow and dark grey CL response. These zircons have both dark grey and yellow interiors, indicating chemical variations within the magma chamber from which the grains grew. Sector zoning is visible in some of the zircons, where the light yellow and dark grey colours do not follow the oscillatory zoning, instead follow grain vertices. Some of the zircons possessed inclusions that luminesced violet under CL. See Fig. 3.19 for a representation of the oscillatory and sector zoned zircons. Only two of the zircon grains are interpreted

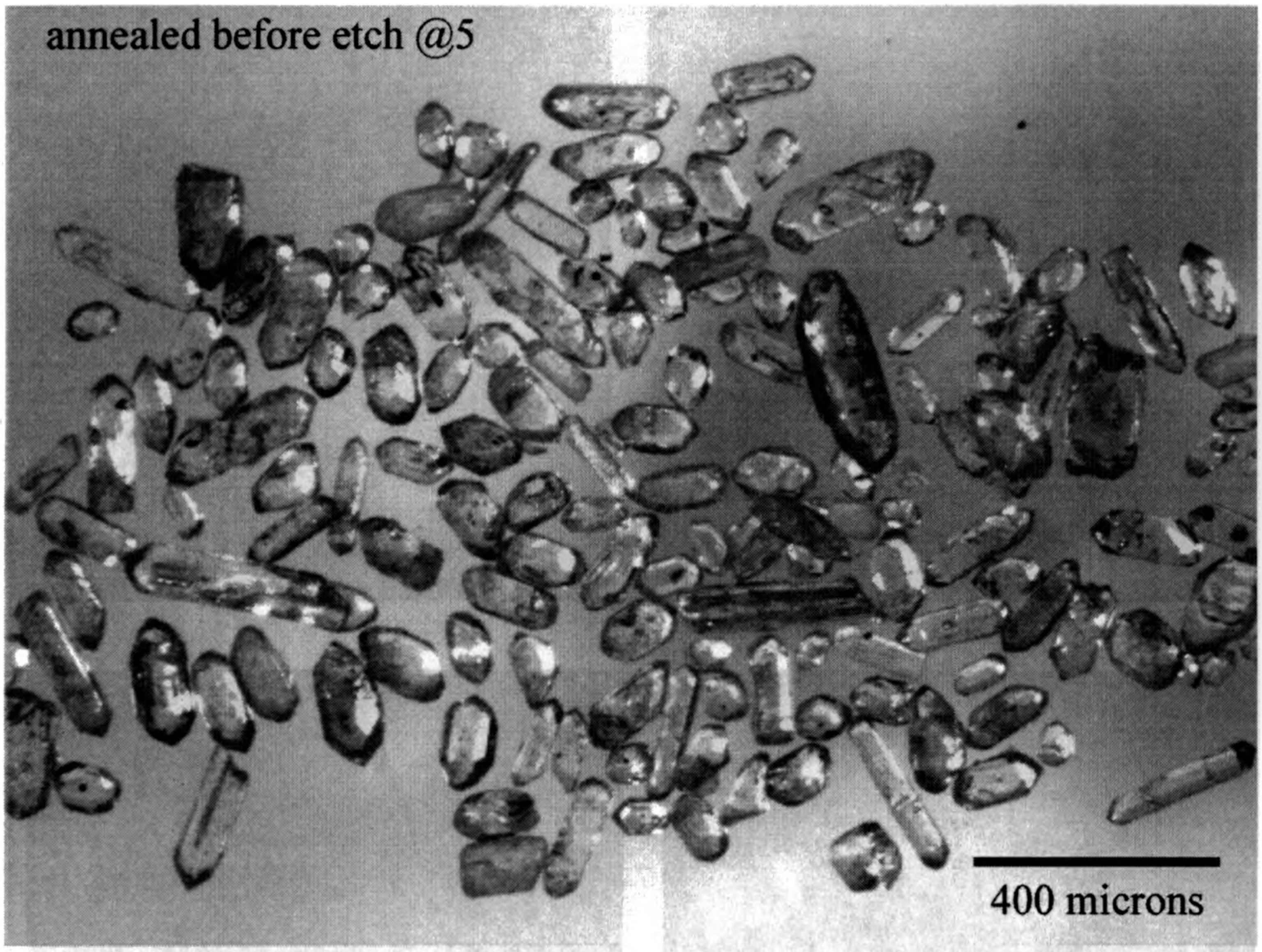

Figure 3.18. Representative zircon population of the Bighorn River Bentonite. This image was taken after the grains were annealed for 30 hours. Note that elongated needle type zircons are present, but a large proportion of the grains are shorter and fatter. The larger grains are seen to have brown discolouration and are not gem quality.

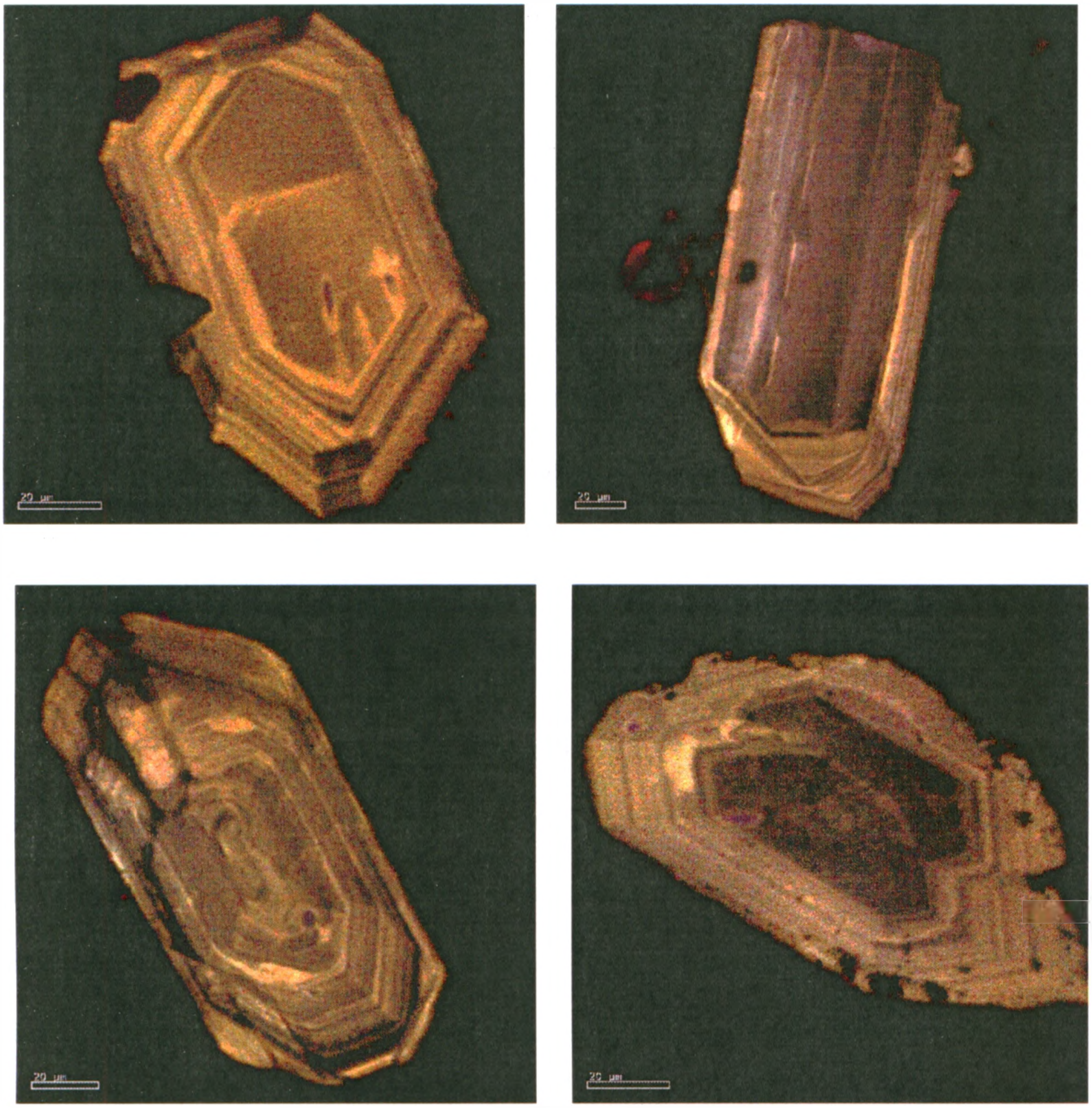

Figure 3.19. Representative CL patterns of zircons from the Bighorn River Bentonite. All show oscillatory zoning, and some show sector zoning (Bottom left image). The bottom right zircon shows a composite zircon CL image, where two grains were sutured together.

to contain xenocrystic inheritance, which is demonstrated through the resorption of the oscillatory zonation (Fig. 3.20). Since only two grains out of a random population of 15 grains shows an indication of inheritance, it could be assumed that only a small percentage of the total population will have inherited cores.

In total, ten zircon grains from the Bighorn Rivier Bentonite were used in ID-TIMS analyses. Three grains were chosen and analyzed in May 2008 (Fig. 3.21), and three more were chosen and analyzed in September 2008 (Fig. 3.22). Four nearly gem quality grains chosen in May 2008 and were all small in size. One grain exhibited a tabular morphology, while the other grains were fairly equant, with slight subhedral morphologies. One of these grains was lost during the anion chromatography procedure, so therefore only three of these grains were analyzed. Three larger grains were chosen in September 2008 and were approximately double the size of the ones previously chosen, being more elongated and wider as well. The three larger grains were chosen to produce more precise isotopic results since these grains likely contain more radiogenic U and Pb. These grains had a tabular morphology, though one grain showed slightly rounded features. All of the grains analyzed in September 2008, exhibited internal defects and cracking, but no visible inclusions and xenocrystic inheritance was readily detectable.

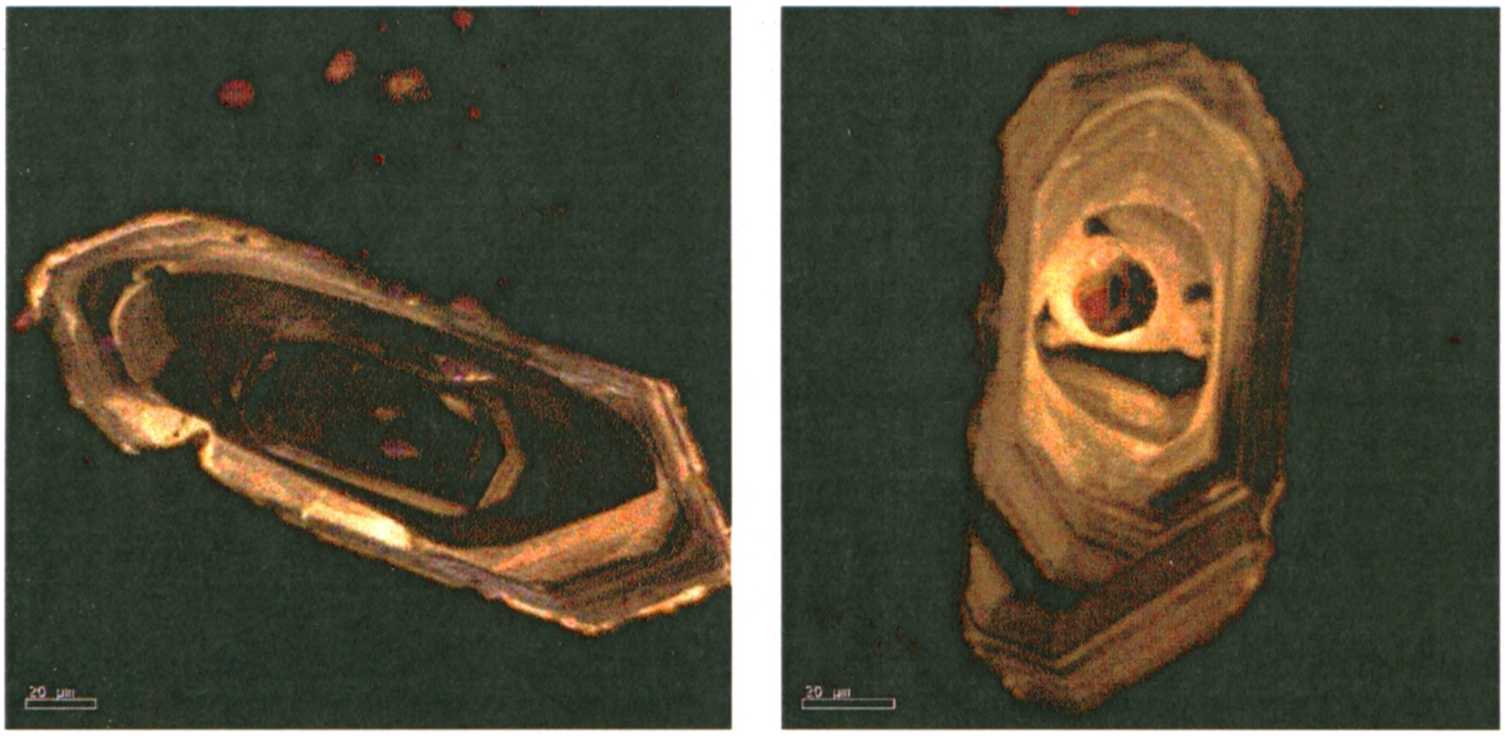

Figure 3.20. CL image of possible xenocrystic cores in two zircons from the Bighorn River Bentonite. Note the truncation of the oscillatory zonation, which gives the outline of a potentially older, inherited core.

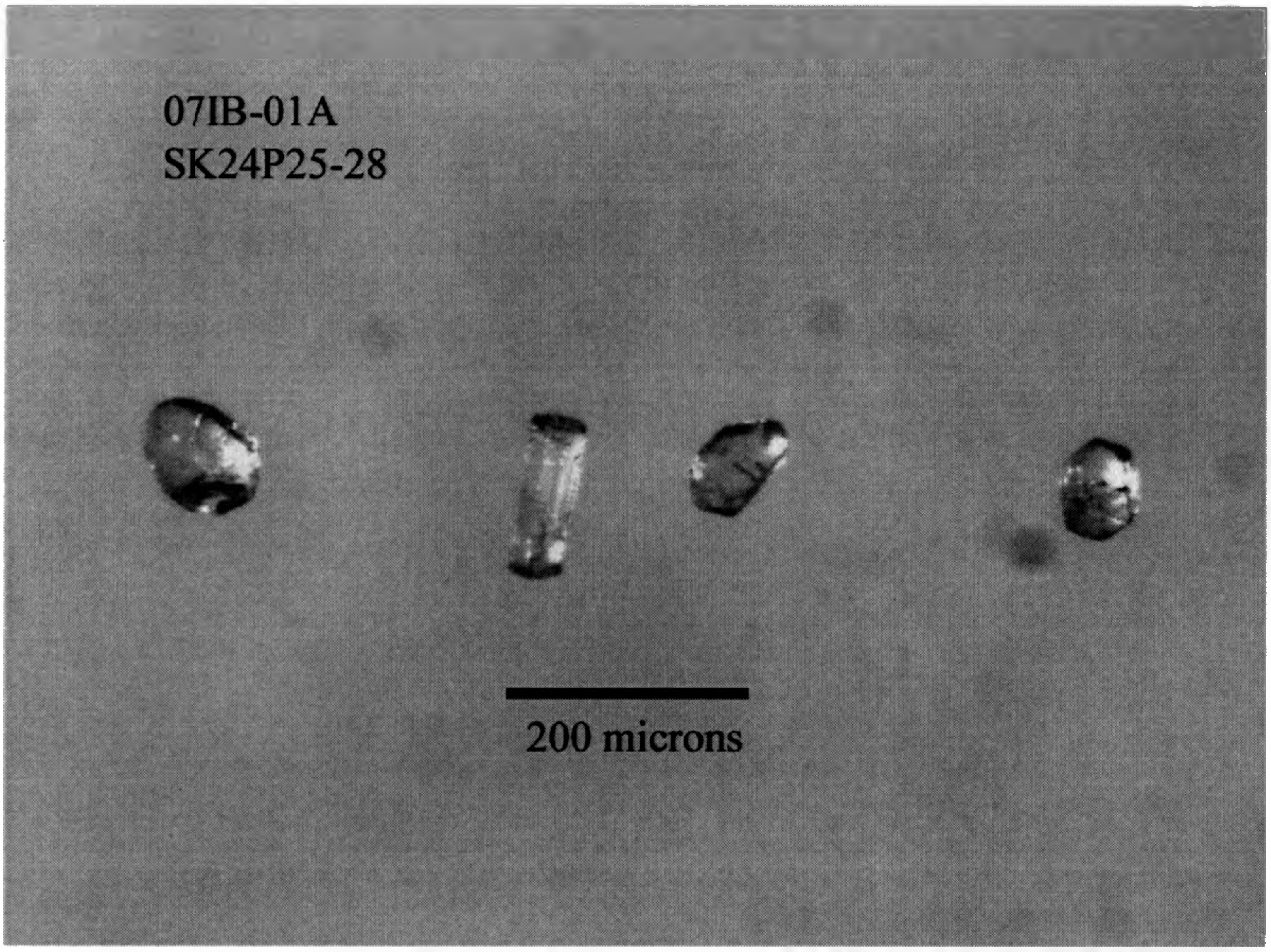

Figure 3.21. Four zircons from the Bighorn River Bentonite that were dated with the ID-TIMS methodology in May 2008. These grains are small and gem quality, with very little internal fracturing. Note that results were obtained for only three of the grains, one of the grains was lost in the chemistry step.

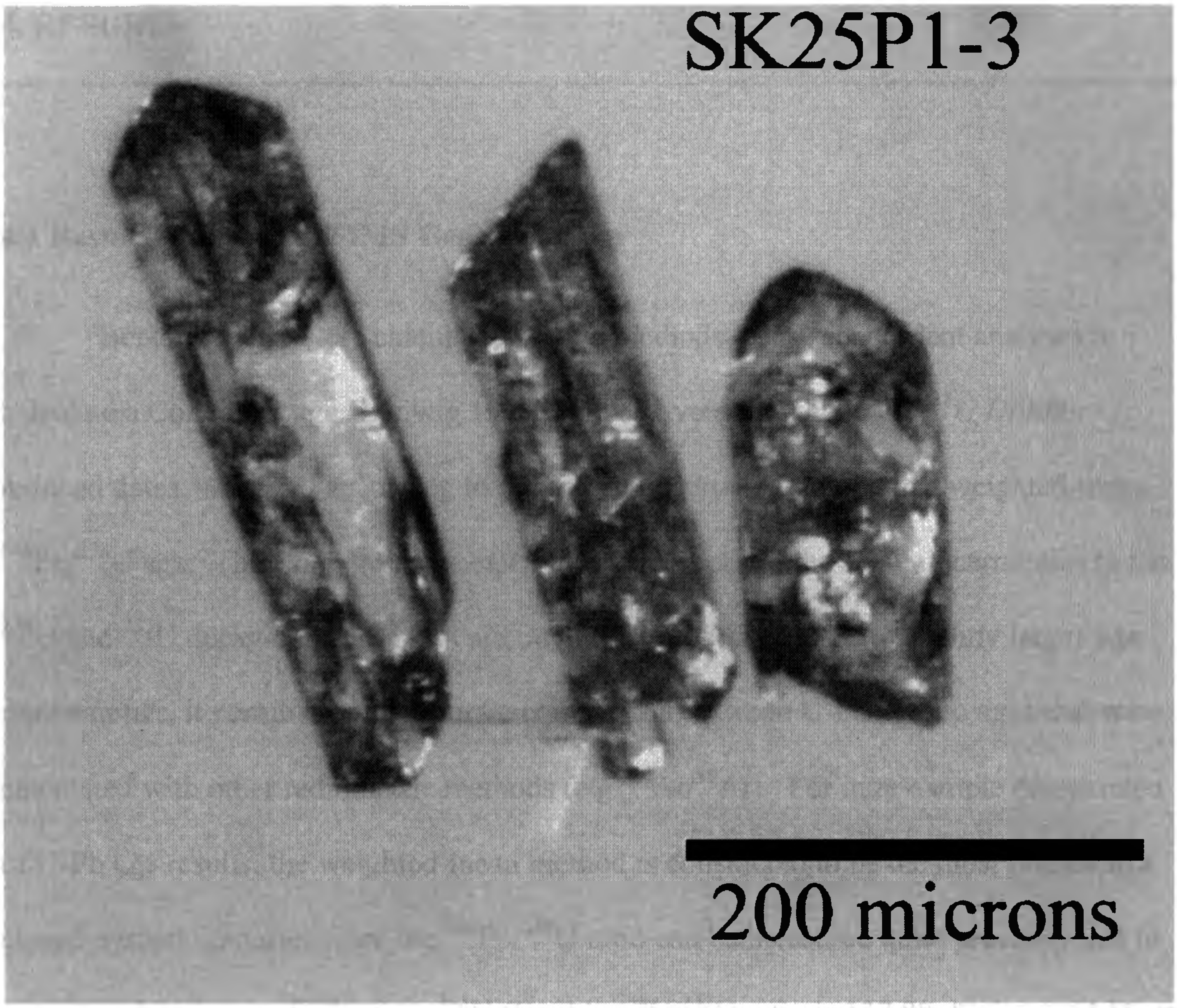

Figure 3.22. Three zircons from the Bighorn River Bentonite that were dated with the ID-TIMS methodology in September 2008. These grains are much larger than the ones analyzed in may, however they all have internal fracturing.

4. RESULTS

4.1 Results of U-Pb ID-TIMS Geochronology

Bentonite ages were calculated by two methods; using concordant analyses to calculate a Concordia age (Ludwig 1998), and by averaging the ^{206}Pb/^{238}U *Utildbu* reduced dates, weighted according to individual uncertainty, to obtain a weighted-mean ^{206}Pb/^{238}U age. The Concordia age calculation incorporates the small uncertainties in the ^{238}U and ^{235}U decay-constants, and although this sometimes leads to slightly larger age uncertainties, it permits for an accurate comparison between U-Pb ages to ages that were calculated with other radiometric methods (e.g. ^{40}Ar/^{39}Ar). For inter-sample comparison of U-Pb age results, the weighted-mean method is considered to be the most precise in a closed-system scenario, since the ^{206}Pb/^{238}U ratio can be measured quite precisely due to a greater abundance of ^{238}U than ^{235}U (Earth's ^{238}U/^{235}U ratio is 137.88; Steiger and Jäger 1977). Furthermore, the ^{207}Pb/^{235}U ratio is susceptible to a small bias if, during mass spectrometry, the shoulder of the larger ^{206}Pb peak raises the background near the neighbouring ^{207}Pb peak through a phenomenon called "lift". The weighted-mean approach, however, assumes that no loss of Pb has affected the ^{206}Pb/^{238}U ratio of the zircon, an assumption that appears to be well-founded if the zircons are pre-treated with the chemical abrasion method (Mattinson 1994), as was done here. The Concordia age is sensitive to this Pb-loss effect (resulting in a very high MSWD) and is used in all age interpretations below as a first-order check on the biasing effects of Pb-loss on the $^{206}Pb/^{238}U$ ages used in the weighted average age calculation.

All reduced data produced with the *Utildbu* program are listed in Table 4.1 and all uncertainties are reported at the 2σ level of confidence.

4.2 X-Bentonite

The U-Pb results for six single crystal zircon analyses of the X-bentonite are presented in Table 4.1. The uranium content of these zircons is within the range for igneous zircons, ranging from 118 ppm to 263 ppm. The common ^{204}Pb blank introduced during analysis is very low when compared to most geochronology laboratories in the world, ranging from 0.4 pg to 2.0 pg (the world's top low contamination laboratories aim to be less than 1.0 pg of common Pb). The reduced $^{206}Pb/^{238}U$ ages have a precision of ~0.1% to 0.3%. The $^{206}Pb/^{238}U$ dates of all six of the grains agree within their 2σ uncertainty, and range between 95.74 ± 0.32 Ma (Zircon 3) and 96.01 ± 0.13 Ma (Zircon 6) (Fig. 4.1). The youngest result (Zircon 3) of 95.74 Ma has the largest uncertainty factor of ±0.32 Ma.

On the Concordia diagram (Fig. 4.2), the analyses are considered "concordant" as the individual error ellipses overlap the Concordia curve. There was no difference between data obtained in the first and second rounds of analyses and the analyses group tightly, yielding a Concordia age of 95.86 ± 0.11 Ma. Additionally, the MSWD is quite low, at 0.42.

Table 4.1. ID-TIMS Analyses of Zircons Extracted from the X-Bentonite, A-X bentonite and Bighorn River Bentonite

Bentonite	Zircon	Weight of Sample (ug)[1]	Concentration			Atomic Ratios							Age ± 2σ Error (Ma)						% Disc
			U (ppm)	Pb (ppm)	Common Pb (pg)	$^{206}Pb/^{204}Pb$	$^{206}Pb/^{238}U$	2σ	$^{207}Pb/^{235}U$	2σ	$^{207}Pb/^{206}Pb$	2σ	$^{206}Pb/^{238}U$	2σ	$^{207}Pb/^{235}U$	2σ	$^{207}Pb/^{206}Pb$	2σ	
X Bentonite	Zircon 1	2.2	263	9.1	0.8	709	0.01497	2.11E-05	0.09959	1.91E-03	0.04824	8.71E-04	95.81	0.13	96.40	1.77	110.85	42.82	13.66
	Zircon 2	2.3	176	6.2	0.5	840	0.01498	2.84E-05	0.09986	1.65E-03	0.04834	7.46E-04	95.86	0.18	96.64	1.52	115.99	36.50	17.48
	Zircon 3	1.7	118	3.0	0.4	465	0.01496	5.01E-05	0.09690	3.89E-03	0.04697	1.78E-03	95.74	0.32	93.91	3.60	47.87	90.34	-100.73
	Zircon 4	5.9	178	16.9	2.0	534	0.01499	2.68E-05	0.09913	2.54E-03	0.04797	1.16E-03	95.90	0.17	95.97	2.34	97.68	57.46	1.84
	Zircon 5	4.3	224	14.8	0.7	1299	0.01497	2.10E-05	0.09889	9.53E-04	0.04790	4.31E-04	95.81	0.13	95.75	0.88	94.37	21.23	-1.53
	Zircon 6	22.0	142	48.2	0.9	3429	0.01501	2.10E-05	0.09929	3.68E-04	0.04799	1.50E-04	96.01	0.13	96.12	0.34	98.92	7.41	2.96
A-X Bentonite	Zircon 1	4.8	213	16.5	0.5	1854	0.01495	1.47E-05	0.09830	5.07E-04	0.04770	2.27E-04	95.63	0.09	95.21	0.47	84.58	11.26	-13.16
	Zircon 2	4.7	256	18.0	0.6	1895	0.01494	2.26E-05	0.09831	4.05E-04	0.04774	1.67E-04	95.57	0.14	95.22	0.37	86.32	8.31	-10.80
	Zircon 3	2.8	209	9.4	0.7	864	0.01489	2.45E-05	0.09382	8.35E-04	0.04568	3.76E-04	95.31	0.16	91.05	0.78	0.00	0.00	-10.80
	Zircon 4	2.5	196	7.8	0.3	1561	0.01497	1.76E-05	0.09871	6.72E-04	0.04782	3.01E-04	95.79	0.11	95.59	0.62	90.49	14.87	-5.91
	Zircon 5	6.4	215	20.3	2.1	655	0.01502	2.81E-05	0.09974	1.17E-03	0.04815	5.27E-04	96.13	0.18	96.54	1.08	106.64	25.87	9.93
	Zircon 6	2.9	153	6.8	0.7	600	0.01495	3.19E-05	0.09827	1.26E-03	0.04767	5.67E-04	95.68	0.20	95.18	1.16	82.86	28.26	-15.58
	Zircon 7	6.0	211	19.4	0.5	2242	0.01504	7.33E-05	0.09954	9.41E-04	0.04798	3.68E-04	96.26	0.47	96.35	0.87	98.47	18.14	2.25
	Zircon 8	4.4	303	21.0	0.4	3619	0.01506	2.14E-05	0.09960	6.20E-04	0.04797	2.70E-04	96.35	0.14	96.40	0.57	97.78	13.30	1.47
	Zircon 9	4.4	197	14.7	0.7	1257	0.01649	3.46E-05	0.13448	1.46E-03	0.05913	5.88E-04	105.46	0.22	128.12	1.30	572.05	21.63	82.23
	Zircon 10	4.4	129	8.9	0.3	2161	0.01514	4.51E-05	0.10200	8.48E-04	0.04887	3.56E-04	96.85	0.29	98.62	0.78	141.66	17.08	31.87
Bighorn River Bentonite	Zircon 1	3.0	320	14.5	0.7	1258	0.01475	2.63E-05	0.09804	1.13E-03	0.04820	5.16E-04	94.41	0.17	94.97	1.04	109.08	25.30	13.55
	Zircon 2	1.6	299	7.7	1.1	429	0.01471	4.06E-05	0.09748	3.07E-03	0.04807	1.43E-03	94.13	0.26	94.45	2.84	102.55	70.76	8.27
	Zircon 3	1.4	376	8.1	0.9	580	0.01469	3.79E-05	0.09534	1.64E-03	0.04705	7.57E-04	94.04	0.24	92.46	1.52	51.95	38.31	-81.61
	Zircon 4	6.6	308	32.3	0.2	8210	0.01474	1.47E-05	0.09743	1.84E-04	0.04794	6.20E-05	94.32	0.09	94.40	0.17	96.47	3.06	2.24
	Zircon 5	7.1	235	27.1	1.1	1473	0.01472	2.49E-05	0.09750	4.89E-04	0.04805	2.10E-04	94.19	0.16	94.47	0.45	101.61	10.31	7.36
	Zircon 6	8.3	223	28.4	0.2	7682	0.01477	5.39E-05	0.09789	3.94E-04	0.04806	6.68E-05	94.53	0.34	94.83	0.36	102.25	3.28	7.60

1. Estimated from sample dimensions and density

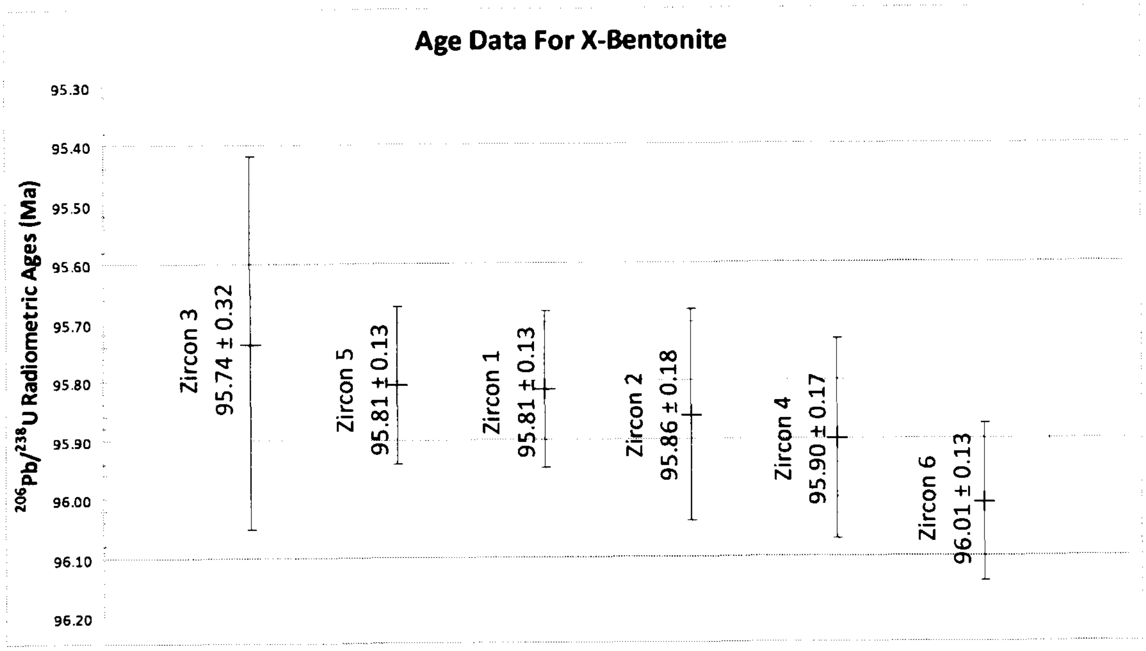

Figure 4.1. ^{206}Pb/^{238}U age data-points for single zircon crystals that were extracted from the X-bentonite. Error bars are at the 2σ level.

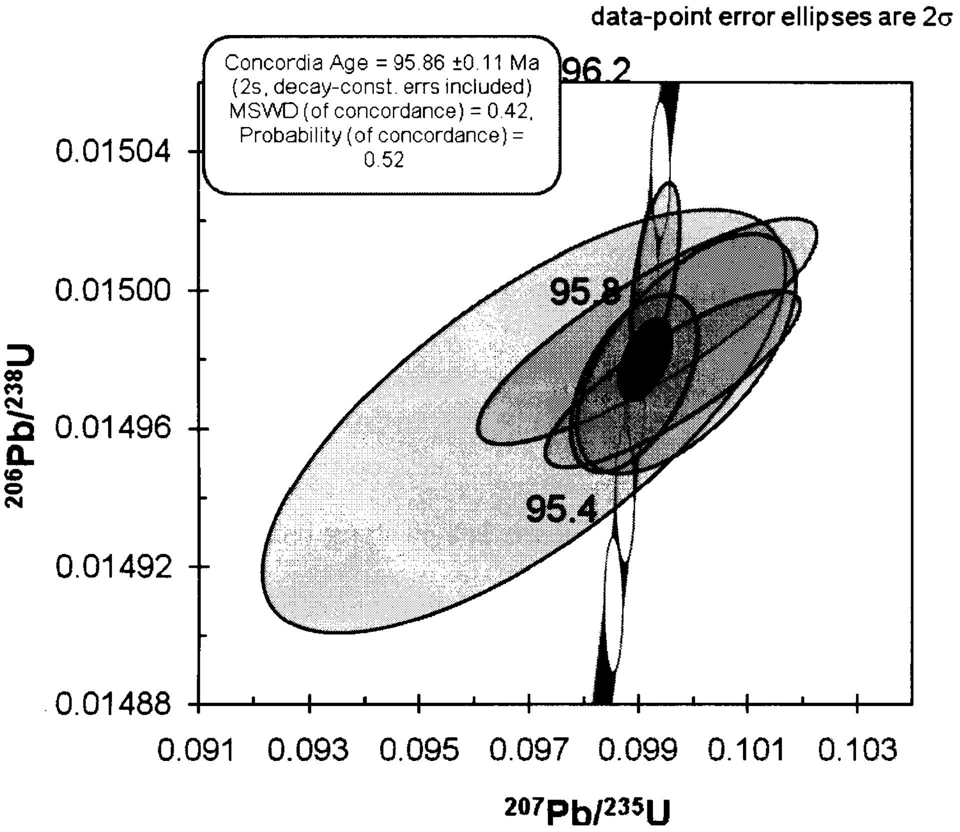

Figure 4.2. Concordia diagram for the X-bentonite. The Concordia curve includes uncertainties with decay-constant errors, and error ellipses are at the 2σ level. Concordia line ages are to the left of the Concordia line and are in units of Ma. The dark grey error ellipse is the mean Concordia age.

The weighted-mean $^{206}Pb/^{238}Pb$ age of this population is 95.87 ± 0.10 Ma (n = 6; Fig. 4.3). It is seen that Zircon 3 is the youngest grain and has the largest amount of uncertainty. When Zircon 3 was excluded from age calculations the $^{206}Pb/^{238}U$ weighted-mean age increased slightly from 95.87 ± 0.10 Ma to 95.88 ± 0.11 Ma (n = 5; Fig. 4.4), and the MSWD increased from 1.4 to 1.5.

4.3 A-X Bentonite

The U-Pb results for ten single crystal zircon analyses of the A-X bentonite are presented in Table 4.1. The uranium content of these zircons is mainly low compared to the other samples, clustering at the low end of the range between 129 ppm to 303 ppm. The common ^{204}Pb in these samples is fairly low as well, ranging from 0.3 pg to 2.1 pg. The $^{206}Pb/^{238}U$ ages were determined by *Utildbu* with a precision of ~0.1 % to 0.5%. The ages range between 95.31 ± 0.15 Ma (Zircon 3) to 105.46 ± 0.22 Ma (Zircon 9), see Fig. 4.5. There is a relatively large amount of scatter in the $^{206}Pb/^{238}U$ ages of the grains. Zircons 5, 7, 8 and 10 are approximately 0.5 m.y. to 1.0 m.y. older than the younger grouping of grains, and Zircon 9 is approximately 10 m.y. older than the youngest analyses. This pattern of age variation is typical for single zircons that contain older, xenocrystic inheritance. Fig. 4.6 shows the ages with the highly xenocrystic Zircon 9 age excluded. It is observed that the older zircons 5, 7, 8, 9 and 10 are older than the measured zircon ages of the underlying X-bentonite, conflicting with the stratigraphic age relationships, and therefore these zircon ages are not included in the age calculations of the A-X bentonite.

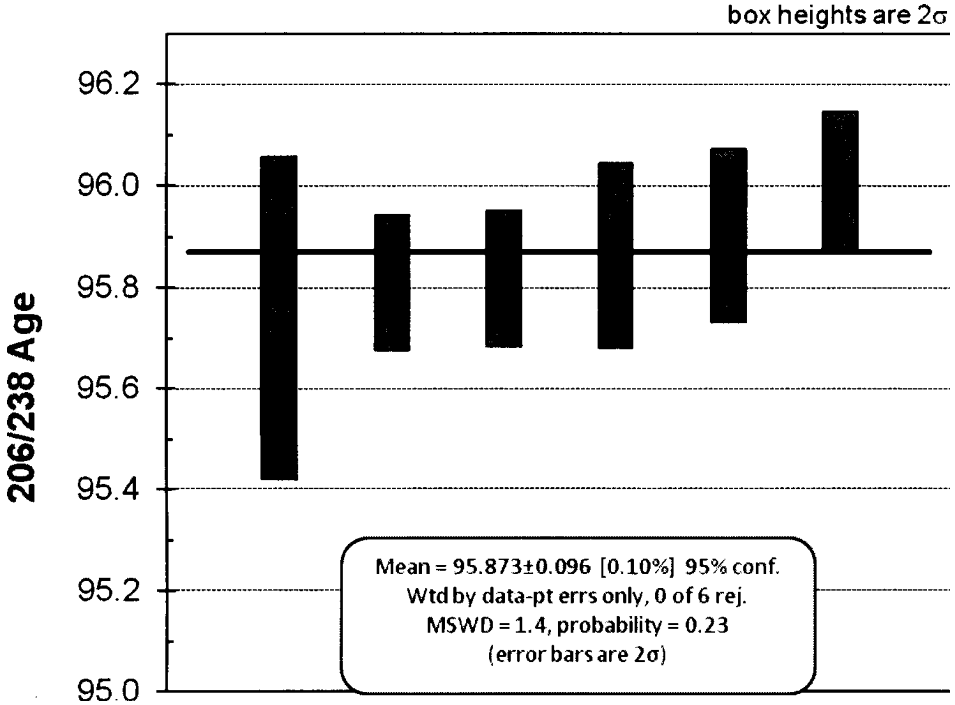

Figure 4.3. $^{206}Pb/^{238}U$ weighted-mean age for the X-bentonite, including all single-grain zircon analyses. This approach does not include decay-constant uncertainties in its calculation. Uncertainties were entered at the 2σ level. The $^{206}Pb/^{238}U$ ages along the vertical axis are in units of Ma. The black line across the figure indicates the weighted-mean for the sample.

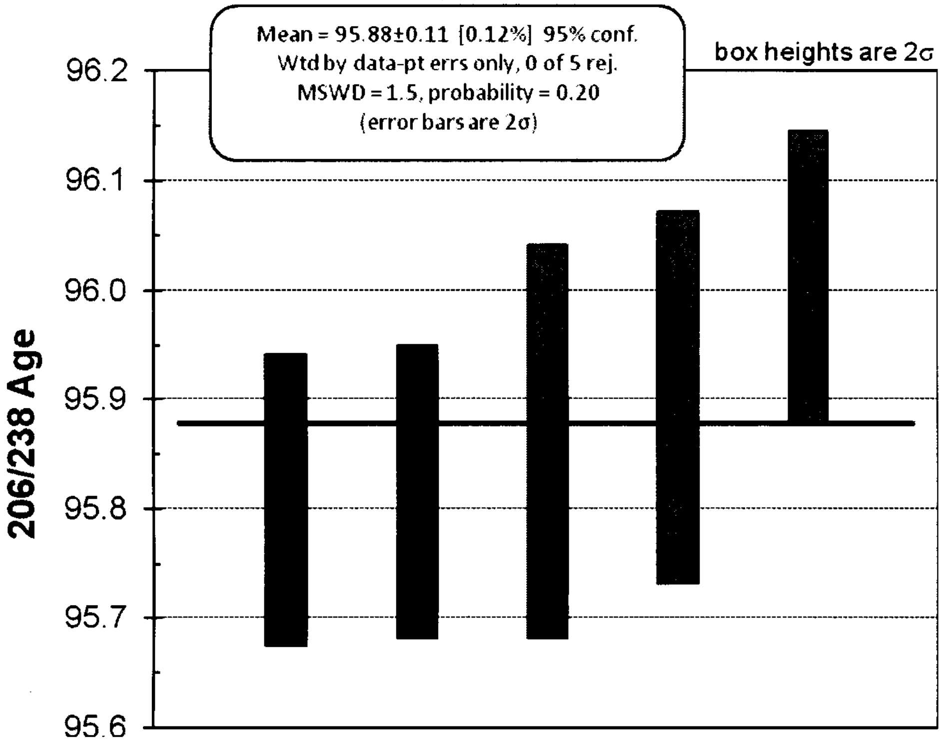

Figure 4.4. $^{206}Pb/^{238}U$ weighted-mean age for the X-bentonite, excluding Zircon 3. This does not include decay-constant errors in its calculation. Uncertainties were entered at the 2σ level. The $^{206}Pb/^{238}U$ ages along the vertical axis are in units of Ma. The black line across the figure indicates the weighted-mean for the sample.

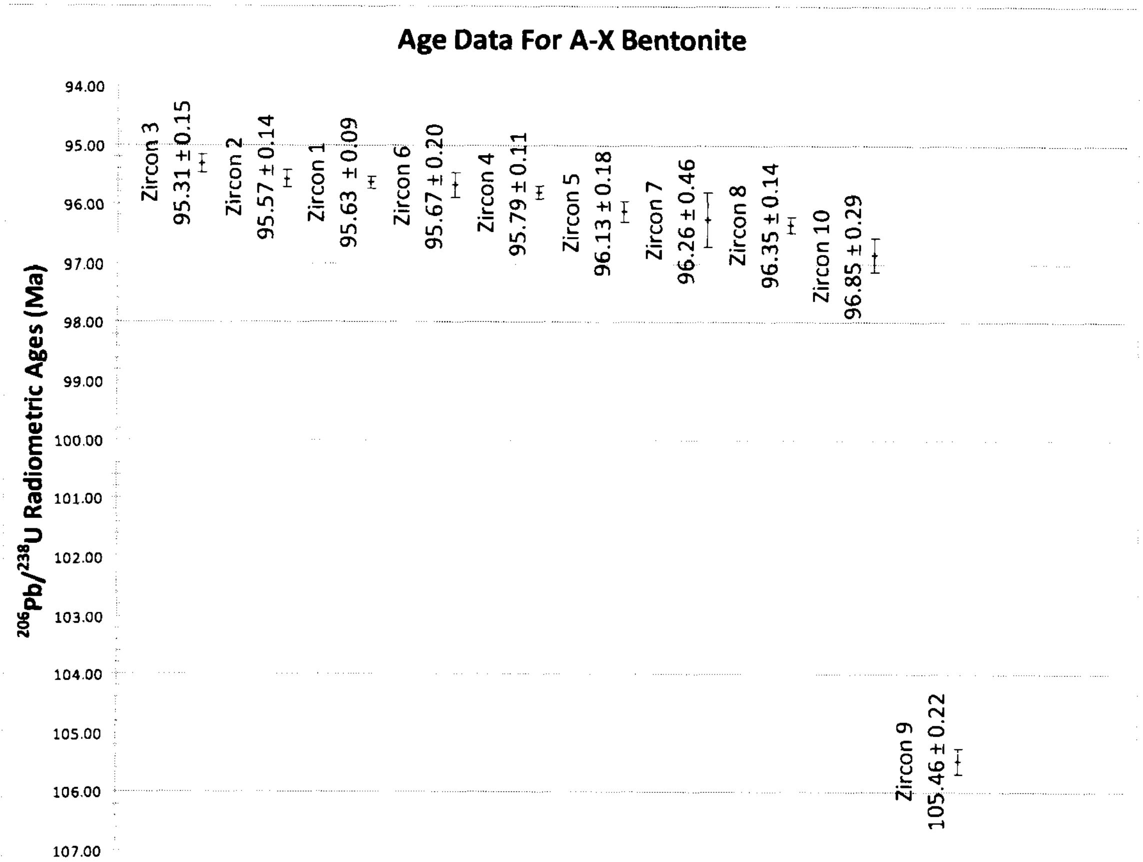

Figure 4.5. $^{206}Pb/^{238}U$ age data-points for single zircon crystals that were extracted from the A-X bentonite. Error bars are at the 2σ level. Note: Zircon 9 is much too old as compared to the other zircon analyses, and this has been attributed to xenocrystic inheritance.

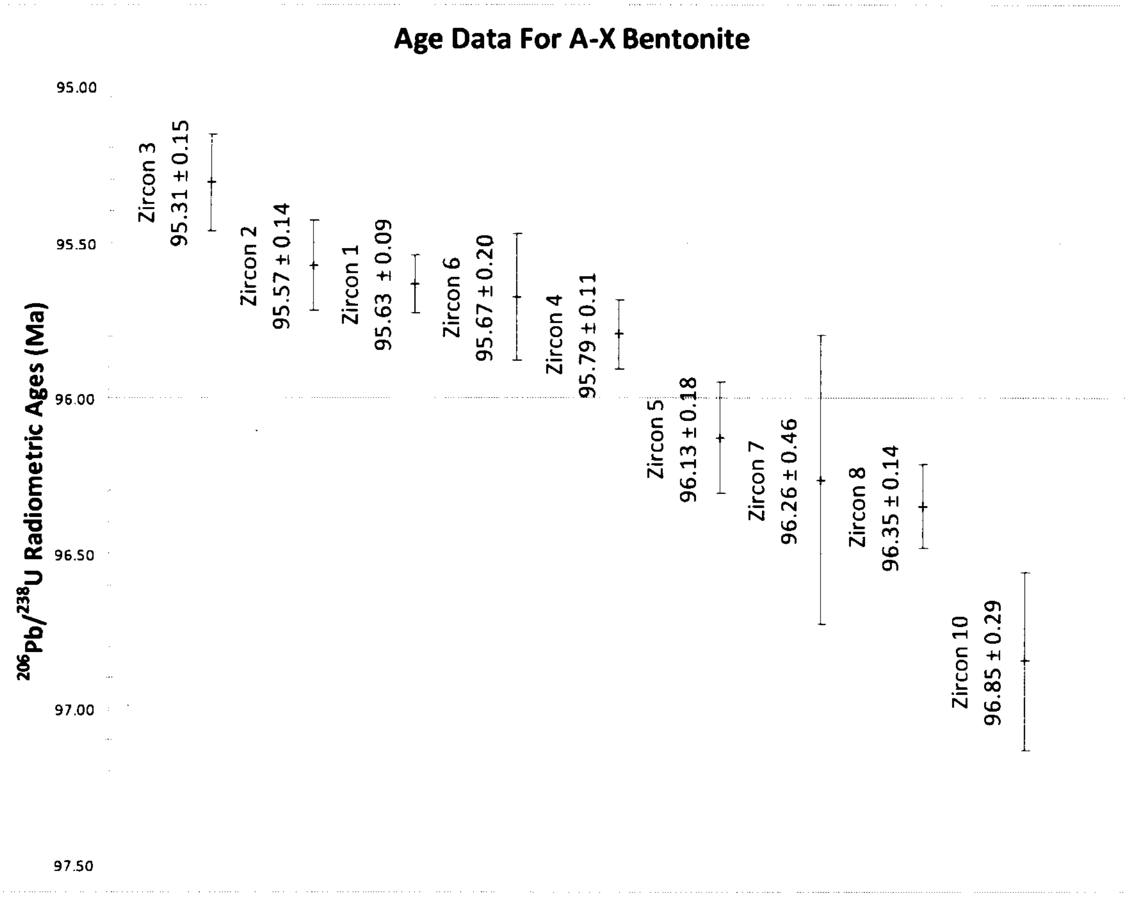

Figure 4.6. ^{206}Pb/^{238}U age data-points for single zircon crystals that were extracted from the A-X bentonite. Error bars are at the 2σ level. Zircon 9 has been excluded from this figure since it showed obvious inheritance. Note: The age data still shows a wide range of variation.

When the youngest subset of data is plotted on a Concordia diagram (n = 5; Fig. 4.7), a Concordia age cannot be calculated by *Isoplot* due to the data points not being equivalent and having a zero probability-of-fit. The data points do plot near one another, although the potentially youngest data point (Zircon 3) has a large reverse discordance and plots far to the left of the Concordia curve, suggesting that there was a problem with the analysis. When Zircon 3 was excluded from the Concordia age calculation, based on its large reverse discordance, the probability-of-fit rose from zero to 0.012 and a somewhat high MSWD of 6.3. Fig. 4.8 shows the Concordia age without consideration of Zircon 3 and the Concordia age with this selected subset (n = 4) was determined to be 95.65 ± 0.12 Ma.

The weighted-mean $^{206}Pb/^{238}U$ age is 95.62 ± 0.20 Ma (n = 5; Fig. 4.9). The probability-of-fit is zero, like that of the first Concordia diagram which included Zircon 3 in its calculation. As seen, Zircon 3 is the youngest grain and does not overlap within its uncertainty of the mean age. When Zircon 3 was manually excluded, the probability-of-fit increased from zero to 0.062, similar to what was seen when calculating the Concordia age, and the MSWD decreased from 6.5 to 2.4. Furthermore, the weighted-mean age increased from 95.62 ± 0.20 Ma to 95.67 ± 0.15 Ma (n = 4; Fig. 4.10).

4.4 Bighorn River Bentonite

The U-Pb results for six single crystal zircon analyses are presented in Table 4.1. The uranium content is high when compared to the other zircons from the other

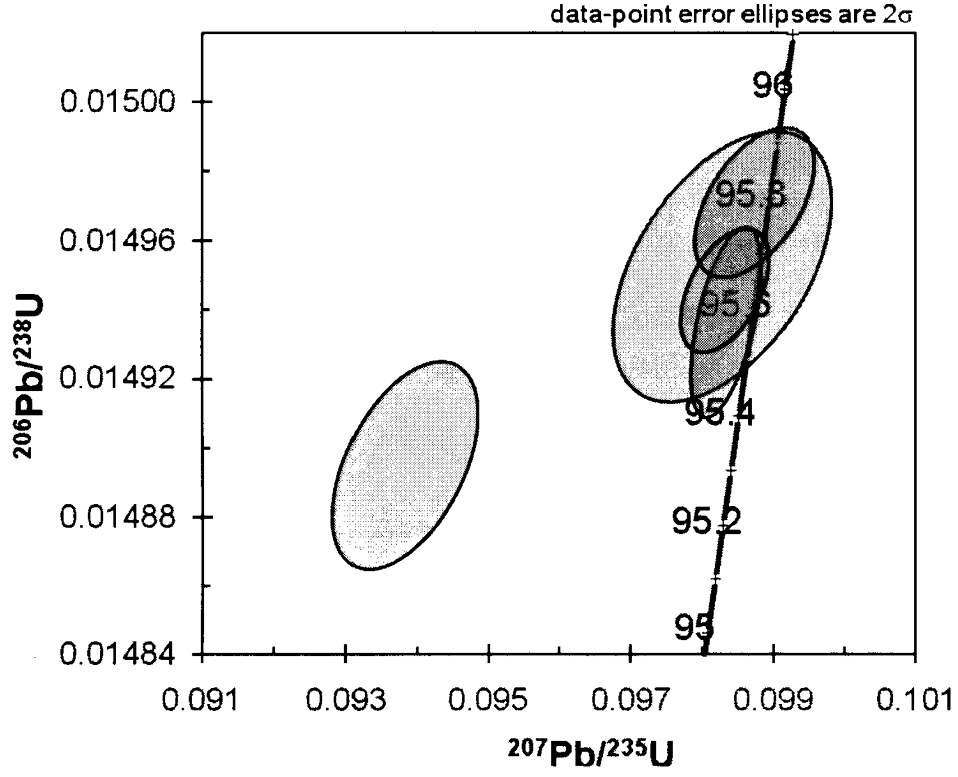

Figure 4.7. Concordia diagram for the A-X bentonite. The Concordia curve includes uncertainties with decay-constant errors, and error ellipses are at the 2σ level. Concordia line ages are to the left of the Concordia line and are in units of Ma. This is not including the zircons that have an age that is older than the proposed X-bentonite age. Note: Zircon 3 is highly reversely discordant.

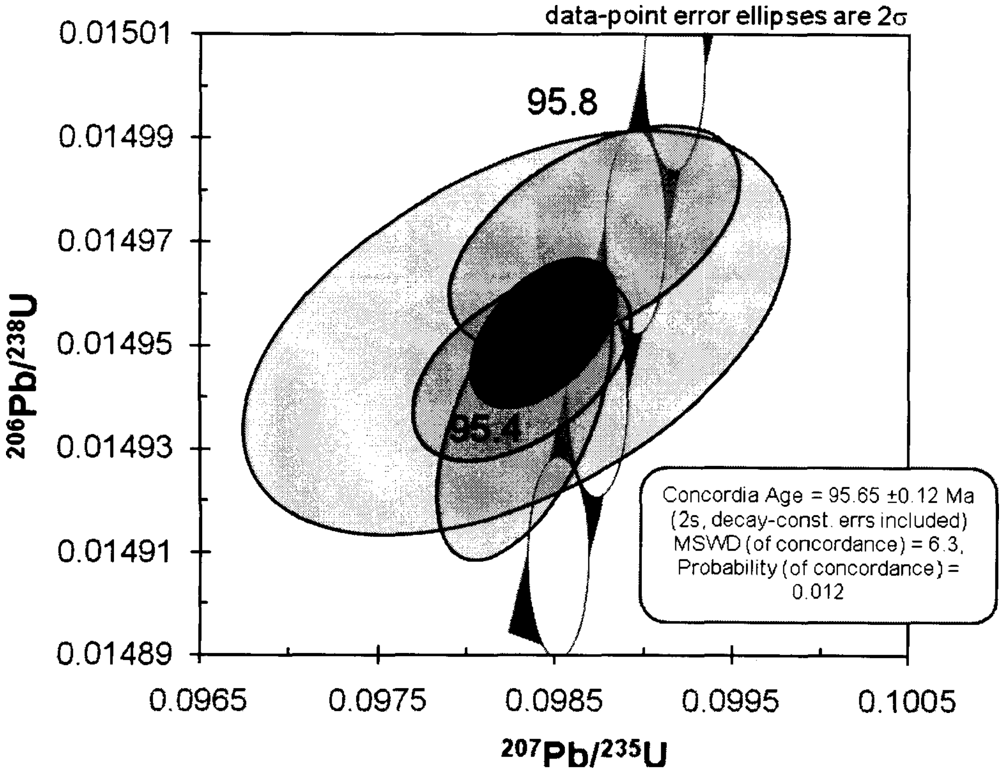

Figure 4.8. Concordia diagram for the A-X bentonite, excluding Zircon 3. The Concordia curve includes uncertainties with decay-constant errors, and error ellipses are at the 2σ level. Concordia line ages are to the left of the Concordia line and are in units of Ma. The dark grey error ellipse is the mean Concordia age.

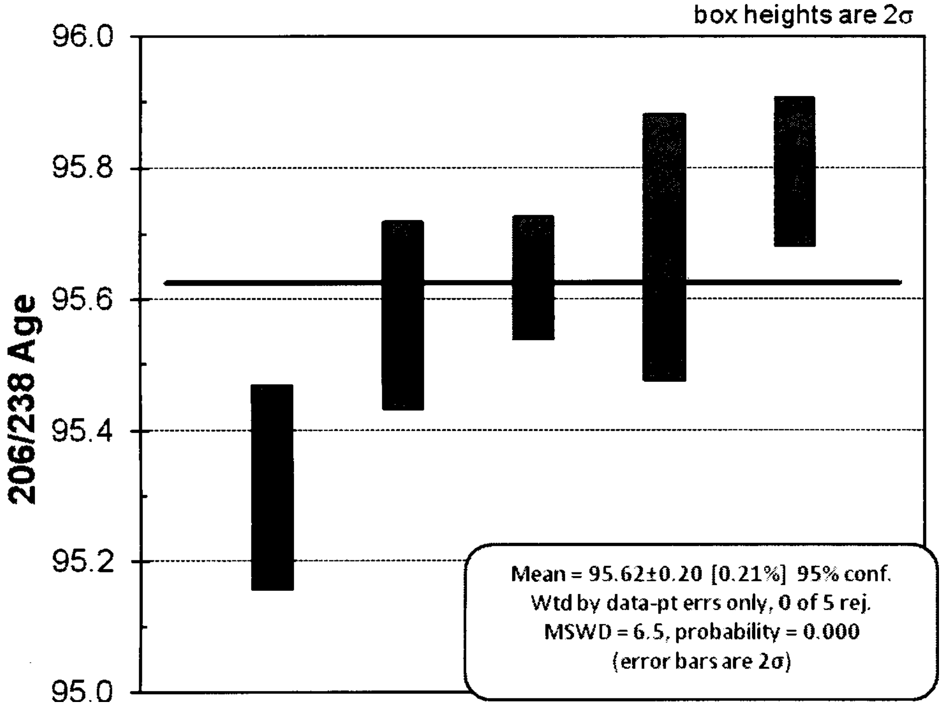

Figure 4.9. ^{206}Pb/^{238}U weighted-mean age for the A-X bentonite. This does not include decay-constant errors in its calculation. Uncertainties were entered at the 2σ level. The ^{206}Pb/^{238}U ages along the vertical axis are in units of Ma. The black line across the figure indicates the weighted-mean for the sample. Note: The probability-of-fit is zero since two of the data-points are not intersected by the weighted-mean age.

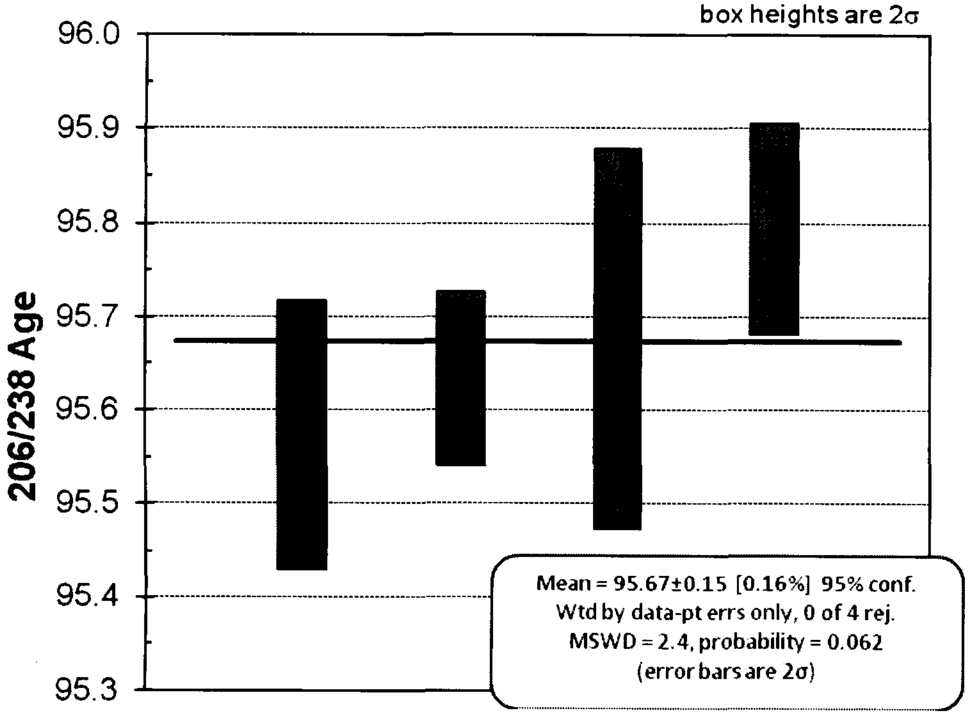

Figure 4.10. $^{206}Pb/^{238}U$ weighted-mean age for the A-X bentonite, excluding Zircon 3. This does not include decay-constant errors in its calculation. Uncertainties were entered at the 2σ level. The $^{206}Pb/^{238}U$ ages along the vertical axis are in units of Ma. The black line across the figure indicates the weighted-mean for the sample. Note: Zircon 4 is slightly older and not within uncertainty of the weighted-mean age.

bentonites, ranging from 223 to 376 ppm. The common ^{204}Pb in these samples is lower than the other samples, ranging from 0.2 pg to 1.1 pg. ^{206}Pb/^{238}U ages were determined by *Utildbu* with a typical precision of ~0.1 % to 0.3%. The ^{206}Pb/^{238}U dates range between 94.04 ± 0.24 Ma (Zircon 3) to 94.53 ± 0.34 Ma (Zircon 6) and all of the grains slightly overlap within their uncertainty (Fig. 4.11).

The analyses are considered "concordant" as the individual error ellipses overlap the Concordia curve (Fig. 4.12). There was no difference between data obtained in the first and second rounds of analysis, and the analyses group tightly, yielding a calculated Concordia age of 94.34 ± 0.19 Ma. However, the MSWD was moderate at 3.6, due to Zircon 6 plotting almost vertically along the Concordia curve due to a large error correlation coefficient. When Zircon 6 was excluded, the Concordia age decreased to 94.29 ± 0.11 Ma, with a low MSWD of 0.66 (Fig. 4.13). Furthermore, the probability-of-concordance increased from 0.057 to 0.42.

The weighted-mean ^{206}Pb/^{238}U age was determined to be 94.29 ± 0.13 Ma ($n = 6$; Fig. 4.14). As seen, Zircon 6 is the oldest grain and has the largest amount of uncertainty, and when excluded based on its large correlation coefficient, the uncertainty of the ^{206}Pb/^{238}U weighted-mean age increased slightly from 94.29 ± 0.13 Ma to 94.29 ± 0.14 Ma ($n = 5$; Fig. 4.15) and the MSWD did not change.

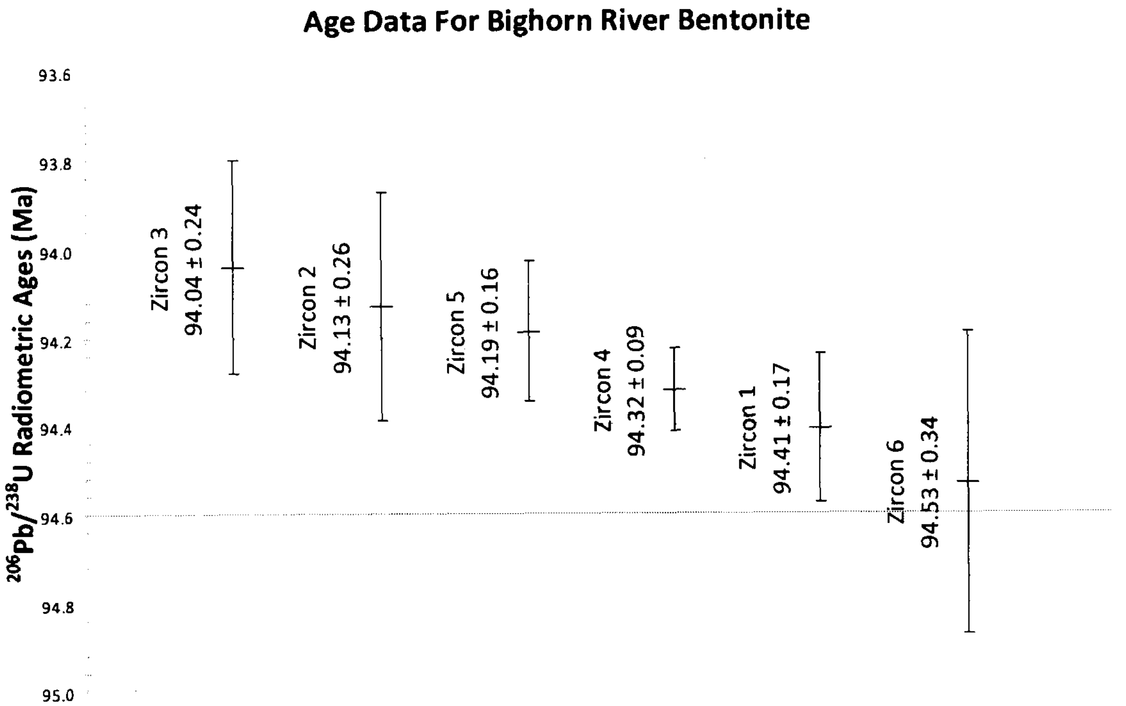

Figure 4.11. ^{206}Pb/^{238}U age data-points for single zircon crystals that were extracted from the Bighorn River Bentonite. Error bars are at the 2σ level.

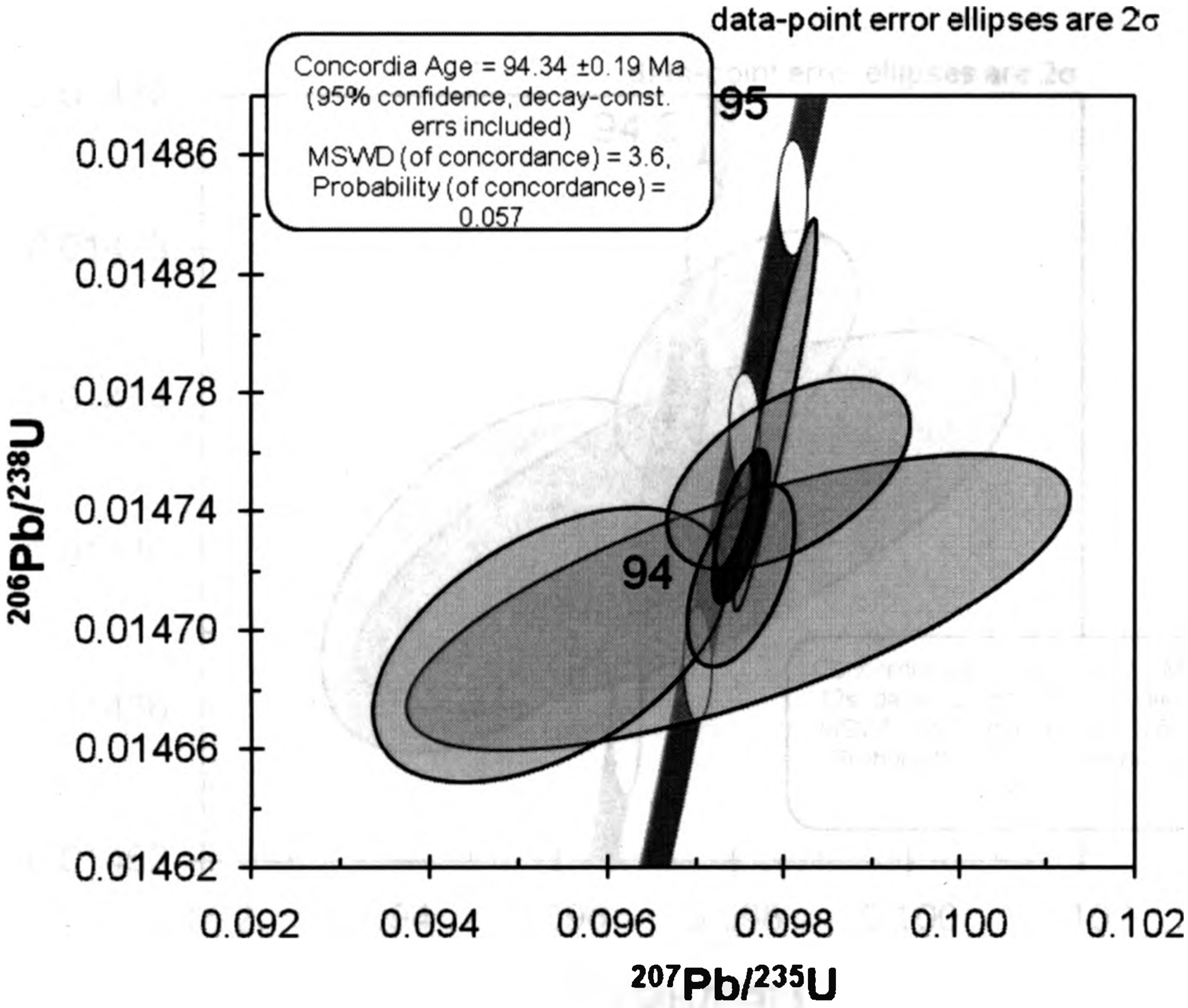

Figure 4.12. Concordia diagram for the Bighorn River Bentonite. The Concordia curve includes uncertainties with decay-constant errors, and error ellipses are at the 95% confidence level. Concordia line ages are to the left of the Concordia line and are in units of Ma. The dark grey error ellipse is the Concordia age ellipse. Note that one ellipse is near vertical, this is Zircon 6. Zircon 3 has a negative discordance and plots slightly to the left of Concordia.

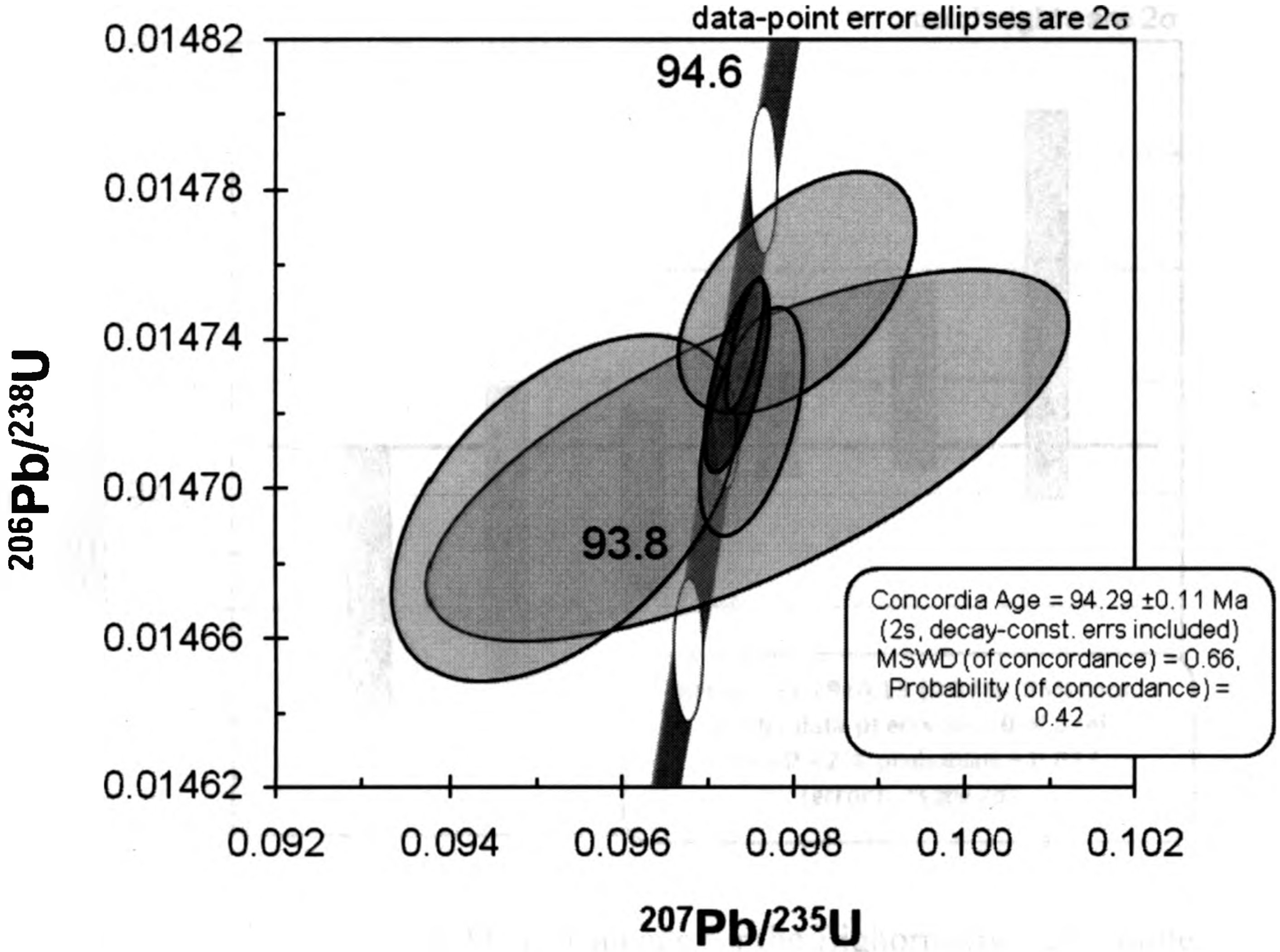

Figure 4.13. Concordia diagram for the Bighorn River Bentonite, excluding Zircon 6. The Concordia curve includes uncertainties with decay-constant errors, and error ellipses are at the 2σ confidence level. Concordia line ages are to the left of the Concordia line and are in units of Ma. The dark grey error ellipse is the Concordia age ellipse.

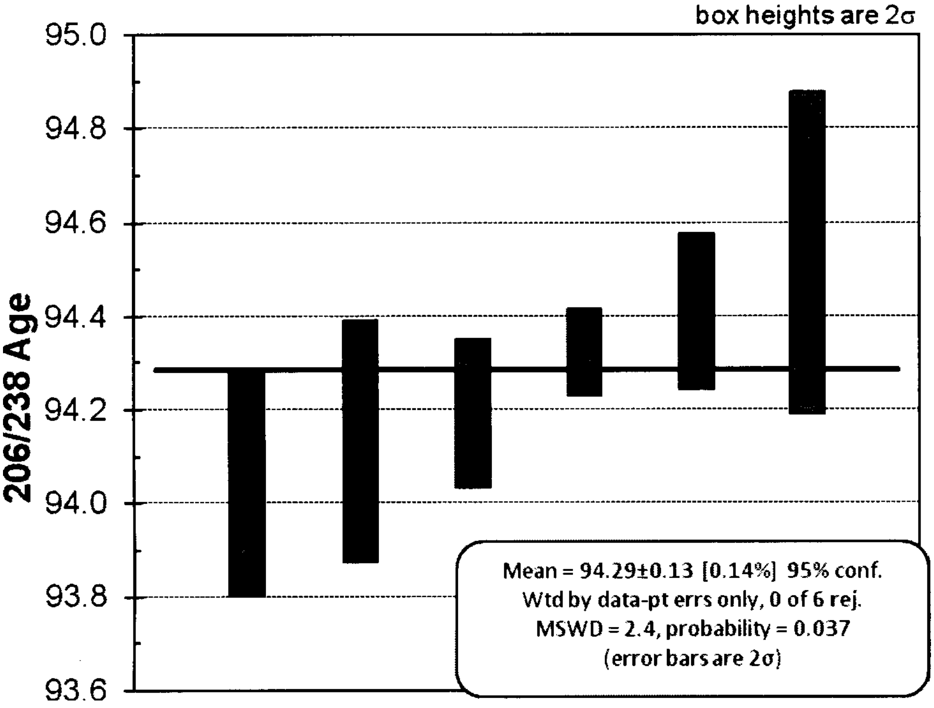

Figure 4.14. ^{206}Pb/^{238}U weighted-mean age for the Bighorn River Bentonite. This does not include decay-constant errors in its calculation. Uncertainties were entered at the 2σ level. The ^{206}Pb/^{238}U ages along the vertical axis are in units of Ma. The black line across the figure indicates the weighted-mean for the sample.

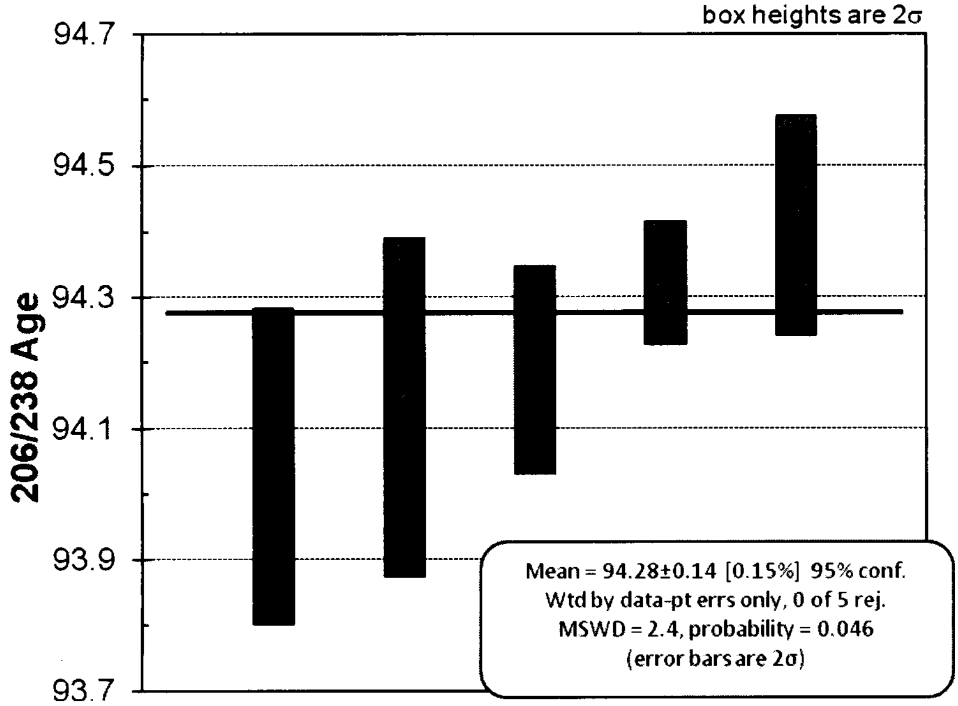

Figure 4.15. ^{206}Pb/^{238}U weighted-mean age for the Bighorn River Bentonite, excluding Zircon 6. This does not include decay-constant errors in its calculation. Uncertainties were entered at the 2σ level. The ^{206}Pb/^{238}U ages along the vertical axis are in units of Ma. The black line across the figure indicates the weighted-mean for the sample.

5. INTERPRETATION AND DISCUSSION

5.1 Interpreted Bentonite U-Pb Zircon Ages

In the interpretation of high-precision U-Pb zircon age data from bentonites, it is recognized that scatter may exist among concordant, single-grain zircon analyses that can be the result of analytical variations between analyses (e.g. signal quality during mass spectrometry) and geologic variation such as differing degrees of zircon residence time in the magma chamber prior to eruption. Analytical reproducibility of mass spectrometry data is on the order of ±0.1%, or for zircons of Cretaceous age, roughly ±0.1 m.y. As mentioned earlier, data scatter can also be due to zircon residence times in magma chambers of up to 0.2 m.y., leading to potential 'geological' scatter of ±0.1 m.y. With present techniques, it is impossible to resolve these two underlying causes of small-scale data variation.

For the X-bentonite, the Concordia age of 95.86 ± 0.11 Ma and the $^{206}Pb/^{238}U$ weighted-mean age of 95.87 ± 0.10 Ma (n = 6) overlap within uncertainty indicating that Pb-loss is not likely affecting the weighted-mean age. The weighted-mean age of 95.87 ± 0.10 Ma (n = 6) is interpreted to be the age of eruption and deposition of the X-bentonite.

For the A-X bentonite, the Concordia age of the youngest concordant subset of analyses is 95.65 ± 0.12 Ma and the $^{206}Pb/^{238}U$ weighted-mean age is taken as 95.67 ± 0.15 Ma (n = 4). Zircon 3 is observed to have a large reverse discordance (plotting to the left of Concordia) which cannot be accounted for by known geologic processes. This discordance is instead believed to be due to isobaric molecular interferences during mass spectrometery (Kamo 2009, pers. comm.), and this is the basis for excluding Zircon 3 from the Concordia age calculation. The Concordia age and the weighted-mean age overlap within uncertainty, indicating that Pb-loss is not likely a factor. However, the age variation among the ten single zircon analyses is typical for zircon populations that contain inherited xenocrystic domains, and therefore duplication of the younger concordant results is needed to confirm the tentative age interpretation of 95.67 ± 0.15 Ma ($n = 4$) as the eruption and deposition age of the A-X bentonite.

For the Bighorn River Bentonite, the Concordia age of 94.29 ± 0.11 Ma ($n=5$) and the $^{206}Pb/^{238}U$ weighted-mean age of 94.29 ± 0.13 Ma ($n = 6$) agree within uncertainty indicating that Pb-loss is not likely affecting the weighted-mean age. The $^{206}Pb/^{238}U$ weighted-mean age 94.29 ± 0.13 Ma ($n = 6$) is interpreted to be the age of eruption and deposition of the Bighorn River Bentonite.

The three $^{206}Pb/^{238}U$ weighted-mean ages for the Bighorn River, the A-X and the X bentonites are 94.29 ± 0.13 Ma, 95.67 ± 0.15 Ma and 95.87 ± 0.10 Ma respectively. Fig. 5.1 shows all three bentonite ages, including their corresponding uncertainties, on the same graph. These dates obey Nicolaus Steno's stratigraphic "Law of Superposition", whereby the age of each sedimentary bed in an undisturbed stratigraphic succession decreases upwards. The tentative age difference between the X-bentonite and the A-X bentonite is 0.2 m.y., whereas the difference between the X-bentonite and the Bighorn River Bentonite is 1.58 m.y. While the age of the Bighorn River Bentonite is clearly resolvable as being younger than the X-bentonite, the interpreted ages for the X and A-X

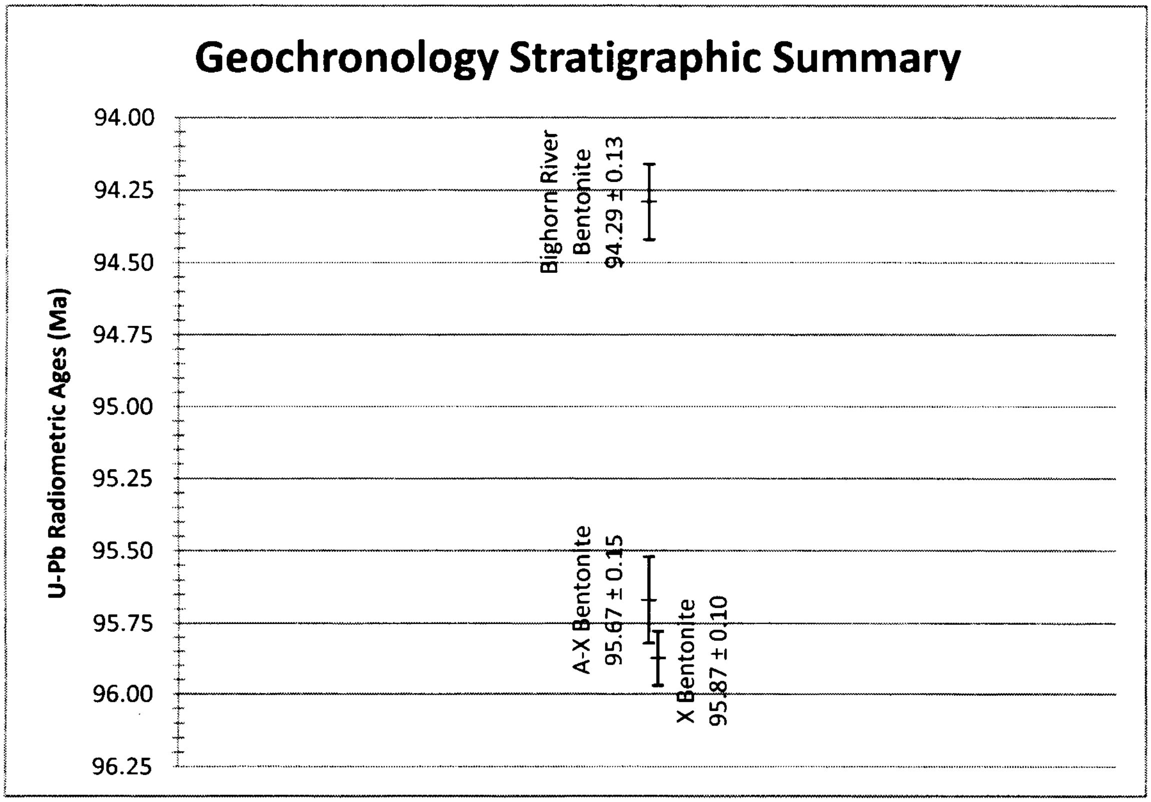

Figure 5.1. Combined age graph of the three bentonites used in this study. Ages are ^{206}Pb/^{238}U weighted-means and their uncertainties are stated at the 2σ level. Note: There is a slight overlap in the uncertainties between the X and A-X bentonites.

bentonites slightly overlap within their 2σ uncertainties by ~40 k.y., or 21.5% of the age difference.

5.2 Comparison of New U-Pb Ages with Previously Published ^{40}Ar/^{39}Ar Ages for Correlative Bentonites in Alberta and the Northern United States

Ridgley et al. (2001) used the ^{40}Ar/^{39}Ar method to radiometrically date bentonites from drill cores in Alberta, Saskatchewan and Montana, see Table 5.1. Ridgley et al. (2001) examined approximately the same stratigraphic interval as this study, and furthermore, the dates that were obtained by Ridgley et al. (2001) were comparable to the dates obtained in this study. However, Ridgely et al. (2001) did not establish a regional correlation scheme for the bentonites that they dated. Tyagi et al. (2007) integrated some of the individual cores from Ridgley et al. (2001) into regional correlations, but details of how the bentonites studied by Ridgley et al. (2001) relate to the marker bentonites traced by Tyagi et al. (2007) are unclear, and therefore their use as stratigraphic markers remains limited.

The interpreted Concordia ages of the bentonites determined from this study may be compared with the literature, although the ages are seemingly not in agreement. The new single zircon U-Pb Concordia age of 95.86 ± 0.11 Ma for the X-bentonite presented here is 0.90 m.y. older than the previously determined ^{40}Ar/^{39}Ar age of 94.96 ± 0.5 Ma (Cobban et al. 2006). Fig. 5.2 shows the previously published X-bentonite dataset in comparison to the new single zircon U-Pb ages. There are no previously published ages

Table 5.1. (Ridgley et al. 2001)

New ^{40}Ar/^{39}Ar Age Dates from Bentonites in the Fish Scales, Belle Fourche, and Second White Specs Formations

Bentonite Number and Well Number on Cross Section	Well	Depth	Age	Number of Analyses	Formation
B1 Cross section A6, B6	Prud Cypress 10-3-9-1W4	31766.85 ft	95.22 Ma	1	Belle Fourche, base of D1
B2 Cross section B9	Esso et al Cessford 6-3MH-24-13W4S	681 m	94.35±0.28 Ma	6	Second White Specks Formation
B3 Cross section B12	AEC A13 Suffield 14-26-19-18W4	664.9 m	93.55±0.75 Ma	3	Second White Specks Formation
B4 Cross section B13	BP et al Alderson 16-7-17-9W4	639.1 m 643.5 m	93.84± 0.72 Ma 93.29±0.45 Ma	3 5	Second White Specs Formation
B5 Cross section B20	POC Amoco Senate 11-22-4-28W3	2794-2796 ft	93.53±0.53 Ma	5	Second White Specks Formation
B6 Cross section B15	Scurry Rainbow Medhat 1 3-10-14-9W4	1920 ft	93.89±0.24 Ma	6	Second White Specks Formation
Not on cross section	Suffield	2233.68 ft	97.59±0.40 Ma	5	Fish Scales Formation

The uncertainty is the standard error of the mean at the 95 percent confidence level. Depth shown as feet or meters depending on when well was drilled.

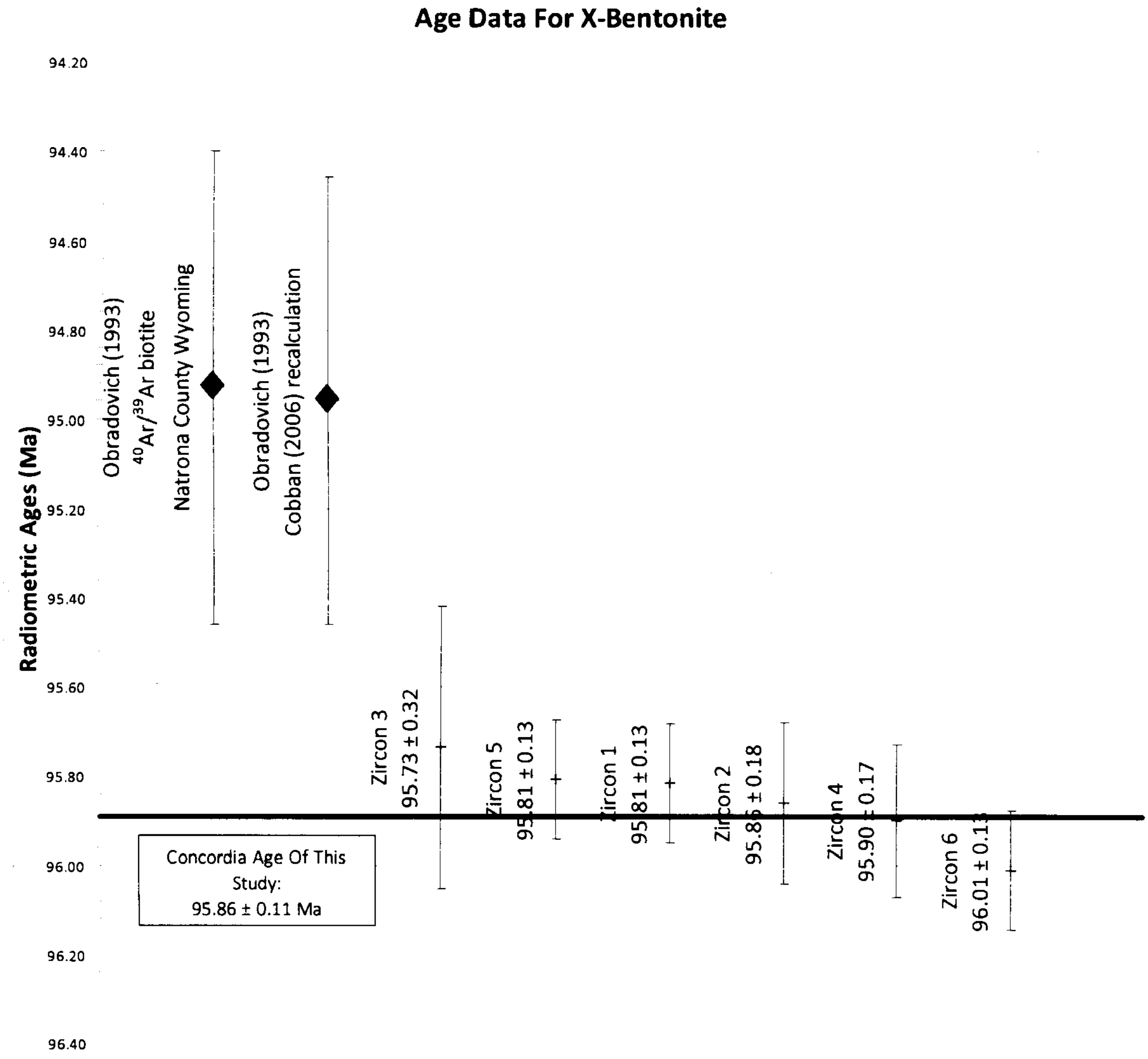

Figure 5.2. All of the previously-published $^{40}Ar/^{39}Ar$ age data and the age data of this study for the X-bentonite. All uncertainties are at the 2σ level. The diamond shapes indicate previous studies. The black line across the graph represents the Concordia age obtained from this study.

for the A-X Bentonite, therefore the preliminary $^{206}Pb/^{238}U$ weighted-mean age determined here of 95.67 ± 0.15 Ma is a primary result that should be treated as a maximum age until the degree to which the present age spectrum is affected by residence time is determined, which is dictated by the fact that one zircon grain is ~360 k.y. younger than the weighted-mean age. Additionally, there is a large amount of scatter in the U-Pb ages, indicating that on a single-grain basis there might be some inheritance, whether it occurred through the incorporation of country-rock zircons or through xenocrystic inheritance. However, based on the U-Pb age and the stratigraphic relationship with the X-bentonite, the tentative U-Pb age for the A-X bentonite is unlikely to decrease by much.

The presently accepted $^{40}Ar/^{39}Ar$ age for the Bighorn River Bentonite is 93.3 ± 0.4 Ma (Obradovich 1993), which is 0.99 m.y. less than the new single zircon U-Pb Concordia age of 94.29 ± 0.11Ma. Fig. 5.3 shows the previously published Bighorn River Bentonite dataset in comparison to the new single zircon U-Pb ages. It is observed that the newly acquired U-Pb ages are consistently older than their previously published $^{40}Ar/^{39}Ar$ counterparts.

As discussed by other authors (e.g., Renne et al. 1998; Min et al. 2000; Renne 2000; Schmitz and Bowring 2001a), an apparent ~ 1% difference exists between the U-Pb and $^{40}Ar/^{39}Ar$ isotopic decay schemes, such that in the Mesozoic, $^{40}Ar/^{39}Ar$ ages can underestimate the true age by ~1 m.y. (see 1.3.2.4 *Comparison of U-Pb and* $^{40}Ar/^{39}Ar$ *Dating*). The new U-Pb ages obtained here strongly support this hypothesis. The 1% age

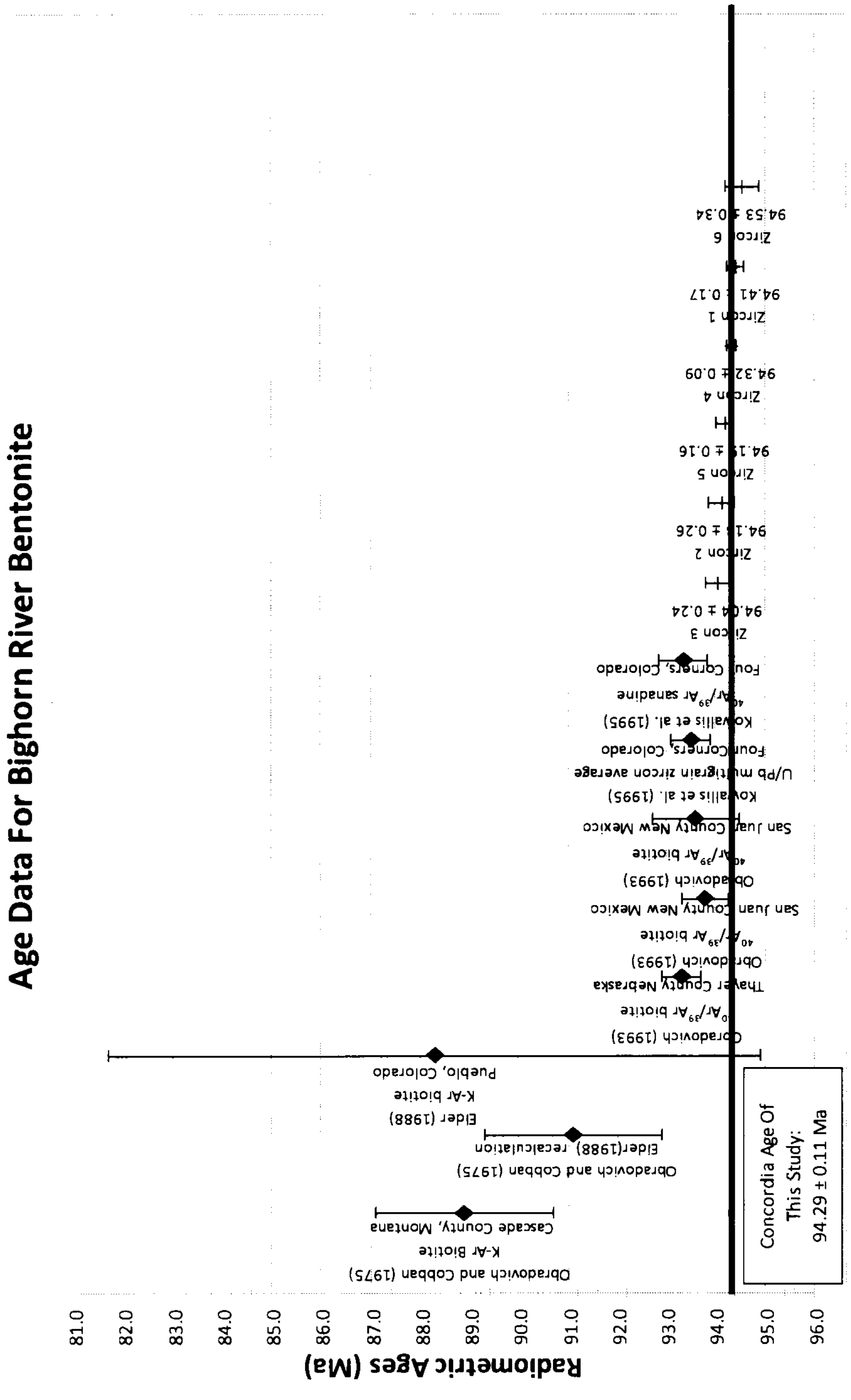

Figure 5.3. All of the previously-published age data and the age data of this study for the Bighorn River Bentonite. All uncertainties are at the 2σ level. Diamonds indicate previous studies. The black line across the graph represents the Concordia age obtained from this study. Note that one of the previous studies (Kowallis et al. 1995) had a multigrain zircon U-Pb average age for the Bighorn River Bentonite, which is in agreement with the previously published $^{40}Ar/^{39}Ar$ data.

increase may be calculated to show the bias between the geochronometer systems by taking 94.96 Ma as the accepted $^{40}Ar/^{39}Ar$ age for the X-bentonite (Cobban et al. 2006) and 93.30 Ma as the accepted $^{40}Ar/^{39}Ar$ age for the Bighorn River Bentonite (Obradovich 1993). The recalculated $^{40}Ar/^{39}Ar$ age for the X-bentonite is 95.91 Ma and is in agreement, within uncertainty, of the U-Pb Concordia age calculated from this study of 95.86 ± 0.11 Ma. The recalculated $^{40}Ar/^{39}Ar$ age for the Bighorn River Bentonite is 94.23 Ma, and is in agreement, within uncertainty, of the U-Pb Concordia age calculated from this study of 94.29 ± 0.11 Ma. Fig. 5.4 and 5.5 graphically shows the 1% bias, with the artificially 1% older $^{40}Ar/^{39}Ar$ dates falling into the uncertainty of the $^{206}Pb/^{238}U$ single zircon ages.

It is interesting to note that the geochronological study by Kowallis et al. (1995) on the Utah equivalent to the Bighorn River Bentonite did include U-Pb zircon analyses. However, it is observed that Kowallis et al. (1995) calculated an average U-Pb age of 93.5 ± 0.4 Ma, which is in agreement with the previously published $^{40}Ar/^{39}Ar$ results and less than the age for the Bighorn River Bentonite calculated in this study by 0.8 m.y. If the 1% bias between the two isotopic decay systems was applied, Kowallis et al. (1995) would have achieved a result 94.44 Ma, which is slightly outside of the uncertainty of the U-Pb results of this study (94.29 ± 0.11 Ma). See Fig. 5.6 for a comparison between the calculated ages of the multigrain zircon analyses of Kowallis et al. (1995) and of the results from this study. An explanation of the difference may be attributed to Kowallis et al. (1995) relying on numerous multigrain zircon batches that were not chemically abraded and may have included grains that had experienced recent Pb-loss.

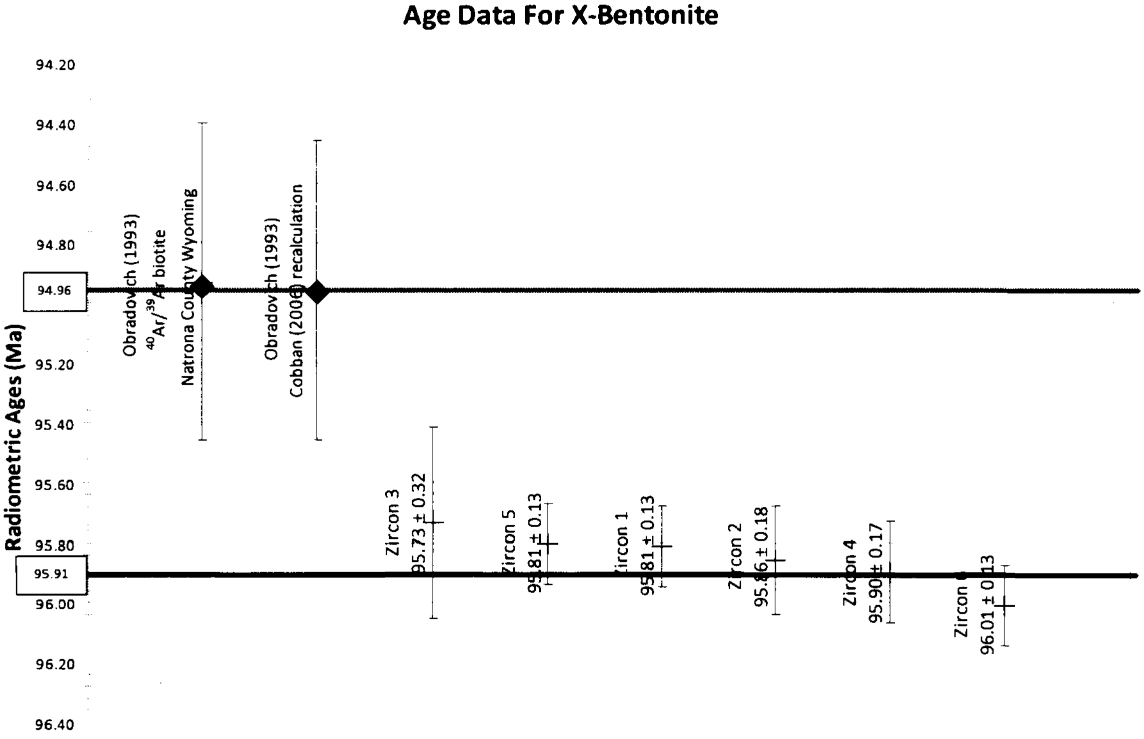

Figure 5.4. Both of the previously-published $^{40}Ar/^{39}Ar$ age data and the age data of this study for the X-bentonite. All uncertainties are at the 2σ level. Diamonds indicate previous studies. The light grey line across the graph represents the accepted $^{40}Ar/^{39}Ar$ age for the X-bentonite. The black line represents a 1% bias between the $^{40}Ar/^{39}Ar$ and U-Pb decay systems when the $^{40}Ar/^{39}Ar$ age is increased by 1%. Note that the black line falls within uncertainty of all of the U-Pb results determined in this study.

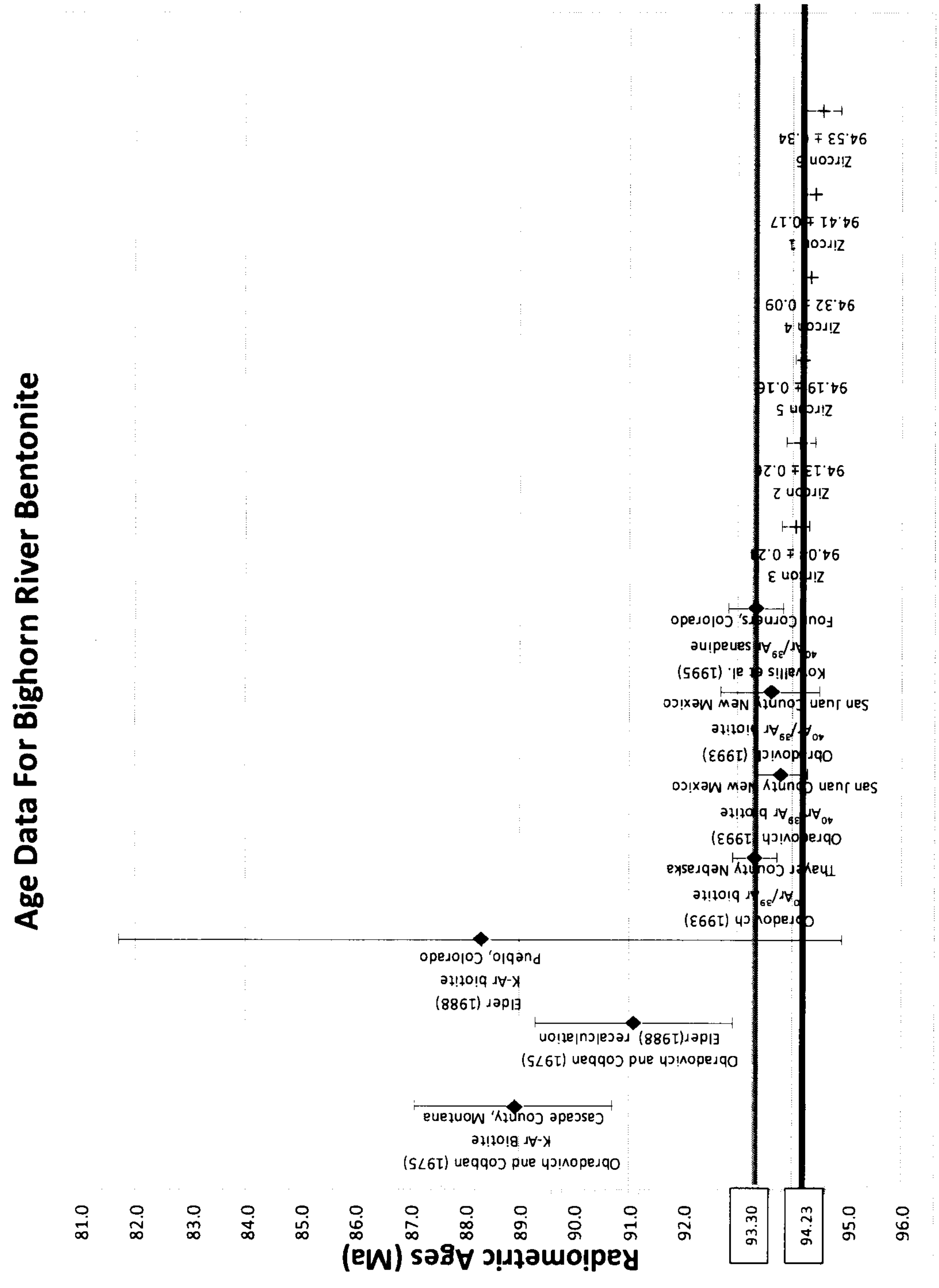

Figure 5.5. All of the previously-published ^{40}Ar/^{39}Ar age data and the age data of this study for the Bighorn River Bentonite. All uncertainties are at the 2σ level. Diamonds indicate previous studies. The light grey line across the graph represents the accepted ^{40}Ar/^{39}Ar age for the Bighorn River Bentonite. The black line represents a 1% bias between the ^{40}Ar/^{39}Ar and U-Pb decay systems when the ^{40}Ar/^{39}Ar age is increased by 1%. Note that the black line falls within uncertainty of all of the U-Pb results determined in this study.

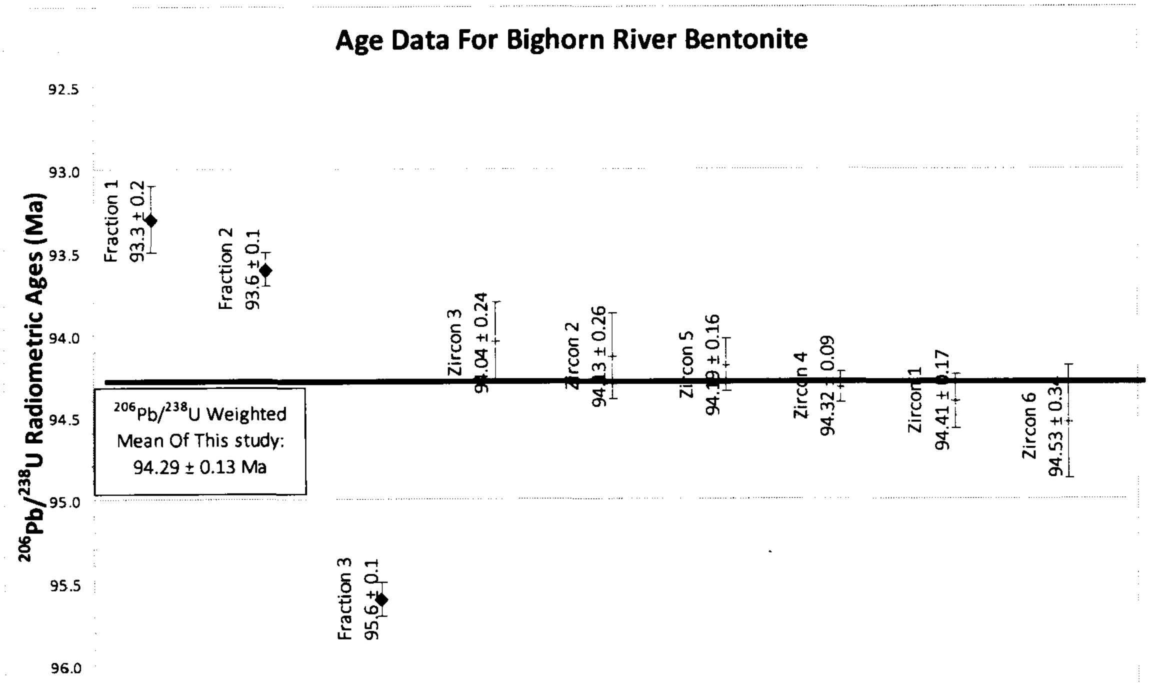

Figure 5.6. Combined age plot for the multigrain zircon $^{206}Pb/^{238}U$ ages of Kowallis et al. (1995) indicated by diamond symbols, and the single-grain zircon $^{206}Pb/^{238}U$ ages obtained here. The black line across the graph represents the weighted-mean age determined here. Uncertainties are at the 2σ level. Note: Fraction 1 and 2 of Kowallis et al. (1995) are younger than the ages determined here, whereas Fraction 3 is older, though this has been attributed to xenocrystic inheritance.

In order to prove the Pb-loss hypothesis, the data of Kowallis et al. (1995) is recalculated here on a Concordia diagram to provide a comparison with the Concordia age of the Bighorn River Bentonite from this study. The data are recalculated using the isotopic ratios that were presented by Kowallis et al. (1995) and reproduced in Table 5.2. Furthermore, the error correlation coefficients (ρ) were calculated from the isotopic ratios and the equation from Ludwig (1992):

$$\rho_{xy} = \frac{E_x^2 + E_y^2 - E_z^2}{2E_xE_y} \qquad \text{Eq. 5.1}$$

Where E_x is the error in the $^{207}Pb/^{235}U$ ratio, E_y is the error in the $^{206}Pb/^{238}U$ ratio and E_z is the error in the $^{207}Pb/^{206}Pb$ ratio. The ^{238}U and ^{235}U decay-constants, and the natural $^{238}U/^{235}U$ ratio used in Kowallis et al. (1995) are the same as were used in this study, allowing for an accurate comparison. A reference Discordia line anchored at present day time (t = 0) and passing through the Kowallis et al. (1995) dataset, produces a calculated upper Concordia intercept age of 95.7 ± 6.3 Ma at the 2σ level (Fig. 5.7). This age is much older than the $^{206}Pb/^{238}U$ average age of 93.5 ± 0.4 Ma that was calculated by Kowallis et al. (1995), however still within uncertainty of the calculated upper Concordia intercept age. The upper intercept age (95.7 Ma) and the large error (±6.3 Ma) is the most probable age of the bentonite if recent Pb-loss had affected some part of the multigrain zircon fractions. In this scenario, the average U-Pb zircon age calculated by Kowallis et al. (1995) may be inaccurate and reflect a case of very slight discordance on a line that is sub-parallel to Concordia, such that the analyses remain technically

Table 5.2. Kowallis et al. (1995) Multigrain zircon data for the equivalent to the Bighorn River Bentonite

		Concentration				Atomic Ratios							Age (Ma)			
Description: sample fraction number	Weight of sample (μg)	U (ppm)	Pb (ppm)	Th (ppm)	Common Pb (pg)	$^{206}Pb/^{204}Pb$	$^{206}Pb/^{238}U$	2σ	$^{207}Pb/^{235}U$	2σ	$^{207}Pb/^{206}Pb$	2σ	$^{206}Pb/^{238}U$	2σ	$^{207}Pb/^{235}U$	2σ
Fraction 1 (n=300)	228	469	7.1	225	19	5884	0.01458	6.0E-05	0.09639	4.0E-04	0.04797	1.2E-04	93.3	0.2	93.4	0.2
Fraction 2 (n=60)	49	364	5.5	167	4	8503	0.01462	4.0E-05	0.0966	2.4E-04	0.04793	6.0E-05	93.6	0.1	93.6	0.1
Fraction 3 (n=152)	181	586	9.2	271	30	4009	0.01494	4.0E-05	0.10092	2.6E-04	0.04898	6.0E-05	95.6	0.1	97.6	0.1

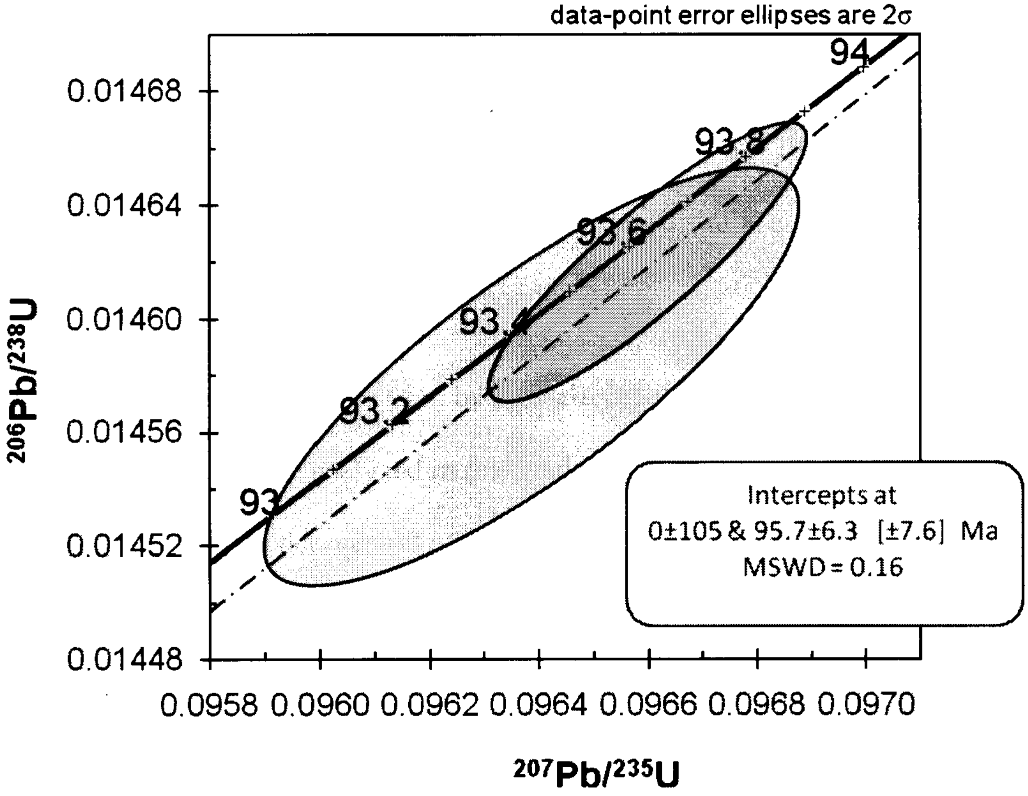

Figure 5.7. Concordia plot using the data obtained by Kowallis et al. (1995). The anomalous old age of fraction 3 that was obtained by Kowallis et al. was excluded. Concordia line ages are to the left of the Concordia line and are in units of Ma. The Discordia line, which is indicated by the subparallel dashed line on the figure above, was anchored at t = 0, and the line shows the effect of Pb-loss.

"concordant", despite having suffered Pb-loss. The Concordia age calculated for the Bighorn River Bentonite in this study (94.29 ± 0.11 Ma; Fig. 4.12), assumes that no Pb-loss has occurred and can be compared to the upper intercept age calculated from the Kowallis et al. (1995) data. The Concordia age for the Kowallis et al. dataset without an anchored Discordia age is presented in Appendix D.

Assuming that the samples used by Kowallis et al. (1995) are time-equivalent to the Bighorn River Bentonite analyzed in this study, the difference in age results caused by Pb-loss is likely due to the method of analysis. In order to remove material that has experienced Pb-loss, Kowallis et al. (1995) air abraded (Krogh 1982) large aliquots of zircons using pyrite. Conversely, the study undertaken here relied on treating the zircons with HF chemical abrasion and it is possible that this method was more rigorous in the removal of metamict zircon material.

5.3 Chronostratigraphic Implications of New Ages

The new ages determined in this study have the potential to refine various chronostratigraphic boundaries of the geological time-scale (Fig. 5.8). The X-bentonite lies within the middle Cenomanian *Acanthoceras amphibolum* ammonite zone and is immediately overlain by the *Plesiacanthoceras wyomingense* Zone (Cadrin et al. 1995). Cobban et al. (2006) proposed that the first appearance of *P. wyomingense* is at 94.96 ± 0.49 Ma, but according to the dates obtained here, the *P. wyomingense* ammonite zone has a lower boundary age of 95.87 ± 0.10 Ma.

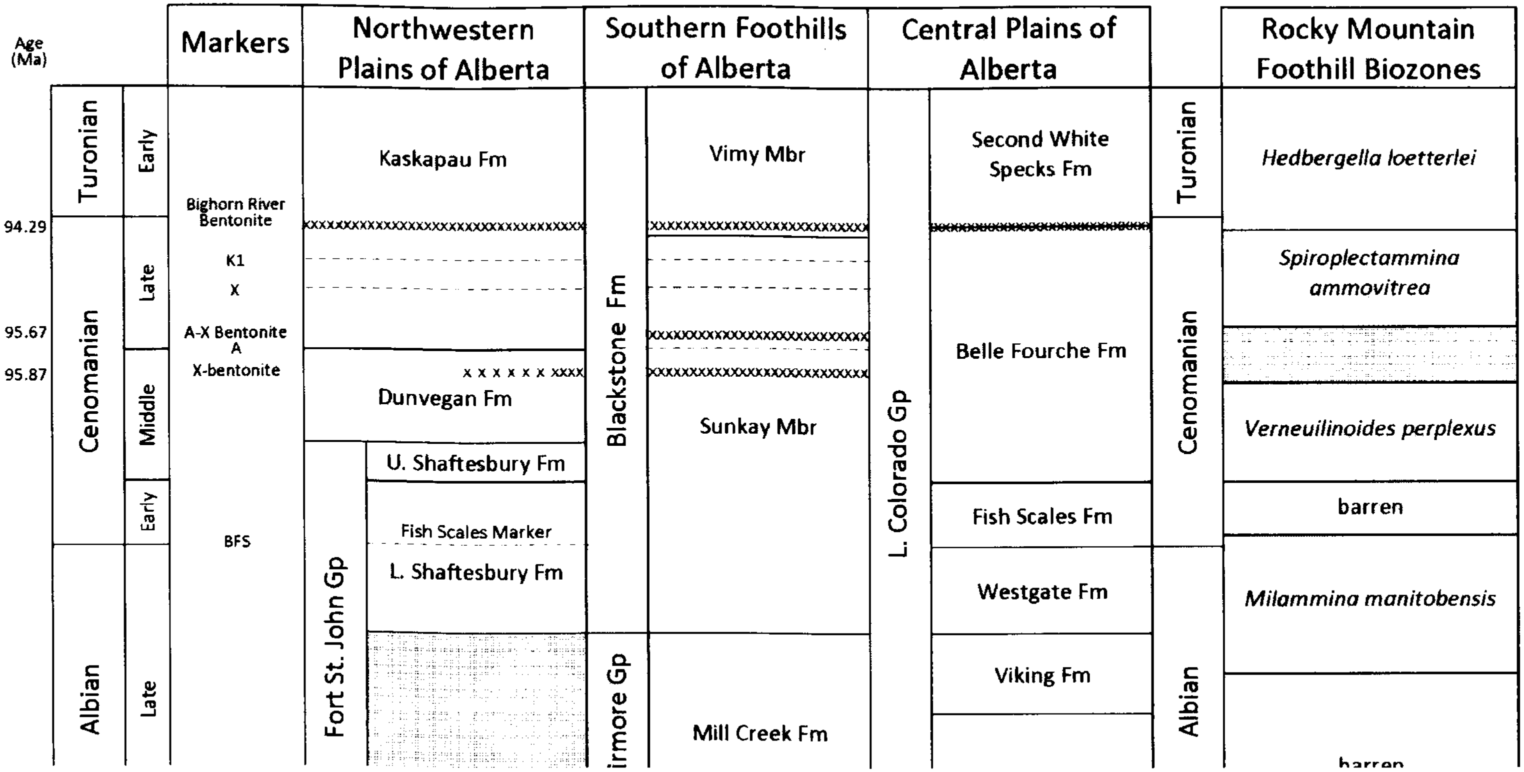

Figure 5.8. Chart summarizing the correlations between the Blackstone Formation in outcrop and the lower Colorado Group in the subsurface. Also indicates the correlation with biostratigraphic units. $^{206}Pb/^{238}U$ weighted-mean ages of the bentonite layers are added to the left side of the figure. XXX, indicates bentonite layer. ---, indicates a bounding surface. K1 and X are bounding surfaces. BFS, Base Fish Scales; Fm, Formation; Mbr, Member; Gp, Group; U, Upper; L, Lower. This chart is not scaled. Modified from Tyagi et al. (2007) and Roca et al. (2008).

Tyagi et al. (2007) showed that the base of the Second White Specks Formation of the Colorado Group is closely approximated by the Bighorn River Bentonite, and therefore the Second White Specks Formation – Belle Fourche Formation boundary lies at 94.29 ± 0.13 Ma. Tyagi et al. (2007) also proposed that the Bighorn River Bentonite is a major chronostratigraphic marker, which approximates the Cenomanian/Turonian boundary. The current age for the Cenomanian/Turonian boundary is 93.6 ± 0.8 Ma (Ogg et al. 2005), which is defined by bed 86 at the GSSP at Pueblo, Colorado (see 1.2.3.4 *Intercontinental Link to the GSSP at Pueblo, Colorado*). Bed 86 is bracketed by two bentonites, Bed 80 below it, and Bed 88 above (Fig. 1.14), which have both been dated through ^{40}Ar/^{39}Ar methods by Obradovich (1993). Bed 80 is a correlative equivalent to the Bighorn River Bentonite, and was dated by ^{40}Ar/^{39}Ar methods three times, 93.30 ± 0.4 Ma, 93.78 ± 0.49 Ma and 93.59 ± 0.58 Ma. Geochronology of Bed 88 yielded an ^{40}Ar/^{39}Ar age of 93.25 ± 0.49 Ma, which is practically indistinguishable from the ages obtained for Bed 80 within its uncertainty; the resolvability of this is below the limits of the ^{40}Ar/^{39}Ar technique. These ages were combined using a spline fit and the uncertainty tries to incorporate possible systematic offsets between ^{40}Ar/^{39}Ar radiometric ages and other methods (Ogg et al. 2005). However, U-Pb techniques are presently more accurate than ^{40}Ar/^{39}Ar dating techniques, and it is seen that the age of the equivalent Bighorn River Bentonite (94.29 ± 0.13 Ma), lies within the age uncertainty span of 1.6 m.y. of the previously published Cenomanian/Turonian ^{40}Ar/^{39}Ar boundary age. Therefore, according to the new age calculated here, the beginning of the Cenomanian/Turonian transition should be refined from 93.6 ± 0.8 Ma to 94.29 ± 0.13

Ma and should be considered as a maximum age for the Cenomanian/Turonian boundary. To solidify this boundary age revision, a bentonite that lies stratigraphically at the same level as the boundary, or immediately above, needs to be dated with U-Pb techniques (see 5.6 *Future Work*).

5.4 Oceanic Anoxic Event II (OAE II)

OAE II is defined in the section, *Intercontinental Link to the GSSP at Pueblo, Colorado* (1.2.3.4). The Bighorn River Bentonite equivalent (Bed 80) exists in the middle of the OAE II curve at the GSSP at Pueblo, Colorado, lying just below the Cenomanian/Turonian boundary. The age of the Bighorn River Bentonite provides an important geochronologic calibration point for the middle of the OAE II curve, both continentally and globally. It has been suggested by Turgeon and Creaser (2008) that OAE II was indirectly triggered by large-scale magmatic activity, but a direct link to a specific event has not been located. Magmatic events in central Yukon occurred at ~92 to 98 Ma, corresponding to the OAE II time interval, but these events are too small to account for the wide-spread nature of OAE II (Mortensen et al 2000; Prokoph et al. 2001). The Caribbean-Colombian plateau basalts are believed to have been active between ~87 to 91.7 Ma, triggering a large-scale release of CO_2, causing global warming and a sea-level rise (Kerr 1998; Prokoph 2001), but this age is ~2.6 m.y. younger than the maximum age of 94.29 Ma Cenomanian/Turonian boundary age that is proposed here and the events are likely not contemporaneous. Therefore, the cause of this anomaly remains open for debate.

5.5 Rates of Sedimentary and Tectonic Processes

The deposition of the X and A-X bentonites coincide with a phase of accelerated flexural subsidence that is related to renewed tectonic loading in the northwest portion of the basin (Plint et al. 2009). These bentonites facilitate the refinement of the length of deposition of Dunvegan allomember A and allow for a first quantification of the rates of sedimentary/tectonic and eustatic changes for this time interval in the foreland basin. The X-bentonite lies within allomember C of the Dunvegan Formation where it disappears northward due to marine reworking. The A-X bentonite exists between the top of allomember A and the X bounding surface, in the lower part of allomember AX-4 of the A-X unit. Fig. 5.9 shows the location of these units with respect to the Dunvegan Formation. The A-X bentonite lies just over three shoaling upward sequences above the top of allomember A (Plint 2009, pers. comm.) and assuming 21 k.y. high-frequency Milankovitch orbital sedimentary sequences, the A-X bentonite is ~60 k.y. younger than the top of Dunvegan allomember A.

As discussed in the section, *Lithostratigraphy of the Western Canada Foreland Basin* (1.2.1.3), isopachs of the younger allomembers D to A show the progressive development of a sedimentary depocenter along the western margin of the basin and collectively show the rotation of the depocenter from perpendicular to parallel with

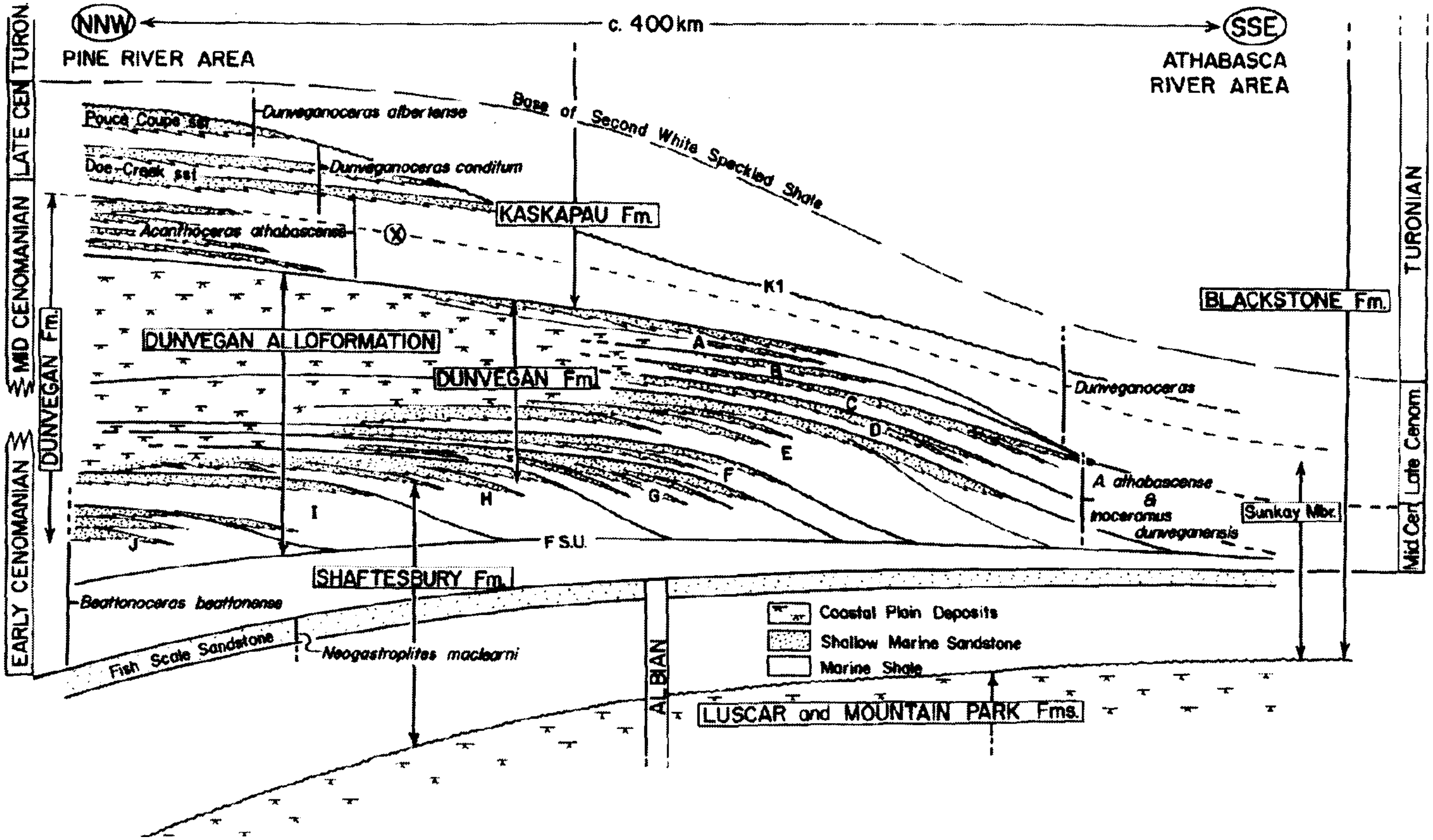

Figure 5.9. Schematic NW-SE composite diagram illustrating the Dunvegan Formation, molluscan biostratigraphy, the stratigraphic terminology applied to the under- and overlying units and the stratigraphic range of important fossil Zones. The boundaries of the lithostratigraphic Dunvegan Formation and the allostratigraphic Dunvegan alloformation are also indication. Note: Dunvegan allomember B has been recently incorporated into Dunvegan allomember A (Hay 2006). Plint (2003).

respect to the present deformation front (Fig. 5.10). When this isopach map is subdivided (Fig. 5.11), it can be seen that allomember C is essentially tabular, showing no evidence of differential subsidence in the orogen-proximal, updip area. However, allomember A indicates a dramatic thickening in the far north-west that is suggestive of renewed tectonic activity. Using these isopach maps (Fig. 5.11) the rate of depocenter formation between allomember C and A time can be generally constrained. The new age for the X-bentonite is 95.87 ± 0.10 Ma and the A-X bentonite is 95.67 ± 0.15 Ma, which indicates that only ~ 200 k.y. elapsed between allomember C and the A-X unit (~440 k.y. considering maximum uncertainties), constraining the maximum length of allomember A deposition. The sedimentary depocenter developed during allomember A time, and therefore the depocenter likely developed in less than 200 k.y.

The renewed and accelerating tectonic subsidence in the north-west portion of the basin during allomember A time led to regression as the accommodation-to-supply ratio gradually shifted in favour of accommodation and a major backstep of the allomember A shoreline occurred (Plint 2003; Plint et al. 2009). Fig. 5.12 shows the low frequency sedimentary backstep of the delta front between allomember C and A time. Using isopach maps created elsewhere (Fig. 5.11), Plint et al. (2009) stated that between allomember C and the top of allomember A, the delta front backstepped about 290 km. Using the time interval developed here for the deposition of allomember A, the backstep occurred at an average rate of 1.45 km/k.y. (1.45 m/year). However, this rate could be lower if the ages of the X and A-X bentonites are considered at the maximum

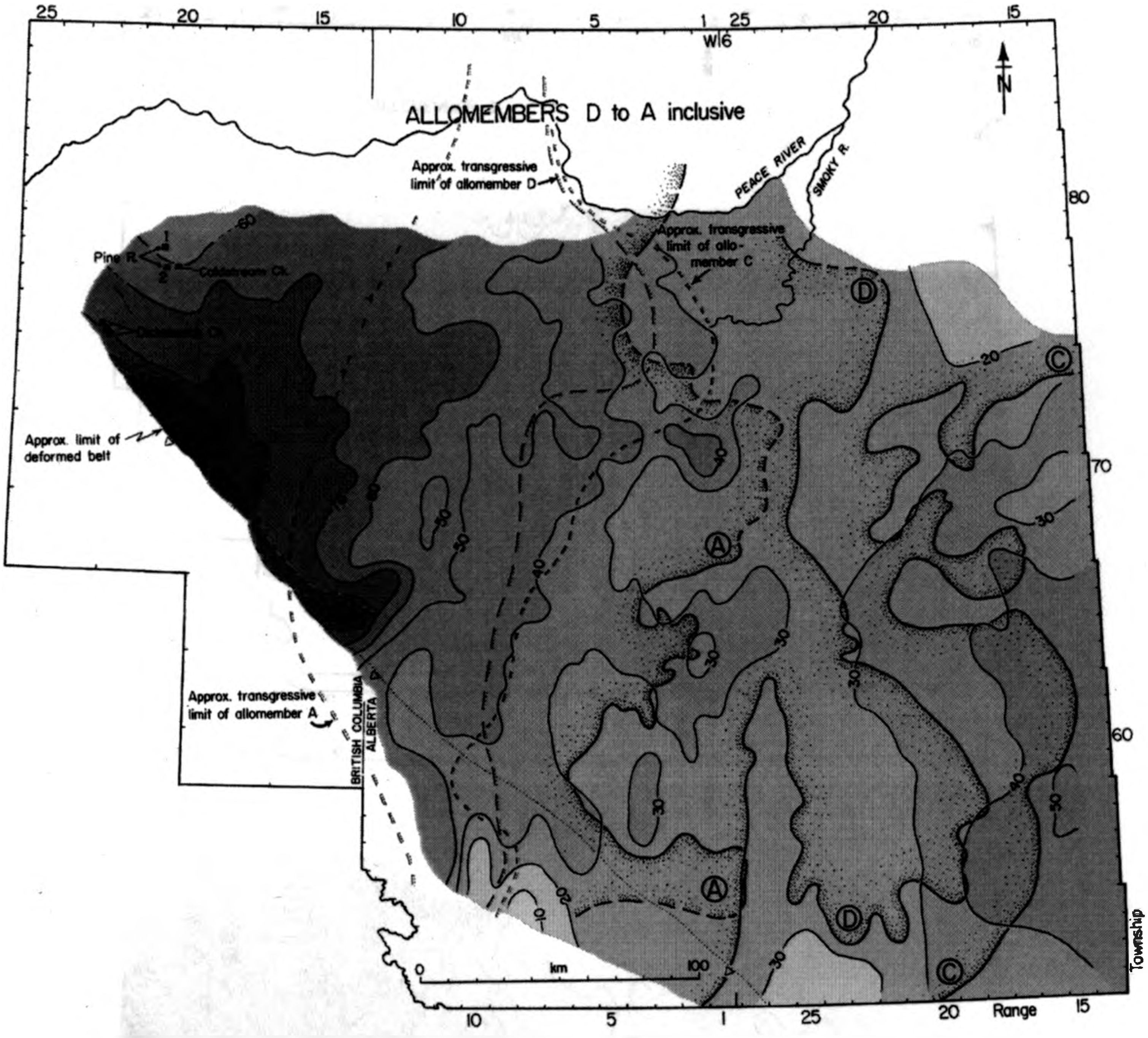

Figure 5.10. Composite map showing the maximum progradational shorelines of Dunvegan allomembers D, C and A, and also the isopachs for the entire D to A interval. Note: The prominent depocenter along the western margin of the study area, and the progressive rotation of the isopach lines. Dashed lines indicate the shorelines during each allomember time. Plint (2003)

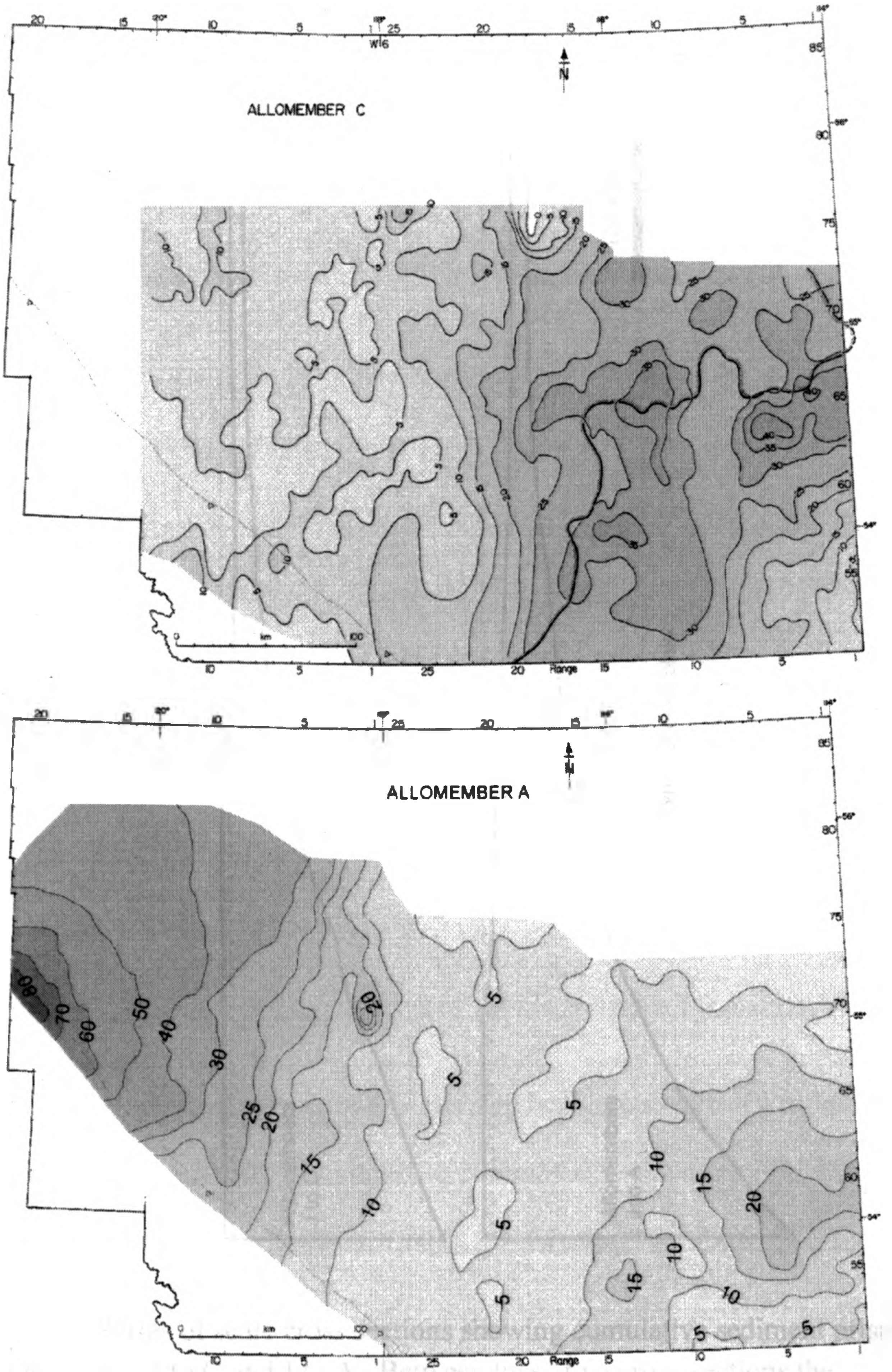

Figure 5.11. Individual isopach maps showing cumulative thickness for Dunvegan allomembers A and C. Allomember C demonstrates a nearly tabular deposition, whereas during allomember A time, a large depocenter developed in the north-west. Hays et al. (2009, in press)

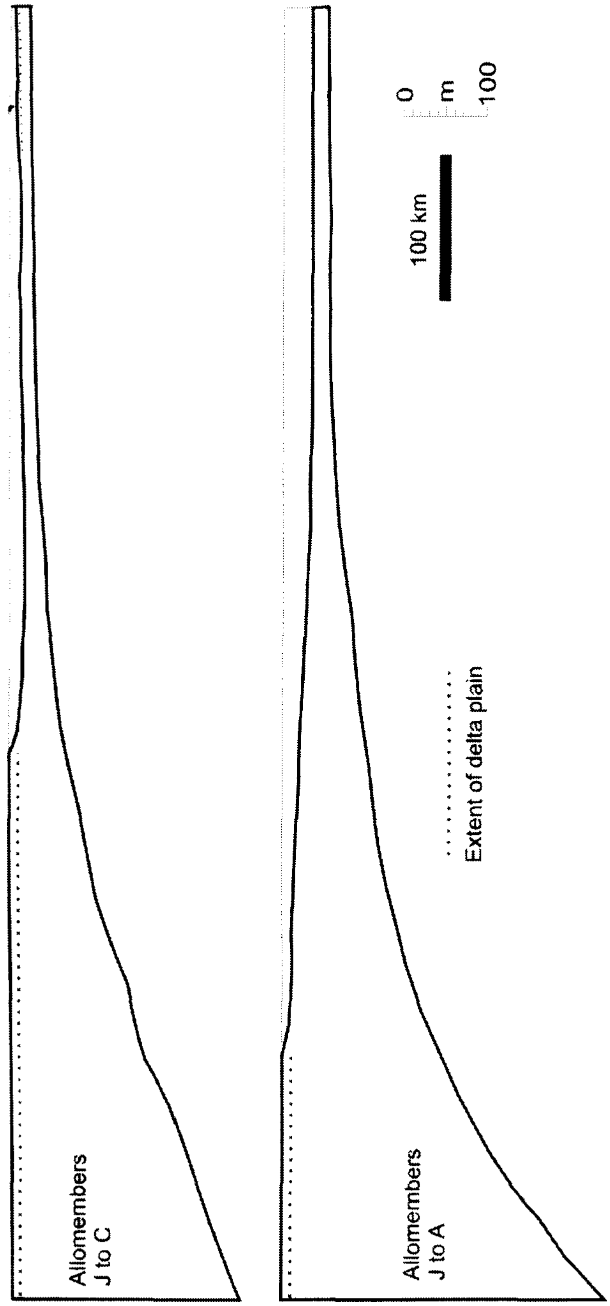

Figure 5.12. Series of scale cross sections showing cumulative sediment prism for allomembers J to C and J to A. Between these two cross-sections the retrograding delta shoreline is quite visible. Additionally, clinoforms cannot be recognized during allomember A time. Plint et al. (2009)

uncertainties. Regardless, it is inferred that the delta front backstep during allomember A time occurred at a rate of meters per year.

5.6 Future Work

This study illustrates the benefits of using the ID-TIMS analytical methodology, but it is only as good as the samples that are used in the analyses. Due to the scatter in the A-X bentonite age data, created by possible xenocrystic inheritance, further data collection for the A-X bentonite is required. Most of the data points were rejected from the A-X bentonite dataset, lowering the number of useful grain analyses to four, which is below the satisfactory number of grains that should be used when calculating the weighted-mean U-Pb age of the bentonite. SEM-CL data for the A-X bentonite could be collected creating a method for the determination of a pattern of xenocrystic inheritance. Furthermore, additional zircons from the A-X bentonite need to be isotopically dated with current U-Pb ID-TIMS techniques to confirm the tentative age determined here.

The techniques used here should be used on bentonites collected from the United States portion of the basin to test and improve continental correlations of Cretaceous events. The B-bentonite from Utah and Colorado is assumed to be the same as the Bighorn River Bentonite (Tyagi et al. 2007) and to test the stratigraphic correlation of the Bighorn River Bentonite, a sample of the B-bentonite that was collected from Cottonwood Canyon, Utah, should be dated with U-Pb ID-TIMS. If the age determined from the B-bentonite is different than the age of the Bighorn River Bentonite then the bentonites are not equivalent, and revisions will need to occur.

Additional bentonites occur at various stratigraphic levels in the Cretaceous succession in Alberta. Isotopically dating these other bentonites will help to further calibrate the geological time-scale, and help to quantify tectonic rates. The next target bentonites include the "Green" and "Blue" bentonites, see Fig. 1.9. The "Blue" bentonite lies a short distance above the Cenomanian/Turonian boundary and can be used to help constrain the Cenomanian/Turonian boundary age. When the "Blue" bentonite age is combined with the Bighorn River Bentonite age that was determined here and stratigraphic bedding rhythms determined elsewhere (Meyers and Sageman 2004), the duration of the worldwide OAE II may be more precisely estimated, see Fig. 5.13. As additional bentonites are dated with high-precision, the time-packages constrained between the bentonites will get smaller, and when combined with detailed allostratigraphy, it may become possible to make realistic determinations of the duration of high-frequency sequences, and establish possible genetic links to Milankovitch orbital rhythms.

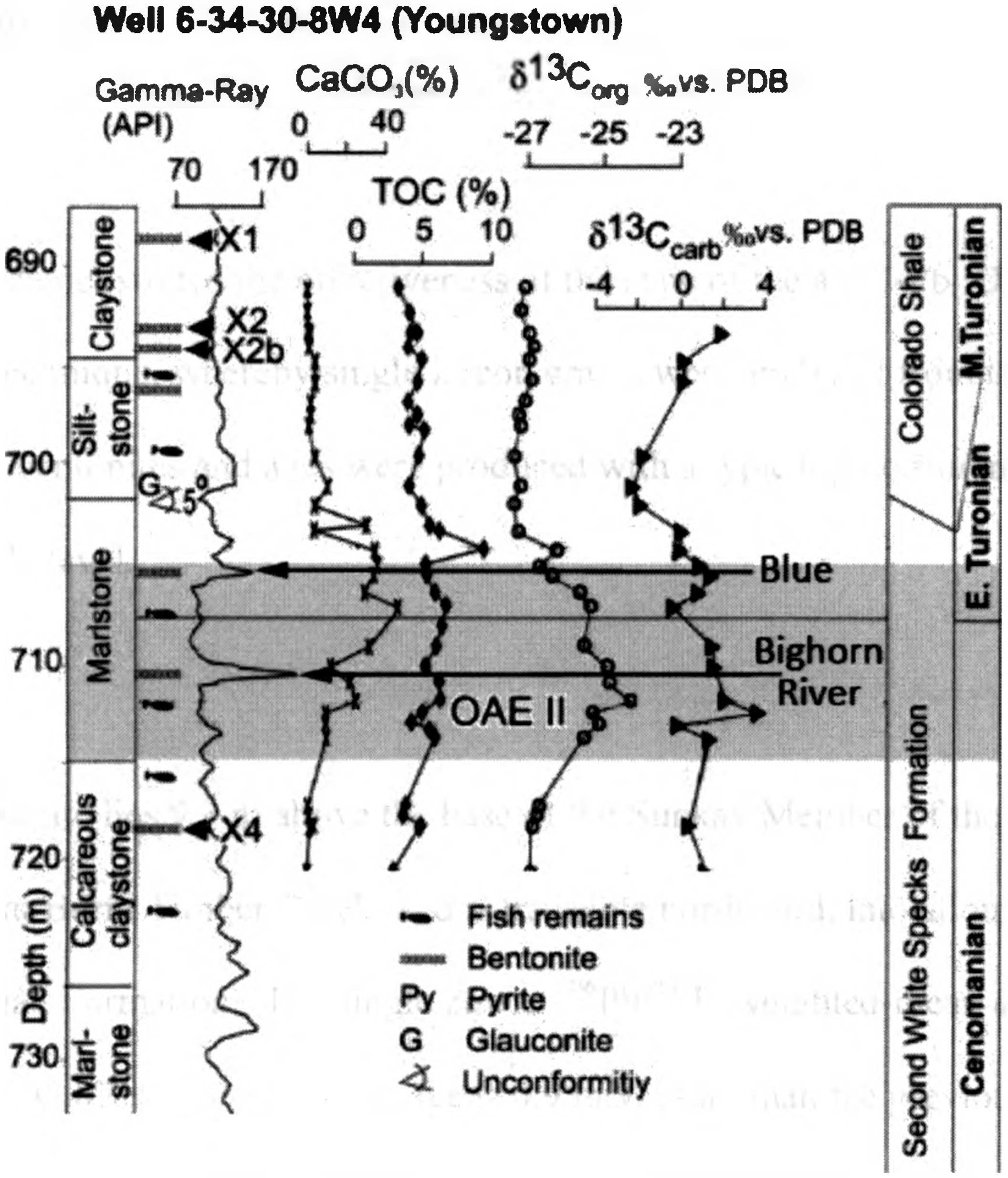

Figure 5.13. Modified OAE II curve showing the locations of the Bighorn River Bentonite and the “Blue” bentonite in relation to the $\delta^{13}C$ isotope excursion. Modified from Prokoph et al. (1997).

6. CONCLUSIONS

1. This study demonstrated the effectiveness of the state of the art U-Pb ID-TIMS analytical technique, whereby single zircon grains were analyzed from three Upper Cretaceous bentonites and ages were produced with a typical precision near the desired 0.1% level.

2. The X-bentonite lies 9.3 m above the base of the Sunkay Member of the Blackstone Formation at Burnt Timber Creek, and is traceable northward, into allomember C of the Dunvegan Formation. The single zircon $^{206}Pb/^{238}U$ weighted-mean age for the X-bentonite is 95.87 ± 0.10 Ma. This age is 0.9 m.y. older than the previously published $^{40}Ar/^{39}Ar$ result, highlighting the current 1% age underestimation of the $^{40}Ar/^{39}Ar$ radiometric technique.

3. The A-X bentonite lies in the middle of the Sunkay Member of the Blackstone Formation, in the A-X Unit, which is between allomember A of the Dunvegan Formation and the X stratigraphic bounding surface. The single zircon $^{206}Pb/^{238}U$ weighted-mean age for the A-X bentonite is 95.67 ± 0.15 Ma. There have been no other previously published ages for the A-X bentonite, and therefore this age sets a new tentative age for the bentonite.

4. The Bighorn River Bentonite lies 4 m above the base of the Vimy Member of the Blackstone Formation at Burnt Timber Creek. The single zircon $^{206}Pb/^{238}U$ weighted-mean age for the Bighorn River Bentonite is 94.29 ± 0.13 Ma. This age is ~ 1 m.y. older than the previously published $^{40}Ar/^{39}Ar$ result.

5. The X-bentonite lies within the *Acanthoceras amphibolum* ammonite zone and is immediately overlain by the *Plesiacanthoceras wyomingense* Zone. It is therefore proposed that the *P. wyomingense* ammonite zone has a lower boundary age of 95.87 ± 0.10 Ma.

6. The Bighorn River Bentonite has been proposed as a major chronostratigraphic marker, which approximates the Cenomanian/Turonian boundary. Therefore, according to the new ages, the Cenomanian/Turonian boundary age should be revised from 93.6 ±0.8 Ma to having a maximum age of 94.29 ± 0.13 Ma, based on its stratigraphic position in relation to the Cenomanian/Turonian boundary.

7. The X and A-X bentonites bracket allomember A of the Dunvegan delta complex. Allomember A demonstrates a dramatic thickening in the far north-west that is suggestive of renewed tectonic activity, and furthermore, allomember A records a major backstep of the Dunvegan delta complex. It is proposed that the formation of a tectonic depocenter in the north-west occurred in less than 200 k.y. and that the Dunvegan delta front backstepped at an average rate no more than 1.45 km/k.y. (1.45 m/yr) during allomember A deposition.

7. References

Armstrong, R.L., and Suppe, J. 1973. Potassium-argon geochronometry of Mesozoic igneous rocks in Nevada, Utah and southern California. Geological Society of America Bulletin, **84**: 1375-1392.

Armstrong, R.L., and Ward, P.L. 1993. Late Triassic to Earliest Eocene Magmatism in the North American Cordillera: Implications for the Western Interior Basin. Geological Association of Canada Special Paper 39, pp. 49-72.

Arthur, M.A., Dean, W.E., and Pratt, L.M. 1988. Geochemical and climatic effects of increased marine organic carbon burial at the Cenomanian/Turonian boundary. Nature, **335**: 714–717.

Bacon, C.R. 1989. Crystallization of accessory phases in magmas by local saturation adjacent phenocrysts. Geochim Cosmochim Acta, **53**: 1055-1066.

Bateman, P.C. 1992. Plutonism in the central part of the Sierra Nevada batholith, California. U.S. Geological Survey Professional Paper 1483, 186 p.

Beaumont, C. 1981. Foreland basins. Geophysical Journal Royal Astronomical Society, **65**: 291-329.

Beckinsale, R.D., and Gale, N.H. 1969. A reappraisal of the decay-constants and branching ratio of 40K. Earth and Planetary Science Letters, **6**: 289-294.

Bloch, J., Schröder-Adams, C., Leckie, D.A., McIntyre, D.J., Craig, J., and Staniland, M. 1993. Revised stratigraphy of the lower Colorado Group (Albian to Turonian), Western Canada. Bulletin of Canadian Petroleum Geology, **41**: 325-348.

Bowring, S.A., and Schmitz, M.D. 2003. High-Precision U-Pb Zircon Geochronology and the Stratigraphic Record. Reviews in Mineralogy & Geochemistry, **53**: 305-326.

Bowring, S.A., Erwin, D., Parrish, R., and Renne, P. 2005. EARTHTIME: A community-based effort towards high-precision calibration of earth history. Goldschmidt Conference Abstracts 2005, A316.

Branca, S., and Del Carlo, P. 2005. Types of eruptions of Etna Volcano AD 1670-2003: implications for short-term eruptive behavior. Bulletin of Volcanology, **67**: 732-742.

Cadrin, A.A.J., Kyser, T.K., Caldwell, W.G.E., and Longstaffe, F.J. 1995. Isotopic and chemical compositions of bentonites as paleoenvironmental indicators of the Cretaceous Western Interior Seaway. Palaeogeography, Palaeoclimatology, Pataeoecology, **119**: 301-320.

Cameron, A.E., Smith, D.E., and Walker, R.L. 1969. Mass spectrometry of nanogram size samples of lead. Analytical Chemistry, **41**: 525-526.

Carey, S.N., and Sigurdsson, H. 1982. Influence of particle aggregation of deposition of distal tephra from the May 18, 1980, eruption of Mount St. Helens volcano. Journal of Geophysical Research, **87**: 7061-7072.

Cherniak, D.J., and Watson, E.B. 2000. Pb diffusion in zircon. Chemical Geology, **172:** 5-24.

Cobban, W.A., and Scott, G.R. 1972. Stratigraphy and ammonite fauna of the Graneros Shale and Greenhorn Limestone near Pueblo, Colorado. United States Geological Survey, Professional Paper 645, 108 p.

Cobban, W.A., and Hook, S.C. 1980. Occurrence of Ostrea beloiti Logan in Cenomanian rocks of Trans-Pecos, Texas. *In* New Mexico Geological Society Guidebook, 31st Field Conf., Trans-Pecos Region. pp. 169-172.

Cobban, W.A., Merewether, E.A., Fouch, T.D., and Obradovich, J.D. 1994. Some Cretaceous shorelines in the western interior of the United States. *In* Mesozoic systems of the Rocky Mountain region, U.S.A. *Edited by* M.V. Caputo, J.A. Peterson, and K.J. Franczyk. Denver, Colorado, Rocky Mountain Section SEPM, pp. 393–414.

Cobban, W.A., Walaszczyk, I., Obradovich, J.D., and McKinney, K.C. 2006. A USGS Zonal Table for the Upper Cretaceous Middle Cenomanian-Maastrichtian of the Western Interior of the United States Based on Ammonites, Inoceramids, and Radiometric Ages. United States Geological Survey, Open File Report 2006-1250, 45 p.

Coney, P.J., and Reynolds, S.J. 1977. Cordilleran Benioff zones. Nature, **270**: 403–406.

Crowley, J.L., Schoene, B., and Bowring, S.A. 2007. U-Pb dating of zircon in the Bishop Tuff at the millennial scale. Geology, **35**: 1123-1126.

Dalrymple, G.B. 1979. Critical tables for conversion of K-Ar ages from old to new constants. Geology, **7**: 558-560.

Davis, D.W., Williams, I.S., and Krogh, T.E. 2003. Historical development in zircon geochronology. Reviews in Mineralogy and Geochemistry, **53**: 145-181.

DeCelles, P.G. 2004. Late Jurassic to Eocene evolution of the Cordilleran thrust belt and foreland Basin system, western USA. American Journal of Science, **304**: 105-168.

DeCelles, P.G., and Currie, B.S. 1996. Long-term sediment accumulation in the Middle Jurassic-early Eocene Cordilleran retroarc foreland basin system. Geology, **24**: 591–594.

Elder, W.P. 1988. Geometry of Upper Cretaceous bentonite beds: Implications about volcanic source areas and paleowind patterns, Western Interior, United States. Geology, **16**: 835-838.

Engebretson, D.C., Cox, A., and Thompson, G.A. 1984. Correlation of plate motions with continental tectonics: Laramide to Basin-Range. Tectonics, **3**: 115–119.

Engebretson, D.C., Cox, A., and Gordon, R.G. 1985. Relative motions between oceanic and continental plates in the Pacific basin. Geological Society of America, Special Paper 206, 59 p.

Ernst, G.G.J., Davis, J.P., and Sparks, R.S.G. 1994. Bifurcation of volcanic plumes in a crosswind. Bulletin of Volcanology, **56**: 159-169.

Faure, G. and Teresa, M. 2005. Isotopes Principles and Applications: Third Edition. Hoboken, John Wiley & Sons, Inc., 928 p.

Fisons PLC. 1992. Micromass *Sector 54* System User's Guide. UK Limited.

Foster, D.A., and Fanning, C.M. 1997. Geochronology of the northern Idaho batholiths and the Bitterroot metamorphic core complex: Magmatism preceding and contemporaneous with extension. GSA Bulletin, **109**: 379-394.

Gerstenberger, H., and Haase, G. 1997. A highly effective emitter substance for mass spectrometric Pb isotope ratio determinations. Chemical Geology, **136**: 309-312.

Gilboy, C.F. 1988. Geology and Natural Gas Production of the Upper Cretaceous Second White-Speckled Shale, Southwestern Saskatchewan. *In* Summary of investigations 1988. Saskatchewan Geological Survey, Saskatchewan Energy and Mines, Miscellaneous. Report 88-4, pp. 183-195.

Gradstein, F.M., Agterberg, F.P., Ogg, J.G., Hardenbol, J., and Backstrom, S. 1999. On the Cretaceous time scale. Neues Jahrbuch fur Geologie und Palaontologie, Abhandlungen, **212**: 1-14.

Gurnis, M. 1992. Rapid continental subsidence following the initiation and evolution of subduction. Science, **255**: 1556–1558.

Hamilton, W., and Myers, W.B. 1967. The nature of batholiths. U.S. Geological Survey Professional Paper 544C, 30 p.

Hardy, S., Duncan, C., Masek, J., and Brown, D. 1998. Minimum work, fault activity and the growth of critical wedges in fold and thrust belts. Basin Research, **10**: 365-373.

Hattin, D.E. 1965. Stratigraphy of the Graneros Shale (Upper Cretaceous) in Central Kansas. State Geological Survey of Kansas Bulletin 178, 83 p.

Hattin, D.E. 1975. Stratigraphy and depositional environment of Greenhorn Limestone (Upper Cretaceous) of Kansas. State Geological Survey of Kansas Bulletin 209, 128 p.

Hay, M.J. 2006. Stratigraphy, Sedimentology, and Paleogeography of the upper Dunvegan FM. Middle-Cenomanian, Alberta, Canada: Interactions Between Deltaic Sedimentation, Flexural Tectonics and Eustacy. Unpublished M.Sc. thesis, The University of Western Ontario, London, Ontario, 197 p.

Hay, M.J., and Plint, A.G. 2009. An allostratigraphic framework for a retrogradational delta complex: the uppermost Dunvegan Formation (Cenomanian) in subsurface and outcrop, Alberta and British Columbia. Bulletin of Canadian Petrolium Geology, **57**: *In Press.*

Hill, B.E., Connor, C.B., Jarzemba, M.S., La Femina, P.C., Navarro, M., and Strauch, W. 1998. 1995 eruptions of Cerro Negro volcano, Nicaragua, and risk assessment for future eruptions. Geological Society of America Bulletin, **110**: 1231-1241.

Hoshkin, P.W.O., and Schaltegger, U. 2003. The composition of zircon and igneous and metamorphic petrogenesis. Reviews in Mineralogy & Geochemistry, **53**: 27-62.

Hyndman, D.W. 1983. The Idaho batholith and associated plutons, Idaho and western Montana. Geological Society of America Memoir, **159**: 213–140.

Jaffey, A.H., Flynn, K.F., Glendenin, L.E., Bently, W.C., and Essling, A.M. 1971. Precision measurements of half-lives and specific activities of 235U and 238U. Physical Review C, **4**: 1889-1906.

Jordan, T.E. 1981. Thrust loads and foreland basin evolution, Cretaceous western united States. American Association of Petroleum Geologists Bulletin, **65**: 2506-2520.

Kauffman, E.G. 1977. Geological and biological overview: Western Interior Cretaceous basin. Mountain Geologist, **14**: 75-99.

Kauffman, E.G. 1984. Paleobiogeography and evolutionary response dynamic in the Cretaceous Western Interior seaway on North America. *In* Jurassic-Cretaceous biochronology of North America. *Edited by* G.E.G. Westermann. Geological Association of Canada, Special Paper 27, pp. 273-306.

Kauffman, E.G., and Caldwell, W.G.E. 1993. The Western Interior Basin in space and time. *In* Evolution of the Western Interior Basin. *Edited by* W.G.E. Caldwell, and E.G. Kauffman. Geological Association of Canada Special Paper 39, pp. 1–30.

Kauffman, E.G., Sageman, B.B., Kirkland, J.I., Elder, W.P., Harries, P.J., and Villamil, T. 1993. Molluscan biostratigraphy of the Cretaceous Western Interior Basin, North America. Geological Association of Canada Special Paper, **39**: 397-435.

Kennedy, W.J. 1984. Ammonite faunas and the 'standard zones' of the Cenomanian to Maastrichtian stages in their type areas, with some proposals for the definition of the stage boundaries by ammonites. Bulletin of the Geological Society of Denmark, **33**: 147-161.

Kennedy, W.J., and Cobban, W.A. 1991. Stratigraphy and interregional correlation of the Cenomanian/Turonian transition in the Western Interior of the United States near Pueblo, Colorado, a potential boundary stratotype for the base of the Turonian stage. Newsletters on Stratigraphy, **24**: 1-33.

Kennedy, W.J., Walaszczyk, I., and Cobban, W.A. 2005. The Global Boundary Stratotype Section and Point for the base of the Turonian Stage of the Cretaceous: Pueblo, Colorado, U.S.A. Episodes, **28:** 93-104.

Kerr, A.C. 1998. Oceanic plateau formation: A cause of mass extinction and black shale deposition around the Cenomanian/Turonian boundary?. Geological Society of London Journal, **155**: 619–626.

Knechtel, M.M., and Patterson, S.H. 1956. Bentonite deposits in marine Cretaceous formations, Hardin District, Montana and Wyoming. U.S. Geological Survey Bulletin 1023, 116 p.

Knight, W.D. 1898. Mineral Soap. Engineering Mining Journal, **66**: 481.

Kowallis, B.J., Christiansen, E.H., Deino, A.L., Kunk, M.J., and Heaman, L.M. 1995. Age of the Cenomanian/Turonian boundary in the Western Interior of the United States. Cretaceous Research, **16**: 109-129.

Kreitner, M.A., and Plint, A.G. 2006. Allostratigraphy and paleogeography of the Upper Cenomanian, Lower Kaskapau Formation in subsurface and outcrop, Alberta and British Columbia. Bulletin of Canadian Petroleum Geology, **54**: 110-137.

Krogh, T.E. 1973. A low contamination method for the hydrothermal decomposition of zircon and extraction of U and Pb for isotopic age determinations. Geochim Cosmochim Acta, **37**: 485-494.

Krogh, T.E. 1982. Improved accuracy of U-Pb zircon ages by the creation of more concordant systems using an air abrasion technique. Geochim Cosmochim Acta, **46**: 637-649.

Krogh, T.E. 1994. Identification of concordant zircons using etch techniques. Abstract for the Eighth International Conference for Geochronology and Cosmochronologic Isotope Geology, US Geological Survey Circular, **1107**: 180.

Krogh, T.E., and Davis, G.L. 1975. The production and preparation of 205Pb for use as a tracer for isotope dilution analyses. Carnegie Institution of Washington Yrbk 1974, pp. 416-417.

Kuhnt, W., Nederbragt, A.J., and Leine, L. 1997. Cyclicity of Cenomanian/Turonian organic-carbon–rich sediments in the Tarfaya Atlantic coastal basin (Morocco). Cretaceous Research, **18**: 587–601.

Lanphere, M.A., and Baadsgaard, H. 2001. Precise K-Ar, 40Ar/39Ar, Rb-Sr, and U/Pb mineral ages from the 27.5 Ma Fish Canyon Tuff reference standard. Chemical Geology, **175**: 653-671.

Leckie, D.A., Schröder-Adams, C.J., and Bloch, J. 2000. The effect of paleotopography on the late Albian and Cenomanian sea-level record of the Canadian Cretaceous interior seaway. GSA Bulletin, **112**: 1179-1198.

Ludwig, K.R. 1992. *Isoplot* A Plotting and Regression Program for Radiogenic-Isotopic Data, Version 2.57. USGS Open-File Report, 91-445, 40 p.

Ludwig, K.R. 1998. On the treatment of concordant uranium-lead ages. Geochimica et Cosmochimica Acta, **62**: 665-676.

Ludwig, K.R. 2000. Decay-constant errors in U-Pb Concordia-intercept ages. Chemical Geology, **166**: 315-318.

Ludwig, K.R. 2003. *Isoplot* 3.0, A Geochronological Toolkit for Microsoft Excel. Berkely Geochronology Center, Special Publication No. 4, 71 p.

Mattinson, J.M. 1972. Preparation of hydrofluoric, hydrochloric, and nitric acids at ultra-low lead levels. Analytical Chemistry, **44**: 1715-1716.

Mattinson, J.M. 1994. A study of complex discordance in zircons using step-wise dissolution techniques. Contributions to Mineralogy and Petrology, **116**: 117-129.

McGookey, D.P., Haun, J.D., McCubbin, D.G., Hale, L.A., Weimer, R.J., Goodell, H.G., and Wulf, G.R. 1972. Cretaceous System. *In* Geologic atlas of the Rocky Mountain region. *Edited by* W.W Mallory. Denver, Rocky Mountain Association of Geologists, pp. 190–228.

McNeil, D.H., and Caldwell, W.G.E. 1974. The Ostrea beloiti beds – a Cenomanian time-stratigraphic unit in the Western Interior of Canada and the United States. *In* Geological Society of America General Meeting. Geological Society of America, Abstracts with Programs, **6:** 867.

McNeil, D.H., and Caldwell, W.G.E. 1981. Cretaceous rocks and their foraminifera in the Manitoba Escarpment. Geological Association of Canada, Special Paper 21, 439 p.

Meyers, S.R., and Sageman, B.B. 2004. Detection, quantification, and significance of hiatuses in pelagic and hemipelagic strata. Earth and Planetary Science Letters, **224:** 55-72.

Milankovitch, M. 1941. Kanon der Erdbestrahlung und seine Anwendung auf das Eiszeitproblem. Belgrade, Serbian Academy of Science, **133**: 633 p.

Min, K., Mundil, R., Renne, P.R., and Ludwig, K.R. 2000. A test for systematic errors in 40Ar/39Ar geochronology through comparison with U/Pb analysis of a 1.1-Ga rhyolite. Geochimica et Cosmochimica Acta, **64**: 73-98.

Mitrovica, J.X., Beaumont, C., and Jarvis, G.T. 1989. Tilting of continental interiors by the dynamical effects of subduction. Tectonics, **8**: 1079–1094.

Miyashiro, A. 1974. Volcanic rock series in island arcs and active continental margins. American Journal of Science, **174**: 321-355.

Monger, J.W.H. 1989. Review of Cordilleran geology. *In* Western Canada Sedimentary Basin: A case history. *Edited by* B.D. Ricketts. Calgary, Canadian Society of Petroleum Geologists, pp. 9-32.

Monger, J.W.H., and Price, R.A. 1979. Geodynamic evolution of the Canadian Cordillera–progress and Problems. Canadian Journal of Earth Science, **16**: 770–791.

Monger, J.W.H., Price, R.A., and Templeman-Kluit, D.J. 1982. Tectonic accretion and the origin of two major metamorphic and plutonic welts in the Canadian Cordillera. Geology, **10**: 70-75.

Mortensen, J.K., Hart, C.J.R., Murphy, D.C., and Heffernan, S. 2000. Temporal evolution of Early and mid-Cretaceous magmatism in the Tintina gold belt. *In* The Tintina gold belt: Concepts, exploration and discoveries. Vancouver, British Columbia and Yukon Chamber of Mines. *Edited by* T. Tucker, and M. Smith. Cordilleran Roundup, Special Volume 2, pp. 49–57.

Nier, A. 1940. A mass spectrometer for routine isotope abundance measurements. Review of Scientific Instruments, **11**: 212-216.

O'Connel, S.C., Dix, G.R., and Barclay, J.E. 1990. The origin, history and regional structural development of the Peace River Arch, Western Canada. Bulletin of Canadian Petroleum Geology, **38**: 4-24.

Oberli, F., Fischer, H., and Meier, M. 1990. High-resolution 238U-206Pb zircon dating of Tertiary bentonites and the Fish Canyon Tuff: a test for age "concordance" by single-crystal analysis. Seventh International Conference on Geolchronology, Cosmochronology and Isotope Geology. Geological Society of Australia Special Publication Canberra 27, 74.

Obradovich, J.D. 1993. A Cretaceous Time Scale. *In* Evolution of the Western Interior Basin. *Edited by* W.G.E. Caldwell, and E.G. Kauffman. Geological Association of Canada, Special Paper 39, pp. 379-396.

Obradovich, J.D., and Cobban, W.A. 1975. A time-scale for the Late Cretaceous of the Western Interior of North America. *In* The Cretaceous System in the Western Interior of North America. *Edited by* W.G.E. Caldwell. Geological Association of Canada, Special Paper 13, pp. 31-54.

Ogg, J.G., Agterberg, F.P., and Gradstein, F.M. 2005. The Cretaceous Period. *In* The Geologic Time Scale 2004. *Edited by* F. Gradstein, J. Ogg, and A. Smith. New York, Cambridge University Press, pp. 344-383.

Parrish, R.R., and Krogh, T.E. 1987. Synthesis and purification of 205Pb for U-Pb for geochronology. Chemical Geology, **66**: 103-110.

Parrish, R.R., and Noble, S.R. 2003. Zircon U-Th-Pb Geochronology by Isotope Dilution – Thermal Ionization Mass Spectrometry (ID-TIMS). Reviews in Mineralogy & Geochemistry, **53**: 183-213.

Parrish, R.R., Bowring, S.A., Condon, D.J., Schoene, B., Crowley, J.L., and Ramezani, J. 2006. EARTHTIME U-Pb tracer for community use. Goldschmidt Conference Abstracts 2006, A473.

Pearce, N.J.G., Westgate, J.A., Perkins, W.T., and Preece, S.J. 2004. The application of ICP-MS methods to tephrochronological problems. Applied Geochemistry, **19**: 289-322.

Plint, A.G. 1996. Marine and nonmarine systems tracts in fourth order sequences in the Early-Middle Cenomanian, Dunvegan Alloformation, northeastern British Columbia, Canada. Geological Society of London, Special Paper 104, pp.159-191.

Plint, A.G. 2000. Sequence stratigraphy and paleogeography of a Cenomanian deltaic complex: the Dunvegan and lower Kaskapau formations in subsurface and outcrop, Alberta and British Columbia, Canada. Bulletin of Canadian Petroleum Geology, **48**: 43-79.

Plint, A.G. 2002. Paleovalley systems in the Upper Cretaceous Dunvegan Formation, Alberta and British Columbia. Bulletin of Canadian Petroleum Geology, **50**: 277-296.

Plint, A.G. 2003. Clastic Sediment Partitioning in a Cretaceous Delta System, Western Canada: Responses to Tectonic and Sea-Level Controls. Geologia Croatica, **56**: 39-68.

Plint, A.G., Tyagi, A., Hay, M.J., Varban, B.L., Zhang, H., and Roca. X. 2009. Clinoforms, Paleobathymetry, and Mud Dispersal Across the Western Canada Cretaceous Foreland Basin: Evidence From the Cenomanian Dunvegan Formation and Contiguous Strata. Journal of Sedimentary Research, **79**.

Price, R.A. 1973. Large-scale gravitational flow of supracrustal rocks, southern Canadian Cordillera. *In* Gravity and tectonics. *Edited by* K.A. De Jong, and R. Scholten. New York, John Wiley and Sons, pp. 491-502.

Prokoph, A., Villeneuve, M., Agterberg, F.P., and Rachold, V. 2001. Geochronology and calibration of global Milankovitch cyclicity at the Cenomanian/Turonian boundary. Geology, **29**: 523-526.

Reid, M.R., and Coath, C.D. 2000. In situ U-Pb ages of zircons from the Bishop Tuff: No evidence for long crystal residence times. Geology, **28**: 443-446.

Reid, M.R., Coath, C.D., Harrison, T.M., and McKeegan, K.D. 1997. Prolonged residence times for the youngest rhyolites associated with Long Valley Caldera: 230Th-238U ion microprobe dating of young zircons. Earth and Planetary Science Letters, **150**: 27-39.

Renne, P.R. 2000. 40Ar/39Ar age of plagioclase from Acapulco meteorite and the problem of systematic errors in cosmochronology. Earth and Planetary Science Letters, **175**: 13–26.

Renne, P.R., Deino, A.L., Walter, R.C., Turrin, B.D., Swisher, C.C. III, Becker, T.A., Curtis, G.H., Sharp, W.D., and Jaouni, A.R. 1994. Intercalibration of astronomical and radioisotopic time. Geology, **22**: 783-786.

Renne, P.R., Swisher, C.C. III, Deino, A.L., Karner, D.B., Owens, T.L., and DePaolo, D.J. 1998. Intercalibration of standards, absolute ages and uncertainties in 40Ar/39Ar dating. Chemical Geology, **145**: 117–152.

Renne, P.R, Mundil, R., Min, K., and Ludwig, K.R. 1999. Progress report on high resolution comparison of argon/argon and uranium/lead systems. 9th annual Goldschmidt Conference Vol. LPI Contribution No. 971, pp. 243-244.

Ridgley, J.L., McNeil, D.H., Gilboy, C.F., Condon, S.M., and Obradovich, J.D. 2001. Structural and Stratigraphic Controls on Sites of Shallow Biogenic Gas Accumulations in the Upper Cretaceous Belle Fourche and Second White Specks-Greenhorn Formations of Southern Alberta, Saskatchewan and Northern Montana. *In* Gas in the Rockies. *Edited by* D. Anderson. Denver, Rocky Mountain Association of Geologists, pp. 241-270.

Roca, X., Rylaarsdam, J.R., Zhang, H., Varban, B.L., Sisulak, C.F., Bastedo, K., and Plint, A.G. 2008. An allostratigraphic correlation of Lower Colorado Group (Albian) and equivalent strata in Alberta and British Colombia, and Cenomanian rocks of the Upper Colorado Group in southern Alberta. Bulletin of Canadian Petroleum Geology, **56:** 259-299.

Roddick, J.C., Loveridge, W.D., and Parrish, R.R. 1987. Precise U/Pb dating of zircon of the sub-nanogram Pb Level. Chemical Geology, **66**: 111-121.

Sageman, B.B., Rich, J., Arthur, M.A., Birchfield, G.E., and Dean, W.E. 1997. Evidence for Milankovitch periodicities in Cenomanian/Turonian lithologic and geochemical cycles, Western Interior USA. Journal of Sedimentary Research, **67**: 286–302.

Sarna-Wojcicki, A.M., Pringle, M.S., and Wijbrans, J. 2000. New 40Ar/39Ar age of the Bishop Tuff from multiple sites and sediment rate calibration for the Matuyama-Brunhes boundary. Journal of Geophysical Research, **105**: 21431-21443.

Schmitz, M.D., and Bowring, S.A. 2001a. U-Pb zircon and titanite systematic of the Fish Canyon Tuff: an assessment of high-precision U-Pb geochronology and its application to young volcanic rocks. Geochimica et Cosmochimica Acta, **65**: 2571-2587.

Schmitz, M.D., and Bowring, S.A. 2001b. The significance of U-Pb zircon dates in lower crustal xenoliths from the southwestern margin of the Kaapvaal craton, southern Africa. Chemical Geology, **172**: 59-76.

Schröder-Adams, C.J., Leckie, D.A., Bloch, J., Craig, J., McIntyre, D.J., and Adams, P.J. 1996. Paleoenvironmental changes in the Cretaceous (Albian to Turonian) Colorado Group of western Canada: microfossil, sedimentological and geochemical evidence. Cretaceous Research, **17**: 311-365.

Scoates, J.S., and Chamberlain, K.R. 1995. Baddeleyite (ZrO2) and zircon (ZrSiO4) from anorthositic rocks of the Laramie anorthosite complex, Wyoming: petrologic consequences and U-Pb ages. American Mineralogist, **80**: 1317-1327.

Scollo, S., Del Carlo, P., and Coltelli, M. 2007. Tephra fallout of 2001 Etna flank eruption: Analysis of the deposit and plume dispersion. Journal of Volcanology and Geothermal research, **160**: 147-164.

Shuster, R.D., and Bickford, M.E. 1985. Chemical and isotopic evidence for the petrogenesis of the northeastern Idaho batholiths. Journal of Geology, **93**: 727-742.

Simon, J.I., Renne, P.R., and Mundil, R. 2008. Implications of pre-eruptive magmatic histories of zircons for U-Pb geochronology of silicic extrustions. Earth and Planetary Science Letters, **266**: 182-194.

Slaughter, M., and Early, J.W. 1965. Mineralogy and geological significance of the Mowry bentonites, Wyoming. Geological Society of America Special paper 83, 116 p.

Sparks, R.S.J., Bursik, M.I., Carey, S.N., Gilbert, J.S., Glaze, L.S., Sigurdsson, H., and Woods, A.W. 1997. Volcanic Plumes. Chichester, John Wiley & Sons, 485 p.

Steiger, R.H., and Jäger. 1977. Subcommission on Geochronology: Convention on the use of decay-constants in geo- and cosmochronology. Earth Planet Sci Lett, **36**: 359-362.

Stott, D.F. 1963. The Cretaceous Alberta Group and equivalent rocks, Rocky Mountain Foothills, Alberta. Geological Survey of Canada, Memoir, **317:** 306 p.

Stott, D.F. 1991. Geotectonic correlation chart, Prairie Provinces and British Columbia. *In* Sedimentary cover of the North American Craton: Canada. *Edited by* D.F. Stott, and J.D. Aitken. Geological Survey of Canada, Geology of Canada, no. 5, wall chart Sheet 2. Studies in Geophysics, National Academy Press, Washington, D.C.

Tilton, G.R., Patterson, C., Brown, H., Inghram, M., Hayden, R., Hess, D., and Larsen. Jr. E. 1955. Isotopic composition and distribution of lead, uranium, and thorium in a Precambrian granite. Geological Society of America Bulletin, **66**: 1131-1148.

Tilton, G.R., Davis, G.L., Wetherill, G.W., and Aldrich, L.T. 1957. Isotopic ages of zircon from granites and pegmatites. EOS Trans, American Geophysical Union, **38**: 360-371.

Toth, M.I., and Stacey, J.S. 1992. Constraints on the formation of the Bitterroot lobe of the Idaho batholiths, Idaho and Montana, from U-Pb zircon geolochronology and feldspar Pb isotopic data. USGS Bulletin 2008, 14 p.

Turgeon, S.A. and Creaser, R.A. 2008. Cretaceous oceanic anoxic event 2 triggered by a massive magmatic episode. Nature, **454**: 323-327.

Tyagi, A., Plint, A.G., and McNeil, D.H. 2007. Correlation of physical surfaces, bentonites, and biozones in the Cretaceous Colorado Group from the Alberta Foothills to southwest Saskatchewan, and a revision of the Belle Fourche – Second White Specks formational boundary. Canadian Journal of Earth Science, **44**: 871-888.

van der Bogaard, P., and Schirnick, C. 1995. 40Ar/39Ar laster probe ages of Bishop Tuff quartz phenocrysts substantiate ling-lived silicic magma chamber at Long Valley, United States. Geology, **23**: 759-762.

Varban, B.L., and Plint, A.G. 2005. Allostratigraphy of the Kaskapau Formation (Cenomanian/Turonian) in the subsurface and outcrop: NE British Columbia and NW Alberta, Western Canada Foreland Basin. Bulletin of Canadain Petroleum Geology, **53**: 357-389.

Villeneuve, M., Sandeman, H.A., and Davis, W.J. 2000. A method for intercalibration of U-Th-Pb and 40Ar-39Ar ages in the Phanerozoic. Geochimica et Cosmochimica Acta, **64**: 4017-4030.

Walker, G.P.L. 1971. Grain-size characteristics of pyroclastic deposits. Journal of Geology, **79**: 696-714.

Wall, J. 1967. Cretaceous foraminifera of the Rocky Mountain Foothills. Alberta Research Council Bulletin 120, 185 p.

Walsh, S.L., Gradstein, F.M., and Ogg, J.M. 2004. History, philosophy, and application of the Global Stratotype Section and Point (GSSP). Lethaia, **37:** 201-218.

Watson, E.B., and Harrison, T.M. 1983. Zircon saturation revisited: temperature and composition effects in a variety of crustal magma types. Earth and Planetary Science Letters, **64:** 295-304.

Watson, E.B., Cherniak, D.J., Hanchar, J.M., Harrison, T.M., and Wark, D.A. 1997. The incorporation of Pb into zircon. Chemical Geology, **141:** 19-31.

Wetherill, G.W. 1956. Discordant Uranium-Lead Ages, I. Trans Am Geophys Union, **37**: 320-326.

Williams, G.D., and Stelck, C.R. 1975 Speculations on the Cretaceous palaeogeography of North America. *In* The Cretaceous System in the Western Interior of North America. *Edited by* W.G.E. Caldwell. Geological Association of Canada, Special Paper 13, pp. 1-20.

Appendix A. Sample descriptions of the entire suite of bentonites collected from Alberta

Bentonite Name	Location	UofT Sample Name	Sample Weight (Before Slurry)	Notes	Zircon Amount
Bighorn River Bentonite	Ram Falls	07-IB-01A	About 115 g (For first sample); 570 g (second sample)	2 Samples + shale samples from footwall and hanging wall; In Kaskapau	Fairly large amt of zircs (100-200?)
Bighorn River Bentonite	Burnt Timber Creek 01	07-IB-01B	Didn't weigh (first sample); 385 g (Second sample)	2 samples; grey; In Kaskapau	Lots of zircons, we will be able to date this one; 2 sample boxes (Sandra's & Ivan's); Sandras: Fairly large amt (100-200 grains?)
B-Bentonite	Cottonwood Canyon	07-IB-02	180 g	Equivalent to Red Bentonite; In Kaskapau; Hard Sample; Lost sample in disk mill	Few zircons, maybe 2 dozen? (12-20 grains)
X-Bentonite	Burnt Timber Creek 03	07-IB-03	1745 g	In Dunvegan	Lots of zircon in sample (400+?)
Green Bentonite	Lynx Creek	07-IB-04	476 g	Top Kaskapuau & Base of Cardium	2 dozen zircons? Low amt of grains (30-40?)
A-X Bentonite	Burnt Timber Creek 01	07-IB-05	115 g	In A-X Unit; brown	Lots of zircons (400+?)
Bentonite In Fish Scales	Cadomin	07-IB-06	430 g	From Fish Scales	Good amt of zirc (a little less than 150ish?)
WC1 Bentonite	Burnt Timber Creek 03	07-IB-07A	68 g	In Westgate; Grey bentonite	Low amt of zircs (30ish?)
WC2 Bentonite	Burnt Timber Creek 03	07-IB-07B	225 g	Possibly same as WC1 Bentonite? In Westgate; Brownish	Low amt of zircs (50ish?)
Bentonite Top Dunvegan Allomember G Upper	Nickerson Creek	07-IB-08A	205 g	From Dunvegan; Some sample lost in MI step (centrifuge tube overflowed)	A good amount of zircs (100ish?)
Un-named	Septimus Creek 01	07-IB-09	200 g	From upper part of Shaftsbury Shale, above IB-06 and below IB-08; 2 cm bentonite 10 m below conglomerate	Not a lot of zirc (50ish?)
Un-named	Wilder Creek 03	07-IB-10	410 g	Same bentonite as IB-09; From upper part of Shaftsbury Shale, above IB-06 and below IB-08; Bentonite 10m below conglomerate; Very red	Some grains are in the big petrie dish (fell out?); fair amt of grains (100-200?)
Un-named	Wilder Creek 04	07-IB-11	250 g	Unknown stratigraphic unit; Bentonite near top of section - Also sampled as 'White Chalcedonic Bed'; peculiar granular bed 1m below top of section	Lots of zircs (200-300?)
Bentonite Base Dunvegan Allomember F (G lower)	Nickerson Creek	07-IB-08B	295 g	From Dunvegan; 3 cm thick bentonite 3 m from top of section; Near the top of the Fish Scales sandstone; Brown	An ok amt of zircs (50-100? Maybe a bit less)
Doe Creek Bentonite	Lynx Creek	07-IB-12	453 g	Possibly X bentonite?	Lots of zirc (400+?)

Appendix B. U-Pb isotopic data for the X-Bentonite, A-X bentonite, Bighorn River Bentonite and Green bentonite

No.	Sample	Weight (mg)	U (ppm)	Th/U	Pbtot (pg)	PbCom (pg)	206Pb/204 measured	207Pb/204 measured	206Pb/238	2 Sig	207Pb/235	2 Sig	207Pb/206	2 Sig	206Pb/238 Age (Ma)	2 Sig	207Pb/235 Age (Ma)	2 Sig	207Pb/206 Age (Ma)	2 Sig	% Disc	Rho Concordia
X BED																						
07IB-03-oldest?																						
sk24p29udt	007IB-03	0.0022	263.3657	0.525816	9.062213	0.805111	708.5747	48.94454	1.50E-02	2.11E-05	9.96E-02	1.91E-03	4.82E-02	8.71E-04	95.81487	0.133745	96.39807	1.765617	110.8503	42.81603	13.66471	0.836504
sk24p30udt	07IB-03	0.0023	176.1036	0.45133	6.2142	0.473066	839.9327	55.37419	1.50E-02	2.84E-05	9.99E-02	1.65E-03	4.83E-02	7.46E-04	95.86038	0.180175	96.64262	1.519211	115.9883	36.49846	17.48266	0.603605
sk24p31udt	07IV-03	0.0017	118.1581	0.409506	3.03959	0.430765	465.1528	36.62721	1.50E-02	5.01E-05	9.69E-02	3.89E-03	4.70E-02	1.78E-03	95.73556	0.317914	93.91338	3.597004	47.87094	90.34002	-100.732	0.71298
sk25p4udt	07IB-03	0.0059	177.5352	0.648459	16.92398	1.951489	533.595	40.35686	1.50E-02	2.68E-05	9.91E-02	2.54E-03	0.047968	1.16E-03	95.90069	0.170028	95.96957	2.344149	97.68166	57.45526	1.836834	0.853084
sk25p5udt	07IB-03	0.0043	224.0659	0.465227	14.82338	0.721523	1299.064	77.02674	1.50E-02	2.10E-05	9.89E-02	9.53E-04	4.79E-02	4.31E-04	95.8068	0.133536	95.75136	0.880496	94.3707	21.23149	-1.5331	0.521703
sk25p6udt	07IB 03	0.022	141.5015	0.483409	48.23453	0.877229	3429.391	179.4865	1.50E-02	2.10E-05	9.93E-02	3.68E-04	4.80E-02	1.50E-04	96.01012	0.133683	96.12277	0.339935	98.91863	7.405913	2.962256	0.566424
AX BED																						
07IB--05																						
sk25p10udt	07IB 05	0.0048	213.0137	0.662011	16.52707	0.533248	1854.103	103.2728	1.49E-02	1.47E-05	9.83E-02	5.07E-04	4.77E-02	2.27E-04	95.63196	9.32E-02	95.20724	0.468683	84.58007	11.265	-13.164	0.492903
sk25p11udt	07OB 05	0.0047	255.9304	0.377123	18.02262	0.613212	1895.066	105.3015	1.49E-02	2.26E-05	9.83E-02	4.05E-04	4.77E-02	1.67E-04	95.57253	0.143749	95.21709	0.374079	86.32273	8.305678	-10.795	0.559337
sk25p12udt	07IB 05	0.0028	208.6031	0.684579	9.448	0.659048	863.9126	54.28121	1.49E-02	2.45E-05	9.38E-02	8.35E-04	4.57E-02	3.76E-04	95.30983	0.155905	91.05208	0.775066	1.06E-11	4.05E-07	-10.795	0.491929
sk25p13udt	07IB-05	0.0025	195.7424	0.587383	7.773565	0.304193	1561.084	89.46663	1.50E-02	1.76E-05	9.87E-02	6.72E-04	4.78E-02	3.01E-04	95.79276	0.111732	95.58814	0.621354	90.48574	14.86878	-5.90872	0.519896
sk25p14udt	07IB-05	0.0064	214.5036	0.309847	20.31487	2.07474	655.0162	46.30552	1.50E-02	2.81E-05	9.97E-02	1.17E-03	4.81E-02	5.27E-04	96.1278	0.178155	96.53649	1.083945	106.6442	25.87426	9.934889	0.509106
sk25p15udt	07IB-05	0.0029	153.1691	0.469028	6.830111	0.731228	600.078	43.37612	1.50E-02	3.19E-05	9.83E-02	1.26E-03	4.77E-02	5.67E-04	95.67516	0.202923	95.18261	1.160715	82.85739	28.26131	-15.5848	0.483634
sk25p63	07IB-05	0.006	211	0.44	19.38193	0.547423	2242.261	122.4367	1.50E-02	7.33E-05	9.95E-02	9.41E-04	4.80E-02	3.68E-04	96.26336	0.465738	96.34884	0.868972	98.46525	18.14401	2.252953	0.589
sk25p64	07IB-05	4.40E-03	303.0	0.53	21.00619	0.35741	3619.401	188.5288	1.51E-02	2.14E-05	9.96E-02	6.20E-04	4.80E-02	2.70E-04	96.34935	0.136082	96.40494	0.572549	97.78036	13.30415	1.474465	0.514
sk25p65	07IB-05	4.40E-03	197.0	0.45	14.7425	0.738907	1256.517	88.90483	1.65E-02	3.46E-05	0.134483	1.46E-03	5.91E-02	5.88E-04	105.4593	0.219172	128.1176	1.304349	572.0504	21.63463	82.22556	0.508
sk25p66	07IB-05	4.40E-03	129.0	0.49	8.880149	0.256186	2160.845	120.4275	1.51E-02	4.51E-05	0.101997	8.48E-04	4.89E-02	3.56E-04	96.84623	0.286373	98.61766	0.781064	141.6589	17.07854	31.87216	0.505
BIGHORN BED																						
07IB-01A																						
sk24p25udt	07IB-01A	0.0030	320.1007	0.446841	14.48881	0.732252	1257.586	75.41	1.48E-02	2.63E-05	9.80E-02	1.13E-03	4.82E-02	5.16E-04	94.40665	0.167129	94.96773	1.043957	109.0827	25.29954	13.55275	0.523625
sk24p26udt	07IB-01A	0.0016	298.984	0.700876	7.687676	1.096156	429.4642	35.39797	1.47E-02	4.06E-05	9.75E-02	3.07E-03	4.81E-02	1.43E-03	94.13132	0.258127	94.45187	2.841267	102.5548	70.75716	8.273737	0.703793
sk24p27udt	07IB-01A	0.0014	376.3159	0.537736	8.103834	0.882064	580.4847	42.09502	1.47E-02	3.79E-05	9.53E-02	1.64E-03	4.71E-02	7.57E-04	94.04016	0.240515	92.46289	1.517558	51.95172	38.31012	-81.6075	0.489628
sk25p1udt	07IB-01A	0.0066	307.7235	0.651368	32.29339	0.234102	8209.935	408.7285	1.47E-02	1.47E-05	0.097431	1.84E-04	4.79E-02	6.20E-05	94.32019	0.093182	94.40196	0.17021	96.46865	3.056225	2.243446	0.767854
sk25p2udt	07IB-01A	0.0071	235.2228	0.7391	27.11344	1.08214	1473.43	85.59729	1.47E-02	2.49E-05	9.75E-02	4.89E-04	4.80E-02	2.10E-04	94.18793	0.158252	94.47063	0.452338	101.6145	10.31253	7.362111	0.531169
sk25p3udt		0.0083	223.4597	0.499679	28.41617	0.229029	7681.698	384.2921	1.48E-02	5.39E-05	9.79E-02	3.94E-04	4.81E-02	6.68E-05	~~94.53201~~	~~0.342465~~	94.82669	0.364268	102.2452	3.281068	7.599296	0.939081
GREEN BED																						
sk25p8udt		0.0035	173.2777	7.76E-02	8.074198	0.555983	1027.846	64.62628	1.45E-02	2.74E-05	9.66E-02	9.11E-04	4.85E-02	4.21E-04	92.48688	0.174032	93.64764	0.843368	123.3179	20.39923	25.18087	0.484529

Appendix C: SEM-CL and SE Zircon Images → Bighorn River Bentonite

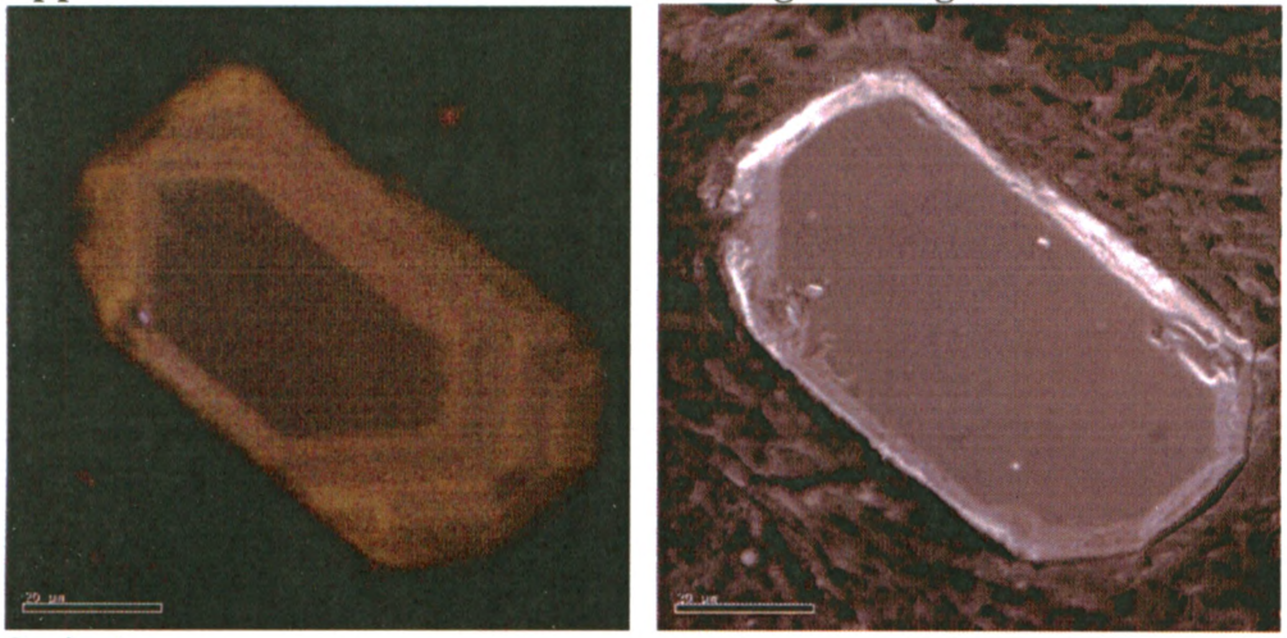

Grain 1

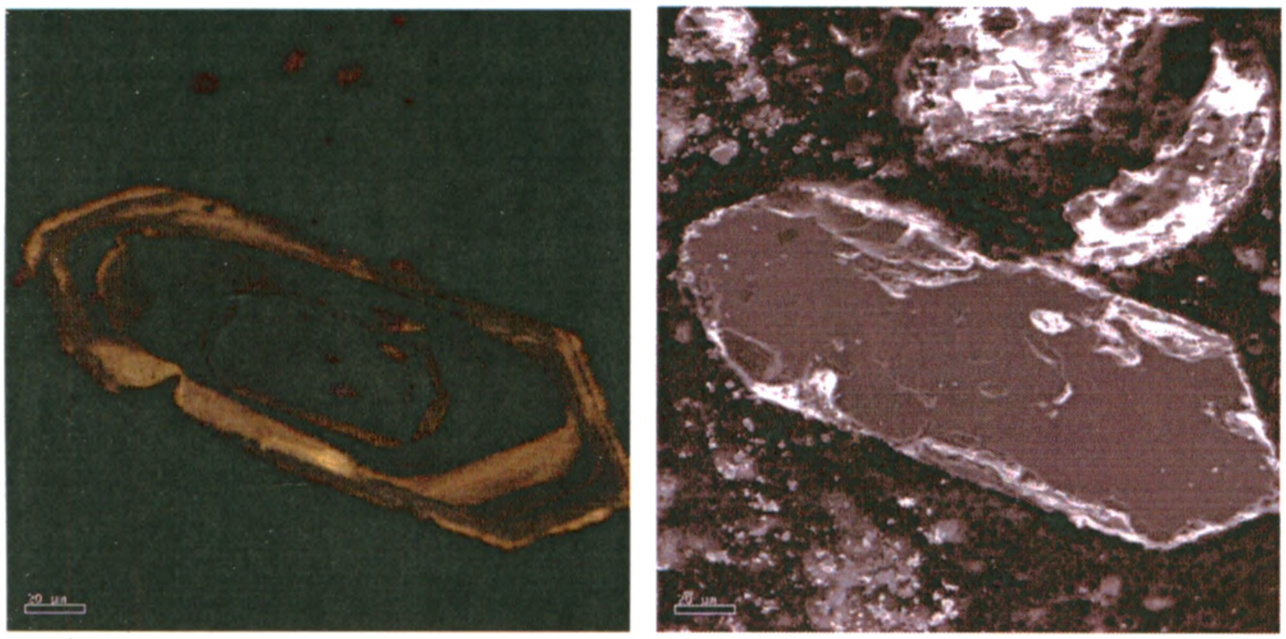

Grain 2

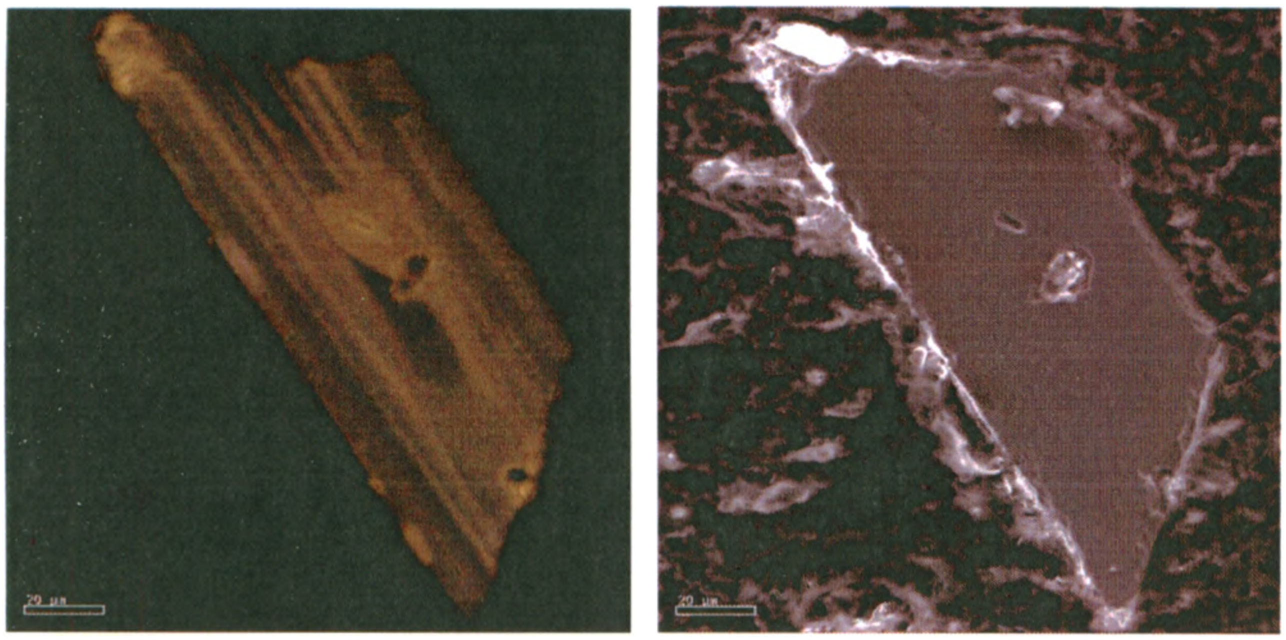

Grain 3

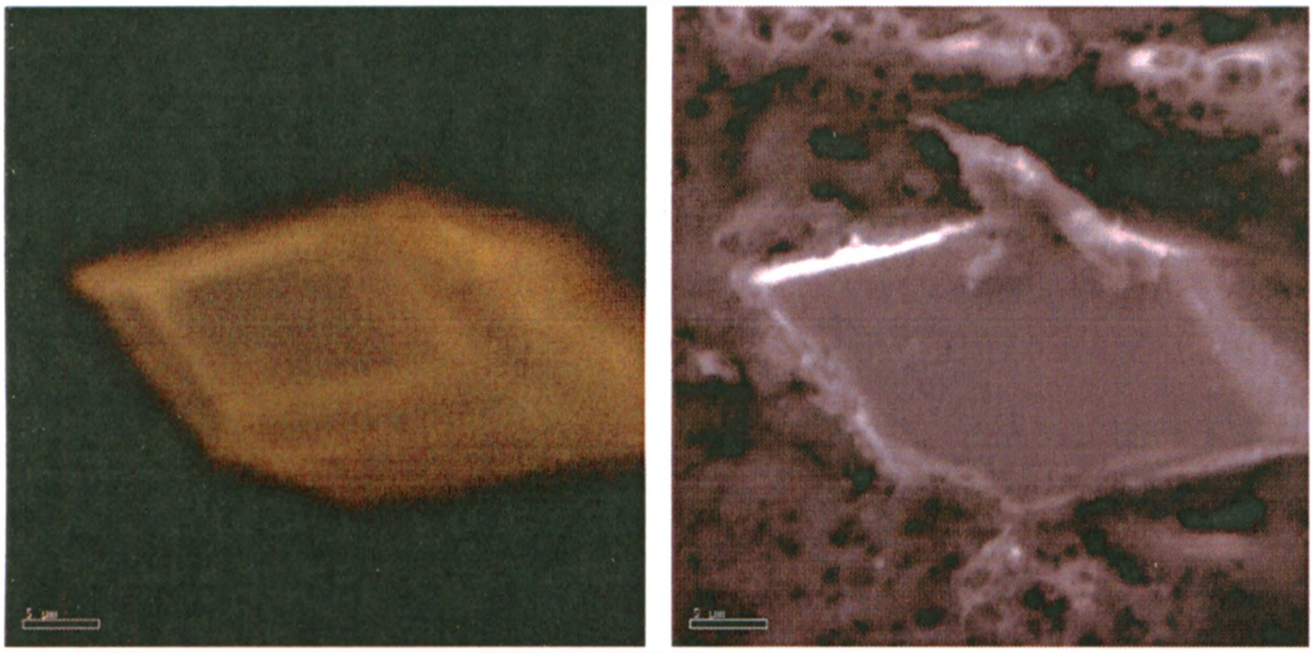

Grain 6

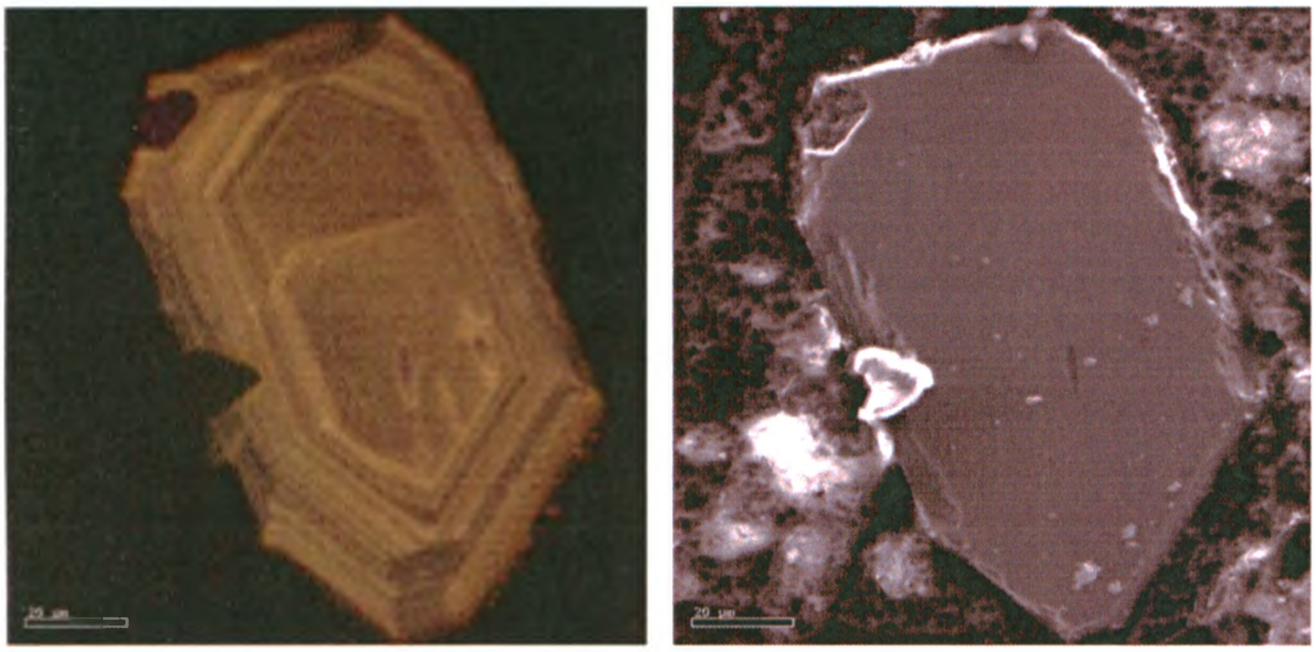

Grain 8

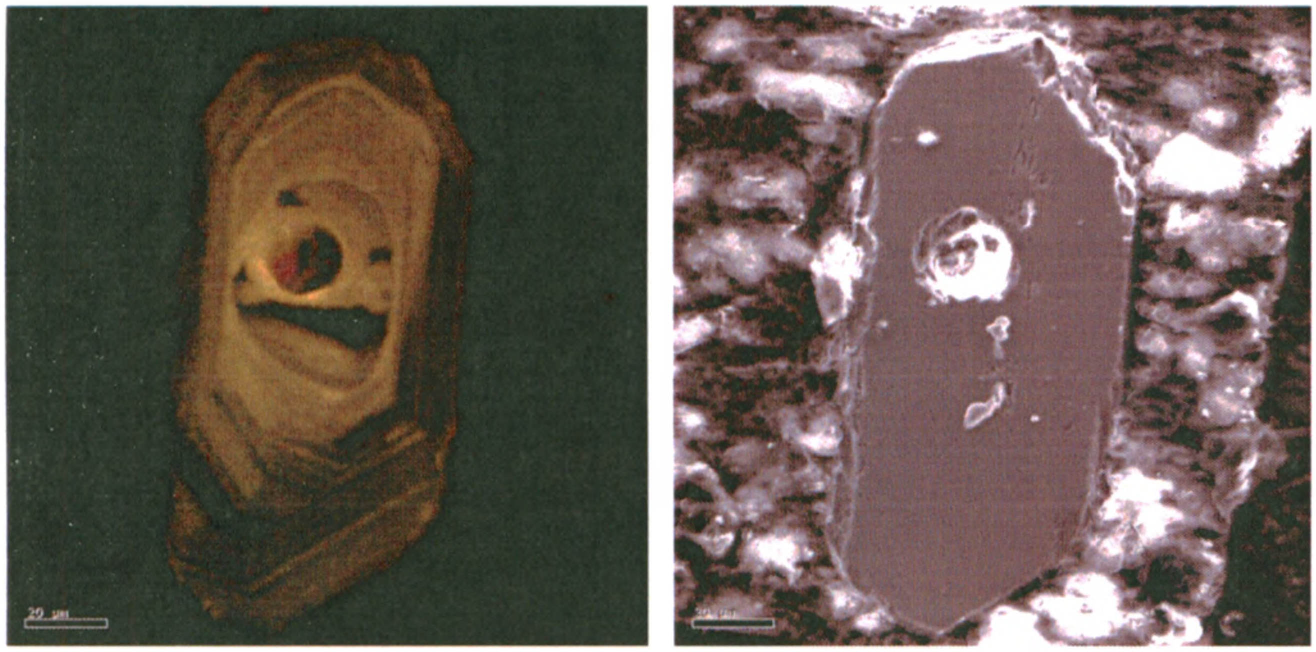

Grain 9

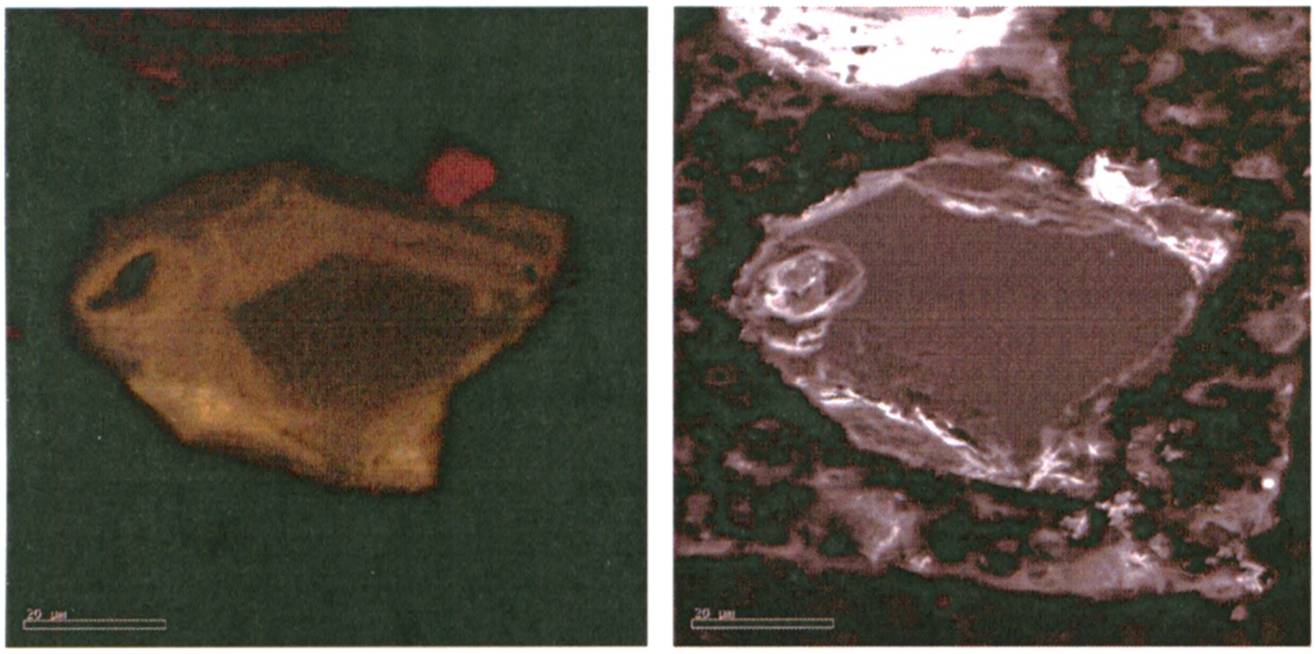

Grain 10

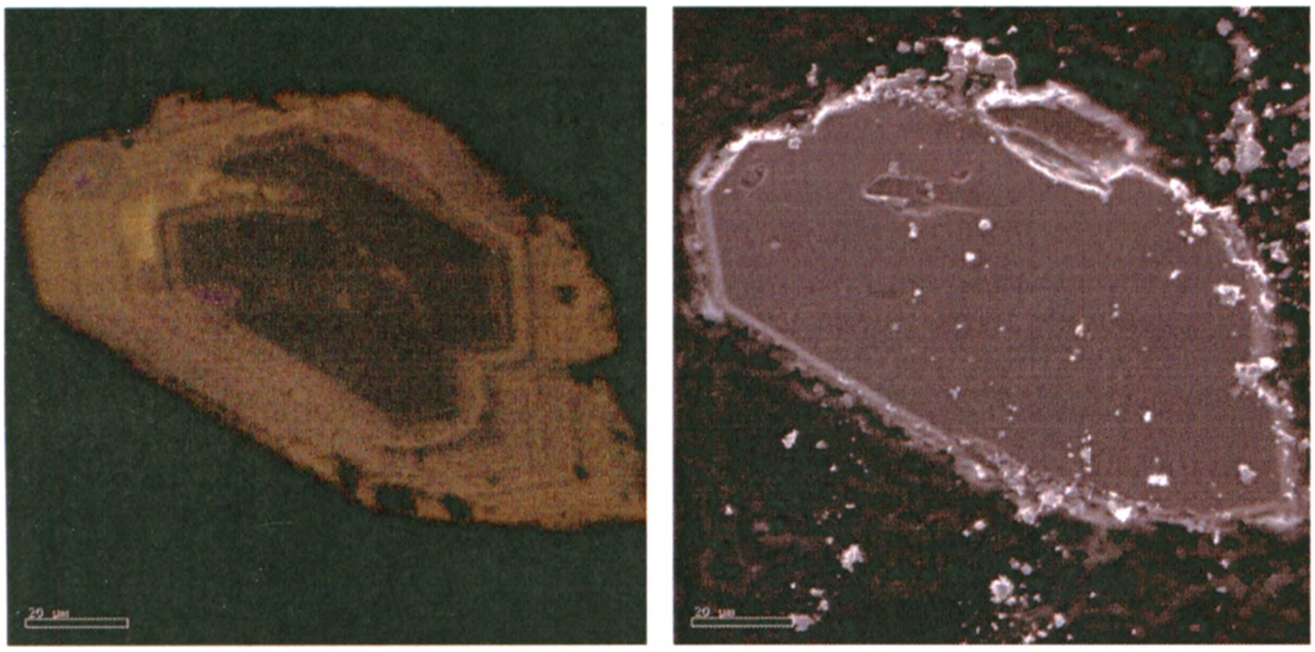

Grain 12

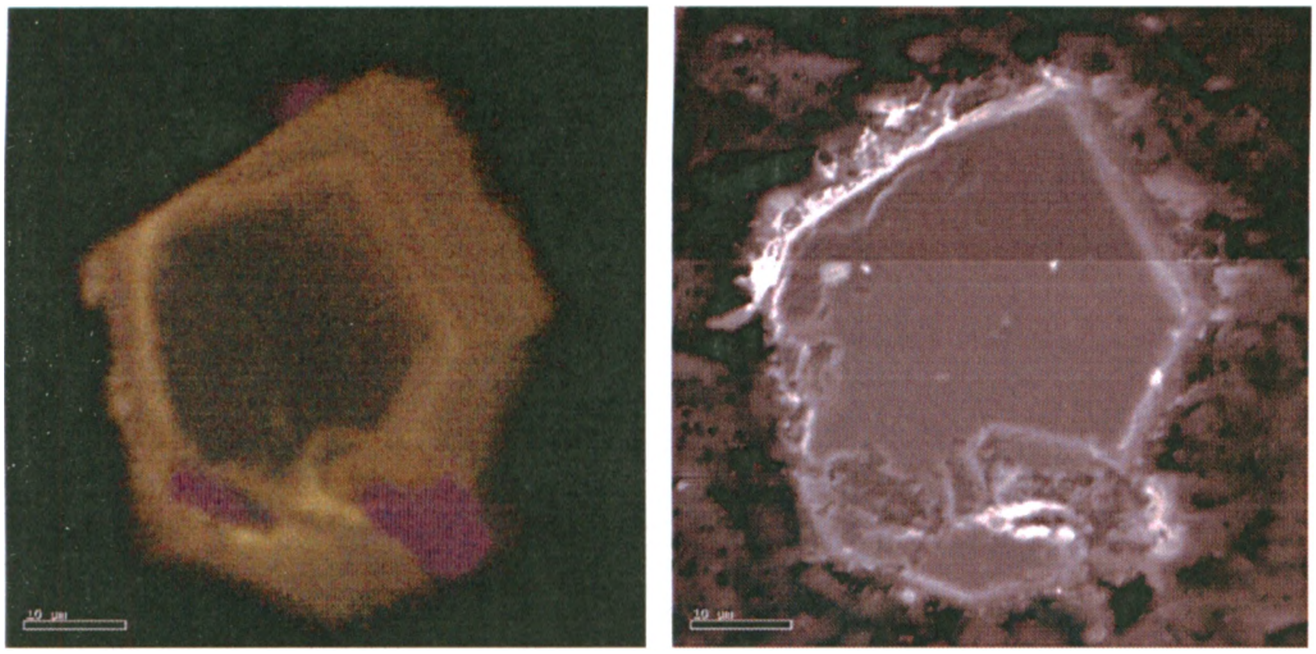

Grain 13

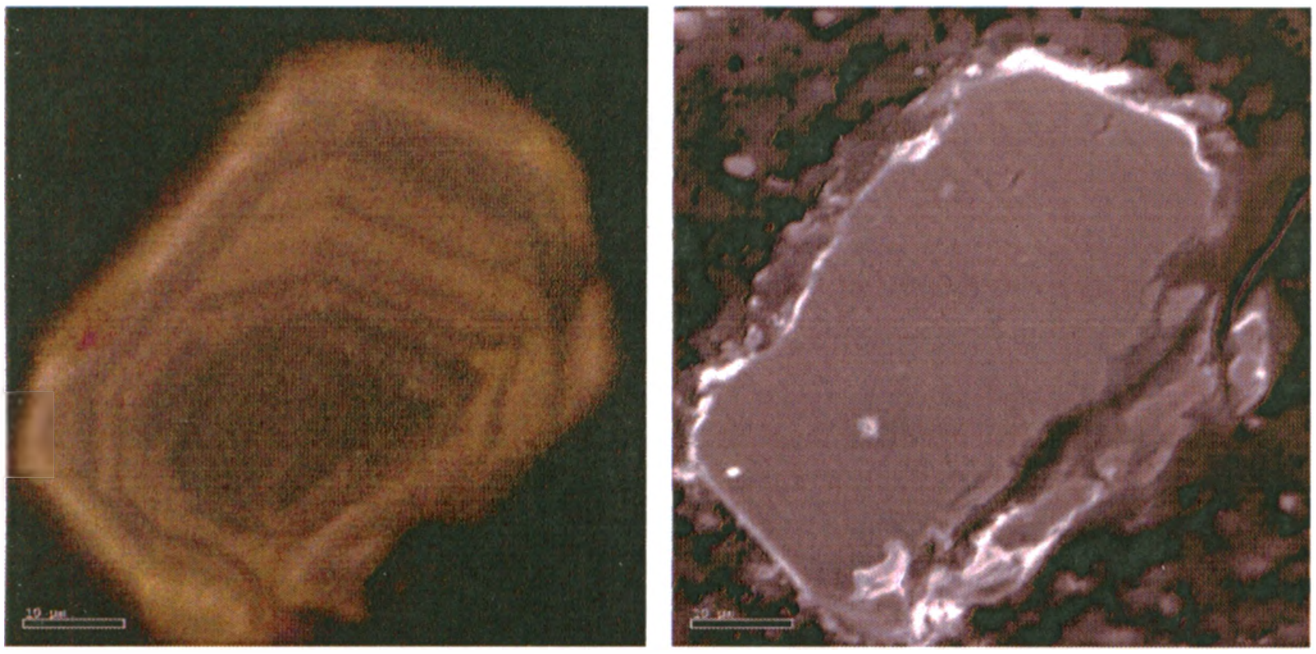

Grain 14

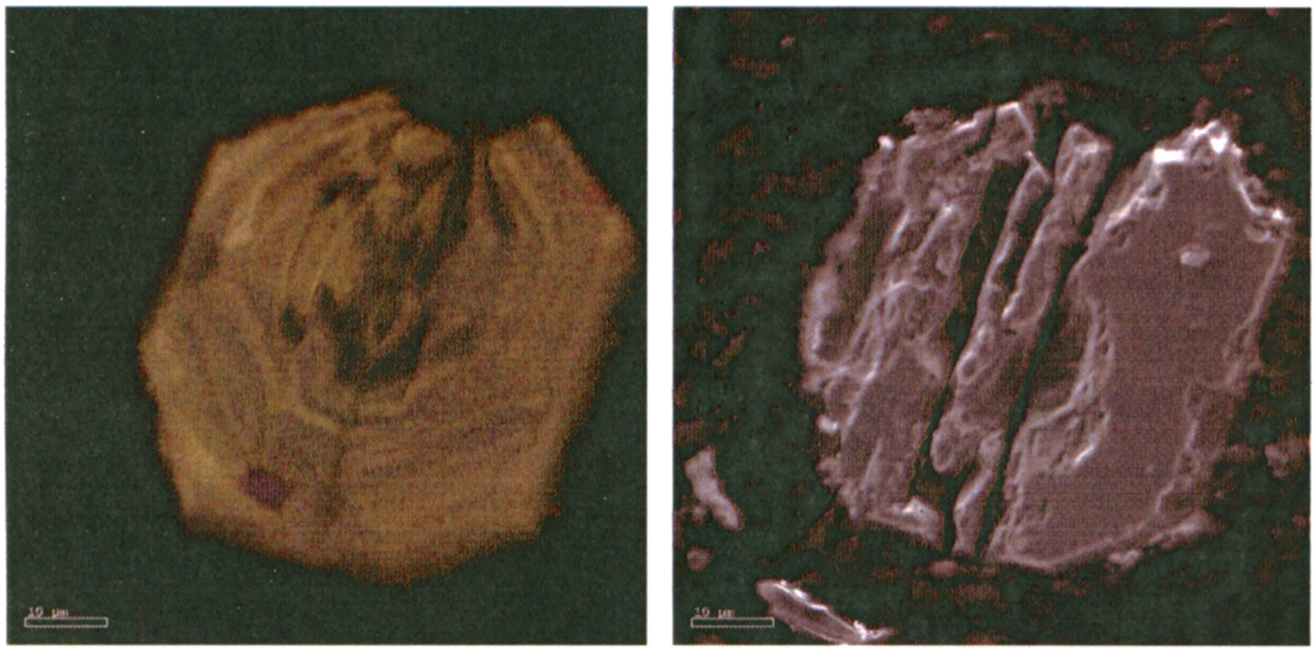

Grain 17

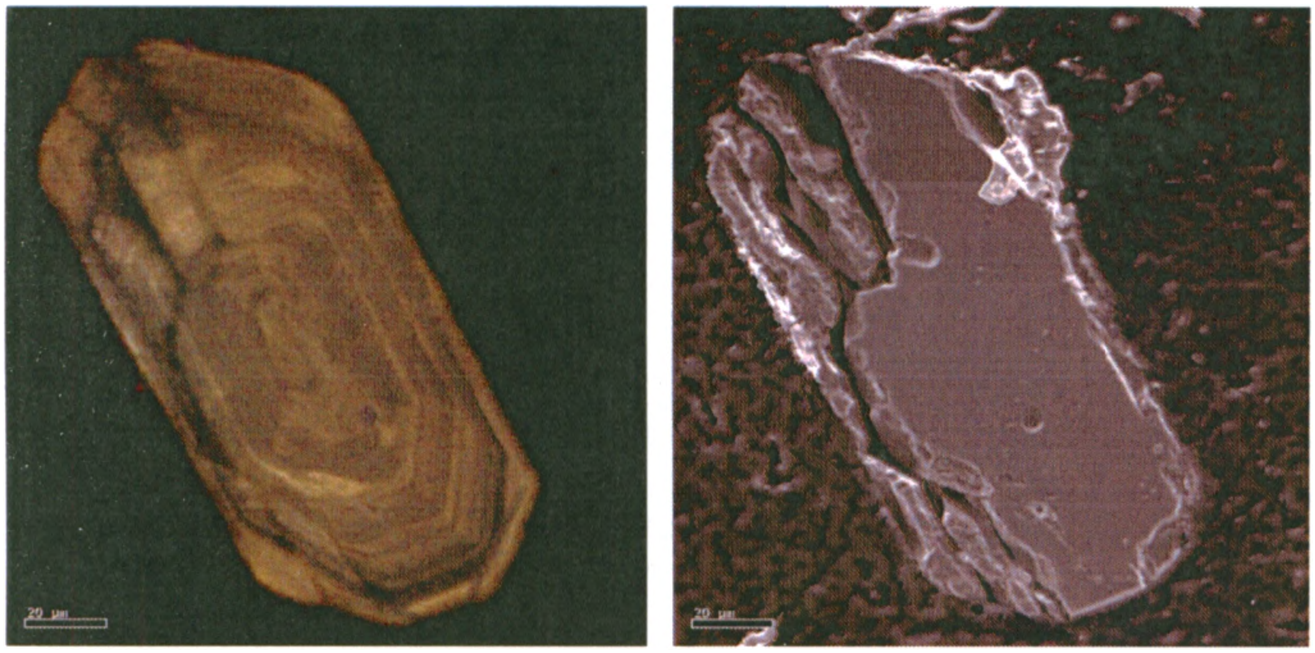

Grain 18

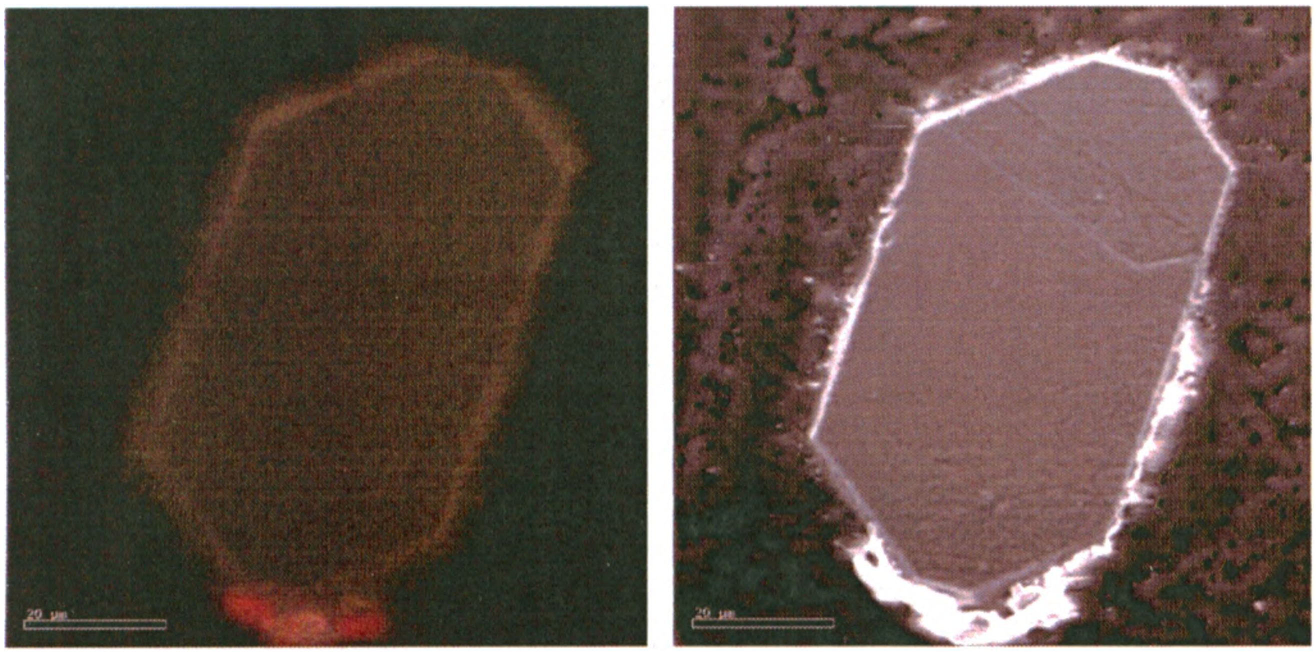

Grain 19

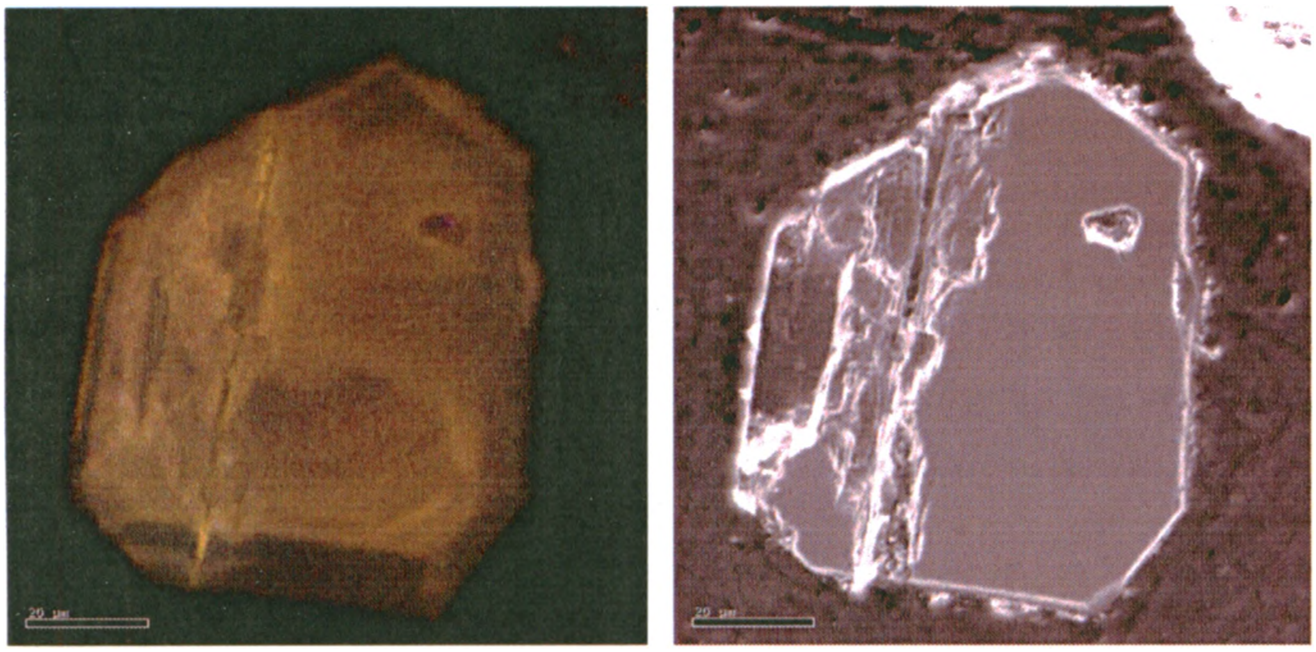

Grain 20

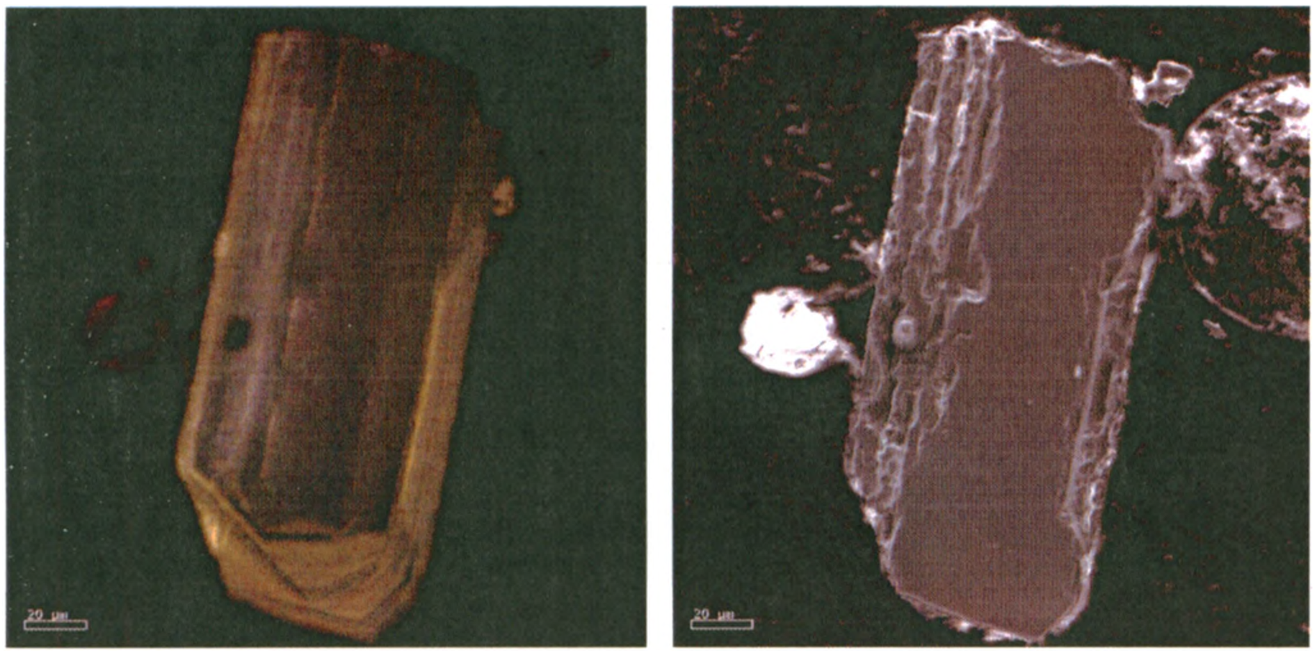

Grain 21

SEM-CL and SE Zircon Images → X- Bentonite – Slide A

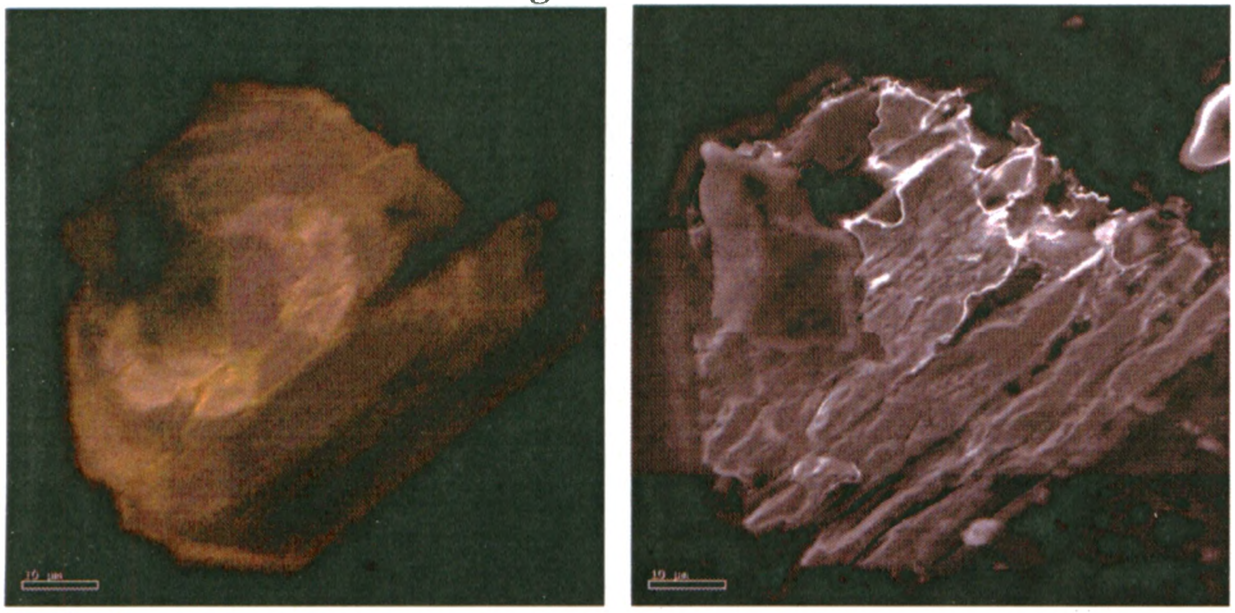

Grain 1

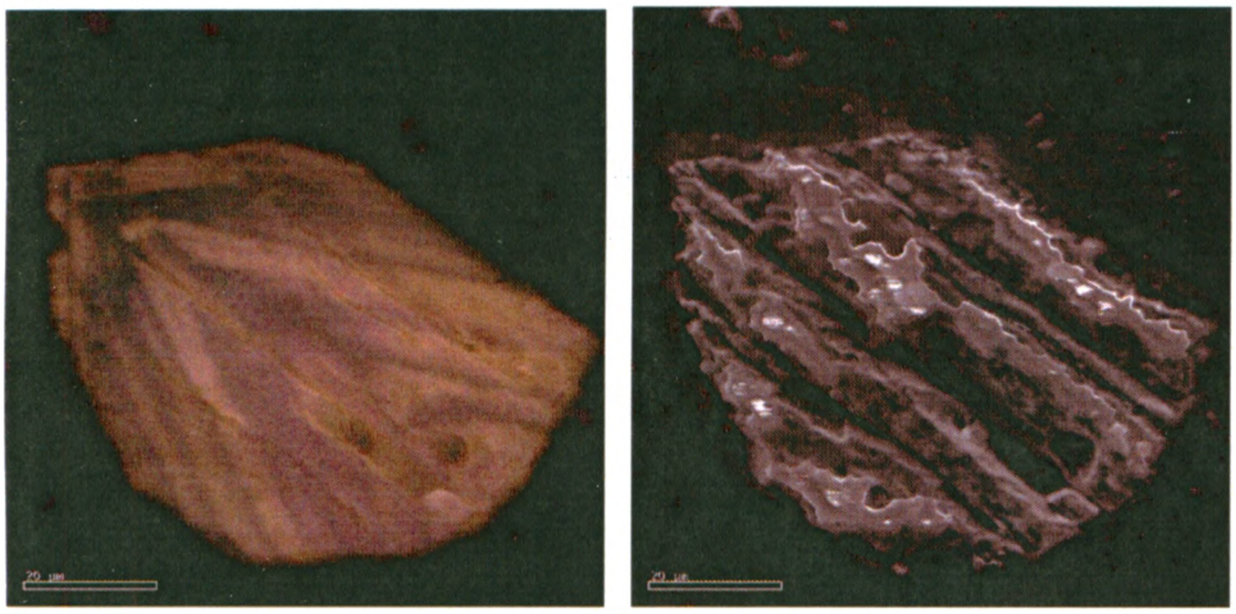

Grain 2

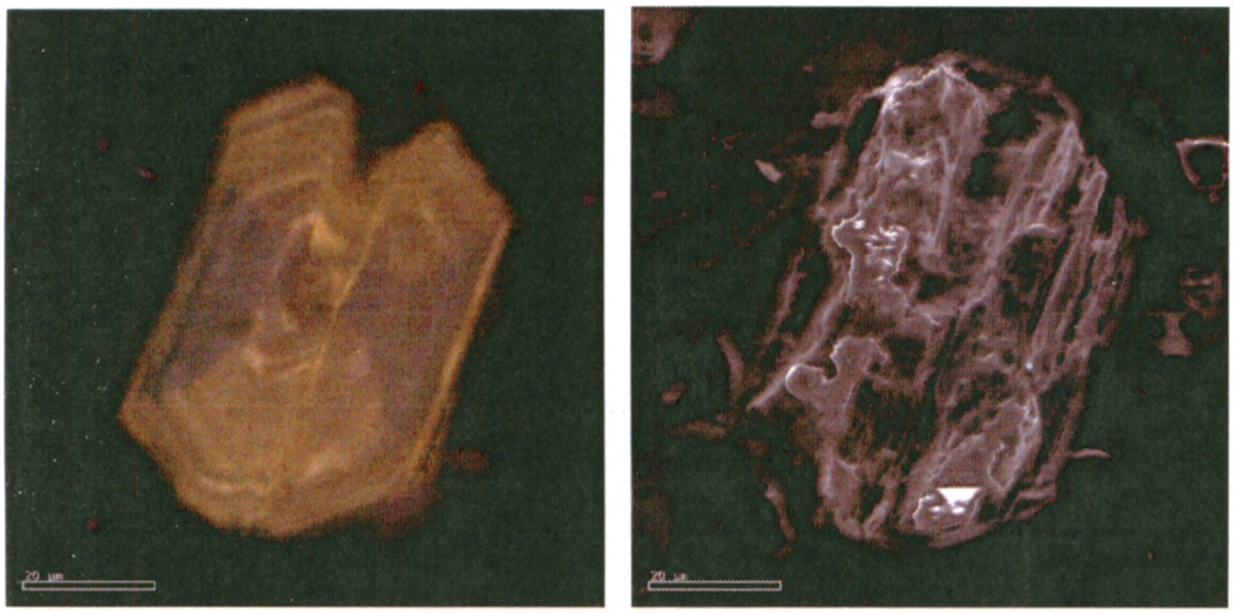

Grain 3

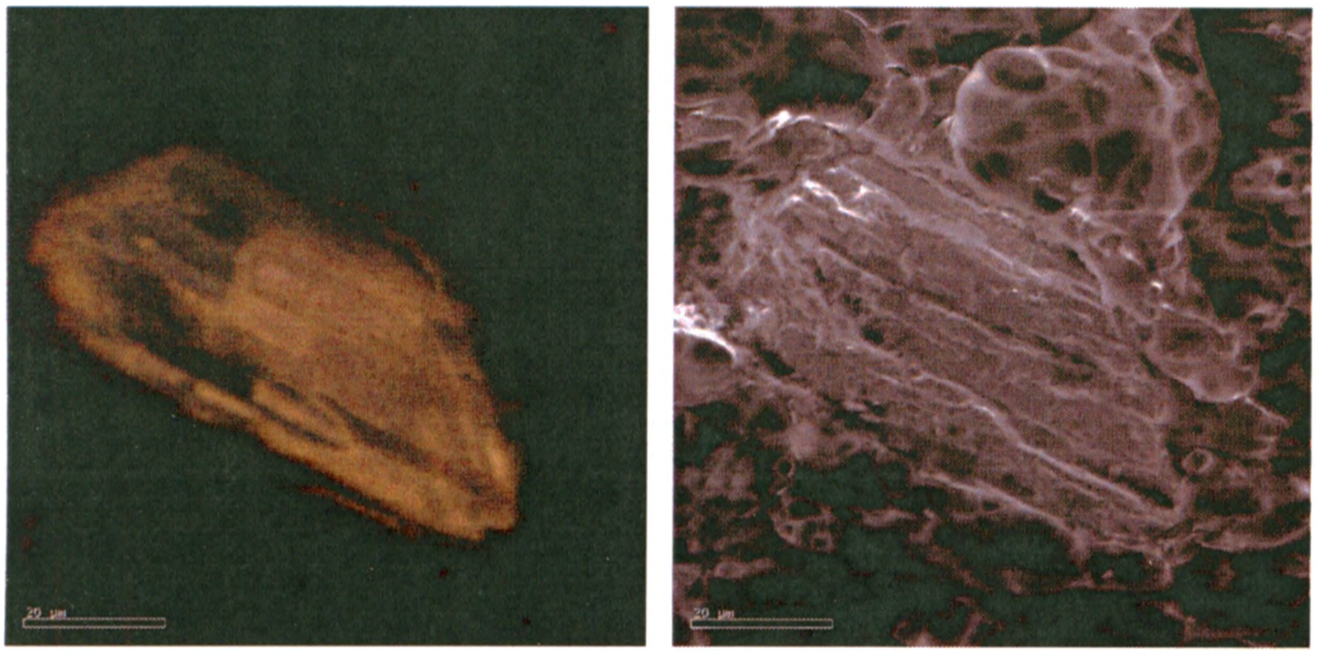

Grain 5

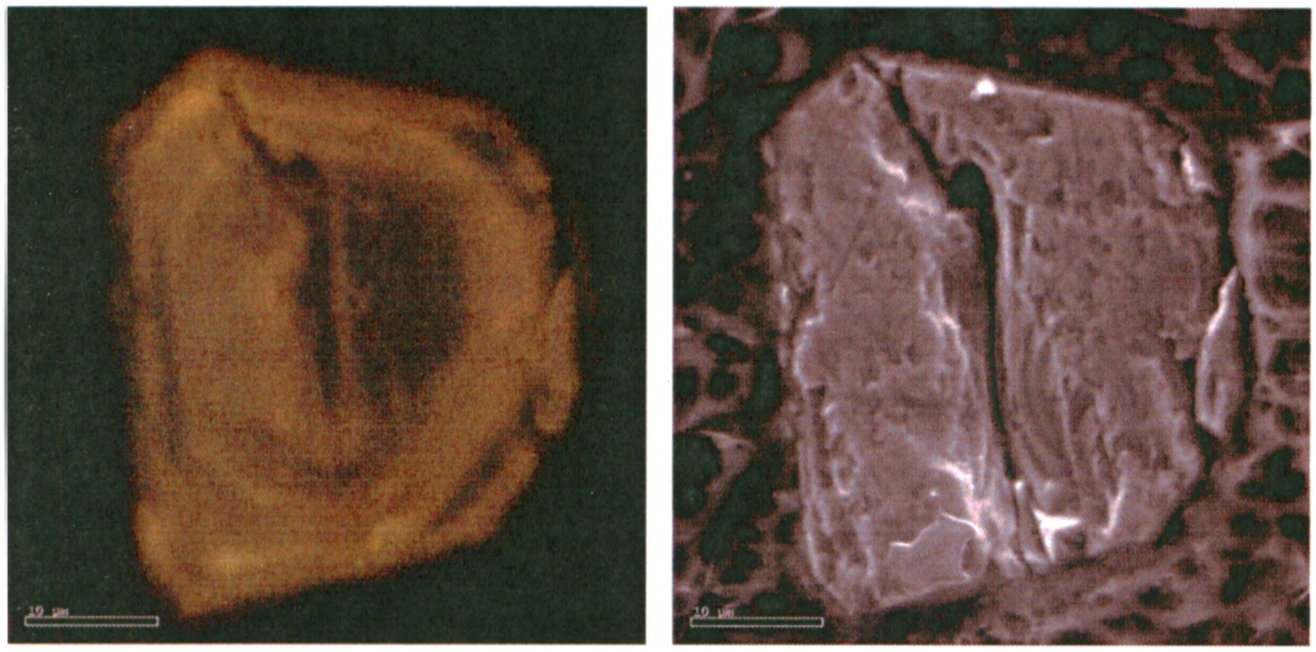

Grain 6

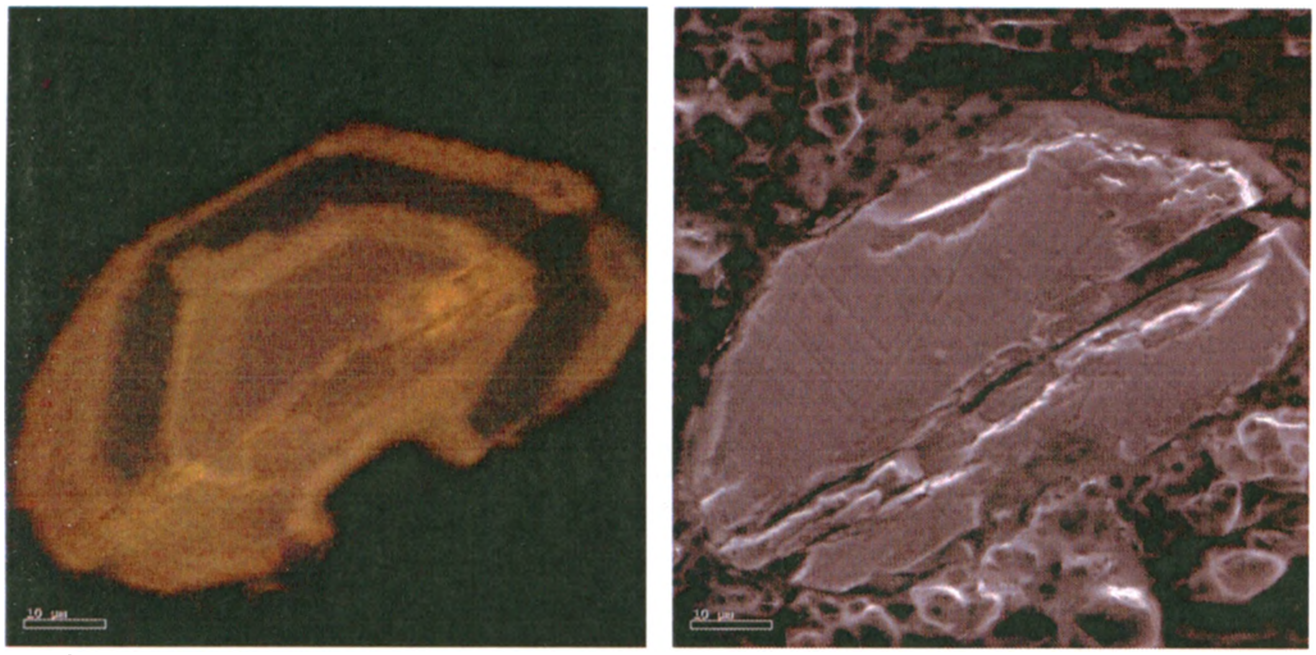

Grain 7

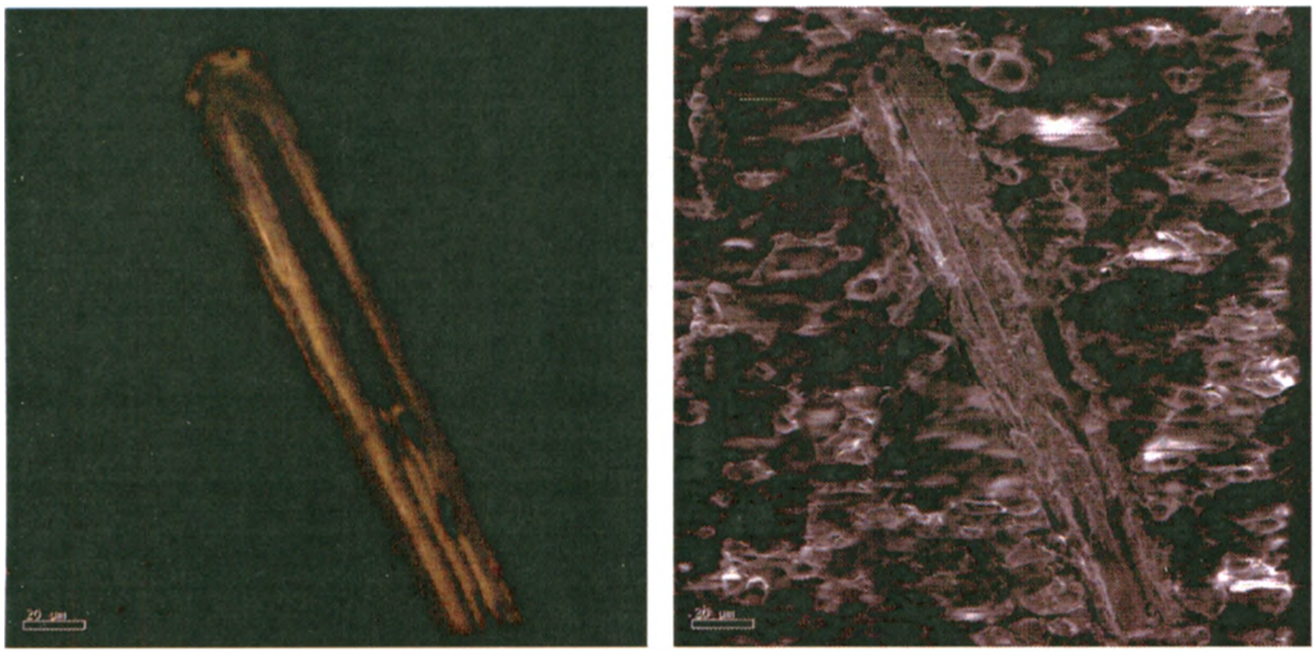

Grain 8

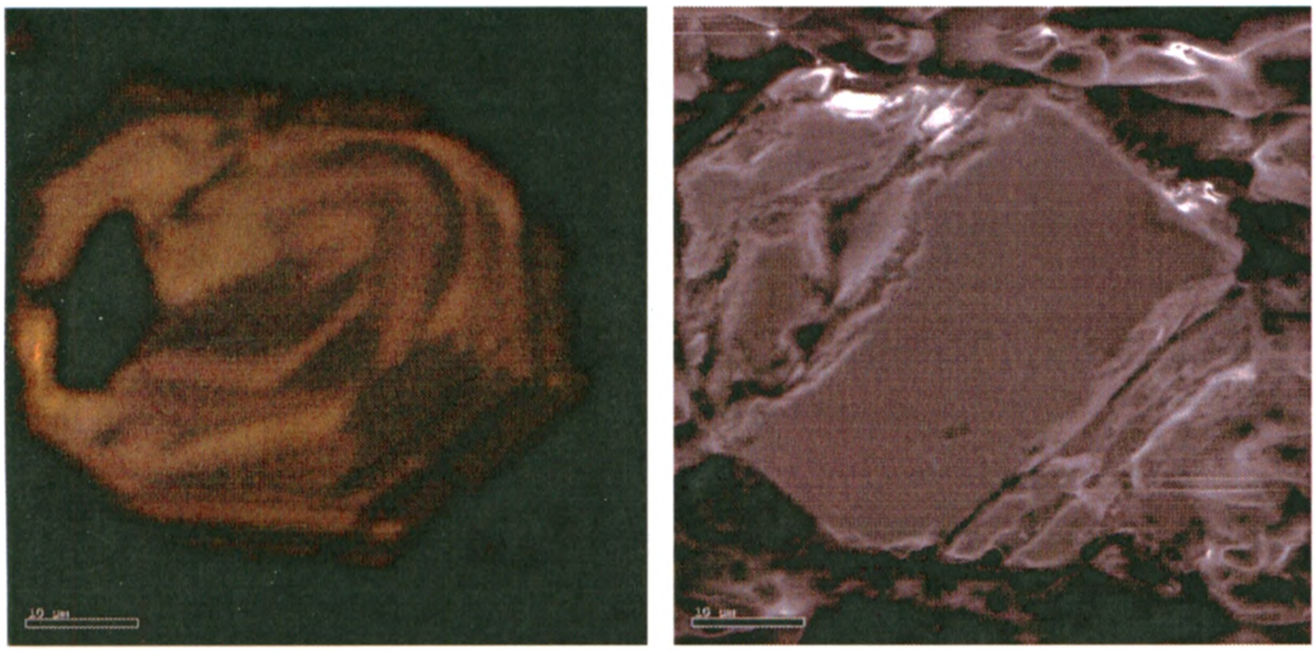

Grain 9

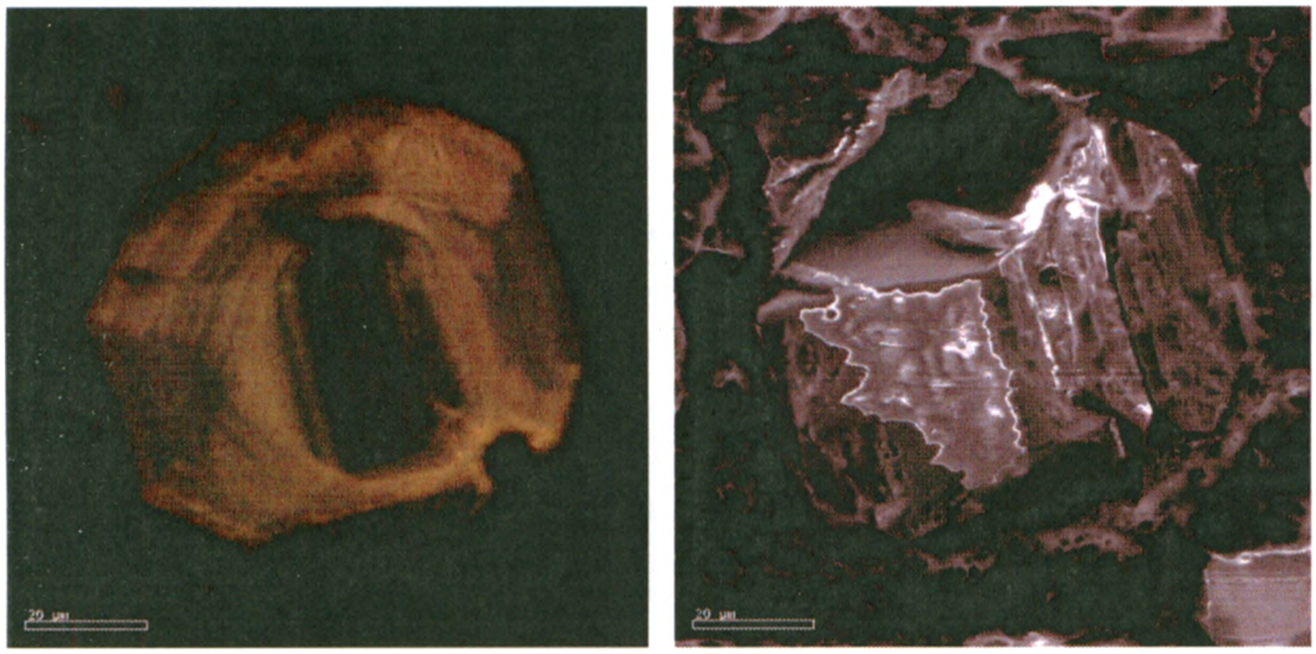

Grain 11

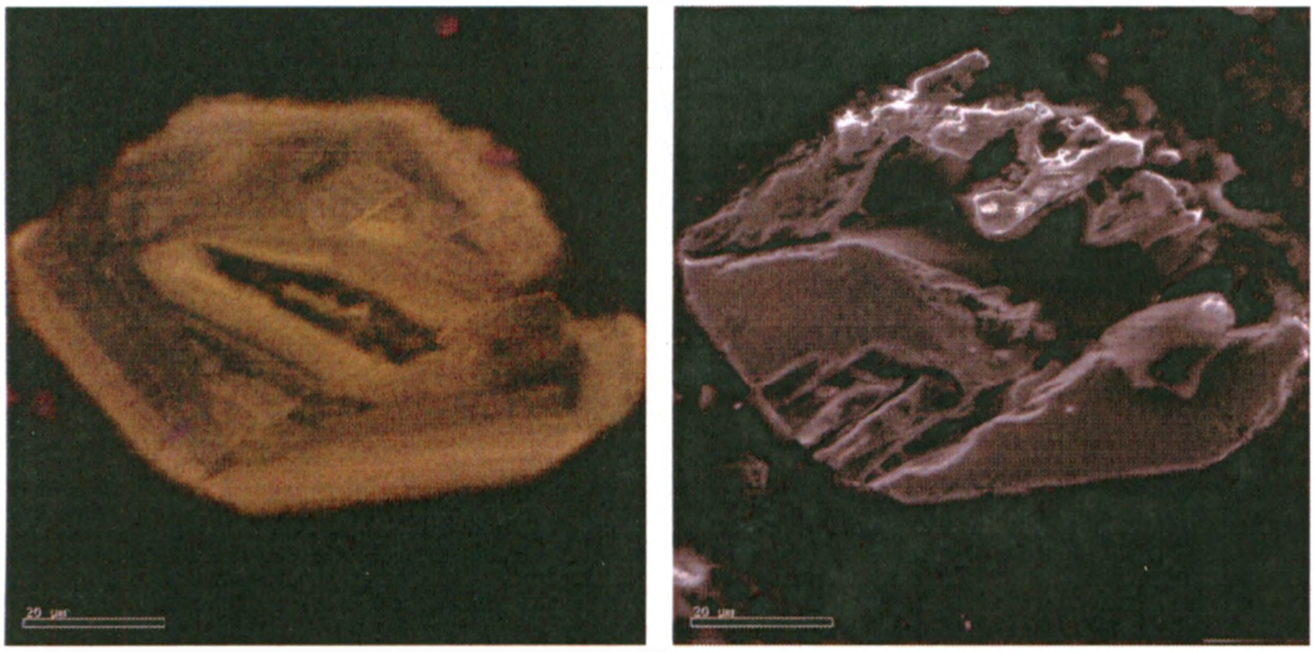

Grain 12

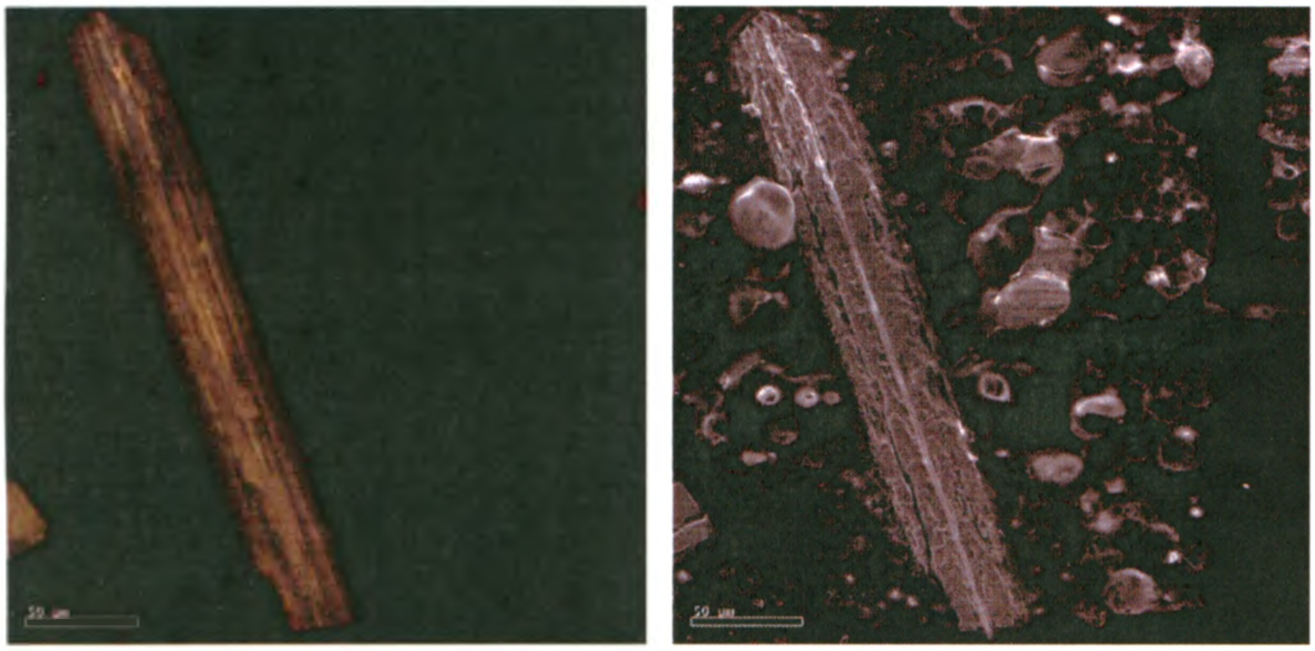

Grain 14

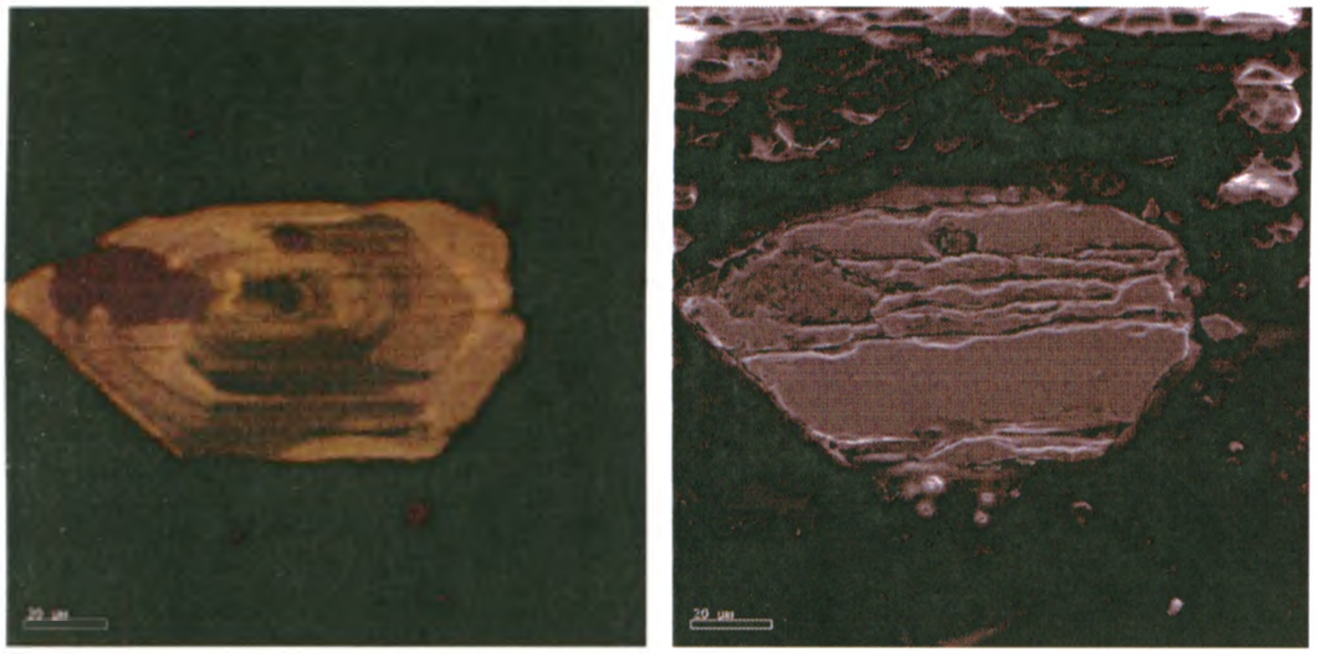

Grain 15

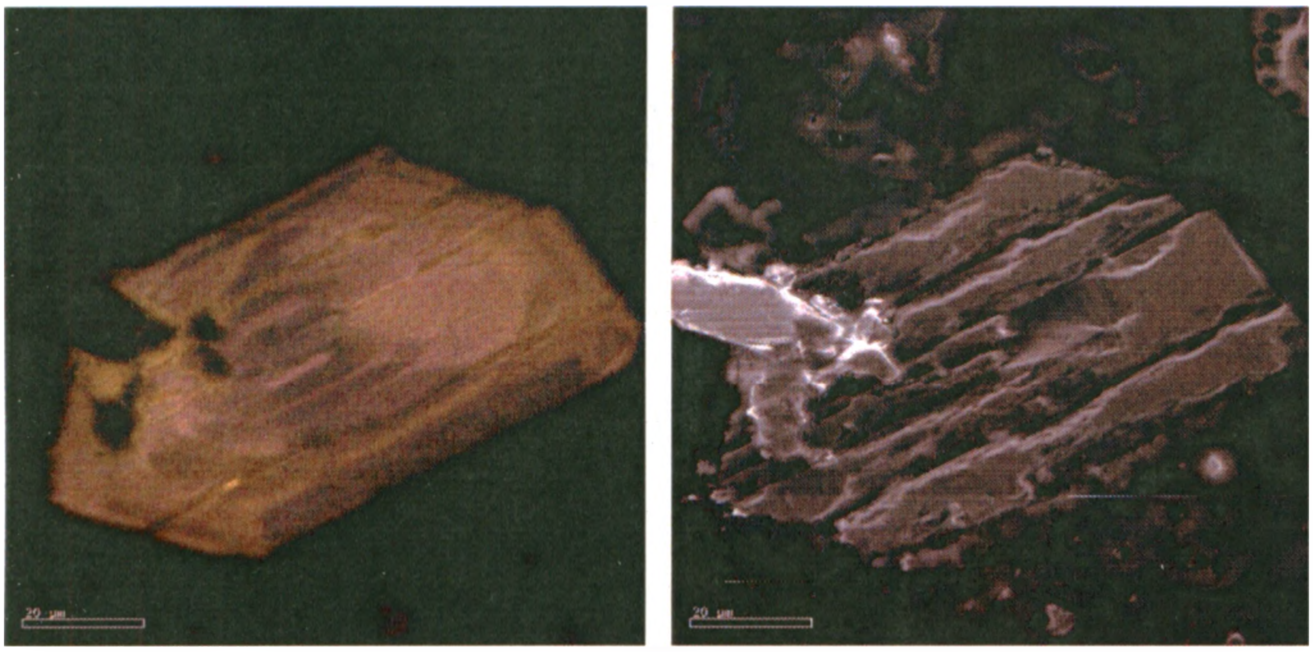

Grain 16

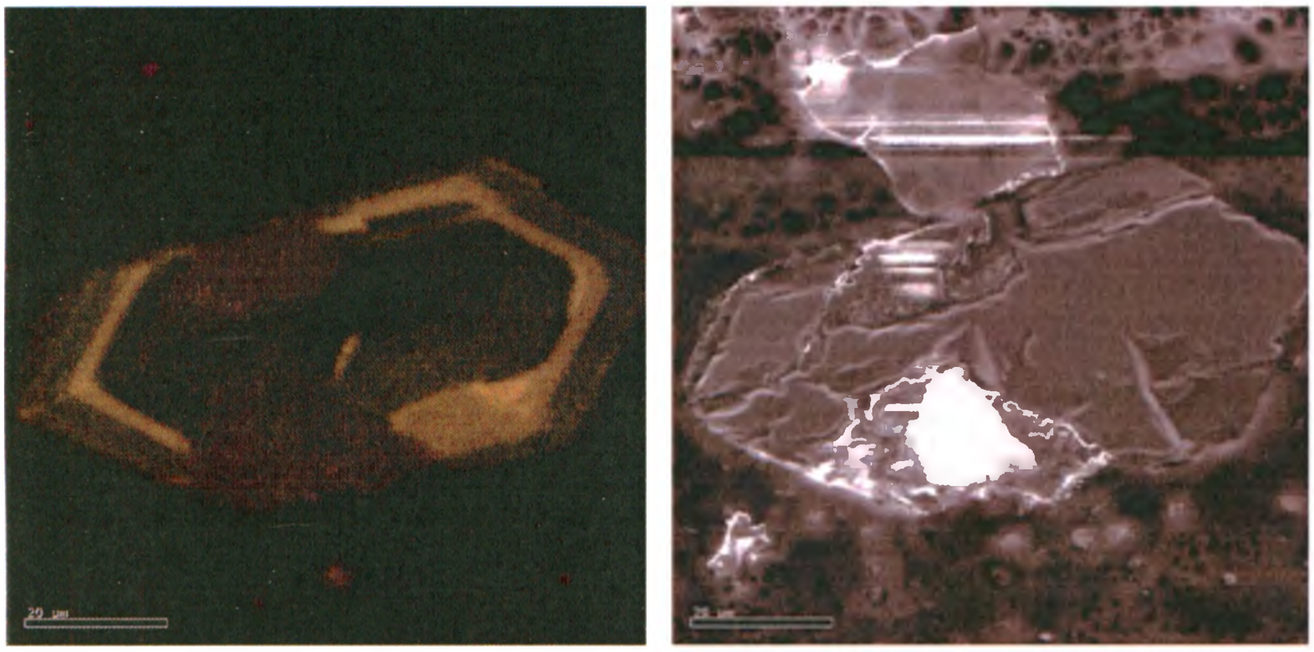

Grain 18

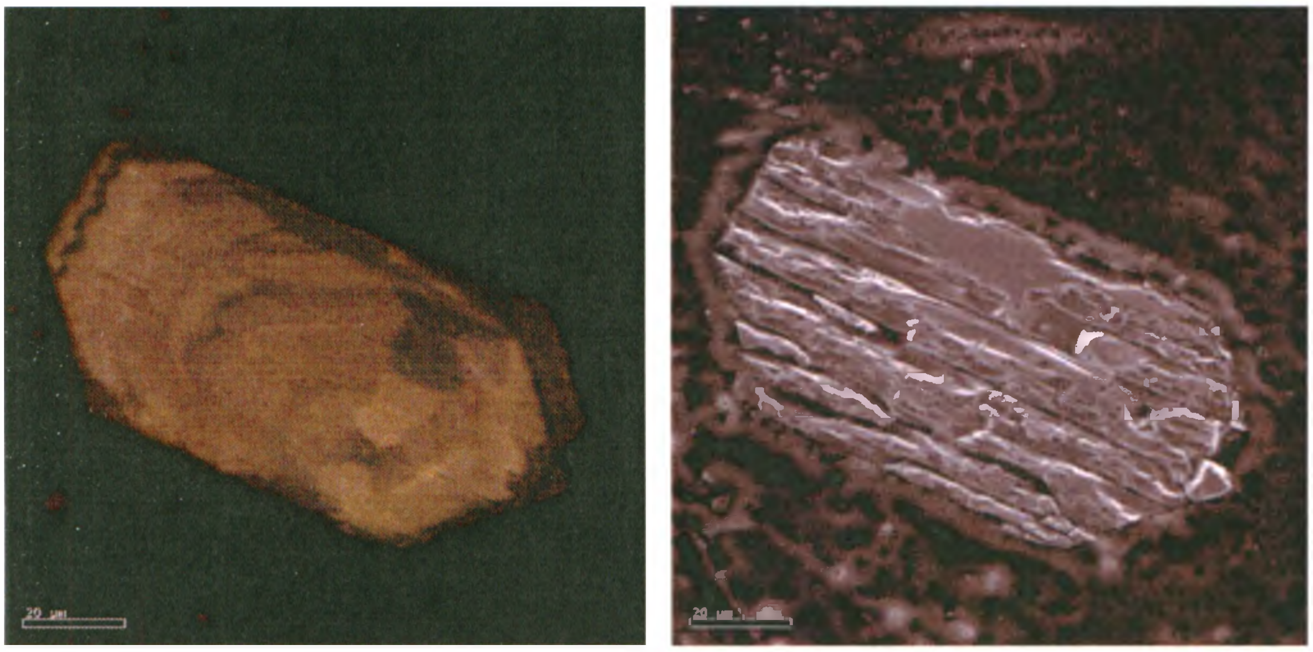

Grain 19

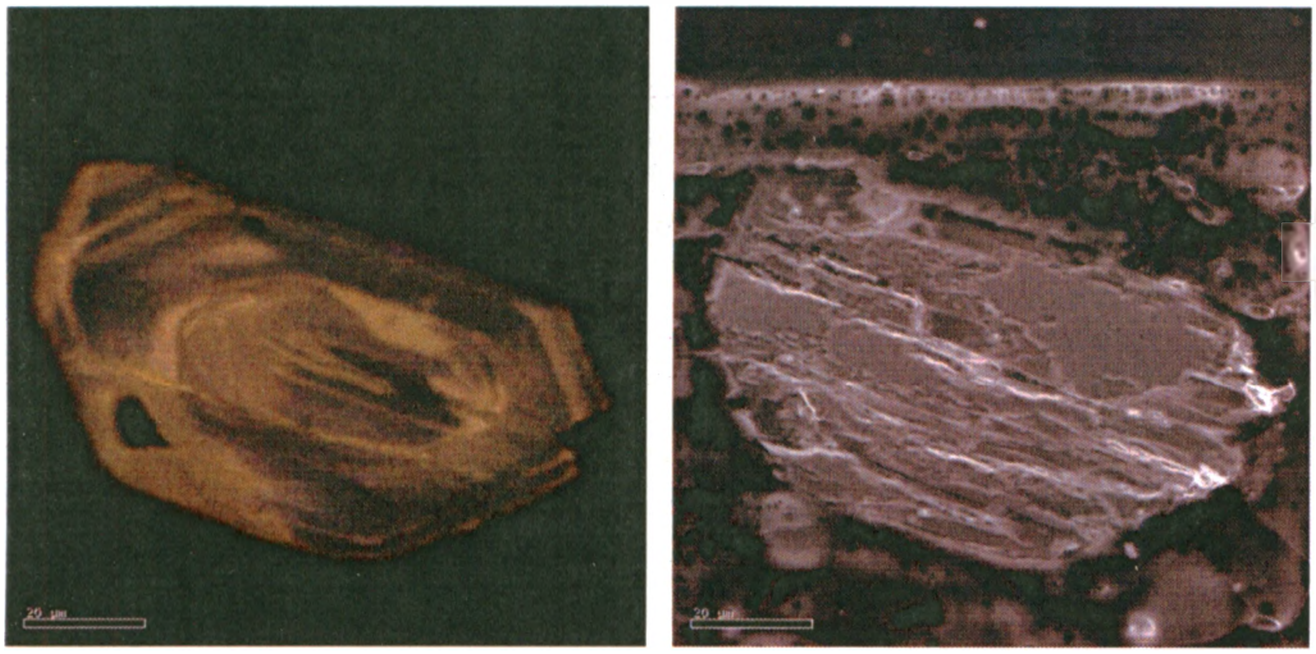

Grain 20

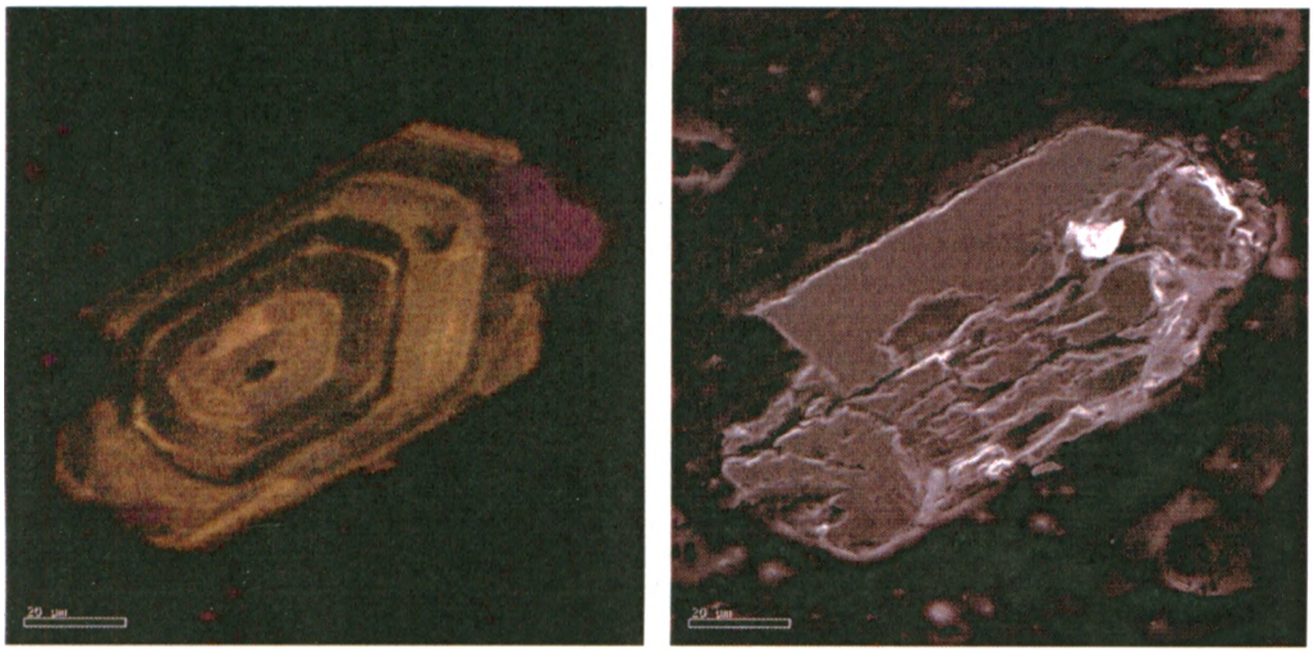

Grain 21

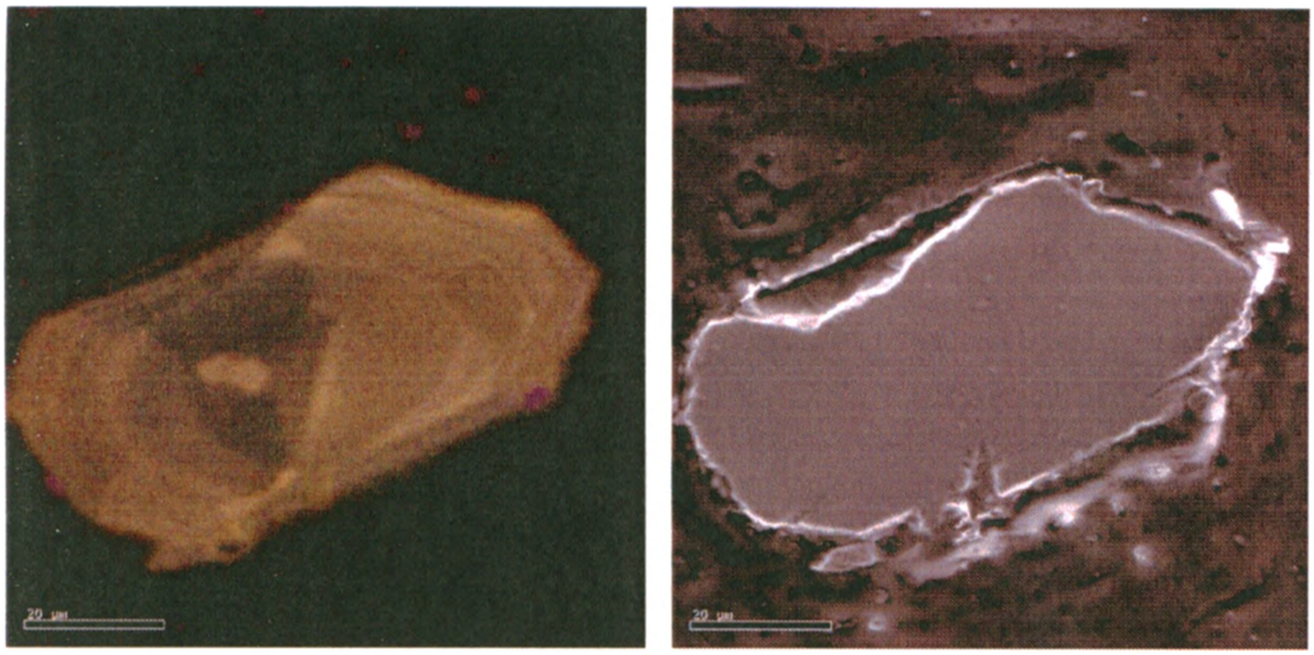

Grain 22

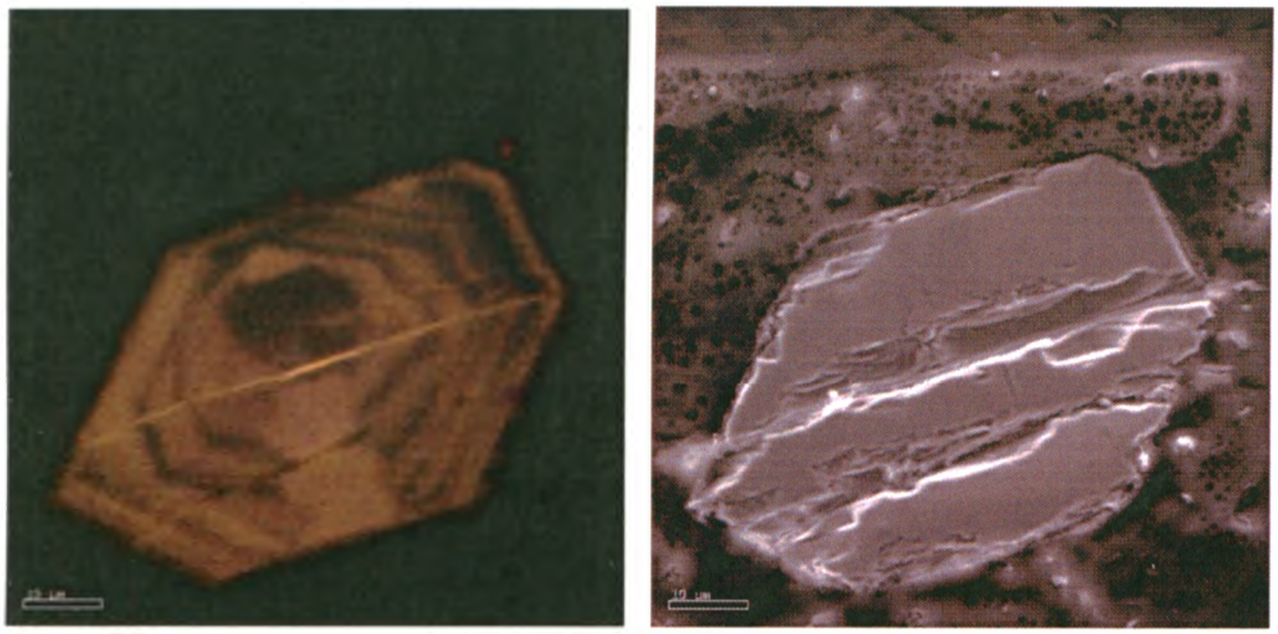

Grain 23

SEM-CL and SE Zircon Images → X- Bentonite – Slide B

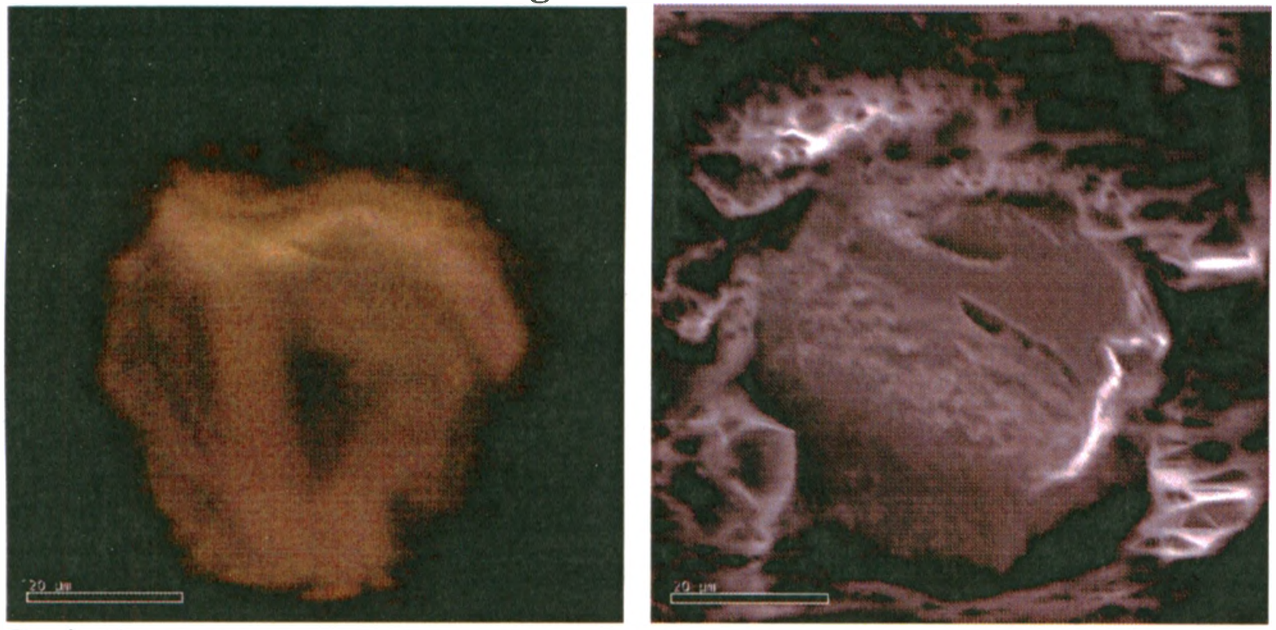

Grain 1

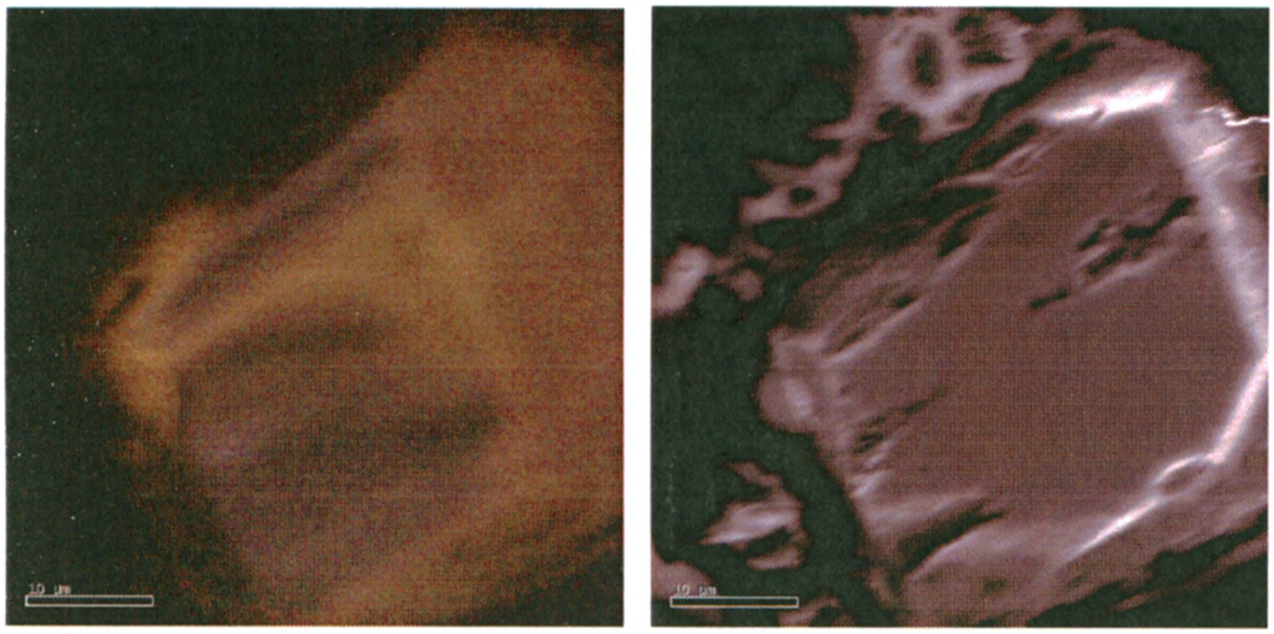

Grain 4

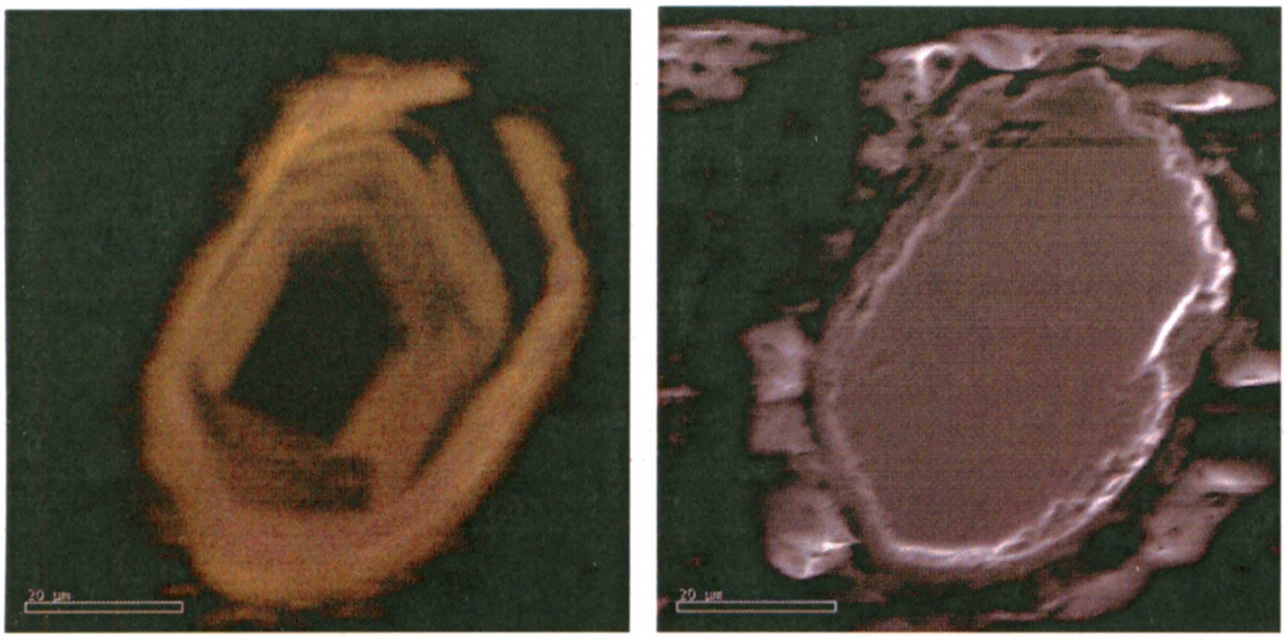

Grain 5

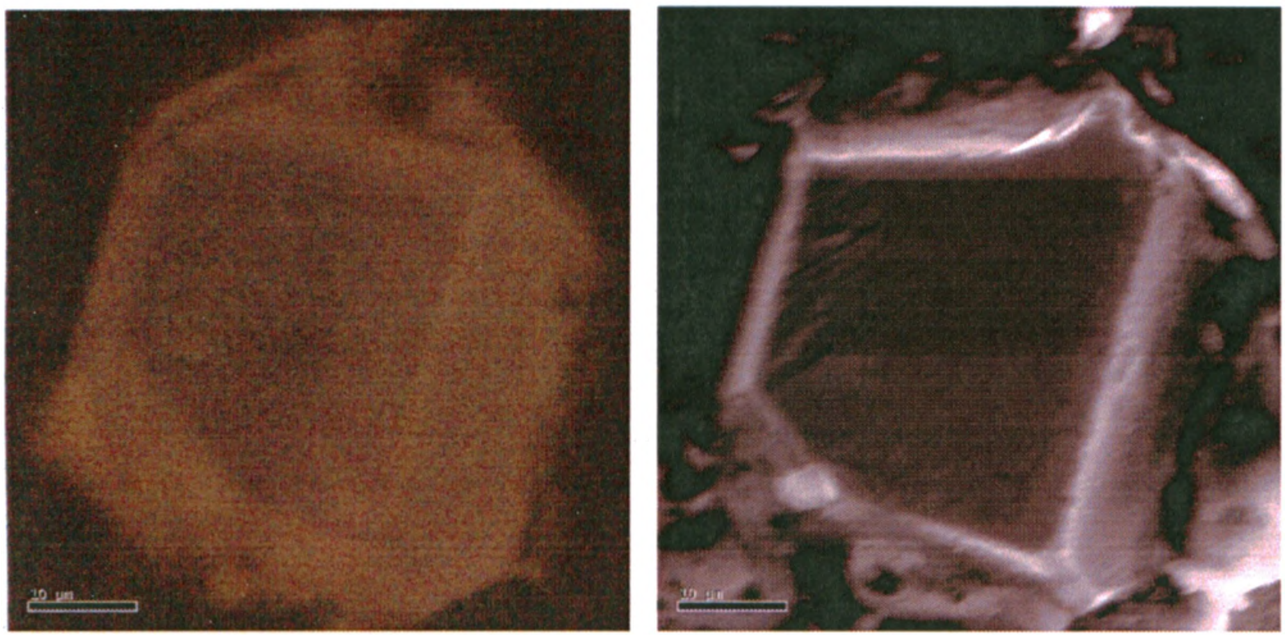

Grain 6

SEM-CL and SE Zircon Images → X- Bentonite – Slide C

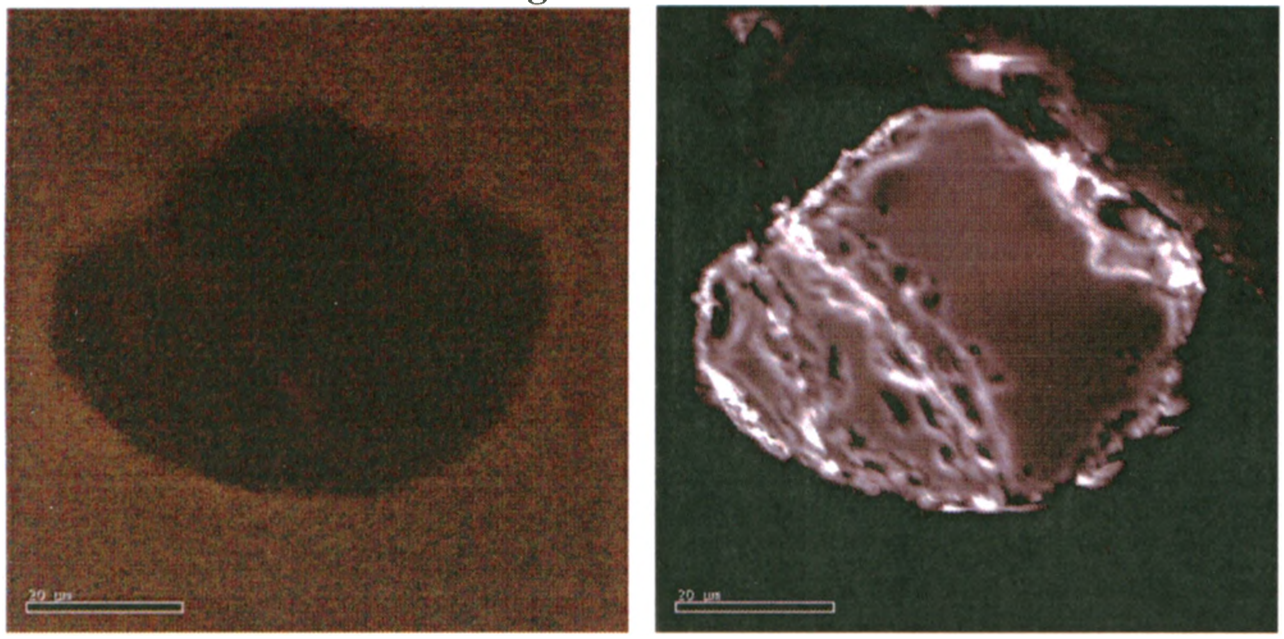

Grain 1

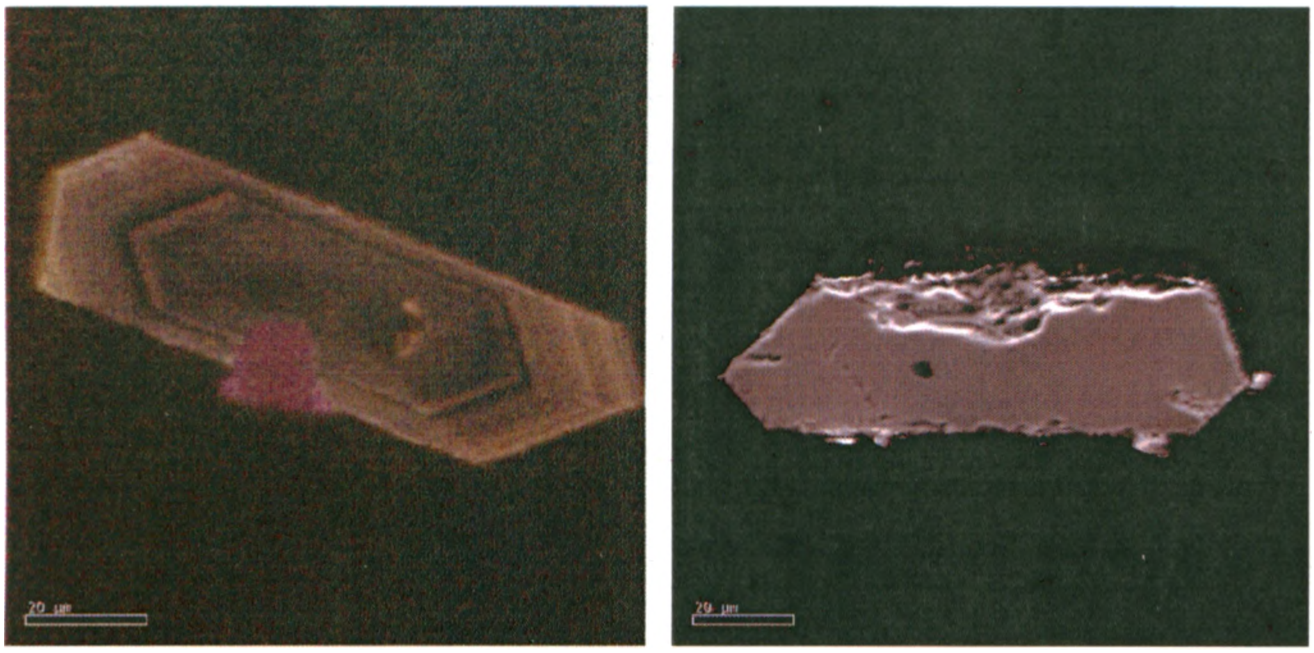

Grain 2

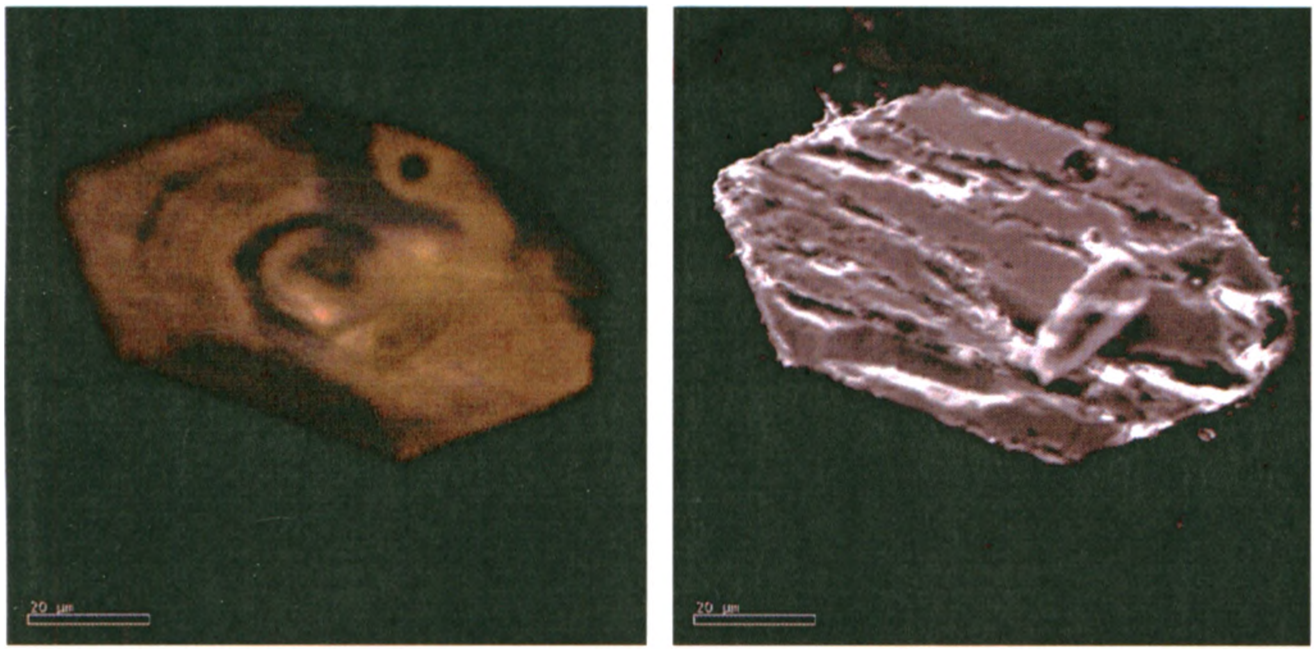

Grain 3

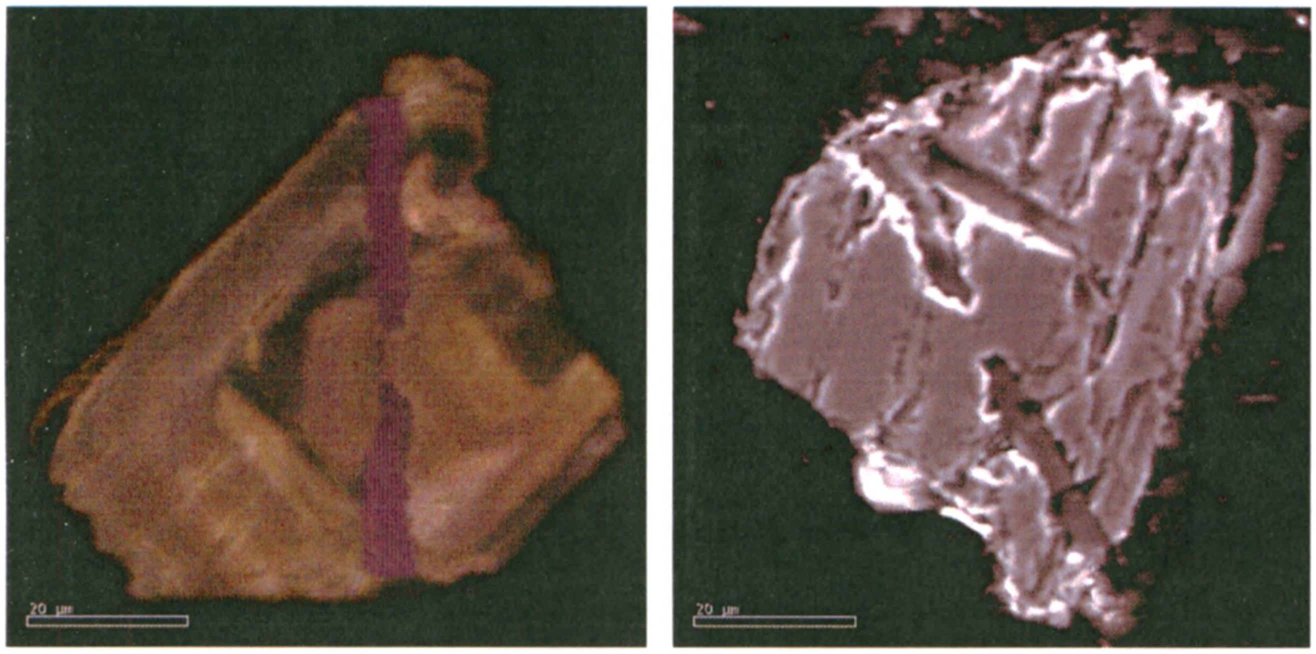

Grain 4

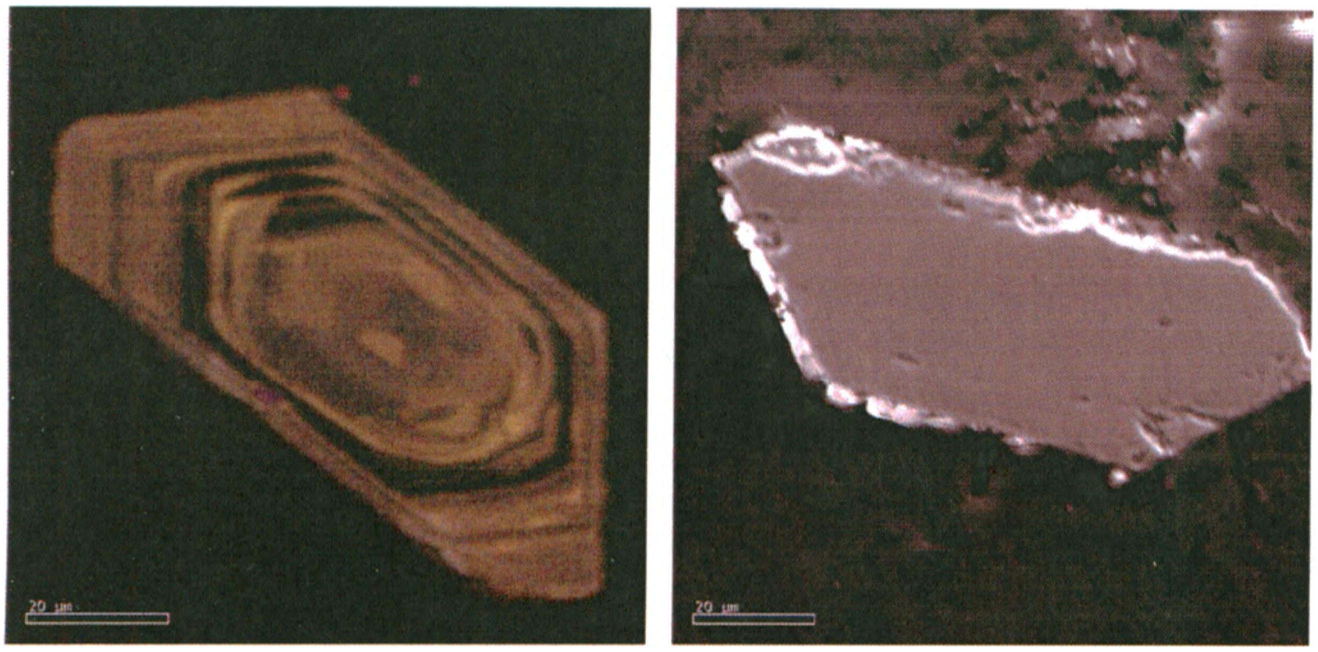

Grain 5

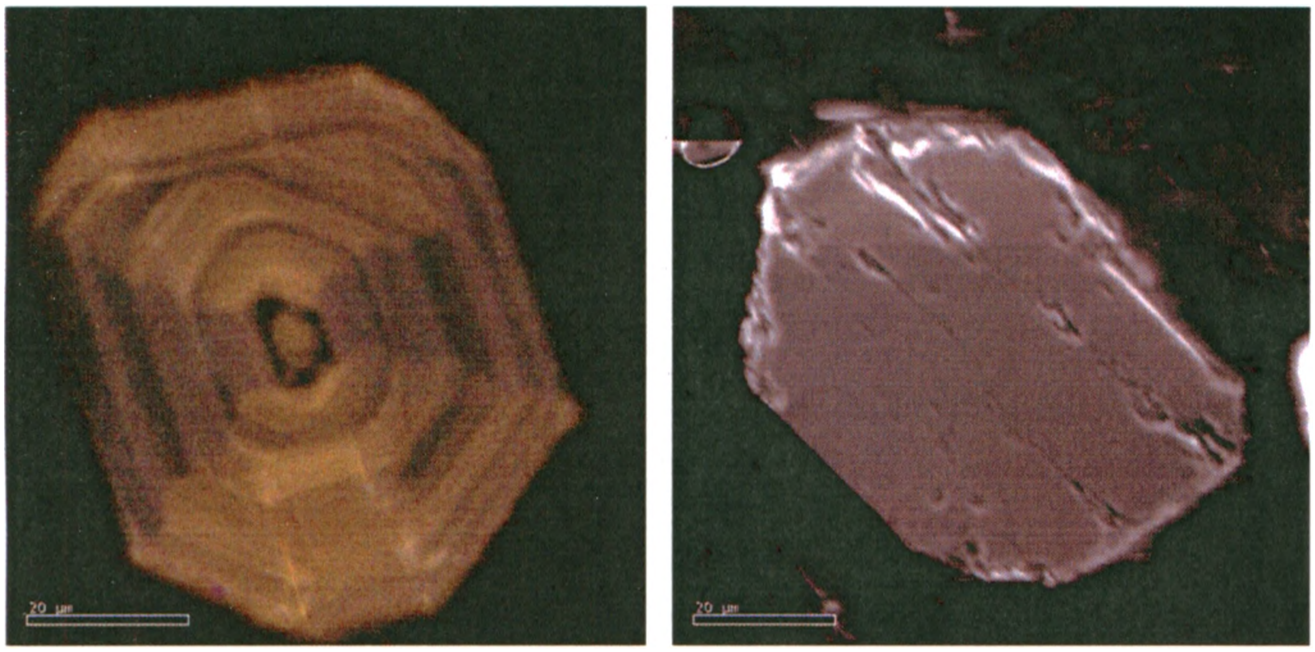

Grain 6

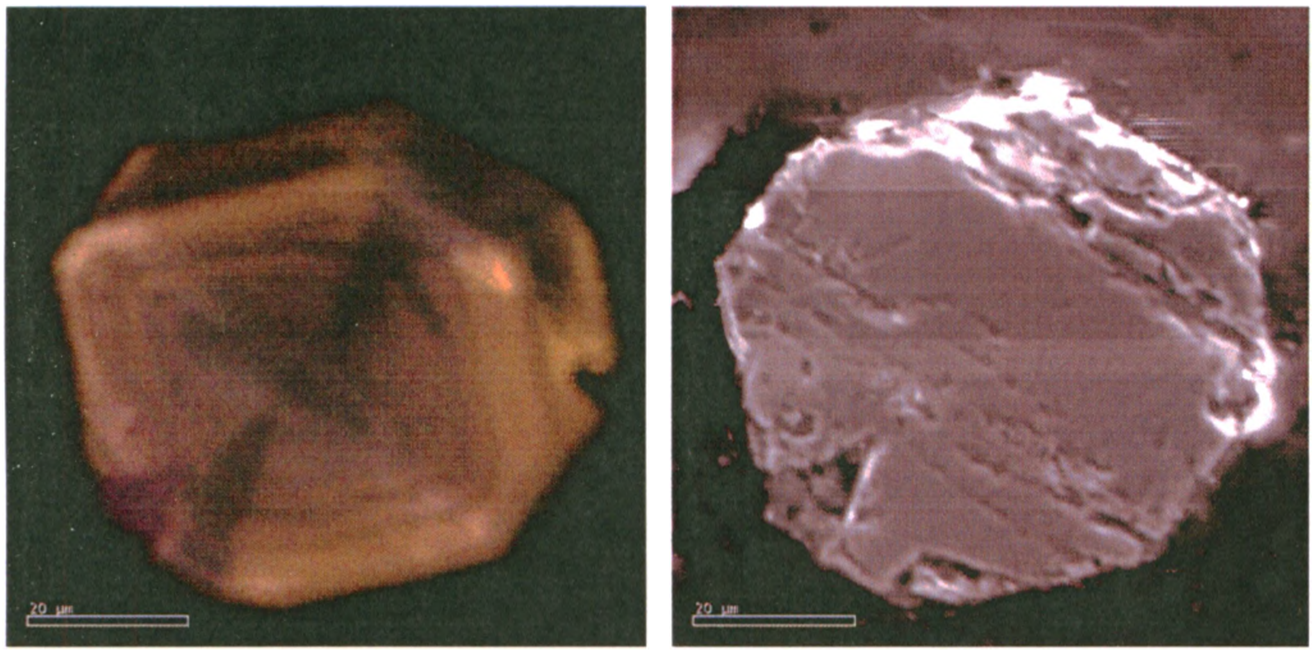

Grain 7

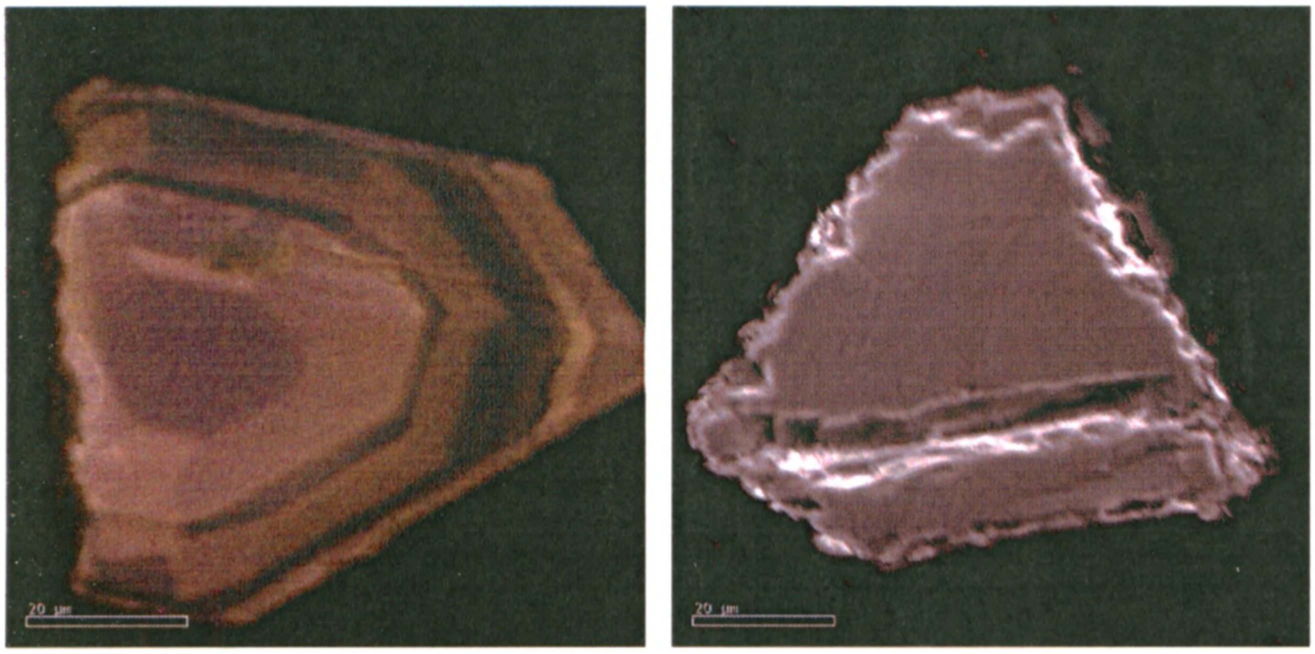

Grain 8

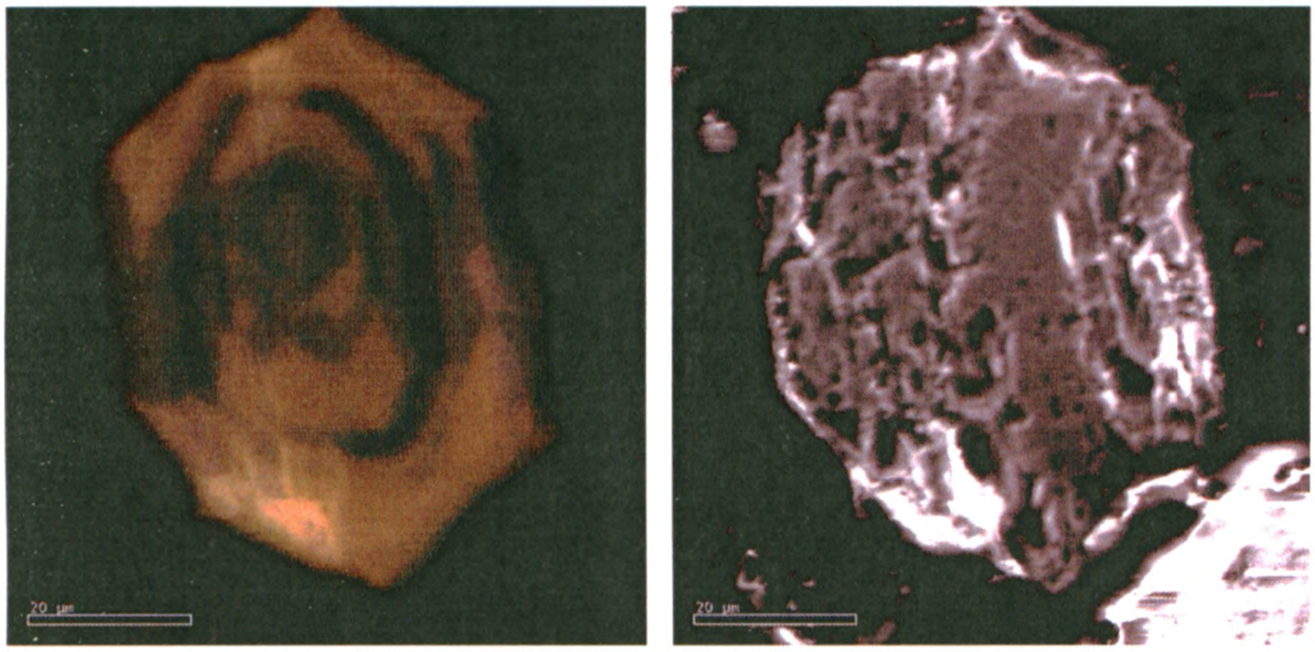

Grain 9

Appendix D: Kowallis et al. (1995) recalculated Concordia diagram

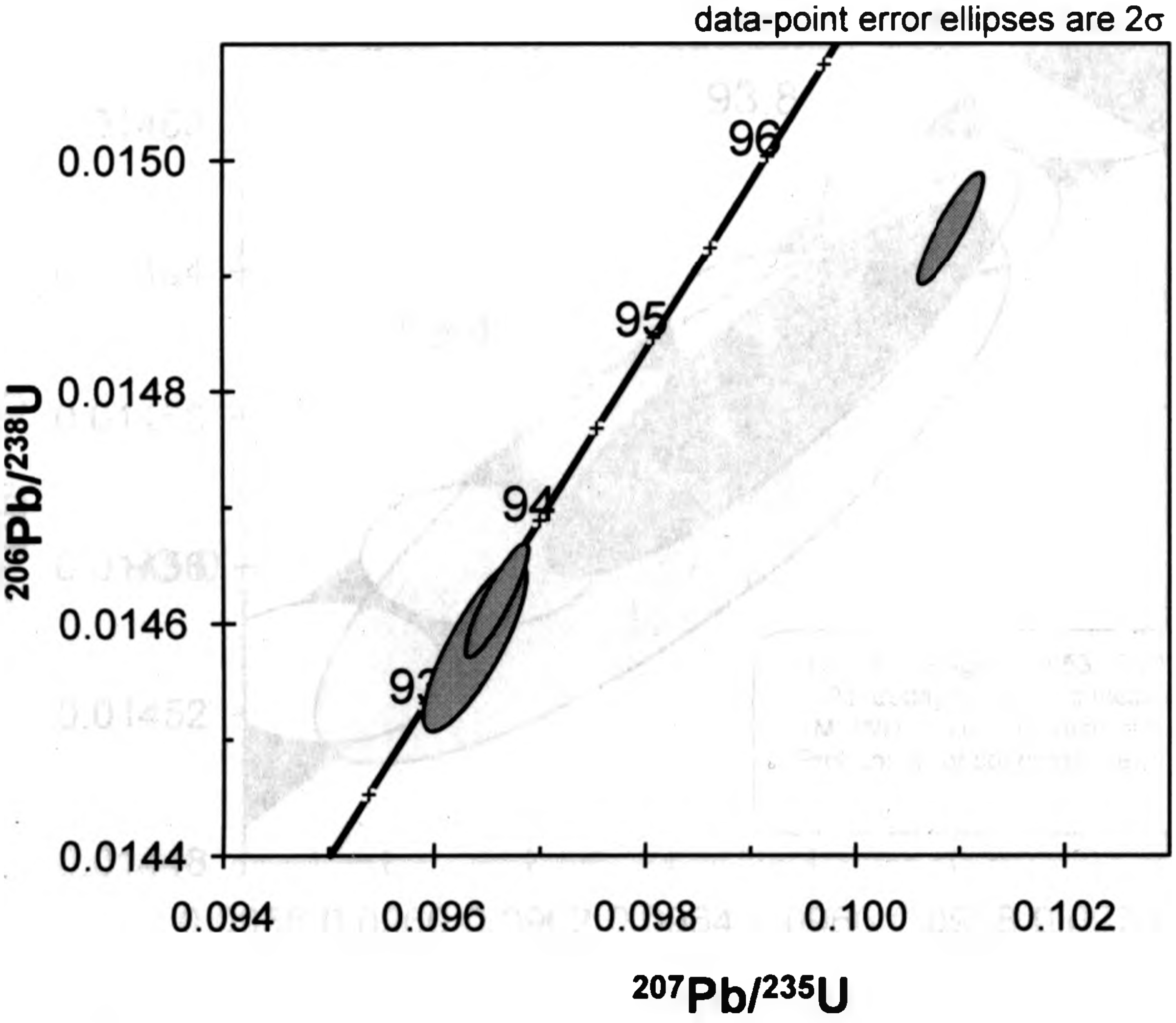

Including the oldest Fraction 3

Kowallis et al. (1995) recalculated Concordia diagram – Concordia age

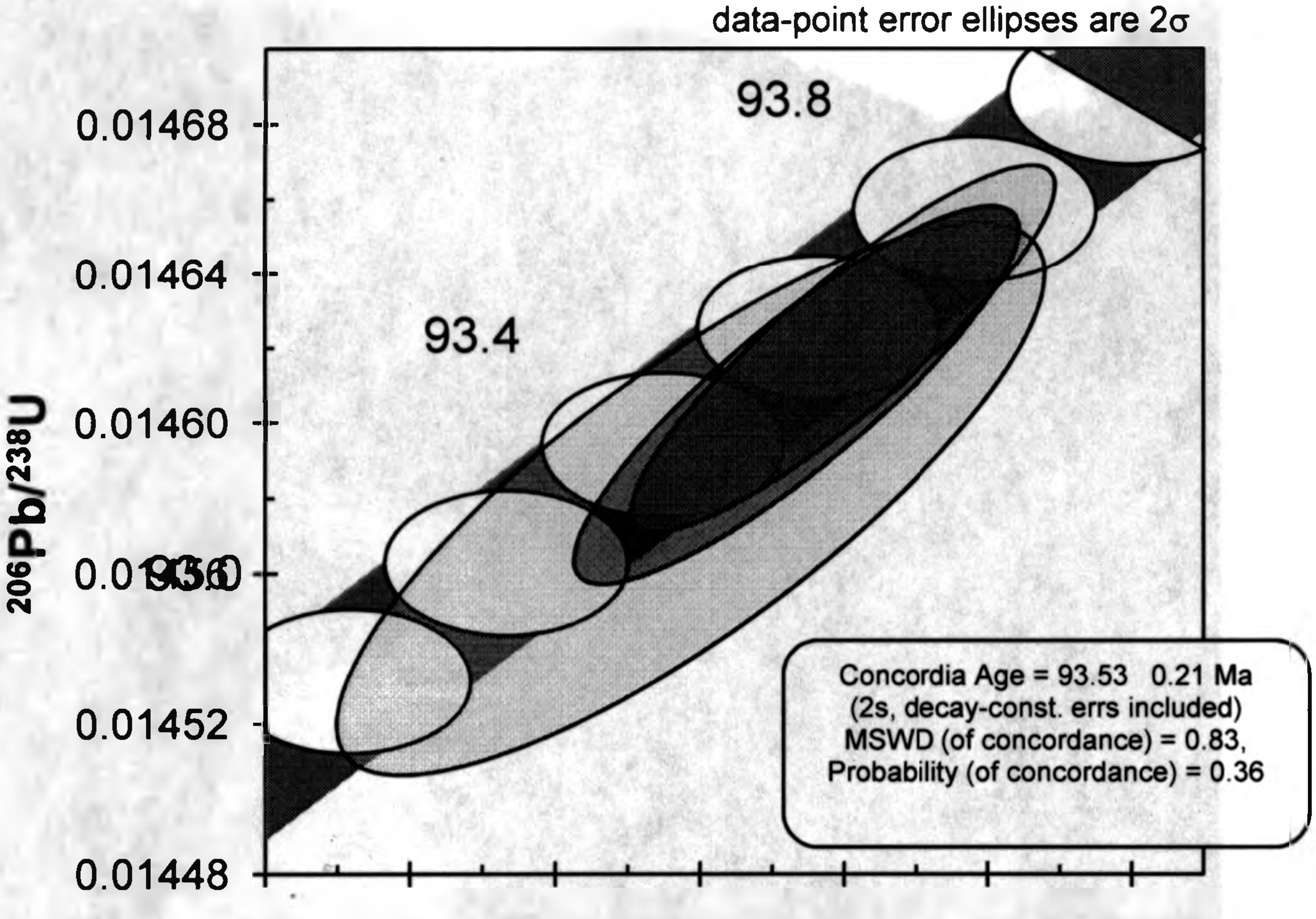

Concordia age of the Kowallis et al. data, which assumes no Pb-loss

Appendix E: Field Photographs

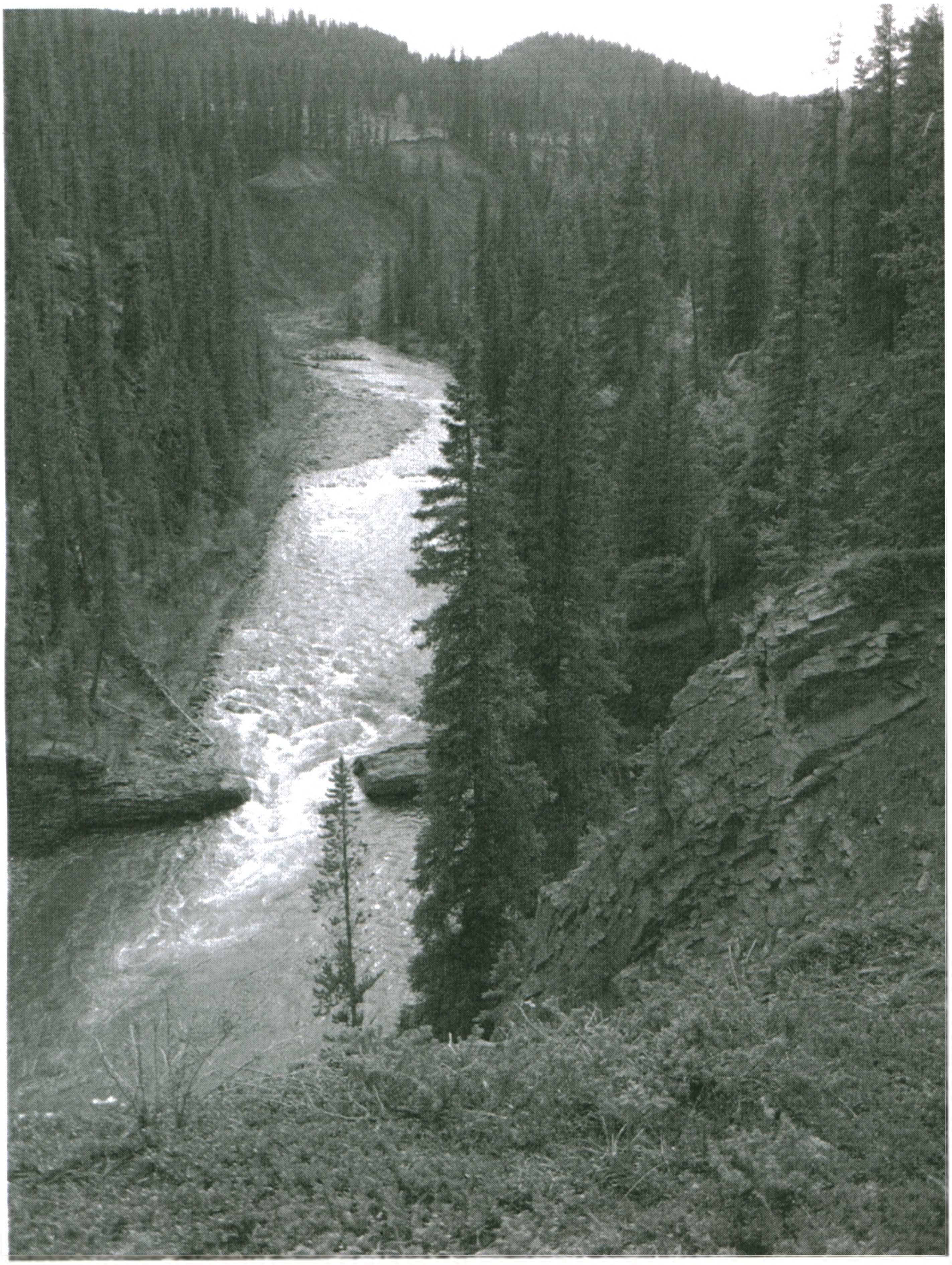

Burnt Timber Creek, Alberta

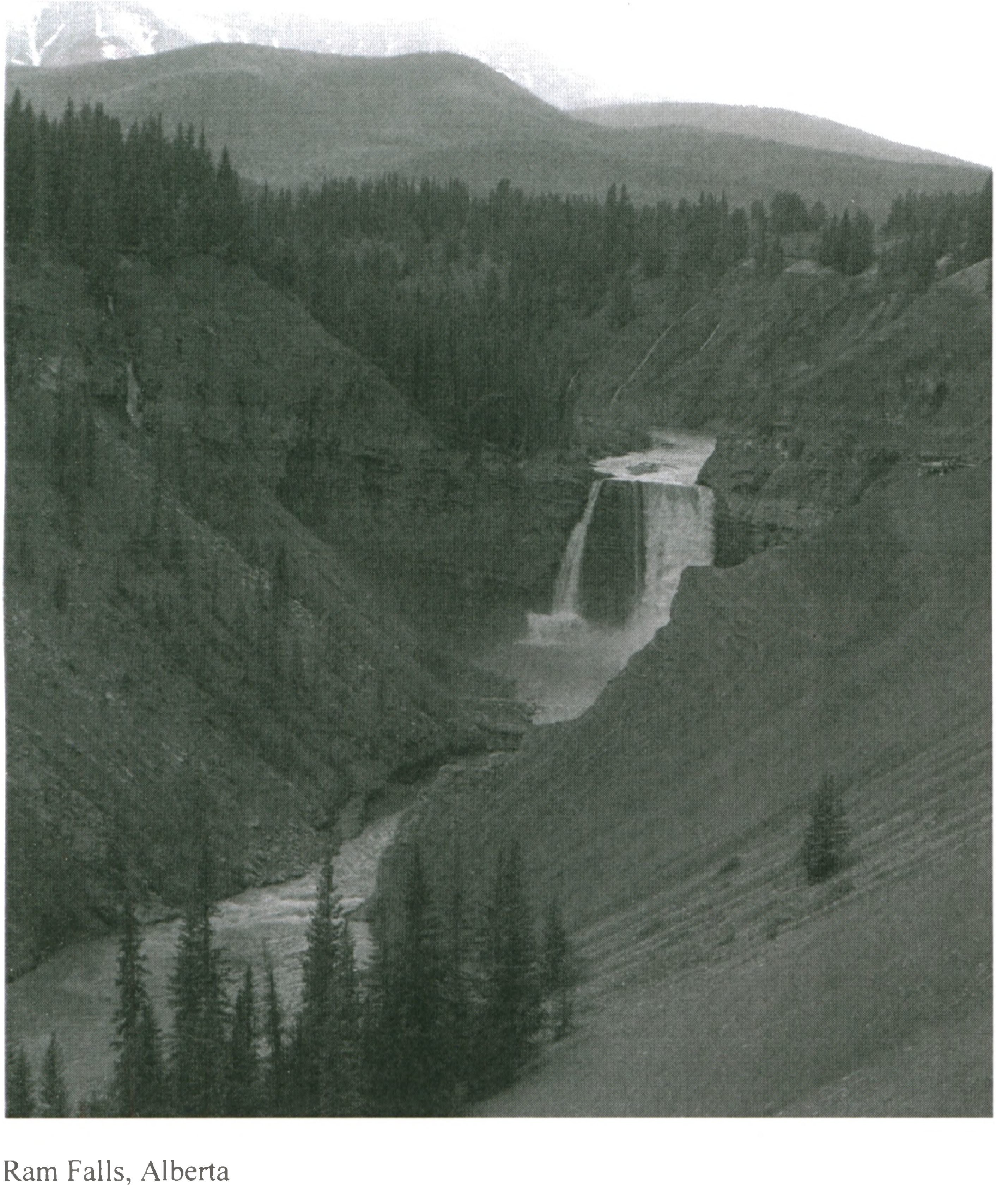

Ram Falls, Alberta

Sampling the Bighorn River Bentonite at Ram Falls, Alberta